Short Pulse X-Ray Generation in Synchrotron Radiation Sources

Ian Peter Stephen Martin

Wolfson College

University of Oxford

Thesis submitted in fulfilment of the requirements for the degree of Doctor of Philosophy at the University of Oxford

Trinity Term, 2011

Short Pulse X-Ray Generation in Synchrotron Radiation Sources

Ian Peter Stephen Martin, Wolfson College, University of Oxford

Thesis submitted in fulfilment of the requirements for the degree of Doctor of Philosophy at the University of Oxford

Trinity Term, 2011

Abstract

This thesis describes an investigation into the performance of different schemes for generating short x-rays pulses via synchrotron radiation emission. A review is given of the methods that have been previously proposed for this task. From this review, three leading schemes are selected for in-depth investigations, each of which explores the boundary of what is presently achievable in accelerator-based light sources.

The first scheme generates short x-ray pulses by operating an electron storage ring in a quasi-isochronous state using a 'low-alpha' lattice. High and low emittance lattices are developed, studied through simulation and then implemented on the Diamond storage ring. Beam dynamics and bunch length measurements are presented for a variety of machine conditions, and an assessment is made of the minimum practically achievable bunch length for stable user operation. Radiation pulses of 1 ps r.m.s. are demonstrated using this scheme.

The second and third schemes investigate performance limits for a linac-based light source through numerical simulations. The first of these generates ultra-short pulses by passing a highly compressed electron bunch through a long undulator to radiate in the 'single-spike' regime. A comparison is made with theoretical predictions for the required electron bunch length to operate in this way, which highlights the need for accurate start-to-end simulations. The final scheme generates ultra-short x-ray pulses through laser manipulation of the electron bunches. The modulated electrons pass through a long undulator with tapered gap, such that only the centre of the modulated portion experiences high free-electron laser (FEL) gain. A method to enhance the FEL output from this scheme using a wavelength filter and grating-compressor is investigated. The sensitivity of the two schemes to jitter sources is determined, and it is demonstrated both schemes are capable of generating GW-level, fully coherent sub-fs soft x-ray pulses. Such pulses would open up the development of time-resolved science to new regimes.

Acknowledgements

My first thanks must go to my supervisors Prof. Ken Peach and Dr. Riccardo Bartolini. Throughout my time at Oxford they have been only too willing to offer me guidance and to allow me to benefit from their vast, combined knowledge and experience. Riccardo in particular has demonstrated an uncanny knack for always knowing the right way to approach a problem.

I would also like to express my gratitude to Prof. Richard Walker, not only for agreeing to fund me throughout this D. Phil., but also for continued interest, advice, and suggestions for new directions in which these studies could be taken. Similarly, I have benefitted greatly from many useful discussions with Dr. Godehard Wüstefeld from the Helmholtz-Zentrum Berlin, for which I am grateful.

There have been many people at Diamond who have supported me during this work. Foremost among these is Dr. Cyrille Thomas, who agreed to a seemingly never-ending series of night shifts to provide the streak-camera bunch length measurements presented in this thesis. Dr. Guenther Rehm, James Rowland and Dr. Jang-Hui Han have all been extremely generous with their time and expertise, as have Beni Singh, Richard Fielder and all members of the Operations and RF groups.

On a more personal note, this acknowledgment would not be complete without recognising the enormous amount I have gained from my family as a whole, and my parents in particular, and to thank them for providing me with the many opportunities I have had in life and inspiring me towards a career in physics.

For indulging me in this endeavour, my final and biggest thanks go to my wife Helen and children Ella and Jacob. They have given me the motivation necessary to complete this task, and helped me to realise what is truly important in life.

Contents

List of Abbreviations

Name	Abbr.
Beam Position Monitor	BPM
Bunch Compressor	BC
Coherent Synchrotron Radiation	CSR
Double Bend Achromat	DBA
Dynamic Aperture	DA
Echo-Enabled Harmonic Generation	EEHG
Focussing-Defocussing	FODO
Free Electron Laser	FEL
Frequency Map	FM
Full Width Half Maximum	FWHM
Harmonic Cascade	HC
High-Gain from Harmonic Generation	HGHG
Insertion Device	ID
Incoherent Synchrotron Radiation	ISR
Longitudinal Space Charge	LSC
Numerical Analysis of Fundamental Frequencies	NAFF
Power Spectral Densisty	PSD
Radio Frequency	RF
Self-Amplification of Spontaneous Emission	SASE
Space Charge	SC
Stable Fixed Point	SFP
Transverse Space Charge	TSC
Unstable Fixed Point	UFP

Commonly Used Symbols

Name	Symbol
Angular Frequency	ω
Cavity Voltage	V_{RF}
Cooperation Length	L_c
Coupling	χ
Emittance	ε, ε_x, ε_y
Energy Loss Per Turn	U_0
Energy Spread	σ_E
Gain Length	L_G
Harmonic Number	h
Momentum Compaction Factor	α_c
Momentum Deviation	δ
Pierce Parameter	ρ_P
Radiation Wavelength	λ_r
Radius of Curvature	ρ
Relativistic Gamma Factor	γ
Relativistic Beta Factor	β
Revolution Frequency	f_{rev}
Solid Angle	Ω
Synchrotron Frequency	f_s
Synchronous Phase	φ_s
Undulator Parameter	a_u
Undulator Period	λ_u

Fundamental Constants

Name	Symbol	Units	Value
Alfvén Current	I_A	A	1.7045057×10^{-4}
Electron Charge	e	C	1.60217953×10^{-19}
Electron Mass	m_e	MeV/c^2	0.510998
Permittivity of Free Space	ε_0	F/m	$8.854187817\times10^{-12}$
Pi	π	-	3.14159265
Reduced Planck Constant	$\hbar$	J.s	1.05457168×10^{-34}
Speed of Light	c	m/s	299792458

Chapter 1

Introduction

Scientific progress can only be achieved through continual refinement and development of the experimental tools with which research is carried out. What was once deemed state-of-the-art quickly becomes obsolete, and measurements that were once beyond experimental resolution are now carried out routinely. Amongst the most powerful tools of investigation are x-rays, as this short-wavelength radiation is capable of resolving the structure of matter on the atomic or molecular length scale. Similarly, measurements of the dynamical properties of matter require a probe with a duration that is short compared to the process that is being studied, a few examples of which are given in Table 1.1 [1-7]. Reducing the radiation pulse length can allow new types of measurement to be made. For example, if the pulse is sufficiently short and intense, images of samples can be taken in a single shot, thereby avoiding sample degradation due to radiation damage [1]. Alternatively, fast-moving objects such as aerosols in free-flight can be imaged, or the evolution of non-equilibrium states can be tracked [2].

Over the last 60 years, synchrotron radiation has developed into the primary source of x-rays for experimental use. This form of light is the characteristic electromagnetic radiation generated by charged particles when accelerated in magnetic fields, acquiring its name after it was first observed at the General Electric 70 MeV

synchrotron accelerator in 1947 [8]; however, the theoretical foundations for the subject go back much further [9]. Synchrotron radiation is used across a broad range of disciplines thanks to its many distinct properties. As the research in each area has progressed, so too have the demands that are placed on the sources of radiation. To cope with these increased demands, great effort has been spent developing sources of synchrotron radiation with ever-improving quality of brightness, coherence, polarisation, stability and pulse structure. The success these developments have brought is clear from the 4 Nobel Prizes for Chemistry awarded in recent years for research carried out using synchrotron radiation sources [10].

In this thesis, significant advances in the production of short radiation pulses are described. A review is given of the various schemes that have been proposed for this task, and following this review several in-depth studies are carried out on the leading schemes for synchrotron radiation facilities.

Timescale	Example physical processes
< ~10ps	Magnetisation dynamics in solids; structural phase transitions
< ~1ps	Relaxation time for molecular systems; energy transfer times between electrons and lattice in crystalline solids
< ~100fs	Chemical bond making / breaking; atomic vibration periods in molecules and solids
< ~10fs	Electron-electron scattering in solids
< ~1fs	Fundamental atomic process e.g. Auger decay; valence electron motion

Table 1.1: Examples of physical processes that occur on a given timescale

1.1 Historical Background

The foundations for the theory of synchrotron radiation were first developed by Liénard in 1898 [9], who derived a formula that describes the energy lost by charged particles travelling on a circular path. This work was later supplemented by Wiechert in 1900 [11], resulting in the so-called Liénard-Wiechert potentials that are used to describe the time-varying electromagnetic fields emitted by a point-charge in arbitrary motion. The theory of synchrotron radiation was later expanded by Schott in his essay on Electromagnetic Radiation in 1912 [12], in which many properties of synchrotron radiation were derived, such as the frequency and angular distribution and polarisation state.

The next significant developments did not take place until the 1940s, at which time betatrons were being used to accelerate electrons on to a target to act as a source of x-rays. The electromagnetic radiation emitted by the electrons during acceleration appeared to place an upper limit on the energy achievable using such accelerators, as noted by Ivanenko and Pomeranchuk in 1944 in a paper submitted to *Physical Review* [13]. This paper was brought to the attention of Blewett, who realised that the energy lost in this way should be detectable in the 100MeV betatron in use at General Electric and would result in shrinkage of the electron orbit at the final energy. Blewett measured the orbit shrinkage in the betatron and found that it agreed with his prediction [14]. The first direct observation of synchrotron light was made in 1947 at the 70 MeV synchrotron at General Electric [8]. This discovery generated great interest, and was followed-up by the detailed measurements characterising the light made by the General Electric group [15], by Tomboulian and Hartman at Cornell [16], and by Ado and Cherenkov at the Lebedev Institute [17]. The experimental

discovery also prompted further development of the theoretical foundations by Schwinger, whose seminal paper on this topic still provides the foundation for modern research on synchrotron radiation [18].

1.2 Synchrotron Radiation

Synchrotron radiation exhibits many distinct properties which make it ideal for use in experimental studies across a broad range of disciplines in physics, chemistry and biology. When travelling on a circular trajectory through a magnetic field, relativistic electrons emit radiation across a wide part of the electromagnetic spectrum from far infra-red to hard x-rays. The radiation is horizontally polarised in the plane of the electron motion, elliptically polarised out of it, and in the laboratory frame the distribution is strongly peaked in the forward direction. Modern synchrotron light sources are able to produce radiation of high flux and high brightness that is tuneable across a broad range of frequencies with a high degree of pointing stability. Due to the fact that the light is emitted by discrete bunches of electrons, the light also has a pulsed time structure making it ideal for use in studying dynamical properties of materials.

1.2.1 Radiation from a Single Electron Travelling in a Uniform Magnetic Field

The spectral and angular characteristics of synchrotron radiation can be derived from the energy I radiated per unit frequency ω per unit solid angle Ω, which for an electron travelling along an arbitrary trajectory is given by [19]

$$\frac{d^2I}{d\omega d\Omega} = \frac{e^2}{16\pi^3\varepsilon_0 c}\left|\int_{-\infty}^{\infty} \frac{\mathbf{n}\times\left[(\mathbf{n}-\boldsymbol{\beta})\times\dot{\boldsymbol{\beta}}\right]}{(1-\mathbf{n}\cdot\boldsymbol{\beta})^2} e^{i\omega(t-\mathbf{n}\cdot\mathbf{r}(t)/c)}dt\right|^2 \tag{1.1}$$

where **n** and **r** are the direction and distance to the observer and **β** is the electron velocity relative to the speed of light. This equation is valid in the far field, for which the velocity (Coulomb) field of the particle can be neglected. It is the $(1\text{-}\mathbf{n}\cdot\boldsymbol{\beta})^2$ term in the denominator that is responsible for the directionality of the emitted radiation. For the special case of a circular trajectory, equation (1.1) can be rewritten as

$$\frac{dI}{d\omega d\Omega} = \frac{e^2}{16\pi^3\varepsilon_0 c}\gamma^2\left(\frac{\omega}{\omega_c}\right)^2 (1+(\gamma\theta)^2)^2\left[K_{2/3}^2(\xi) + \frac{(\gamma\theta)^2}{1+(\gamma\theta)^2}K_{1/3}^2(\xi)\right] \tag{1.2}$$

In equation (1.2), θ defines the vertical angle to the plane of the electron orbit and ω_c *is* the critical frequency, above which the emitted radiation intensity begins to decrease rapidly ($\omega_c = 3c\gamma^3/2\rho$, where ρ is the orbit radius). The argument for the modified Bessel function $K_n(\xi)$ is defined as

$$\xi = \frac{\omega}{2\omega_c}(1+(\gamma\theta)^2)^{3/2} \tag{1.3}$$

The two terms enclosed in square brackets in equation (1.2) give the amount of radiation polarised in the horizontal and vertical planes respectively. The relative intensity emitted as a function of vertical angle is plotted in Fig. 1.1 for several different frequencies of radiation. From this it is apparent that the angular divergence reduces significantly with increasing frequency of emitted radiation, (i.e. shorter wavelength radiation is emitted at smaller angles).

The energy distribution as a function of frequency can be obtained by integrating equation (1.2) across all angles, leading to the result

$$\frac{dI}{d\omega} = \frac{\sqrt{3}e^2}{4\pi\varepsilon_0 c}\gamma\frac{\omega}{\omega_c}\int_{\omega/\omega_c}^{\infty} K_{5/3}\left(\frac{\omega}{\omega_c}\right)d\left(\frac{\omega}{\omega_c}\right) \tag{1.4}$$

This equation is often re-expressed in terms of the normalised spectrum $S(\omega/\omega_c)$ as

$$\frac{dI}{d\omega} = \frac{2e^2}{9\varepsilon_0 c}\gamma S(\omega/\omega_c) \tag{1.5}$$

$$S(\omega/\omega_c) = \frac{9\sqrt{3}}{8\pi}\frac{\omega}{\omega_c}\int_{\omega/\omega_c}^{\infty} K_{5/3}\left(\frac{\omega}{\omega_c}\right)d\left(\frac{\omega}{\omega_c}\right) \tag{1.6}$$

The spectral photon flux F can also be expressed using the normalised spectrum, and for a circular trajectory is usually given in terms of the number of photons emitted per second, per unit angle, per unit bandwidth:

$$\frac{dF}{d\psi} = \frac{4}{9}\frac{e^2}{4\pi\varepsilon_0\hbar c}\frac{\Delta\omega}{\omega}N_e\gamma S(\omega/\omega_c) \tag{1.7}$$

In equation (1.7), ψ is the angle in the orbital plane and N_e is the number of circulating electrons. The curve is plotted in Fig. 1.2 for several different beam energies. A related quantity to the photon flux is the radiation brightness B, defined as

$$B = \frac{F}{(2\pi)^2\sqrt{\sigma_x{}^2+\sigma_r{}^2}\sqrt{\sigma_y{}^2+\sigma_r{}^2}\sqrt{\sigma_{x'}{}^2+\sigma_{r'}{}^2}\sqrt{\sigma_{y'}{}^2+\sigma_{r'}{}^2}} \tag{1.8}$$

Where σ_x, $\sigma_{x'}$, σ_y and $\sigma_{y'}$ are the size and divergence of the electron beam in the horizontal and vertical planes and σ_r and $\sigma_{r'}$ are the size and divergence of the photon beam. The source brightness is therefore a measure of both the number of photons emitted and their concentration in phase-space and is a conserved quantity (unlike photon flux density).

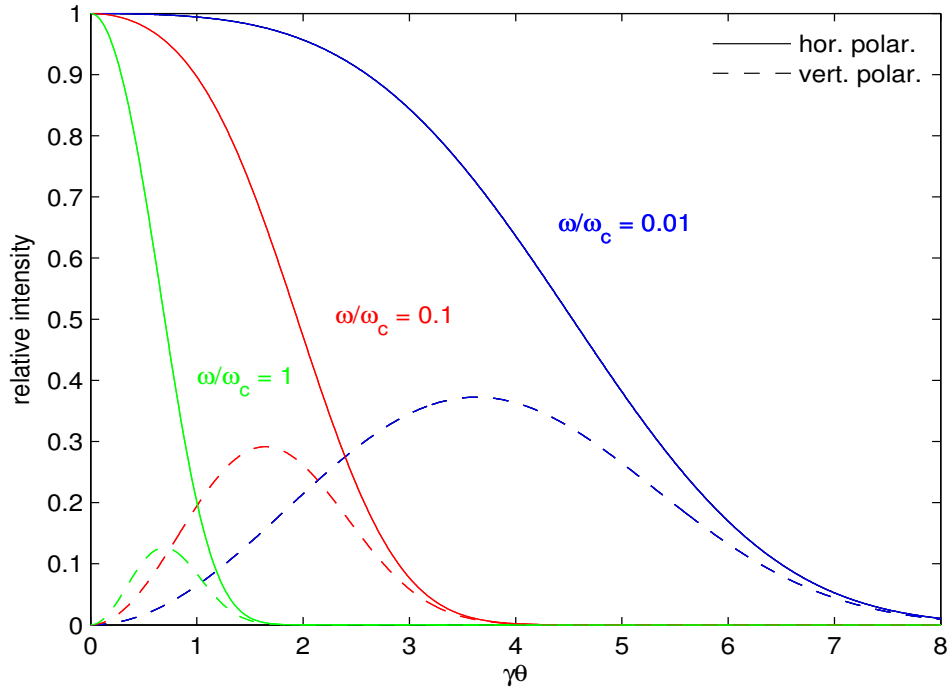

Figure 1.1: Relative intensity of synchrotron radiation emitted as a function of the angle from the plane of the electron orbit.

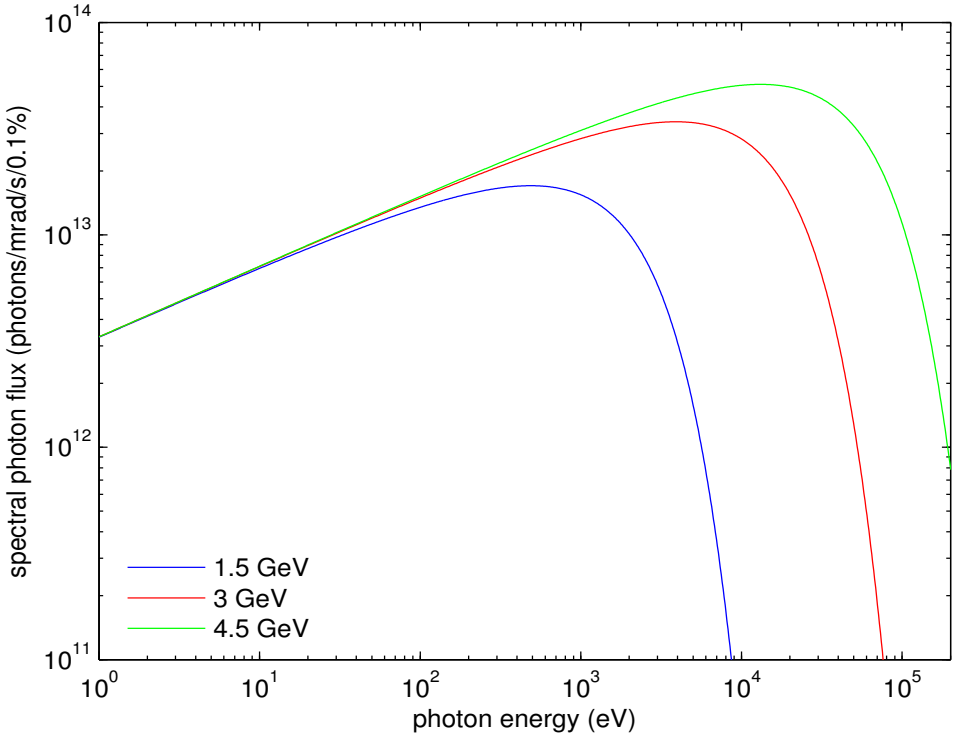

Figure 1.2: Photon flux emitted as a function of energy assuming 300mA and 7.1m orbit radius.

The total instantaneous power radiated by a single electron can be found by integrating equation (1.5) across all frequencies to give

$$P = \frac{e^2 c}{6\pi\varepsilon_0}\frac{\gamma^4}{\rho^2} \tag{1.9}$$

Since $\gamma = E/mc^2$, the instantaneous power is inversely proportional to the fourth power of the particle rest mass, implying that synchrotron radiation losses are only significant for electrons and positrons and are negligible for protons below TeV energies, and that the radiated power increases rapidly with particle energy. The average power radiated by a beam of electrons of current I_b is given by

$$P_{ave} = \frac{e}{3\varepsilon_0}\frac{\gamma^4}{\rho^2} I_b \tag{1.10}$$

and can be very large. For example, taking the Diamond Light Source parameters of orbit radius 7.13m, 3GeV electron energy and a beam current of 300mA, the average power radiated is ~300kW.

1.2.2 Radiation from a Single Electron Travelling in a Periodic Magnetic Field

Some of the properties of synchrotron radiation can be enhanced by making the electrons travel through a periodic magnetic field rather than travelling on a uniform arc [20]. Such a field is produced by *insertion devices*, which consist of a periodic array of magnets of alternate polarity. The emitted radiation in this case depends upon the particular details of the magnetic field distribution. If the magnetic field in the insertion device is very high, then the electrons will oscillate with large amplitude and

the emitted photon energy and output flux will increase. An insertion device which produces such effect is known as a *multipole wiggler*. If the insertion device has a sufficient number of periods, and assuming the electron deflection angle is not too large, then interference effects become important, and the radiation spectrum consists of a single resonant wavelength plus harmonics. In this case the radiation brightness can become very large, and the insertion device is generally termed an *undulator*.

The deflection angle can be quantified using the undulator parameter a_u:

$$a_u = \frac{e\lambda_u \sqrt{\langle {B_u}^2 \rangle}}{2\pi m_e c} \tag{1.11}$$

For undulators, a_u is around ~1; for wigglers a_u is typically greater than ~4-5. The resonant wavelength λ_r of an insertion device is given by [20]

$$\lambda_r = \frac{\lambda_u}{2n\gamma^2}(1 + {a_u}^2 + \gamma^2\theta^2) \tag{1.12}$$

where n is the harmonic number, λ_u is the period and θ is the observation angle. For an insertion device, the energy radiated per unit frequency per unit solid angle given by equation (1.1) can be re-expressed as

$$\frac{d^2I}{d\omega d\Omega} = \frac{e^2\gamma^2N^2}{4\pi\varepsilon_0 c} L\left(\frac{N\Delta\omega}{\omega_r}\right) F_N(a_u, \theta, \phi) \tag{1.13}$$

where N is the number of undulator periods, ω_r is the resonant frequency and $\Delta\omega = \omega - n\omega_r$. The function $L(N\Delta\omega/\omega_r)$ gives the line-shape for each harmonic, and is defined as

$$L\left(\frac{N\Delta\omega}{\omega_r}\right) = \frac{\sin^2(N\pi\Delta\omega/\omega_r)}{N^2 \sin^2(\pi\Delta\omega/\omega_r)} \tag{1.14}$$

The function $F_N(a_u,\theta,\phi)$ represents an integration of the magnetic field over a single period, and is given by

$$F_N(a_u,\theta,\phi) = \frac{\omega^2}{4\pi^2\gamma^2}\left|\int_{-\lambda/2\boldsymbol{\beta}c}^{\lambda/2\boldsymbol{\beta}c}\big(\mathbf{n}\times(\mathbf{n}\times\boldsymbol{\beta})\big)e^{i\omega(t-\mathbf{n}\cdot\mathbf{r}/c)}dt\right|^2 \tag{1.15}$$

The functions $F_N(a_u,\theta,\varphi)$ and $L(N\Delta\omega/\omega_r)$ are plotted in Fig. 1.3 for the case of $N = 10$ and $a_u = 0.71$ for a planar undulator. From this it is clear that, along a planar undulator axis, only odd-harmonics of the radiation appear, and that emission away from harmonics of the resonant frequency is strongly suppressed.

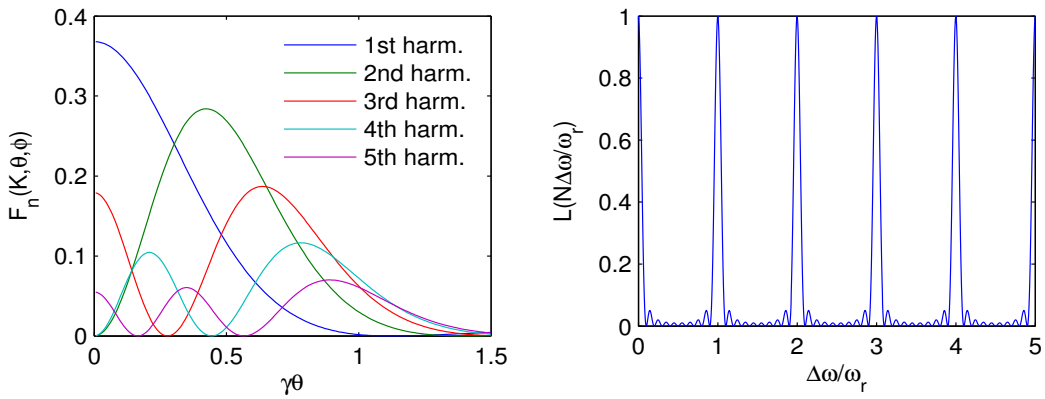

Figure 1.3: Angular harmonic distribution function (left) and line-width (right) for the case of a planer undulator of 10 periods and $a_u = 0.71$.

1.2.3 Coherent Emission of Radiation

One property of synchrotron light relevant to particular classes of experiment is the coherence [21, 22]. This is a measure of how well a wave can exhibit interference patterns; two points of an electromagnetic field are said to be coherent if the phase difference between two points remains fixed. Coherence can be further broken down

into temporal coherence and spatial coherence. Temporal coherence describes the correlation (predictability) of the field amplitude at a fixed location observed at different times; spatial coherence describes how well correlated the field amplitude is at different points in space at a fixed time.

1.2.3.1 Temporal Coherence

From equation (1.1), the radiation field ε_r with phase φ_k due to a single electron at position z is

$$\varepsilon_r \propto e^{i(\omega t - \varphi_k)} \tag{1.16}$$

where $\varphi_k = 2\pi z/\lambda$ and λ is the radiation wavelength. Since the radiation power is proportional to $|\varepsilon_r|^2$, then summing up over n_e electrons the total power becomes

$$\begin{aligned} P(\omega) &= P_e(\omega) \sum_{j,k}^{n_e} e^{i(\omega t - \varphi_j)} e^{-i(\omega t - \varphi_k)} \\ &= P_e(\omega) \left(n_e + \sum_{j \neq k}^{n_e} e^{i(\varphi_k - \varphi_j)} \right) \end{aligned} \tag{1.17}$$

where $P_e(\omega)$ is the power emitted at frequency ω by a single electron. If the longitudinal distribution of electrons is totally random and much longer than the radiation wavelength, then the final summation in equation (1.17) will average to zero and $P(\omega) = n_e Pe(\omega)$. If, however, the electrons are bunched over a distance shorter than the radiation wavelength, all particles will emit with the same relative phase and the summation tends to $n_e (n_e\text{-}1)$. In general, equation (1.17) can be re-expressed as

$$P(\omega) = P_e(\omega)\left(n_e + n_e(n_e - 1)f(\omega)\right) \tag{1.18}$$

where *f(ω)* is a form factor related to the longitudinal particle distribution *n(z)*

$$f(\omega) = \left|\int_{-\infty}^{\infty} n(z)e^{i2\pi z/\lambda}dz\right|^2 \tag{1.19}$$

The form factor varies between 0 for an infinitely long, randomly distributed bunch and 1 for a point source. Clearly, if the number of electrons is large, the enhancement given by temporally coherent emission can be many orders of magnitude greater than the incoherent contribution.

1.2.3.2 Spatial Coherence

Spatial coherence is achieved when the transverse phase space area of the electron beam is much smaller than the radiation wavelength.

$$\sigma_z \sigma_{z'} \leq \frac{\lambda}{4\pi} \tag{1.20}$$

If this condition is met, the source is said to be *diffraction limited*, i.e. the radiation beam-size due to diffraction at a given distance dominates over the initial electron beam-size. Since the transverse phase space area of the electron beam is defined by the emittance ($\sigma_z\ \sigma_z' = \varepsilon_z$), the degree of spatial coherence increases as the electron beam emittance is reduced. Spatial coherence is increasingly difficult to achieve as the radiation wavelength decreases. For example, at λ = 1μm the emittance would need to be below 80 nm.rad. For hard x-rays (λ = 1Å), the required emittance drops to 8 pm.rad.

1.2.4 Free-Electron Lasers

A free-electron laser (FEL) is a device for enhancing the synchrotron radiation emitted by a beam of electrons inside an undulator [23-26]. There are many different configurations for FELs, but the underlying mechanism is common to all. FELs work by a resonant exchange of energy between the electrons and the electromagnetic field they generate. Inside the undulator, the electrons will either gain or lose energy to the electromagnetic field, depending upon their relative phase in the combined undulator–radiation potential. As they travel along the undulator axis, the electrons begin to bunch together at the radiation wavelength, increasing the fraction of electrons emitting in phase and hence amplifying the initial electromagnetic field.

Inside an FEL it is predominantly the fundamental Gaussian mode that is amplified, meaning the emitted radiation has excellent transverse coherence (unlike the general case for spontaneous undulator radiation). The wavelength of the radiation is continuously tuneable, either by changing the electron energy or by altering the undulator gap.

1.2.4.1 Self-Amplification of Spontaneous Emission

In a self-amplification of spontaneous emission (SASE) FEL, the amplification occurs in a single pass along a long undulator. The process has three distinct phases, namely an initial start-up period (lethargy), a period of exponential gain and a saturation phase.

At the entrance of the undulator, electrons typically have a longitudinal distribution with random phase structure. On the radiation wavelength scale this distribution is not perfectly smooth, but rather it contains a small degree of local micro-bunching which leads to small variations in the initial longitudinal field intensity. The initial bunching is referred to as the shot-noise. As the electrons travel along the undulator, the emitted radiation field begins to act back on the electrons, initiating the energy exchange and therefore the bunching process. As the field amplitude increases, its phase shifts with respect to the electrons, increasing the fraction of energy lost by the electrons to the radiation field. The instability continues until a maximum amount of energy has been extracted and the radiation field is at its peak (i.e. in saturation). Figure 1.4 shows a schematic of how the electron phase space and radiated power evolve along the undulator as the FEL interaction proceeds.

Since the initial spontaneous radiation field is not uniform along the bunch, the efficiency of the bunching and hence the field growth along the undulator for different parts of the bunch is also non-uniform. This growth rate is quantified by the gain length of the FEL. The condition for resonant emission in an undulator dictates that the radiation field will slip ahead of the electron bunch by one wavelength per undulator period. For electron bunches that are long in comparison to the cooperation length (L_c) of the FEL, (defined as the total radiation slippage distance in one gain length), the radiation field in one part of the bunch develops independently from the rest. This leads to the characteristic, spiky temporal distribution and frequency spectrum of SASE sources (see Fig. 1.5). Each spike is in itself temporally coherent, but random phases develop between each spike, with each spike approximately $2\pi L_c$ long [27].

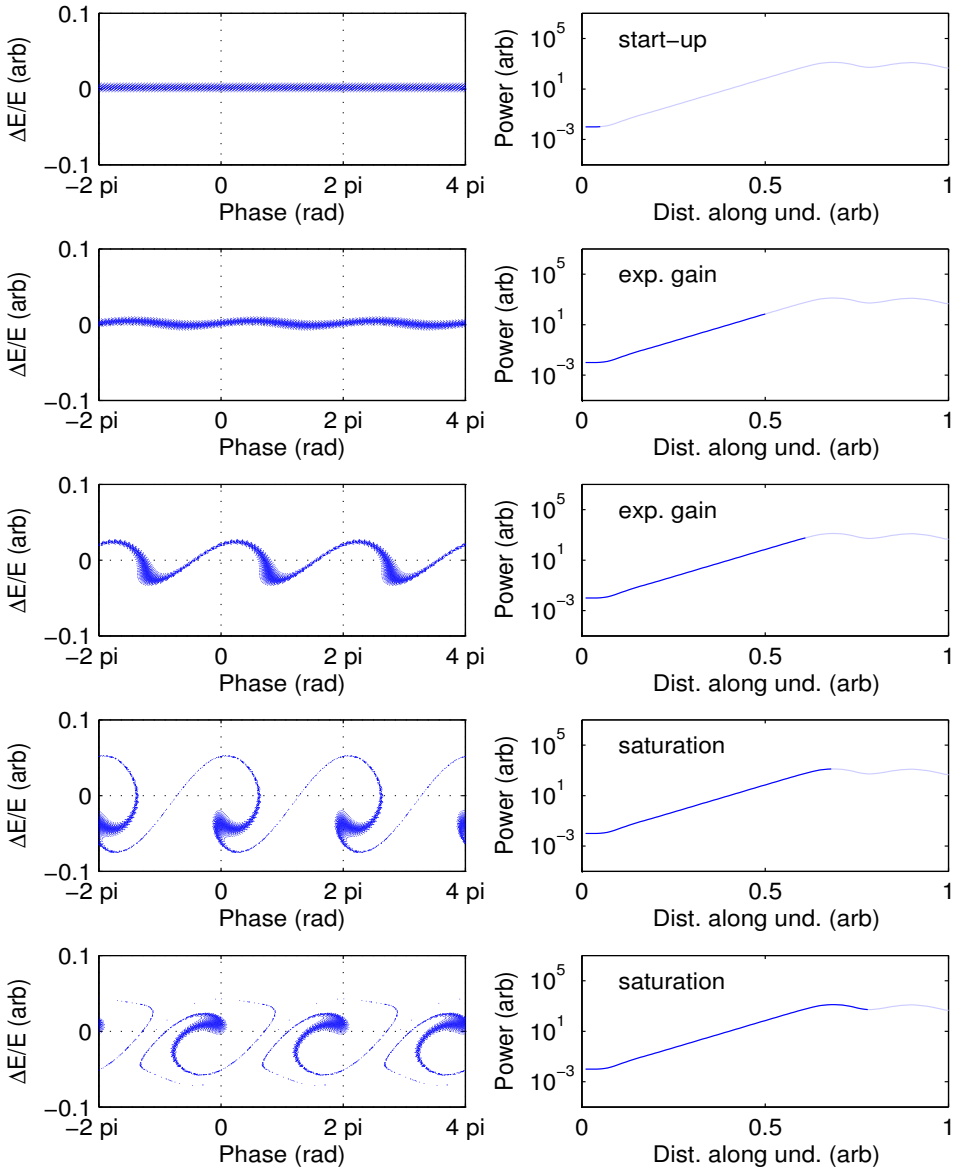

Figure 1.4: Schematic showing how the electrons bunch and rotate in phase space along with the radiated power at various points along the undulator for a high gain SASE-FEL. In this example, the electrons start with a uniform energy and phase distribution.

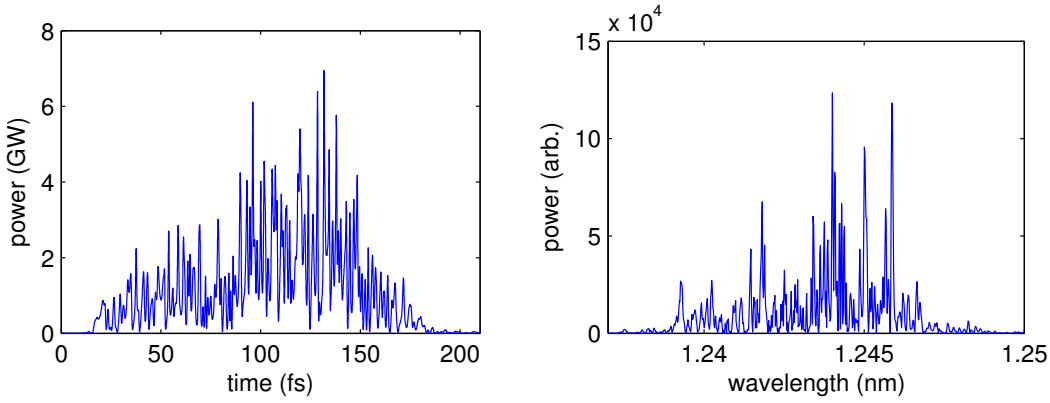

Figure 1.5: Characteristic temporal (left) and spectral (right) output from a high-gain SASE FEL for which the electron bunch length is much longer than the FEL cooperation length (~250fs FW compared to ~0.1fs). The output consists of $\sim 2\pi L_c/L_{bunch}$ temporally coherent spikes, with random phases between each spike.

1.2.4.2 Parameterisation of the FEL process

During the period of exponential gain, the radiation power is given by

$$P(z) = gP_0 e^{z/L_G} \tag{1.21}$$

where P_0 is the initial spontaneous radiation power, g is a coefficient relating the fraction of the initial power coupled into the fundamental mode, L_G is the gain length and z is the longitudinal distance along the undulator.

A fundamental scaling parameter which arises from the 1D theory for high-gain FELs is the Pierce parameter (ρ_P), defined as

$$\rho_P = \frac{1}{2\gamma}\left(\frac{I}{I_A}\frac{\lambda_u{}^2 a_u{}^2 [JJ]^2}{4\pi^2 \sigma_x{}^2}\right)^{1/3} \tag{1.22}$$

where I is the electron beam current, I_A is the Alfvén current, σ_x is the transverse electron beam size, λ_u is the undulator period, a_u is the undulator parameter, γ is the relativistic factor and $[JJ]$ is the Bessel function factor

$$[JJ] = \left[J_0\left(\frac{\xi}{2}\right) - J_1\left(\frac{\xi}{2}\right)\right]; \qquad \xi = \frac{a_u{}^2}{(1 + a_u{}^2)} \tag{1.23}$$

Using this parameterisation, the 1D theoretical gain length of the radiation power is given by

$$L_G = \frac{\lambda_u}{4\pi\sqrt{3}\rho_P} \tag{1.24}$$

and hence the cooperation length (L_c) is

$$L_C = \frac{\lambda_r}{4\pi\sqrt{3}\rho_P} \tag{1.25}$$

The Pierce parameter gives a measure of the efficiency of the FEL process; a large value indicates short gain lengths - large power growth, and so electron beams with high peak current, low emittance and low energy are favoured.

The simplified 1D FEL theory neglects a number of effects which can degrade the performance of an FEL, such as the emittance and energy spread of the electron beam, diffraction of the radiation field and variation of the electron bunch parameters along its length. In order to account for these effects in a convenient fashion, M. Xie proposed a universal scaling of the 1D equations [28]. According to this work, a scaled gain length can be found from

$$L_{G,Xie} = L_G(1 + \Lambda) \tag{1.26}$$

where Λ is a function of various parameters such as beam emittance, energy spread, Rayleigh length, resonant wavelength and 19 constants arrived at from numerical fitting. Equation (1.26) implies a scaled Pierce parameter can be defined

$$\rho_{Xie} = \frac{\rho_P}{1 + \Lambda} \tag{1.27}$$

which in turn suggests the cooperation length will be longer than the 1D theory predicts ($\rho_{Xie} < \rho_P$).

For many applications a high degree of temporal coherence for the radiation pulse is required. A quantative measure of this is given by the time-bandwidth product for the pulse, i.e. by

$$\Delta t \Delta \upsilon = \frac{1}{\lambda_r}\frac{\Delta\lambda}{\lambda_r}\Delta s \tag{1.28}$$

where Δs is the pulse length and $\Delta\lambda$ is the spectral width. The minimum value for the time-bandwidth product is set by the Fourier transform limit, which for a Gaussian profile is $2ln(2)/\pi$ (~0.44). If the time-bandwidth product is close to this, this indicates the pulse duration is approaching the minimum achievable value. In general, SASE sources are far from being transform-limited, indicating a poor longitudinal coherence.

1.3 Synchrotron Radiation Sources

The development of synchrotron radiation facilities is commonly described in terms of ‘generations’ of machine. The first generation of machines were built for high-

energy physics research, with research using synchrotron light carried out parasitically from the bending magnets. These machines were initially ramping synchrotrons, but quickly developed into electron-storage ring based machines in order to make use of the enhanced flux and beam stability. Examples of the first ramping synchrotrons include the Synchrotron Ultraviolet Radiation Facility (SURF) at the National Bureau of Standards in the U. S. A., the Institute for Nuclear Studies – Synchrotron Orbital Radiation ring (INS-SOR) in Japan and the Deutsches Elektronen-Synchrotron (DESY) in Germany. These were quickly followed by synchrotron radiation facilities built at storage rings such as Tantalus I and SPEAR in the U.S.A. and AdA in Italy.

The second generation of facilities were purpose-built specifically for the dedicated use as synchrotron radiation sources. This enabled the machines to be designed and operated with conditions specifically suited to the production of synchrotron radiation. The first of this generation of machine was the Synchrotron Radiation Source (SRS) in the UK, closely followed by the NSLS and Aladdin in the U.S.A. and the Photon Factory in Japan.

The next (third) generation of facility aimed to increase brightness rather than flux alone. This entailed designing rings to have low emittance and dedicated space for insertion devices from the outset. Third generation facilities can be further split into high energy (6-8GeV) machines designed for the production of hard x-rays (such as the ESRF in France, APS in the U.S.A. and Spring-8 in Japan) and low energy (1-2GeV), soft x-ray machines (such as the ALS in the U.S.A. and Elettra in Italy). Increasingly however, as insertion device technology has progressed, medium energy (2-3.5GeV) facilities such as the U.K.'s Diamond Light Source have been

constructed, and are now able to serve both user communities simultaneously, delivering synchrotron light across a broad spectral range from far infrared to hard x-rays.

Whilst third generation light sources are still being designed and constructed today, fourth generation machines are already coming online. Rather than using electron storage rings, fourth generation facilities are based on single-pass, high gain FELs which utilise high-brightness electron linacs in combination with long undulators, producing light with peak brightness many orders of magnitude greater than can be achieved with third generation facilities. Fourth generation light sources currently operational include FLASH in Germany and LCLS in the U.S.A., FERMI in Italy and SACLA in Japan have recently achieved lasing and the European X-FEL in Germany is under development. Further information about light sources can be found at [29].

1.4 Short-Pulse Synchrotron Radiation

Although ultrafast pulses (< few fs) are already available using optical lasers, converting these to the x-ray region is difficult. Techniques such as High-Harmonic Generation (HHG) [30] and relativistic Thompson scattering [31] are available, but the number of photons per pulse is low. Extension of synchrotron radiation sources to this time domain is clearly desirable.

In conventional synchrotron radiation sources, the pulse duration is dictated by the length of the electron bunches circulating in the storage ring. For first generation machines, the natural (low-current) bunch lengths were of the order 100ps, but with the development of low emittance, stronger focussing lattices this has decreased to

~10-20ps for modern machines. However collective effects can cause significant bunch lengthening with current [32]. The natural bunch length for selected synchrotron radiation facilities over time is plotted in Fig. 1.6.

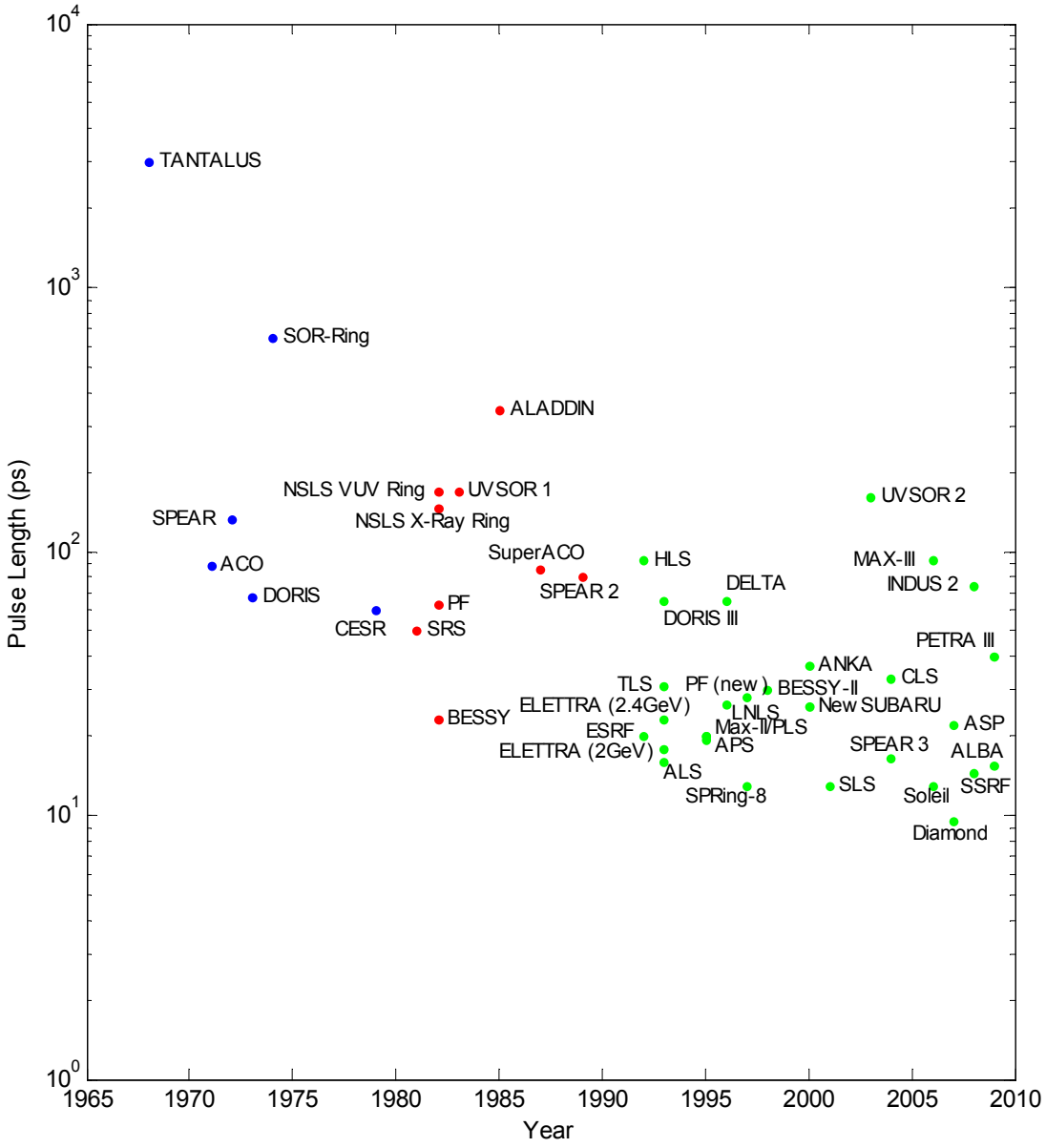

Figure 1.6: Natural electron bunch length for a selection of synchrotron radiation facilities.

In order to address the needs of scientific research, significant effort has been carried out in recent years to develop sources of synchrotron radiation with reduced pulse duration. On third generation facilities, equilibrium electron bunch lengths below 1ps have been demonstrated by operating with low-momentum compaction factor lattices [33], and radiation pulses of ~100fs have been produced by modulating the electron energy with an external laser [34]. Transient methods have also been tested to reduce the synchrotron radiation pulse duration, but as yet none have been able to demonstrate pulses below ~4ps [35, 36]. Techniques to reduce the pulse duration are still being developed at most third generation facilities.

Fourth generation, single-pass machines are more naturally suited to the production of short radiation pulses. Since the electron bunches acquire a natural energy gradient during the acceleration process, they can be highly compressed by passing them through a magnetic chicane. Soft x-ray pulses of ~10fs duration have been demonstrated at FLASH using this technique [37], and indications are that hard x-ray pulses lasting <10fs have been produced at LCLS in low charge mode [38].

1.5 Thesis Layout

The work contained in this thesis begins by presenting an overview of short pulse generation schemes for synchrotron radiation sources. Following this, three techniques are investigated in detail; one as applied to a third generation user facility and two for a fourth generation light source. Implicit in the application to user facilities is the need that the selected short pulse generation schemes must be demonstrated to be practical, robust and straight-forward to implement, as well as

capable of producing radiation pulses short enough to be of interest for current experimental research activities.

The structure of the thesis is as follows. Chapter 2 presents an overview of the different schemes that have been either proposed or implemented on both third and fourth generation synchrotron radiation sources. Chapter 3 discusses the design and implementation of two low momentum compaction lattices for the Diamond storage ring [39]. In-depth numerical studies for two short-pulse schemes applied to the UK's New Light Source conceptual facility design are presented in Chapter 4 [40]. Conclusions and future work are discussed in Chapter 5.

Chapter 2

Review of Short Pulse Generation Schemes

Various schemes have been proposed in recent years for the generation of short pulse radiation. Initially these were focussed on storage ring based facilities, but with the advent of fourth generation light sources attention has predominantly turned to what can be produced using linac-based facilities. The two types of machine should be considered complementary however, since although fourth generation light sources produce radiation pulses with vastly improved peak power, coherence and pulse duration, third generation facilities still allow high average brightness, high repetition rates and excellent transverse stability. Although the large number of third generation light sources worldwide allows much greater access to these facilities, the number of places able to offer short radiation pulses is still limited.

In this chapter the various schemes that have been proposed for generating short radiation pulses are reviewed. Where possible, reference is given to the best results achieved to date with each scheme, with predicted performance from simulation given otherwise. Section 2.1 describes schemes proposed for third generation light sources, and schemes for fourth generation facilities are described in Section 2.2.

2.1 Storage Ring-Based Schemes

The various methods that have been proposed for short pulse generation in storage rings fall into three broad categories: bunch slicing, bunch deflection and bunch compression. Bunch slicing schemes make use of a short laser pulse to give an energy modulation to the central portion of a circulating electron bunch, such that the light emitted from the energy modulated slice is spatially separated from the main bunch in dispersive sections of the storage ring [34, 41-43]. Lasers can also be used to produce short x-ray pulses directly through Thomson scattering [44]. Bunch deflection techniques generate a spatial separation for the light emitted by different portions of the bunch by causing the head and tail to oscillate in opposite directions, for example by using crab cavities [45, 46]. The light emitted from a short section of the bunch can then be selected using slits or optically compressed using asymmetrically-cut crystals in the beamline optics. Transient deflection using a vertical kicker magnet has also been investigated [35]. Finally, bunch compression techniques such as the use of a third harmonic cavity [47] or a low momentum compaction (low-alpha) lattice [33, 48] shorten the equilibrium bunch length of the circulating electrons. In this way short pulses are generated using light from the whole of the bunch.

2.1.1 Bunch Slicing

Modulation of the electron energy by an external laser for the purposes of short pulse generation, commonly known as femto-slicing, was first proposed by A. Zholents and M. Zoloterev [41]. In this scheme, a short laser pulse propagates with an electron bunch through an undulator (the modulator), during which time energy is exchanged

between the electron distribution and the electric field of the laser pulse. The direction of this energy exchange depends upon the phase of the laser field relative to the electrons. Following this energy modulation, the electron bunch passes through a dispersive section of the storage ring, such that the light emitted by the un-modulated part travels in a different direction to that emitted by the energy modulated electrons and can be blocked by an aperture restriction. The duration of the x-ray pulse is then approximately the same duration as the optical laser pulse used to create the energy modulation. The main components of the scheme are shown in Fig. 2.1.

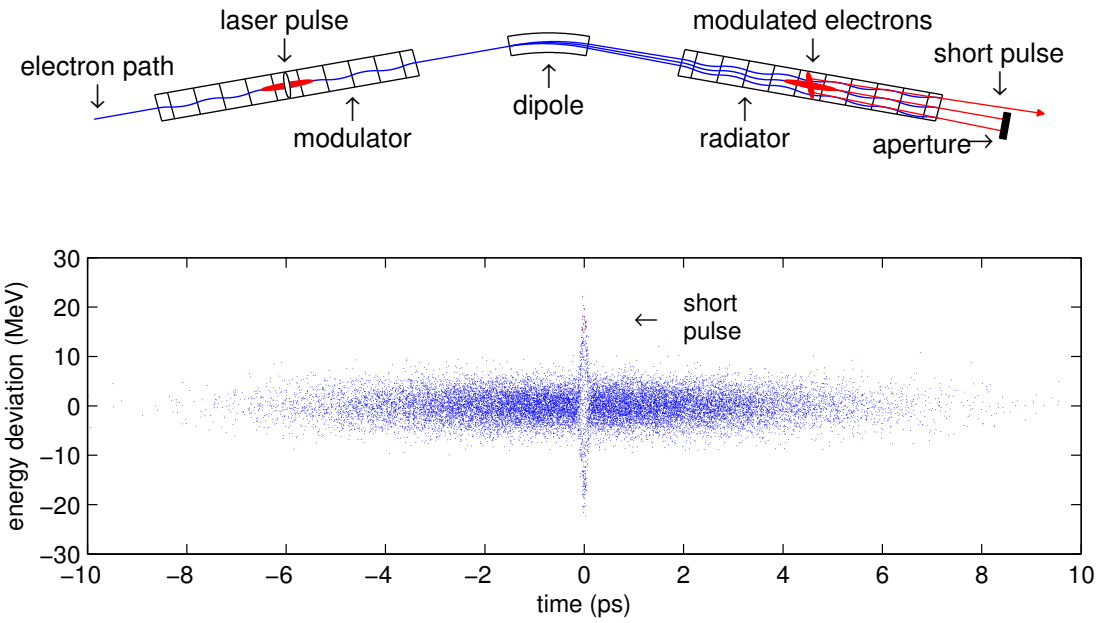

Figure 2.1: Typical layout of a femto-slicing scheme for a storage ring. The radiator can consist of either a dipole or an undulator (top). Energy modulation given to a 8ps long electron bunch for a 100 fs FWHM, 5mJ, 800nm laser modulation (bottom).

Efficient energy exchange between the laser electric field and electrons occurs when the laser wavelength is matched to the resonant wavelength of the undulator modulator (equation (1.12)). The energy change ΔE is then given by the relation [34]

$$\Delta E \cong \sqrt{4\pi\alpha A_L \hbar\omega_L \frac{{a_u}^2}{1+{a_u}^2}\frac{M_u}{M_L}}\cos\varphi_L \qquad (2.1)$$

where α is the fine structure constant, A_L, ω_L, φ_L and M_L are the laser pulse energy, frequency, phase and number of periods respectively and M_U is the number of undulator periods. Typically, the modulating laser has a wavelength of 800nm, ~25-100fs duration and a few mJ pulse energy and is sufficient to give an energy modulation to the electrons several times larger than the intrinsic energy spread (i.e. about ~1% energy deviation).

The number of electrons involved in the interaction, and hence the number of photons in the short pulse, are drastically reduced compared with standard operation. This reduction can be estimated from the ratio of laser pulse duration to electron bunch length (τ_L / τ_e), the ratio of laser repetition rate and electron bunch frequency (f_L / f_e) and the fraction of electrons which have the correct phase with respect to the laser field to have maximum energy gain (~0.2). For typical operating parameters, the final reduction in intensity is ~10^{-8}.

The duration of the x-ray pulse emitted by the electrons is longer than the modulating laser pulse due to the slippage of the laser pulse over the electrons in the modulator ($M_u\lambda_L/c$) and the difference in electron path length between the modulator and radiator. The path length difference Δl can be calculated from the electron phase space coordinates and the transport matrix between modulator and radiator, R [43]

$$\Delta l = R_{51}x + R_{52}x' + R_{56}\frac{\Delta E}{E_0} \qquad (2.2)$$

Femto-slicing beamlines suffer from a background to the short x-ray pulse, partially due to light emitted by the transverse tails of the main bunch, but also by light emitted

by electrons modulated on previous laser cycles which have not yet damped to the equilibrium conditions. This problem increases with increasing laser repetition rate and is worse for machines with long damping times [42, 43].

Femto-slicing was first demonstrated at the ALS using a bending magnet as the source point [34], later upgrading to an undulator beamline [49]. Following this, femto-slicing facilities were installed in the BESSY II ring [43] and at the SLS [42], and one is in the process of being installed at SOLEIL [50]. Beamline results from both BESSY and SLS suggest x-ray pulses of <~150fs FWHM are being produced with ~10^6 photons per second.

2.1.2 Bunch Deflection

2.1.2.1 Deflection Using Crab Cavities

In this scheme, a transverse-deflecting RF cavity is used to give a vertical kick to an electron bunch that is correlated along its length, such that the head and tail oscillate in opposite directions. When passing through an undulator, the light emitted is spatially separated in vertical position and time (chirped), meaning a short pulse can be extracted by either installing vertical slits in the beamline, or by compressing the chirped pulse using asymmetrically-cut crystals. Following this, a second cavity is used to remove the chirp given by the first cavity, thus confining the deflection to a small section of the storage ring. This idea was first proposed by A. Zholents et al. [45], and a schematic showing the main components is given in Fig. 2.2.

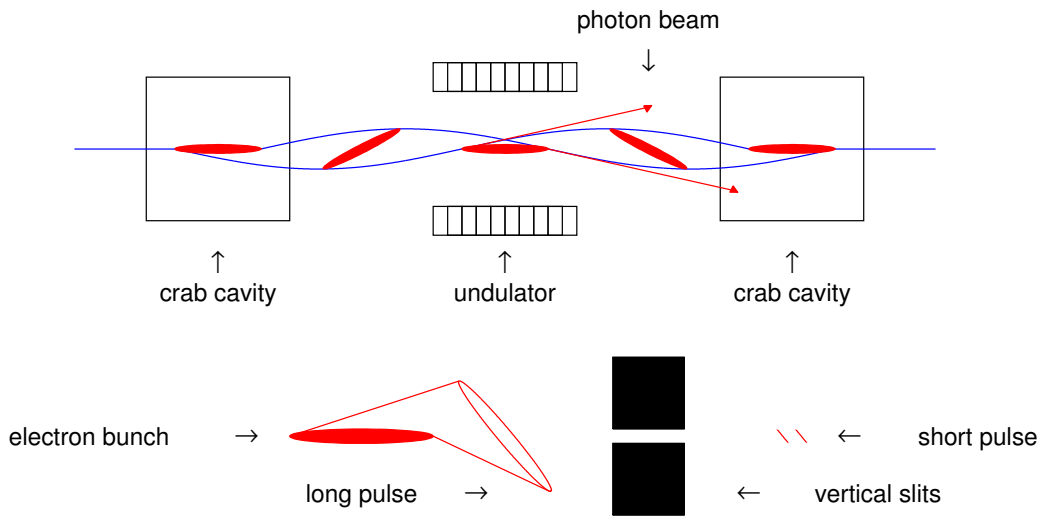

Figure 2.2: Typical layout of a crab-cavity scheme for a storage ring.

The deflecting cavity is set to operate in the TM_{110} mode, for which the electric and magnetic fields in cylindrical coordinates are

$$E_z = 2\varepsilon_r J_1(kr)\sin(\varphi)\cos(\omega t + \psi) \tag{2.3}$$

$$cB_r = 2\varepsilon_r J_1(kr)\cos(\varphi)\sin(\omega t + \psi)/kr \tag{2.4}$$

$$cB_\varphi = 2\varepsilon_r J_1'(kr)\sin(\varphi)\sin(\omega t + \psi) \tag{2.5}$$

where ε_r is the electric field amplitude, k, ω and ψ are the cavity wave-number, angular frequency and phase and J_1 is the Bessel function of the first kind. The deflection given to the electron bunch as a function of the longitudinal coordinate z can be calculated from the Lorentz equation, which for an electron bunch of energy E_0 travelling on-axis ($r = 0$) through a cavity of length L gives

$$y'(z) = \frac{e\varepsilon_r L}{E_0}\sin(kz) \tag{2.6}$$

In order to resolve different slices of the beam, the angular motion of each slice must be larger than the convolution of the radiation opening angle ($\sigma_{r'}$) and the electron

beam vertical divergence ($\sigma_{y'}$). In this case, the minimum pulse duration that can be produced using this scheme is [46]

$$\sigma_t \cong \frac{E_0}{e\varepsilon_r Lck}\sqrt{\frac{\beta_{y,ID}}{\beta_{y,rf}}}\sqrt{{\sigma_{y'}}^2 + {\sigma_{r'}}^2} \tag{2.7}$$

The use of asymmetrically cut crystals to compress the photon pulse rather than using vertical slits alone to select a short slice can increase the number of photons per pulse by an order of magnitude [51].

For the scheme to be feasible, the vertical phase advance between the first crab cavity and the undulator source point should be an integer multiple of π such that the angular separation between the radiation emitted at the head and tail of the bunch is at a maximum. Similarly, the storage ring optics must be tuned such that the phase advance between the two deflecting cavities is an integer multiple of π to ensure perfect cancelation of the two kicks and confine the oscillation to a short section of the storage ring and prevent a growth in the vertical emittance. Effects which can prevent perfect cancellation of the two kicks include [46]:

- Focussing errors in the lattice such as different beta-functions at the two cavities or phase advance error
- Cavity roll about the beam axis
- Cavity phase and voltage errors
- A non-zero chromaticity combined with energy spread leading to a variation in the phase advance within the bunch

- Non-zero momentum compaction combined with energy spread leading to a variation in the time-of-flight between the two cavities

- Sextupoles between the two cavities leading to coupling between the horizontal and vertical planes, along with a tune shift with amplitude and hence a spread in the phase advance

At present, no crab cavity short pulse facility is in operation. The APS is developing a scheme with pulsed cavities operating at 1kHz repetition rate, for which the pulse duration is expected to be 2ps FWHM [52]. A variation has also been proposed for SPRing8, in which four deflecting cavities are placed in a single long straight and used to create a closed bump for the beam. The light is extracted from the electron beam at the point where its displacement (rather than angle of motion) is at a maximum [53]. A preliminary assessment of applying a crab cavity scheme to the Diamond storage ring was made in [54], in which it was concluded only minor adjustments to the optics would be required to implement this scheme, with pulse durations down to below 1ps possible for 3GHz deflecting cavities of 1.25MV peak voltage.

2.1.2.2 Transient Short Pulses from Vertical Deflection

A third short-pulse scheme makes use of the fact that, in storage rings, betatron and synchrotron motion is coupled if the chromaticity is non-zero. Under these conditions, an electron beam that is kicked vertically will slowly acquire a tilt along

its length that is fully developed after half a synchrotron period. The tilt develops because the average momentum deviation (and hence vertical betatron oscillation frequency) for particles moving towards the head of the bunch in the RF bucket is different from those travelling towards the tail [35]. The tilt angle θ_{yz} at position s is given by [55]

$$\theta_{yz}(\Delta\varphi, s) = -\frac{\omega_{RF}}{c}\sqrt{\beta_y(s)\beta_y(s_0)}\Theta\frac{\xi_y}{h\alpha_c}(1-\cos(Q_s\theta))e^{-\xi^2}\cos\Upsilon \qquad (2.8)$$

where $\Delta\varphi = \varphi - \varphi_s$ is the longitudinal coordinate within the bunch, φ_s is the synchronous phase, ω_{RF} is the RF cavity angular frequency, β_y is the vertical beta function, s_0 is the position of the vertical kicker of kick angle Θ, ξ_y is the vertical chromaticity, h is the harmonic number, α_c is the momentum compaction factor, Q_s is the synchrotron tune, θ is the orbit angle and

$$\xi^2 = \frac{1}{2}\left(\frac{\xi_y\sigma_\delta}{Q_s}\right)^2(1-\cos^2(Q_s\theta))$$

$$\Upsilon = Q_y\theta + \Psi_{s,0} - \frac{\xi_y}{h\alpha_c}(1-\cos(Q_s\theta))\Delta\varphi$$

Since the orbit angle θ increments by 2π on every turn, then from equation (2.8) the tilt angle will be at a maximum when $Q_s\,\theta = \pi$, or after half a synchrotron period. A short pulse can be selected from the tilted beam using vertical slits in the beamline. In this simple model, and in the limit of zero slit-width, the minimum pulse length that can be produced by this scheme σ_t is related to the vertical beam size σ_y by

$$\sigma_t \cong \frac{\sigma_y}{\theta_{yz}} \qquad (2.9)$$

This can be several orders of magnitude less than the nominal electron bunch length. However, there are various effects which can lead to decoherence of the beam and a

deterioration of the signal, such as amplitude-dependent tune shifts, horizontal to vertical coupling, radiation damping, quantum fluctuations, wakefield effects and higher order chromaticity. Once these effects are accounted for, and assuming the bunch current is still small enough that wakefield effects can be neglected, the compression ratio R between kicked and un-kicked bunch lengths is [35]

$$R \approx \sqrt{\frac{2}{1 - exp(-\pi a_E / Q_s)}} \tag{2.10}$$

where $a_E = (1/2\pi)(T_0/\tau_E)$ is the longitudinal damping coefficient, T_0 is the revolution time and τ_E is the longitudinal damping time.

Using this scheme, measurements taken at the APS have demonstrated a reduction in pulse length from 27.4ps to 4.2ps (standard deviation) [35], and SPRing8 have demonstrated a reduction from 34ps to 7ps (FWHM) [56]. Similar experiments at the ALS estimate a compression ratio of ~10 can be achieved [57].

2.1.3 Bunch Compression

2.1.3.1 'Low-Alpha' Operation

Another method for generating short radiation pulses is to reduce the equilibrium length σ_l of the circulating electron bunch. The natural bunch length is set by the energy spread σ_E, synchrotron frequency f_s and the momentum compaction factor α_c of the lattice

$$\sigma_l = \frac{c\alpha_c}{2\pi f_s}\sigma_E \tag{2.11}$$

where the synchrotron frequency is given by

$$f_s = f_{rev}\sqrt{\frac{h\,\alpha_c \cos\varphi_s eV_{RF}}{2\pi E_0}} \tag{2.12}$$

and h is the harmonic number, V_{RF} is the cavity voltage and f_{rev} is the revolution frequency. Since the energy spread is an intrinsic property of the electron bunch and the bend radius (caused by the stochastic emission of synchrotron radiation), the only way to compress an electron bunch at a fixed energy is to either increase the cavity voltage gradient (which is subject to hardware limitations) or adjust the quadrupole magnets to minimise the momentum compaction factor and make the storage ring isochronous. This is achieved in low-alpha lattices [48].

Whilst the repetition rate of radiation pulses provided by a low alpha lattice is as high as standard operation (set by the number of bunches and revolution frequency), the radiation intensity is substantially reduced due to the limitation in maximum bunch current caused by the onset of the micro-bunching instability [58]. This onset occurs at increasingly lower values as the bunch length is reduced, limiting the stored charge and lowering the radiation intensity by several orders of magnitude.

In principle, the momentum compaction factor can be adjusted to make the bunch length arbitrarily small. However, there are several effects which place a lower limit on the value that can be achieved in practice [39]. Firstly, the bunch length given by equation (2.11) is valid only in the limit of zero current, i.e. it neglects all collective effects which can cause the bunch length to grow, such as potential well distortion and turbulent bunch lengthening [21, 59-60]. Higher order terms in the equations of motion become increasingly significant as α_c is reduced, resulting in a minimum for

the effective value of α_c. Lastly, closed orbit motion is found to increase in inverse proportion to the momentum compaction factor, again leading to a minimum acceptable value of α_c. However, bunch lengths as low as 0.7ps (standard deviation) have been demonstrated at BESSY II using this technique [33].

2.1.3.2 Higher Harmonic Cavity

The RF gradient and hence equilibrium electron bunch length can be modified by the use of an RF cavity operating at a harmonic of the main cavities. Depending upon the phase of this cavity, the slope of the accelerating voltage at the synchronous phase can be altered, thereby changing the longitudinal focussing force and modifying the current distribution. The use of such a cavity was originally proposed in order to lengthen the bunch and increase the lifetime [61]; later the system was considered for operation in bunch shortening mode [47, 62].

The total RF voltage as seen by the electron beam can be expressed as

$$V_{tot}(\varphi) = V_{RF}\sin(\varphi) + kV_{RF}\sin(n(\varphi - \varphi_s)) \tag{2.13}$$

where n is the ratio between the harmonic and main cavity frequencies and k is the ratio between the voltages. Assuming the phase of the harmonic cavity is adjusted to maximise the voltage gradient seen by the bunch, the resulting change in bunch length is given by [47]

$$\sigma_{l,harm} = \sigma_l \Big/ \sqrt{1 - \frac{nk}{\cos\varphi_s}} \tag{2.14}$$

An example of how the total RF voltage and equilibrium bunch length is affected by the addition of a 3rd harmonic cavity is shown in Fig. 2.3.

Since the harmonic cavity for bunch shortening is tuned to be zero at the synchronous phase, the cavity does not contribute to the compensation of synchrotron radiation losses and needs only a relatively small amount of power to operate. The reduction in bunch length is expected to be independent of bunch current, although for the shortest pulses a low bunch current is still favoured to avoid the effects of potential well distortion and turbulent bunch lengthening. Several light sources have carried out measurements of bunch length with harmonic cavities operational. Measurements at the NSLS-VUV ring demonstrated a reduction from 169ps to 110ps for a 4th harmonic cavity [63], and bunch shortening factors up to 2 have been observed at Super-ACO for a 5th harmonic cavity [64]. Simulations carried out for BESSY-II suggest a reduction factor of 4.5 could be achieved with a 10MV 3rd harmonic cavity, increasing to a factor 10 if the cavity voltage is 50MV. This would give a 300fs long bunch for the low-alpha lattice [65]. Preliminary calculations for the Diamond storage ring suggest a 30% reduction in bunch length could be achieved for a passive 3rd harmonic cavity at 1.1MV [54].

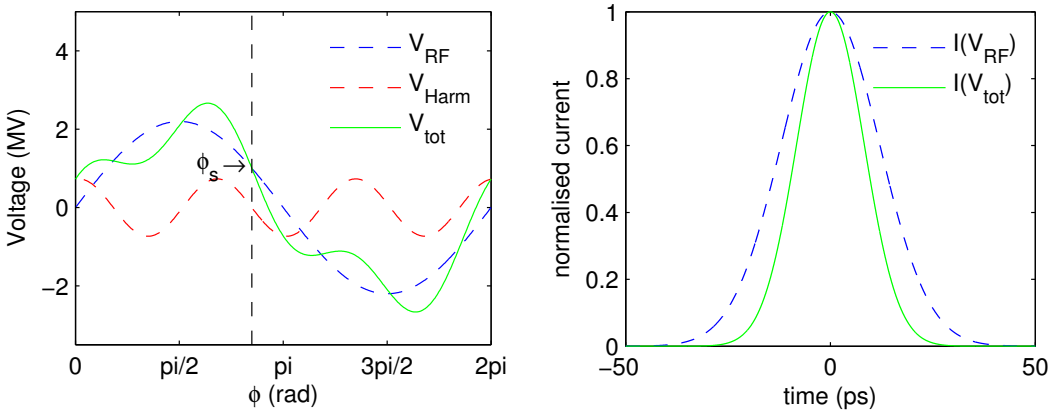

Figure 2.3: Cavity voltage as a function of phase for a 3rd harmonic cavity set to operate in bunch shortening mode (left). Current distribution with and without the harmonic cavity (right). The calculations assume V_{RF} = 2.2MV, k = 0.5, n = 3, E_0 = 3GeV, $\varphi_s = \pi$ - 0.474, $\alpha_c = 1.7\times10^{-4}$, h = 936, $\sigma_E = 9.6\times10^{-4}$ and f_{rev} = 534kHz.

2.1.3.3 Transient Short Pulses from RF Cavity Modulation

In this scheme, a longitudinal instability is excited in the bunch by modulating the storage ring RF at twice the synchrotron frequency, the result of which is a quadrupole oscillation in the bunch shape. The electron distribution alternates between having a short bunch length - high energy spread and a long bunch length - low energy spread. For each oscillation, the minimum (maximum) bunch length decays (grows) exponentially.

The variation proposed in [36] requires two RF cavities separated in RF phase by 90˚ with peak voltages set to equal the energy loss per turn ($V_1 = V_2 = U_0$). In this set-up, the synchronous phase coincides with the on-crest phase of cavity 2 and the zero-crossing phase of cavity 1, i.e. cavity 2 provides the acceleration for the beam and cavity 1 provides the longitudinal focussing (see Fig. 2.4). The longitudinal focussing can then be varied without altering the synchronous phase, either by modulating the voltage of cavity 1 or the phase of cavity 2 (assuming the phase deviations are small). In other words, the synchrotron frequency is modulated without inducing longitudinal oscillations of the bunch centroid. For the case of phase modulation, the synchrotron frequency becomes [36]

$$f_s{}^2 = f_{rev}{}^2 \frac{h\alpha_c e}{2\pi E_0}[V_1 - V_2\Delta\varphi\cos(\omega_m t)] = f_{s0}{}^2[1 - \Delta\varphi\cos(\omega_m t)] \quad (2.15)$$

where $\Delta\varphi$ and ω_m are the modulation amplitude and angular frequency respectively. The longitudinal equation of motion can therefore be written as

$$\frac{d^2\varphi}{dt^2} + (2\pi f_{s0})^2[1 - \Delta\varphi\cos(\omega_m t)]\varphi = 0 \qquad (2.16)$$

Equation (2.16) is that of a driven parametric oscillator, with approximate solution given by

$$\frac{\langle\varphi^2(t)\rangle}{\langle\varphi^2(0)\rangle} \approx [e^{2\alpha_m t}\cos^2(2\pi f_{s0}t + \pi/4) + e^{-2\alpha_m t}\sin^2(2\pi f_{s0}t + \pi/4)] \qquad (2.17)$$

where the instability growth rate α_m is equal to $\pi f_s \Delta\varphi/2$. Equation (2.17) has exponentially growing and exponentially decaying terms, with each having maxima occurring twice every synchrotron period in anti-phase. In [36], the modulation is stopped after a few cycles to avoid particle loss from the exponential growth term. The evolution in bunch length is shown in Fig. 2.4, for which the parameters for the Diamond storage ring have been used.

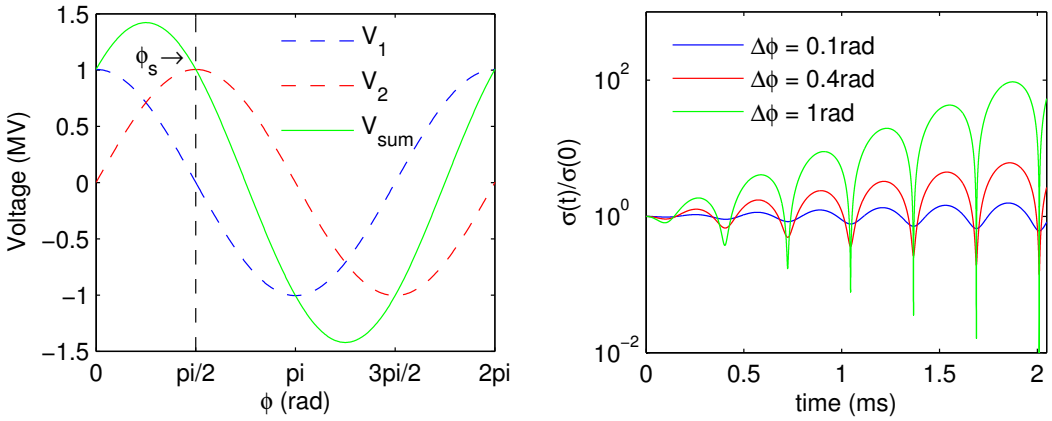

Figure 2.4: Cavity voltage as a function of phase for the RF modulation scheme (left). Electron bunch length as a function of time for various phase modulation amplitudes (right). The calculations assume $V_1 = V_2 = 1.005$MV, $E_0 = 3$GeV, $\alpha_c = 1.7\times10^{-4}$, $h = 936$ and $f_{rev} = 534$kHz.

The simple model described above neglects several important limiting effects such as quantum excitation, radiation damping, RF bucket non-linearities and bunch shape distortions due to collective effects. For the case of the APS, these effects were found to limit the maximum bunch compression to a factor of 2, whilst at the same time reducing the growth rate of the instability [36]. Simulations demonstrated that in fact a pseudo-equilibrium state could be reached, provided the modulation amplitude was kept small.

One advantage of this scheme over other schemes is that it can be used in conjunction with high bunch currents and low emittance, helping to preserve the high average brightness of standard operation. However, as with the higher harmonic cavity scheme, the shortest pulses are still produced when small bunch currents are used in order to avoid the effects of potential well distortion and turbulent bunch lengthening. In addition, the increase in energy spread that comes with the reduction in bunch length leads to a broadening of the spectral lines for an undulator radiation source along with an increase in the effective emittance, both of which will tend to reduce the overall source brightness.

2.1.4 Performance Summary

	Estimated Pulse Duration (FWHM)	Intensity Relative to Standard User Mode	New Hardware Required	Repetition Rate	Compatible with Standard User Mode
Femto-slicing	~150 fs	$\sim 10^{-8}$	Yes	~1 kHz	Yes
Crab Cavity	~2 ps	$\sim 2\times 10^{-6}$ to ~1	Yes	~1 kHz to 500 MHz	Yes
Vertical Kick	5-10 ps	$\sim 10^{-6}$	No	~1 kHz	No
Low Alpha	2-10 ps	$\sim 10^{-2}$	No	Up to 500 MHz	No
Harmonic Cavity	~50% reduction	~1	Yes	Up to 500 MHz	Yes
RF Modulation	~50% reduction	$\sim 10^{-5}$	No	~5 kHz	No

Table 2.1: Summary of performance for 3rd generation light sources

2.2 Linac-Based Schemes

In recent years there have been many proposals for generating short radiation pulses from linac-based, fourth generation light sources. The majority of these are yet to be demonstrated in practice, but promise radiation pulses which are several orders of magnitude shorter than can be produced using storage ring based schemes, with extremely high peak brightness and greatly improved transverse and longitudinal coherence. Unlike third generation light sources, these machines are not limited by the effects of radiation damping and excitation, producing intrinsically shorter pulses.

As with third generation light sources, the short pulse generation schemes can be split into two broad categories, namely compression schemes and electron bunch manipulation schemes. The simplest method to produce a short radiation pulse on a linac-based facility falls into the first category. This involves using a magnetic chicane to compress the electron bunch; a standard component for all fourth generation light sources [66, 67]. This is most effective when carried out at very low bunch charge in order to avoid emittance and energy spread degradation from collective effects, allowing high-gain, single pass FELs to operate in the single-spike regime [68]. One alternative to compressing the electron bunch is to compress the radiation emitted by a long electron bunch; this can be achieved if the electron bunch has an energy gradient, as the radiation emitted in an undulator will then have a wavelength variation along the pulse length. A pair of diffraction gratings can then be used to compress the radiation pulse [69].

Bunch manipulation schemes arrange for only a select portion of the electron bunch to reach saturation in a high-gain, single pass FEL. The first one of these to have been proposed involves passing a relatively long electron bunch through a slotted foil inside a magnetic chicane, thereby spoiling the emittance of all but a short section of the bunch. The consequence of this is that only the section of the bunch that retains a low emittance will reach saturation [70]. The majority of bunch manipulation schemes use an external few-cycle laser pulse to modify the electron bunch properties. This interaction gives rise to an energy or trajectory perturbation in a short section of the bunch, which then allows the radiation emitted by this portion to be selectively amplified to saturation in a FEL (see for example [71-77]). The advantage of these laser-based schemes is that they allow tight synchronisation control; a key requirement for pump-probe type experiments [78].

2.2.1 Compression Schemes

2.2.1.1 Bunch Compression in a Magnetic Chicane

The simplest technique for reducing the length of an electron bunch is to compress it in a magnetic chicane. For this type of compression it is necessary to first create an energy-time correlation (chirp) along the bunch length such that the head of the bunch is lower in energy than the tail. When passing through a magnetic chicane, the distance travelled by the head will be longer than for the tail of the bunch, allowing the tail to catch up with the head and reducing the bunch length. The simplest design for a magnetic chicane is the 4-magnet C-type chicane (as used in the LCLS and European X-FEL designs [79, 80]); however, many other designs exist, such as S-type, wiggler, double-chicane and FODO compressors [66, 67]. A schematic of bunch compression with a C-type chicane is shown in Fig. 2.5.

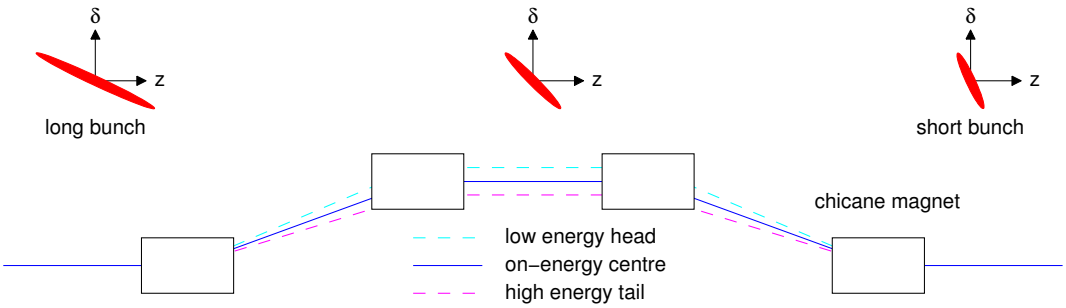

Figure 2.5: Schematic of longitudinal bunch compression in a magnetic chicane.

The deviation in path length (Δz) for an off-energy particle travelling through a chicane can be calculated from the transfer matrices and the relative energy deviation (δ), according to

$$\Delta z = R_{56}\delta + T_{566}\delta^2 + U_{5666}\delta^3 + \cdots \qquad (2.18)$$

where R, T and U are the first, second and third order transfer matrices and R_{56} is the longitudinal dispersion, analogous to α_c in storage rings.

The energy chirp is given to the electron bunch by accelerating it slightly off-crest in the main linac. The energy at the exit of the linac will be

$$E(z) = E_{initial} + eV_{RF}\cos(\varphi + 2\pi z/\lambda_{RF}) \tag{2.19}$$

where $E_{initial}$ is the energy at the entrance to the main linac, φ is the phase-offset relative to the peak field, V_{RF} is the linac RF voltage, λ_{RF} is the RF wavelength and the energy at the centre of the bunch is $E(0) = E_0$. The energy chirp, h, is defined as

$$\begin{aligned} h &= \frac{1}{E_0}\frac{dE}{dz} \\ &= -\frac{2\pi e V_{RF}}{E\lambda_{RF}}\sin(\varphi) \end{aligned} \tag{2.20}$$

Using this definition, in the linear approximation ($z << \lambda_{RF}$) the relative energy deviation of a particle after acceleration is simply $\delta = hz + \delta_0$. Assuming the electron bunch has an initial, uncorrelated energy spread of σ_E, the electron rms bunch length after compression will be

$$\sigma_z = \sqrt{(1 + hR_{56})^2{\sigma_{z0}}^2 + {R_{56}}^2{\sigma_E}^2} \tag{2.21}$$

In principle it is possible to set $hR_{56} = -1$, and so the minimum bunch length is limited by the initial energy spread. The linear approximation provides only a first estimate however. The initial electron bunch length can be a significant fraction of the RF wavelength, meaning the bunch will acquire a curvature in longitudinal phase space which limits the minimum bunch length that can be achieved. This effect can be

partially corrected using a higher-harmonic cavity to linearize the longitudinal phase space before compression, or with nonlinear elements inside the compressor to control T_{566} [81]. A schematic of electron bunch compression with and without linearization is shown in Fig. 2.6.

A side effect of using magnetic bunch compressors is that they can be a major source of emittance growth. For example, incoherent synchrotron radiation (ISR) emission in the chicane bending magnets leads to an uncorrelated increase in both the projected (total) and slice (short section) emittance, along with a growth in the energy spread. This problem increases with increasing beam energy. Coherent synchrotron radiation (CSR) emission can lead to an increase in the projected emittance. This effect occurs because radiation emitted at the tail overtakes the rest of the bunch within the bending magnet, leading to a correlated energy loss along the bunch length and is strongest for short bunches and strong bending magnets. CSR can also lead to a micro-bunching instability, in which any initial density or energy modulations within the bunch will be amplified [82]. ISR and CSR effects can be mitigated by having a small horizontal beta function at the final chicane magnet [83].

Space-charge effects can also become important when compressing the bunch, perturbing both the transverse and longitudinal bunch dimensions. In particular, longitudinal space-charge (LSC) can lead to an energy modulation within the bunch which will be converted into a density modulation in the magnetic chicane. Since space-charge forces scale with $1/E^2$, it is preferable to avoid strong compression at low energies. However, as has already been noted, compression at high energy can increase emittance growth from ISR and nonlinearity in the longitudinal phase space. As such, a staged compression is frequently preferred.

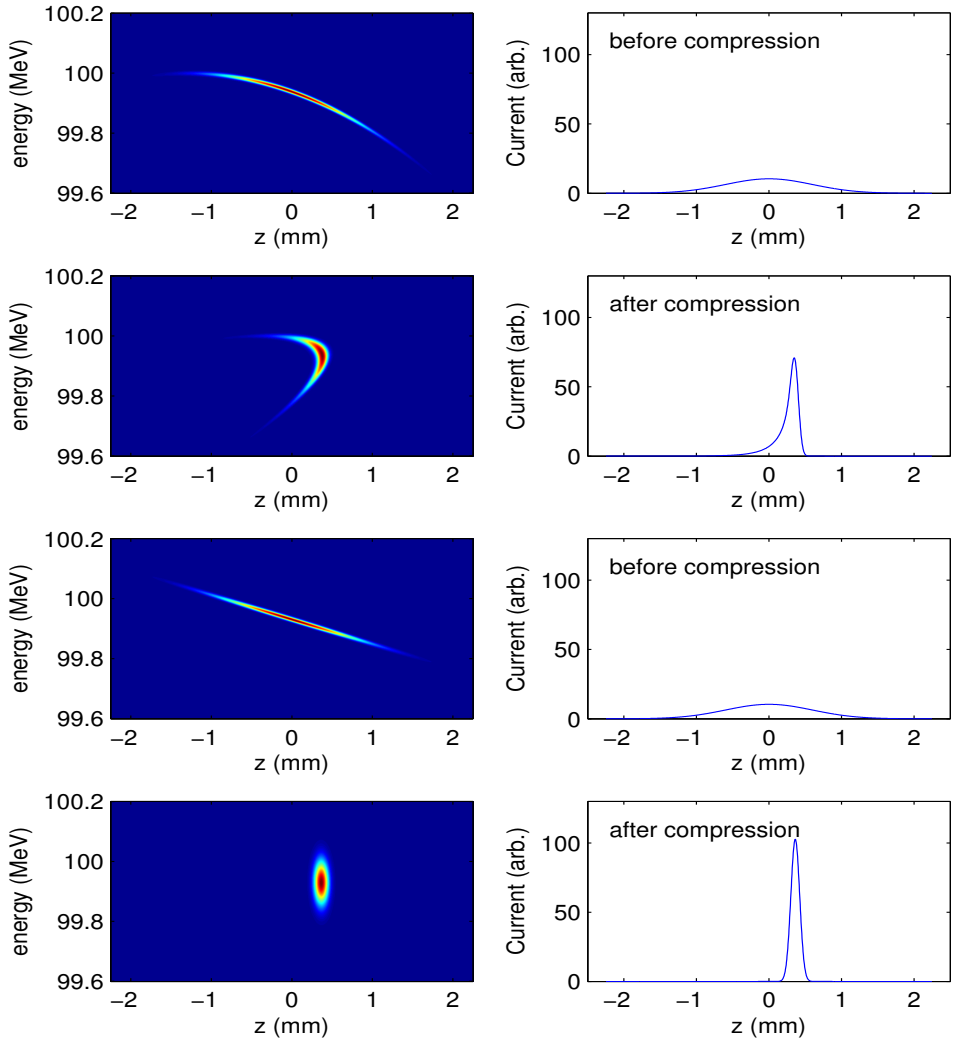

Figure 2.6: Schematic of the longitudinal bunch compression before and after compression, with and without harmonic linearization of the longitudinal phase space (bottom 4 and top 4 plots respectively). A shorter bunch and higher peak current can be achieved with linearization.

Electron bunch compression can also be limited by fluctuations in the chicane magnet power supplies (which alter R_{56}), or by jitter in the linac RF phase or amplitude (which will lead to fluctuations in the energy chirp). Similarly, longitudinal wake fields will alter the chirp. This is not necessarily a problem (and can even be

beneficial), but to avoid fluctuations in the chirp the bunch charge stability from the electron gun must be high.

Magnetic bunch compression is a pre-requisite for fourth generation light sources, but can also be used for short-pulse facilities based on spontaneous radiation sources (rather than FELs) [84]. At FLASH and LCLS, electron bunch lengths of ~10fs or below have been achieved in this way [85, 86].

2.2.1.2 Single Spike Operation

Whilst electron bunch compression is standard in many fourth generation light sources, ultra-short (sub fs) bunch lengths can only be reached in the limit of very low bunch charge when degradation due to collective effects such as CSR, wakefields and space-charge can be avoided. Single spike emission for SASE-FELs is an example of an operating mode that benefits from this potential reduction in electron bunch length.

As described in Section 1.2.4.1, the SASE process in a high-gain, single-pass FEL can lead to the electromagnetic radiation field developing independently in one part of the bunch from the rest. This is due to the fact that the radiation field will slip forward over the electron bunch by only one resonant wavelength (λ_r) per undulator period, and unless the length of the electron bunch is very short the radiation field produced in one section does not have time to interact with the remainder of the bunch before the end of the undulator. As such, the final radiation pulse consists of many separate spikes in the temporal and spectral domains [27].

In order to generate just a single SASE radiation spike, the electron bunch length L_e must be matched to the cooperation length of the FEL (see equation (1.25)), i.e.

$$L_e \leq 2\pi L_c \tag{2.22}$$

Low charge, single spike operation is currently of interest to many projects, primarily because of the simplicity of implementation (no new hardware required), the short pulse duration achieved (potentially <1fs), the high level of temporal coherence and the lack of any background radiation pedestal [86-88]. However, since the FEL process is initiated by the random, spontaneous emission of the electrons, large shot-to-shot fluctuations in the output power are expected. Additionally, any jitter in the arrival time of the electron beam is transferred directly into timing jitter in the FEL output (typically 10-15fs rms), which can be several times larger than the FEL pulse duration. One further drawback with this mode of operation is that machine diagnostics are very difficult to operate at such low bunch charges.

2.2.1.3 Optical Compression of a Chirped Pulse

As an alternative to producing a single radiation spike, it has been suggested that the total radiation pulse emitted by a relatively long bunch can be reduced to the width of a single spike by aligning all spikes on top of each other using a double-grating compressor [69]. This can be achieved using the radiation emitted by an energy-chirped electron bunch. A schematic of the compressor is shown in Fig. 2.7.

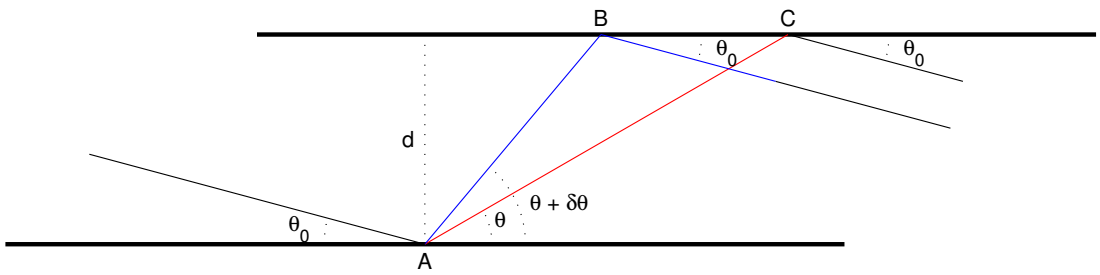

Figure 2.7: Schematic of the double-grating pulse compressor. The distance travelled by the radiation emitted at the head of the electron bunch is longer than that emitted by the tail, allowing the back of the radiation pulse to catch up with the front.

The radiation pulse emitted by an energy-chirped electron bunch will have a frequency variation along its length, such that the wavelength of each SASE spike is correlated to its longitudinal position z within the bunch. This follows directly from the resonance condition,

$$\lambda_r(z) = \frac{\lambda_u}{2\gamma(z)^2}(1 + {a_u}^2) \tag{2.23}$$

From first-order diffraction theory, the scattering angle of the radiation from the first grating, θ, is related to the incident angle θ_0, the grating line separation a and the radiation wavelength

$$\lambda_r(z) = a(\cos\theta_0 - \cos\theta) \tag{2.24}$$

The scattering angle is therefore a function of the position of the spike within the pulse. If the radiation wavelength at the front of the pulse is longer than at the tail, the scattering angle will be larger. After scattering from a second grating, the exit angle is equal to the incident angle, but the longer-wavelength radiation will have travelled further than the shorter wavelength radiation, allowing the back of the pulse to catch up with the front.

In [69], a compression factor F was defined, where F is the difference in path length divided by the initial radiation pulse length, σ_{rad}. From Fig. 2.7, the difference in path length is given by AC - AB - BC×cos(θ_0), and so F is a function of a, d, λ_r, θ_0 and the electron bunch energy chirp. Calculations carried out for the LCLS suggested that with $\lambda_r = 1.5\times10^{-10}$, a = 0.1μm, d = 1.2m and θ_0 = 0.05rad, the pulse duration can be reduced from ~70fs to ~1fs, the width of a single spike. This scheme has the advantage over single spike operation that the intensity fluctuations are reduced by a factor $\sqrt{N_s}$, where N_s is the number of radiation spikes, and that the full bunch charge can be maintained, meaning no reduction in pulse intensity. However, both schemes suffer from arrival time jitter at the sample due to the lack of tight synchronisation control.

2.2.2 Bunch Manipulation Schemes

2.2.2.1 Short Pulse Selection Using a Slotted Foil

The SASE process in a high-gain, single pass FEL is very sensitive to the electron beam emittance. If the emittance is too large, the transverse motion of the electrons will smear out the beam longitudinally as it travels along the undulator length, preventing the electrons from bunching at the resonant wavelength and thereby suppressing the gain of the FEL. This suggests that a short radiation pulse can be created in a SASE-FEL by spoiling the emittance of all but a short section of the electron bunch. This is achieved in the slotted-foil method proposed in [70].

A schematic showing the main components required by the scheme is given in Fig. 2.8. In this method, a thin, slotted foil (e.g. a beryllium foil of ~15μm thickness) is placed in the path of the electron beam at the centre of a magnetic chicane. At this point, the horizontal displacement of the head and tail of the bunch from the centre is at a maximum due to the combination of the energy chirp and the dispersion of the chicane magnets. Coulomb scattering of the electrons when passing through the foil ensures that both the horizontal and vertical emittance will increase in all but the part of the bunch that passes through a narrow slot in the foil.

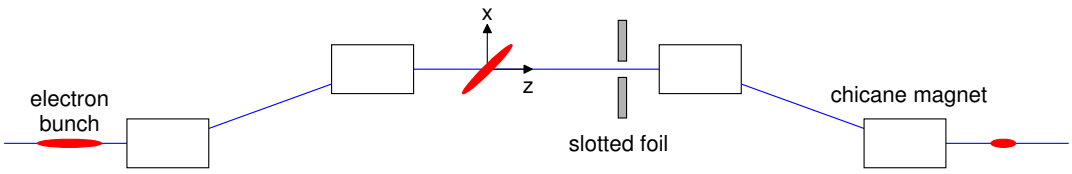

Figure 2.8: Schematic of the slotted-foil short pulse generation scheme. The emittance of the electron bunch is spoiled as it passes through the foil along its whole length, barring a short section in the centre that passes through a narrow vertical slot.

The minimum pulse duration achievable occurs for a slit half-width Δx of a few times the betatron beam size, i.e. $\Delta x = 3\sqrt{\beta_x \varepsilon_x}$. In the centre of the chicane, this half-width will be much smaller than the projected r.m.s. electron beam size, σ_x. The minimum pulse duration is therefore

$$\Delta t_{FWHM} = 2\frac{\Delta x}{\sigma_x}\sigma_{tf} \tag{2.25}$$

where σ_{tf} is the final electron bunch length after compression. Reducing the slit half width to much below this value will reduce the current in the slice, preventing the

FEL pulse from reaching saturation. Simulations carried out for the LCLS suggest that an FEL pulse of 2fs FWHM can be produced using the standard machine operating conditions and a foil with a 250μm slot-width. Further studies using a more aggressive set of operating parameters suggest this pulse length can be brought down to ~0.5fs FWHM, albeit with timing jitter of the order 100fs and fluctuations in the electron bunch peak current (and hence FEL pulse energy) [89]. Initial trials of the method on the LCLS suggest pulses <10fs have been produced [38].

The main advantage this scheme has over others is that it requires only minimal changes the machine hardware and can be implemented on any existing design. Variations on this scheme involve having a vertical taper in the slot width to allow the pulse length to be controlled, or to use more than one slot to produce additional FEL pulses with a time delay controlled by the slot separation. As an alternative to a slotted foil the electron beam could be collimated (thereby removing the background spontaneous emission signal from the remainder of the bunch), however, the collimator wakefields could potentially degrade the brightness of the remaining electron beam. Using a slotted foil also has the advantage of keeping the full beam charge, improving the performance of machine diagnostics.

2.2.2.2 Wavelength Selection Schemes

There have been several proposals for short pulse generation based on resonant wavelength selection. The first of these was proposed by A. Zholents and W. Fawley [71], the layout for which is shown in Fig. 2.9.

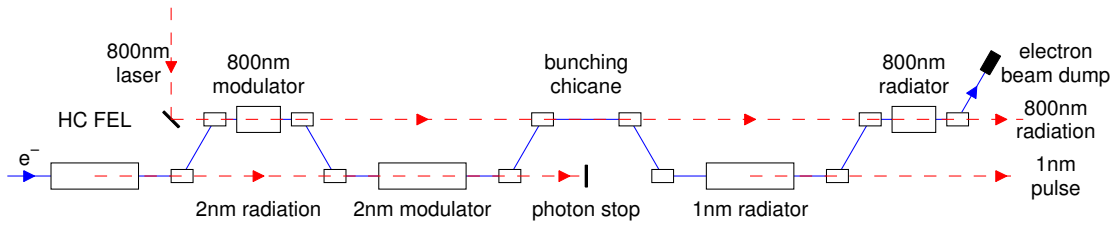

Figure 2.9: Schematic of the scheme proposed by Zholents and Fawley.

The scheme has many components, beginning with a harmonic-cascade (HC) FEL [90]. This produces a 100fs long pulse of radiation at 2nm wavelength from a 2ps long electron bunch, leaving the front of the electron bunch free from FEL interaction (i.e. maintaining high beam quality, small energy spread). The unperturbed electrons interact with a few-cycle (5fs FWHM) 800nm laser pulse inside an undulator, giving a sinusoidal energy modulation to a short section at the front of the electron bunch (c.f. Section 2.1.1). Following this, the electrons pass through a second undulator. This undulator is set to be resonant at 2nm wavelength just for the electrons at the very centre of the laser-modulated portion of the bunch (the electrons that acquired the largest amplitude of energy modulation). The 2nm wavelength HC FEL pulse created upstream can then be used as a seed for the second undulator section. Only the electrons at the centre of the laser-modulated portion will have the correct energy-offset to be resonant with the HC FEL pulse, meaning all other electrons will remain largely unaffected. The electron bunch then passes through a magnetic chicane in order to turn the 2nm energy modulation into a density modulation, and then through an undulator resonant at 1nm (the 2nd harmonic of the density modulation). Only the pre-bunched electrons will radiate strongly, as the radiator is kept short enough to prevent SASE radiation from developing in the remainder of the bunch. This will then generate a short, 1nm radiation pulse which is inherently synchronised with the initial, few-cycle 800nm laser pulse.

Using this method, Zholents and Fawley predicted it should be possible to generate a 0.1fs FWHM long pulse at 1nm wavelength. The difficulty of producing such pulses clearly lies in the complexity of the scheme, and ensuring good temporal overlap between electrons and seed radiation fields.

A similar scheme was also proposed by Saldin et al. [72]. This time however, the short FEL pulse is produced via the SASE mechanism rather than seeding with an HC FEL pulse, allowing a conceptually simpler set-up. The main components of the scheme are shown in Fig. 2.10.

The scheme requires a high-brightness source of electrons which can be made to interact with a few-cycle laser pulse with carrier-envelope phase stabilisation inside an undulator resonant at the laser wavelength (800nm in this case). As with the Zholents scheme, this interaction leaves the electrons with an offset in energy several times larger than the intrinsic energy spread (see Fig. 2.10). If this bunch is made to pass through a long undulator, it will generate SASE radiation such that the radiation produced by the electrons with the largest energy offset will be offset in frequency from the main SASE pulse, and therefore can be separated using a monochromator.

For the scheme to work, the energy modulation given to the electrons by the few-cycle optical laser pulse must be several times larger than the intrinsic SASE bandwidth of the FEL in order to give sufficient separation in frequency space from the main SASE pulse. The duration of the few-cycle laser pulse must also be short enough that only the electrons interacting with the very centre of the laser pulse gain the largest energy modulation. Using this scheme, Saldin et al. estimated that a 0.3fs FWHM long pulse can be generated at 0.1nm wavelength with ~1GW peak power. However, there will be significant shot-to-shot fluctuations in power level due to the

fact that the process starts up from phase-noise in the electron distribution, and due to jitter in the electron bunch characteristics caused by linac fluctuations.

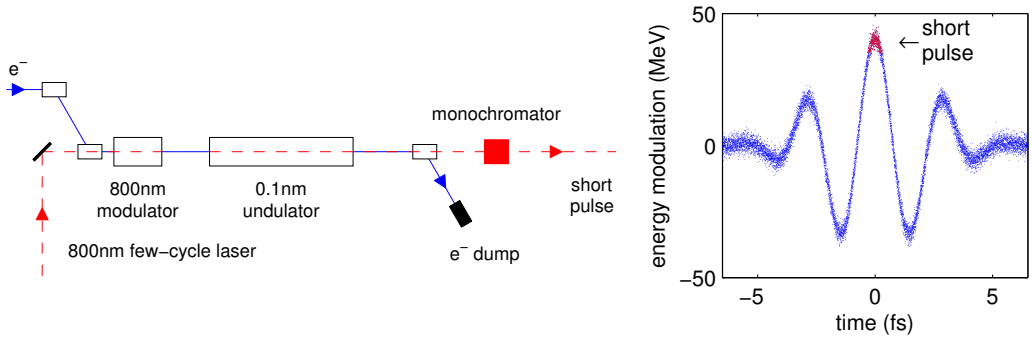

Figure 2.10: Schematic of the scheme proposed by Saldin, Schneidmiller and Yurkov.

A variation of this scheme is to split the long undulator into two sections, the first of which acts in the way described above to create a long SASE radiation pulse at the reference wavelength, with a short pulse centred at the point of maximum energy modulation from the few-cycle laser and offset in frequency from the main pulse [73]. After passing through a magnetic chicane, the electron bunch can be delayed with respect to the SASE pulse such that the portion that is offset in frequency now overlaps with electrons at the reference (i.e. un-modulated) energy. The electron bunch then travels along the second undulator, in which the short pulse acts as a seed field and is amplified to saturation. The remainder of the initial SASE pulse is not amplified as it lies outside the bandwidth of the second undulator. As such, in this scheme the monochromator is no longer required.

Saldin et al. estimate that the output peak power can be increased from ~1GW using the original set up to ~100GW assuming a taper for the second undulator. However, this pulse will sit on top of a background SASE pulse generated by the remainder of the bunch. It was estimated a contrast ratio of 400:1 in peak power can be achieved, corresponding to 1.3:1 in energy for a 100fs long electron bunch.

2.2.2.3 Short Pulses from Current Enhancement

For a SASE FEL, an increase in the peak current for the electron bunch will lead to a reduction in gain length (meaning the radiation will reach saturation earlier) as well as an increase in the radiation power at saturation [23]. This suggests that if the current in a short section of the bunch can be significantly enhanced, the radiation generated from this section will dominate over that from the remainder of the bunch, particularly if the SASE process is stopped before the main pulse reaches saturation. This is the basis for the short pulse scheme suggested by Zholents and Penn [74].

The method used to enhance the current in a short section of the bunch is similar to standard bunch compression in a magnetic chicane. However, rather than creating an energy-chirp across the whole bunch by accelerating it off crest in the main linac, an energy chirp is created in a short section by energy modulation with one or more few-cycle laser pulses inside an undulator. Two lasers are used for the example given in [74], one 1200nm laser pulse of 7.5fs FWHM and one 1600nm laser pulse of 10fs FWHM. Both lasers have carrier-envelope phase stabilisation, with the phase of the lasers set to have zero electric field amplitude at the peak of the envelope waveform and are timed to interact with the same group of electrons within the bunch. Since the two lasers have different wavelengths, the combination acts to increase the gradient of energy chirp in the centre of the modulated section, but suppress it from developing elsewhere. Following the energy modulation, the energy chirp is converted into a density modulation by passing the electron bunch through a magnetic chicane. For the example analysed in [74], the peak current increases from 3.4kA to 19kA as a result of this interaction, reducing the gain length by a factor of two.

The main components of the scheme are shown in Fig. 2.11, and the effect of the laser modulation and bunch compression on the electron bunch parameters is shown in Fig. 2.12.

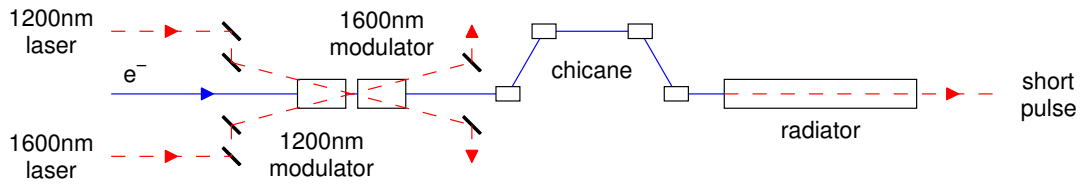

Figure 2.11: Layout of the enhanced-SASE short pulse scheme.

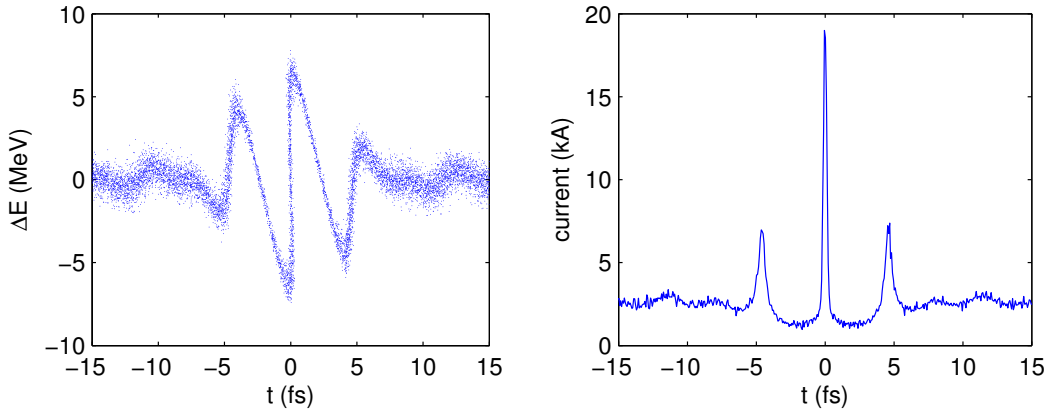

Figure 2.12: Longitudinal phase space of the electron bunch after energy modulation by two few-cycle lasers and compression in a magnetic chicane (left). Resulting current distribution for the electron bunch (right).

In this scheme there is a trade off between having a large energy modulation in order to keep the chicane as weak as possible (to avoid emittance growth from CSR) and keeping the modulation small enough that the energy spread for the high current peak is not too large. Since the FEL interaction grows from phase noise in the initial electron distribution, the radiation pulses generated by this scheme suffer from large shot-to-shot fluctuations of ~40% in peak power. However, using the baseline LCLS

parameters it was estimated in [74] that radiation pulses of 40GW peak power, 0.25fs FWHM could be created, with adjacent peaks of ~1GW peak power and a background signal of 100MW average power from the remainder of the 100fs long electron bunch. The main difficulties of this scheme lie in achieving a temporal overlap of the 1200nm and 1600nm laser pulses with the centre of the electron bunch distribution. However, this can be made easier by using a common source for the two laser pulses.

This technique has also been recently revisited by Ding et al. [91]. The main difference in this case was that the effects of longitudinal space charge on the electron distribution were given more consideration. It was identified that because of the high charge density in the current peaks, space-charge forces cause a secondary energy chirp to develop in the electron distribution as it travels along the main undulator, with a larger chirp developing with increasing peak current. For uniform undulator gap this energy chirp is large enough to suppress the SASE gain for the peak current spike, preventing the short radiation pulse from developing. However, the authors found that by tapering the main undulator gap, the energy chirp could be compensated allowing the pulse to grow for the current spike whilst simultaneously suppressing the FEL gain in the remainder of the bunch [75]. As a result, the tolerances on the modulating laser pulses could be relaxed, allowing pulses as long as 25fs FWHM (10 optical cycles) to be used.

Using a tapered undulator, simulations demonstrated it would be possible to generate radiation pulses with peak power of 2.3GW of 0.1fs FWHM, twenty times larger than the power generated by the adjacent current peaks and two hundred times larger than the background SASE pulse from the main electron bunch.

2.2.2.4 Selected Amplification in Tapered Undulators

The compensation of a localised energy chirp in an electron bunch by tapering the gap of the undulator in a SASE FEL mentioned in the previous section was examined in detail by Saldin et al. [75]. The principle behind this compensation can be understood by considering an electron bunch with a linear energy variation along its length. At the entrance to the undulator, the resonant wavelength for electrons will be different to that of the electrons at the front (as given by equation (2.23)). As the bunch travels along the undulator, the radiation emitted by electrons at the back of the bunch will gradually slip forward to electrons with a different energy and different resonant wavelength. As such, the bunching efficiency and FEL gain will be degraded or even strongly suppressed. However, if the gap of the undulator is altered in order to compensate the change in electron energy to give a resonant wavelength that equals the wavelength of the radiation emitted at an earlier time, efficient bunching and strong FEL gain can be maintained. The required change to the undulator parameter as a function of energy chirp can be calculated from

$$\frac{1}{a_u}\frac{da_u}{dz} = -\frac{\lambda_r}{\lambda_u}\frac{(1+{a_u}^2)}{{a_u}^2}\frac{1}{c\gamma}\frac{d\gamma}{dt} \tag{2.26}$$

Such a combination of undulator taper and energy-chirped electron bunch will produce a frequency-chirped SASE radiation pulse whose central wavelength shifts along the undulator length. Saldin et al. suggested this principle could be used as the basis for a short pulse generation scheme [75].

The layout of the scheme is shown in Fig. 2.13 and bears close resemblance to the second scheme outlined in Section 2.2.2.2. As in the earlier method, an energy

modulation is given to a short section of the electron bunch through interaction with a few-cycle laser, this time operated in sine-mode in order to give maximum energy chirp in the centre of the distribution. Similar chirps will also develop at adjacent laser periods, albeit with decreasing gradients. The undulator gap is then set to compensate the strong energy chirp such that there is strong SASE gain for this section, whilst the taper effectively suppresses the FEL gain in the remainder of the bunch, leading to the development of a single, short SASE radiation pulse.

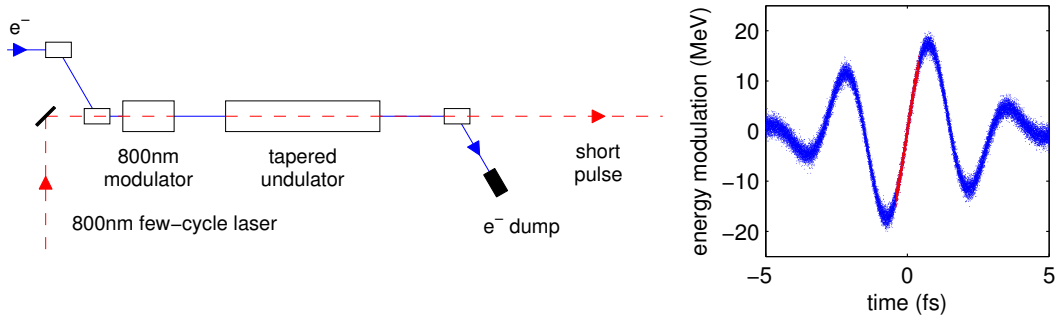

Figure 2.13: Schematic of the tapered undulator scheme. The electron bunch interacts with a 5fs FWHM, 800nm pulse with sine phase to create an energy chirp, and then passes through a long undulator with tapered gap.

Taking the European XFEL parameters, simulations demonstrated that pulses of 0.2fs FWHM, 100GW peak power could be created with a 95% contrast ratio in pulse energy compared to the background signal from the remainder of the bunch. As such, this scheme offers an improved contrast ratio compared to many of the other proposed short pulse generation schemes, and does so with minimal hardware changes from the baseline FEL facility. However, since the FEL emission is based on the SASE mechanism, shot-to-shot fluctuations in peak power are expected to be large.

The method was also examined in detail by Fawley, who demonstrated the scheme scales well to longer wavelengths [92]. In this paper both SASE and seeded configurations were examined at a variety of resonant wavelengths. At 8nm, the SASE scheme was able to produce 0.8GW pulses of 2fs FWHM and the seeded scheme produced 1.5fs FWHM pulses of similar power with a short saturation length. The effect of the frequency chirp was also examined in more detail, and it was identified that both the sign and magnitude of the chirp could be controlled which is potentially beneficial to some types of experiment. Alternatively the chirp could be used to further compress the pulse using the method outlined in Section 2.2.1.3.

2.2.2.5 Selected Amplification Through Angular Modulation

As an alternative to modulating the electron energies, an external modulating laser pulse can also be used to give a transverse kick to the electrons when operated in the TEM_{10} mode [76]. The angular modulation $\Delta x'$ given to the electrons at the exit of the modulating undulator in this case can be calculated from

$$\Delta x'(q,\upsilon,\widehat{\sigma_\tau},s) = \frac{2\sqrt{2}a_u}{{\gamma_0}^2}\sqrt{\frac{P_L}{P_0}}\left\{J_0\left(\frac{\xi}{2}\right) - J_1\left(\frac{\xi}{2}\right)\right\} f(q,\upsilon,\widehat{\sigma_\tau},s)\sin(k_L s + \varphi_L) \qquad (2.27)$$

where $q = L_u/z_0$, L_u is the length of the undulator, z_0 is the laser Rayleigh length, $\upsilon = 2N\delta\gamma/\gamma_r$ is the undulator detuning parameter, $\widehat{\sigma_\tau} = \sigma_\tau/\tau$ is the scaled bunch length, s is the electron coordinate within the bunch, N is the number of undulator periods, P_L is the laser peak power, $P_0 = I_A mc^2/e$, I_A is the Alfven current, J_0 and J_1 are Bessel

functions of the first kind, $\xi = a_u^2/(1+ a_u^2)$, k_L is the laser wave-number and φ_L is a phase offset. The integral f is carried out over the modulating undulator length, and is given by

$$f(q,\upsilon,\hat{\sigma_\tau},s) = q\int_{-0.5}^{0.5}\frac{\cos(2\pi\upsilon\hat{z}-2\tan^{-1}(q\hat{z}))}{1+q\hat{z}}\exp\left(-\left(\frac{\hat{z}}{2\hat{\sigma_\tau}}-\frac{s}{2c\sigma_\tau}\right)^2\right)\mathrm{d}\hat{z} \quad (2.28)$$

The effect of the angular kick is that the electrons will perform transverse oscillations several times larger than the horizontal beam size along the FEL length, with the result that these electrons will experience a larger slippage with respect to the SASE radiation pulse compared to the on-axis electrons (i.e. a phase shift), and a reduced FEL gain. However, if the electron bunch is sent along the main undulator at an angle $-\Delta x'_{max}$, only the electrons at the peak of the angular modulation will travel along the main undulator on-axis and experience strong FEL gain, and it is the remainder of the bunch that suffers from gain degradation. An example of the angular modulation of such an electron bunch is given in Fig. 2.14.

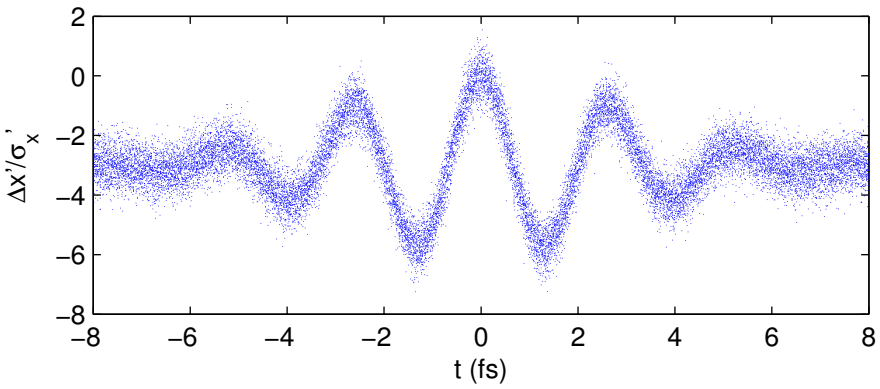

Figure 2.14: Angular modulation of the electron bunch after interaction with a few-cycle laser pulse inside an undulator. All but the electrons at the peak of the interaction region will suffer from gain degradation in the main undulator due to slippage effects.

The main difficulty with achieving this scheme lies in tuning the trajectory of the electron bunch in the main undulator such that only the electrons at the peak of the laser interaction region will travel on-axis. The efficiency with which this region develops a short radiation pulse compared to the rest of the bunch depends on both the properties of the modulating laser and the beta-functions in the main undulator. Simulations for a hypothetical hard x-ray SASE FEL (λ_r = 0.15nm) demonstrated pulses of 0.18fs FWHM duration, assuming a 2μm wavelength modulating laser pulse. In [76] it was also suggested that the scheme could be further improved by combining the trajectory modulation with an energy modulation to enhance the current in the central slice in the same way as described in Section 2.2.2.3. In this case, the pulse duration was reduced to 0.11fs FWHM with a peak power of 100GW.

2.2.2.6 Echo-Enabled Harmonic Generation

In order to avoid the intrinsic shot-to-shot variability associated with SASE-based short pulse schemes it is necessary to use either a seed laser pulse of sufficient power to dominate the spontaneous emission from the electron bunch, or to pre-condition the electron beam to have strong, uniform bunching at the resonant wavelength before it enters the main undulator. Echo-Enabled Harmonic Generation (EEHG) is a scheme that performs the latter [93]. The original concept was not specifically aimed towards short pulse generation, but can easily be adapted for this task [77, 94-95]. The layout for the most straight-forward configuration of this scheme is shown in Fig. 2.15.

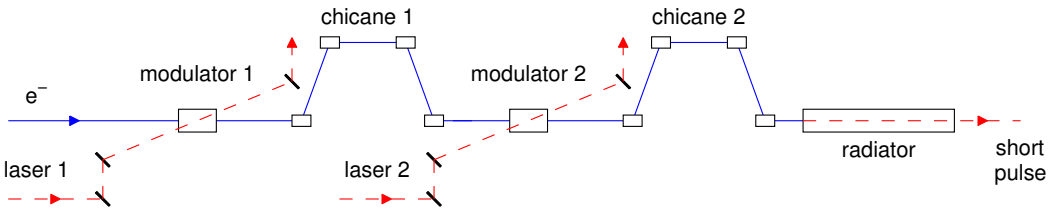

Figure 2.15: Machine layout required for the EEHG-based scheme.

The first stage involves adding a sinusoidal energy modulation to the electron bunch via interaction with a long, external laser pulse of wavelength λ_1 inside an undulator resonant at the same wavelength (see Fig. 2.16). This energy modulation needs to be a few times larger than the intrinsic energy spread. The electron bunch is then made to pass through a strong magnetic chicane which converts the sinusoidal energy modulation into a series of energy bands at a given position within the electron bunch. At this point there is no significant density modulation.

The next step adds a second energy modulation to the electrons, this time using a few-cycle laser of wavelength λ_2 in a short (1 or 2 period) undulator, again resonant at the external laser wavelength. A second magnetic chicane can then be used to convert the few-cycle energy modulation into a density modulation in the same way as described in Section 2.2.2.3. This time however, since the electron bunch retains the energy bands imposed on the electrons by the interaction with the first laser, the central current peak in fact contains a fine structure density modulation of a much shorter wavelength than either of the modulating lasers. The longitudinal phase space at each stage is shown in Fig. 2.16.

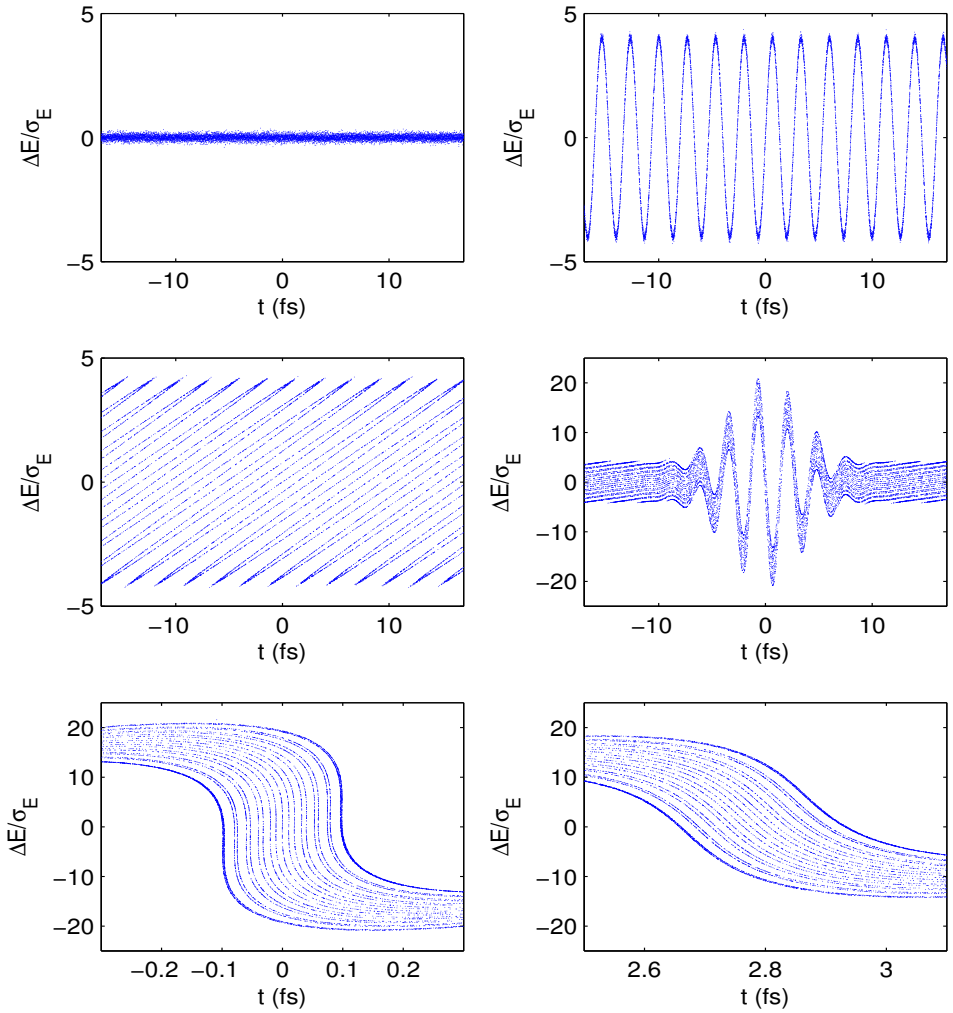

Figure 2.16: Electron bunch longitudinal phase space at each point in the EEHG short pulse scheme. Distribution before first laser modulator (top left). Energy modulation acquired after modulator 1 (top right). Energy banding imposed after first chicane (middle left). Energy modulation added on top of energy banding by few-cycle laser (middle right). Central current peak after second chicane showing fine structure density modulations (bottom left). Side current peak does not gain significant bunching so will not radiate strongly (bottom right).

After the initial beam-conditioning described above, the density modulations inside central current peak have a wavelength λ_{mod} where

$$\frac{2\pi c}{\lambda_{mod}} = n\frac{2\pi c}{\lambda_1} + m\frac{2\pi c}{\lambda_2} \tag{2.29}$$

and m and n are integers. The bunching factor is found to be a maximum for $n = \pm 1$, and assuming correctly optimised chicane strengths, modulation amplitudes and for $m > 4$, the maximum bunching factor is given by [98]

$$|b_m| \approx \frac{0.39}{m^{1/3}} \tag{2.30}$$

This is in contrast to high-gain harmonic generation (HGHG) schemes [90], in which the maximum bunching factor tends towards $|b_k| \approx \left(0.68/k^{1/3}\right)\exp(-k^2/2A^2)$, giving a much lower bunching efficiency at high harmonics of the modulating laser frequencies compared to the EEHG scheme.

Upon entering the main radiator undulator, only the pre-bunched part of the electron bunch will radiate strongly. The length of the radiator is kept relatively short to prevent the SASE process from building up in the remainder of the bunch.

Simulations of this scheme are at an early stage, and there are several open questions about the performance of the scheme at x-ray wavelengths, such as whether the additional energy spread from incoherent synchrotron radiation emission in the first chicane will blur out the energy bands, whether coherent synchrotron radiation in the second chicane will distort the energy modulation given by the few-cycle laser and whether longitudinal space charge has a significant effect on the micro-bunching. However, initial studies suggest 1nm wavelength pulses of 100-200MW peak power lasting 20as FWHM should be achievable [77, 95].

2.2.2.7 Longitudinal Space Charge Amplifier

The most recent example of how a few-cycle optical laser pulse can be used to generate short pulses of synchrotron radiation was outlined in [96]. This scheme makes use of the longitudinal space charge (LSC) driven micro-bunching instability which occurs in linacs with magnetic bunch compressors [97]. The instability arises from small, random density fluctuations present in the electron beam, which when combined with a source of impedance such as LSC or CSR lead to an energy modulation at the same scale. If this bunch passes through a magnetic chicane the energy modulations will be converted into a density modulation, enhancing the initial fluctuations and resulting in the micro-bunching instability. For normal operation, great care is taken to suppress this effect.

Rather than trying to avoid the LSC-driven micro-bunching instability, the proposed scheme takes advantage of it by optimising the chicane strengths, lengths of drift space and beta-functions in order to maximise the gain at a given wavelength of interest (λ_{LSC}). Several stages of drift space and chicane can then be used to maximise the bunching at the given wavelength and reach saturation.

In order to generate a short radiation pulse from the LSC-bunched electron beam, a few-cycle optical laser pulse operated in sine-mode is used to give a linear energy-chirp h in the centre of the laser modulated portion, the amplitude of which must be significantly larger than the energy modulation acquired from the LSC instability. The electron bunch is then passed through a final magnetic chicane of strength R_{56}. As described in Section 2.2.1.1 this will compress the chirped region by a factor C where

$$C = \frac{1}{1 - hR_{56}} \tag{2.31}$$

such that the LSC-bunched wavelength becomes $\lambda_f = \lambda_{LSC}/C$ and the peak current in the compressed section is enhanced by a factor C. The end result is the majority of the electron bunch is bunched at wavelength λ_{LSC}, with a short section in the centre of the laser-modulated region with bunching at wavelength λ_f. If the bunch then travels through an undulator resonant at λ_f, significant FEL amplification will only occur in the section of the electron distribution with bunching at wavelength λ_f, with negligible gain elsewhere. No detailed simulations of the scheme were carried out in [96]; however it was estimated a 4nm wavelength pulse of 0.1fs FWHM and sub-GW peak power could be generated. A layout of the scheme is shown in Fig. 2.17.

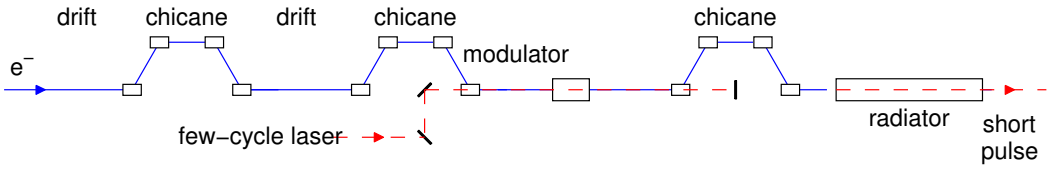

Figure 2.17: Layout for a LSC-amplifier based scheme. Several stages of drift and magnetic chicane are used to amplify small-scale density fluctuations present in the electron beam at a particular wavelength. A few-cycle laser adds an energy chirp to the centre of the bunch, and a chicane compresses the chirped region thereby reducing the wavelength of the bunching.

2.2.3 Performance Summary

	Estimated Pulse Duration	Peak Power	Background to Short Pulse	Repetition Rate	Synchronised
Bunch Compressor	~10 fs	-	No	Linac	No
Single Spike	~1 fs	~1 GW	No	Linac	No
Optical Compression	~1 fs	-	No	Linac	No
Slotted Foil	~0.5-2 fs	5-10 GW	Yes	Linac	No
Wavelength Selection (1)	<0.1 fs	5-10 MW	Yes	LASER	Yes
Wavelength Selection (2)	~0.3 fs	~1 GW	Yes	LASER	Yes
Wavelength Selection (3)	~0.3 fs	~100 GW	Yes	LASER	Yes
Current Enhancement	~0.1 fs	~2 GW	Yes	LASER	Yes
Tapered Undulator	~0.2 fs	~100 GW	Yes	LASER	Yes
Angular Modulation	~0.2 fs	-	Yes	LASER	Yes
EEHG	~0.02 fs	100-200 MW	Yes	LASER	Yes
LSCA	~0.1 fs	<1 GW	Yes	LASER	Yes

Table 2.2: Summary of performance for 4th generation light sources

2.3 Summary

One of the goals of this thesis is to identify which short pulse generation schemes would be suitable for use in a large-scale user facility. As such, the source of radiation must be robust, practical and generate light with properties that are useful for current research.

The review given in this Chapter has identified that, for third generation light sources there is presently no stand-out scheme for the generation of short radiation pulses, but rather each scheme has its own merits. For example, femto-slicing is capable of generating the shortest pulses, but does so with a drastic reduction in photon flux. Bunch deflection with crab-cavities can potentially operate with the full bunch charge of standard operation, but requires the installation of substantial new hardware which is both expensive and time consuming. Transient methods such as RF cavity modulation or vertical kicking can also produce short pulses with a relatively high photon flux, but there are concerns about how such pulses could be used in an experiment due to the lack of predictability and stability of the short pulse. Low-alpha operation has the benefit of being able to provide short pulses with a higher brightness and repetition rate than some other schemes, provides good stability and has the advantage that it does not require any additional hardware to be implemented and in principle can be applied to any existing light source. The price to pay is a reduction in bunch charge from that of standard user operation, and a marginal increase in pulse duration over that which can be obtained with femto-slicing.

Short pulse schemes for fourth generation light sources can be split into two categories, those that do and those that do not use an external few-cycle laser to

modify the properties of a short section of the electron bunch. Schemes that do not use an external laser all potentially suffer from large jitter in the arrival time of the short pulse of a magnitude that is many times larger than the pulse duration itself. The most straightforward of these schemes is the single-spike mode of operation which can generate pulses of very high peak power thanks to the excellent electron beam quality that is possible when the linac is operated with low bunch charge. Slicing schemes using a few-cycle modulating laser vary in their complexity and in the properties of the final pulse that is produced. Since they are all initiated by an external laser pulse, the arrival time of the FEL pulse at the experiment can be controlled to a very high precision; however, the background signal generated by the un-modulated section of the electron bunch can be a significant fraction of the total pulse energy. The tapered undulator scheme suppresses this background signal, resulting in an improved contrast ratio over other schemes. The tapered undulator scheme requires minimal additional hardware compared to other schemes, making it an attractive proposition compared to other schemes when being considered for use in a user facility.

Taking all potential strengths and weaknesses into account, the schemes that have been selected for further study are therefore low-alpha operation of the Diamond storage ring, single spike operation of the New Light Source and application of the tapered undulator scheme to the New Light Source. Studies of low-alpha operation are contained in Chapter 3, and studies of the two schemes for the New Light Source are described in Chapter 4.

Chapter 3

Short Pulse Generation from a Quasi-Isochronous Storage Ring

The review given in Chapter 2 highlighted the benefits of basing a short pulse generation scheme on a low momentum compaction factor (low-alpha) lattice over some of the other methods that have been proposed. Of these, the main advantage lies in the ease with which it can be implemented, its reliability and the stability of the (pico-second) radiation source. Other benefits include having a higher average brightness and repetition rate than can be achieved using other schemes, along with the fact it does not require costly new hardware to be installed.

In this Chapter, the development and implementation of two low-alpha lattices for the Diamond storage ring is presented. The theory of operating with near-zero momentum compaction factor (alpha) is reviewed in Section 3.1, examining in particular the dependence of the longitudinal motion on the higher order terms in the expansion of alpha with momentum deviation. Details of the two low-alpha lattice solutions are discussed in Section 3.2, and various simulations made to characterise the lattices are presented in Section 3.3. The final part of this Chapter is devoted to the application of the two lattices to the Diamond storage ring, including details of beam dynamics and bunch length measurements made under a variety of conditions.

3.1 Theory of Low-Alpha Operation

3.1.1 Introduction

Electrons circulating in a storage ring have an intrinsic momentum spread due to the stochastic emission of synchrotron radiation. This momentum spread results in a finite electron bunch length, since in general the revolution time is dependent upon the particle energy. By making the storage ring isochronous, all electrons will travel the same distance in one revolution and the electron bunch length can be made, to a first approximation, arbitrarily small.

The change in path length with momentum deviation is set by alpha, and in the absence of collective effects it is this that determines the electron bunch length (along with various RF cavity and lattice parameters). In the limit of zero bunch current, the natural electron bunch length is given by the equation

$$\sigma_0 = \frac{c\alpha_c}{2\pi f_s}\sigma_E \tag{3.1}$$

where α_c is the momentum compaction factor, f_s is the synchrotron frequency and σ_E is the natural energy spread. The synchrotron frequency is given by

$$f_s = f_{rev}\sqrt{\frac{h\,\alpha_c \cos\varphi_s e V_{RF}}{2\pi E_0}} \tag{3.2}$$

where h is the harmonic number, V_{RF} is the cavity voltage, f_{rev} is the revolution frequency, φ_s is the synchronous phase and E_0 is the electron energy. Since f_s also depends upon alpha, σ_0 scales with the square root of alpha. In order to reduce the natural bunch length one can try to minimise σ_E (which is fixed by the beam energy

and dipole bending radius), maximise f_s (limited by the maximum RF cavity voltage) or minimise alpha.

3.1.2 The Momentum Compaction Factor

Alpha is defined as the relative change in path length in one revolution of the storage ring with respect to the relative particle momentum deviation, δ

$$\alpha_c = \frac{\Delta l / l_0}{\delta} \tag{3.3}$$

where $\delta = \Delta p/p_0$, p_0 is the nominal particle momentum and l_0 is the circumference. Alpha is typically expanded as a power series in momentum deviation. Different definitions exist for this expansion; in this thesis the definition

$$\alpha_c(\delta) = \alpha_1 + \alpha_2\delta + \alpha_3\delta^2 + O(\delta^3) \tag{3.4}$$

is used. The leading order terms in the expansion can be calculated using (see Appendix A)

$$\alpha_1 = \frac{1}{l_0}\oint \frac{\eta_1(s)}{\rho} ds \tag{3.5}$$

$$\alpha_2 = \frac{1}{l_0}\int \frac{\eta_1'(s)^2}{2} + \frac{\eta_2(s)}{\rho} ds \tag{3.6}$$

$$\alpha_3 = \frac{1}{l_0}\int \eta_1'(s)\eta_2'(s) - \frac{\eta_1(s)\eta_1'(s)^2}{2\rho} + \frac{\eta_3(s)}{\rho} ds \tag{3.7}$$

Here, ρ is the dipole bend radius, η is the dispersion, η' is its spatial derivative and the subscripts 1, 2 and 3 refer to the order in the expansion with momentum deviation. In

order to minimise α_1 the storage ring linear optics needs to be tuned such that the integrated dispersion inside the bending magnets is close to zero. This can be done with quadrupole magnets. The α_2 term has two components; the first is fixed by $\eta_1'(s)$, and the second depends upon the value of $\eta_2(s)$ in the bending magnets. The value of $\eta_2(s)$ can be controlled using sextupole magnets, and can in principle be tuned to set α_2 to zero. An expression describing the way the sextupole magnet strength affects α_2 was presented in [48], where it was shown that the change in α_2 depends upon only the integrated sextupole strength (*SL*), the circumference of the ring and the dispersion at the sextupole location.

$$\Delta\alpha_2 = -\frac{SLl_0}{3}\left({\eta_x}^3 - 3\eta_x{\eta_y}^2\right) \tag{3.8}$$

Clearly, an efficient reduction in α_2 requires focussing sextupoles in regions of high horizontal positive dispersion. Good control of α_3 and above requires higher order multipole magnets (octupoles to control α_3, decapoles to control α_4 and so on).

3.1.3 Longitudinal Motion

For highly relativistic electron beams and in the absence of quantum fluctuations, the equations governing the longitudinal motion can be written as [48]:

$$\varphi'(\delta) = h\left(\frac{\Delta\ell}{\ell} + \alpha_1\delta + \alpha_2\delta^2 + \alpha_3\delta^3\right) \tag{3.9}$$

$$\delta'(\varphi) = \frac{eV_{RF}}{2\pi E_0}\left[\sin\varphi - \sin\varphi_s\right] \tag{3.10}$$

where the term $\Delta\ell/\ell$ represents all momentum independent path lengthening effects such as those due to betatron oscillations, closed orbit errors or a change in RF frequency. Equations (3.9) and (3.10) can be derived from the following Hamiltonian.

$$H(\varphi,\delta) = h\left[\frac{\Delta\ell}{\ell}\delta + \frac{\alpha_1}{2}\delta^2 + \frac{\alpha_2}{3}\delta^3 + \frac{\alpha_3}{4}\delta^4\right] + \frac{eV_{RF}}{2\pi E_0}[\cos\varphi - \cos\varphi_s + (\varphi - \varphi_s)\sin\varphi_s] \tag{3.11}$$

The longitudinal motion has stable and unstable fixed points which occur when both $\varphi' = 0$ and $\delta' = 0$. The fixed points occur at phases $\varphi = \varphi_s$ and $\varphi = \pi - \varphi_s$, and the momentum deviations are given by the roots of equation (3.9), i.e. by

$$\frac{\Delta\ell}{\ell} + \alpha_1\delta + \alpha_2\delta^2 + \alpha_3\delta^3 = 0 \tag{3.12}$$

The particle motion exhibits different behaviour depending upon the relative strength of each term in alpha. For high-performing low-alpha lattices, effects up to third order or even higher are relevant. The different regimes are discussed further in the following sections.

3.1.3.1 First Order Approximation

Under normal operating conditions, α_1 is large and to a first approximation all higher order terms in alpha can be neglected. In these conditions, there exists a single stable region in longitudinal phase space, for which there is one stable fixed point (SFP) of motion and one unstable fixed point (UFP). The boundary separating stable and unstable motion (the separatrix) is determined by the value of the Hamiltonian at the UFP, which from equation (3.12) is at the location $\varphi = \pi - \varphi_s$ and $\delta = -\Delta\ell / \ell\alpha_1$. After

substituting these values into equation (3.11), the maximum momentum deviation for oscillations around the SFP is found to be

$$H\left(\pi-\varphi_s,-\frac{\Delta\ell}{\ell}\frac{1}{\alpha_1}\right)=H(\varphi_s,\delta_{max})$$

$$-\frac{h}{2\alpha_1}\left(\frac{\Delta\ell}{\ell}\right)^2+\frac{eV_{RF}}{2\pi E_0}[(\pi-2\varphi_s)\sin\varphi_s-2\cos\varphi_s] \\ =h\left[\frac{\Delta\ell}{\ell}\delta_{max}+\frac{\alpha_1}{2}{\delta_{max}}^2\right] \tag{3.13}$$

which for the case $\Delta\ell/\ell = 0$ reduces to the result

$$\delta_{max}=\varepsilon_{RF}=\sqrt{\frac{2eV_{RF}}{\pi h\alpha_1 E_0}\left[\left(\frac{\pi}{2}-\varphi_s\right)\sin\varphi_s-\cos\varphi_s\right]} \tag{3.14}$$

The seperatrix between stable and unstable motion in this regime is shown in Fig. 3.1. In this plot, $\Delta\ell/\ell$ and φ_s have been assumed to be zero.

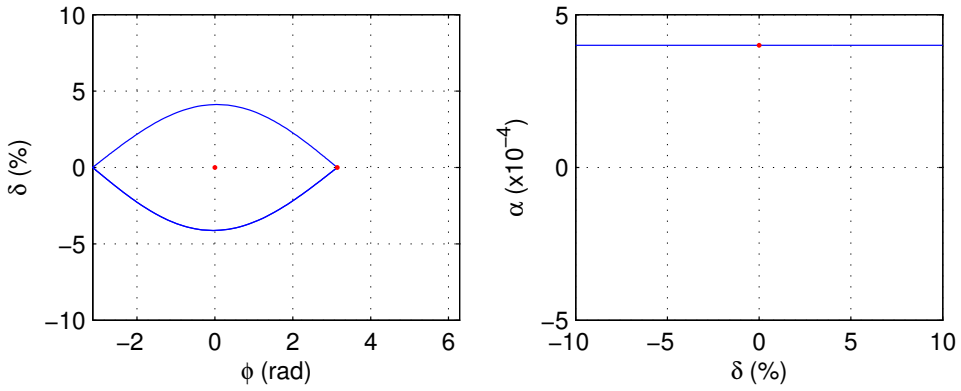

Figure 3.1: Figure showing a typical separatrix between stable and unstable motion for the case of E_0 = 3GeV, f_{RF} = 499.654GHz, φ_s = 0, V_{RF} = 3MV, α_1 = 4×10^{-4} and neglecting all higher order terms in alpha (left). Corresponding value of $\alpha(\delta)$ (right). The red dots show the positions of the stable and unstable fixed points of motion.

3.1.3.2 Second Order Approximation

For the case where α_2 is small but non-negligible compared to α_1, α_2 has a perturbative effect on the particle motion. Two new fixed points appear in the longitudinal phase space, with the momentum offsets given by the solutions of equation (3.12) as

$$\delta_{1,2} = -\frac{\alpha_1}{2\alpha_2}\left(1 \pm \sqrt{1 - \frac{4\alpha_2}{{\alpha_1}^2}\frac{\Delta\ell}{\ell}}\right) \tag{3.15}$$

There are now two stable RF buckets bounded by two separatrices. If $\alpha_1 >> \alpha_2$, the new stable region is far from the original RF bucket, with the shape of each separatrix close to that of the linear case. Under these conditions equation (3.14) is still a good approximation to the now asymmetric momentum acceptance. This regime is usually described as the RF bucket regime. As the magnitude of α_1 is reduced relative to α_2, the two buckets are brought closer together and the shapes of the buckets are distorted until they eventually merge and share the two UFPs. Further reduction of α_1 leads to the two buckets exchanging UFPs and separating again. The motion is now operating in the so-called alpha-bucket regime. Under these conditions the size of the stable region reduces rapidly, with the maximum bucket height now defined by the distance between the SFPs and UFPs.

$$|\delta_{SFP} - \delta_{USF}| = \frac{\alpha_1}{\alpha_2}\sqrt{1 - \frac{4\alpha_2}{{\alpha_1}^2}\frac{\Delta\ell}{\ell}} \tag{3.16}$$

In order to stay in the RF bucket regime and hence maintain good momentum acceptance, the following condition should be met [99].

$$\alpha_1 \geq \alpha_{1,transition} = \sqrt{3}\varepsilon_{RF}\alpha_2\left(1 - \frac{4\alpha_2}{{\alpha_1}^2}\frac{\Delta\ell}{\ell}\right)^{-3/4} \tag{3.17}$$

In practice, large momentum acceptance can be ensured by correcting α_2 to zero [48].

A plot illustrating how the size of the stable region in longitudinal phase space rapidly shrinks when moving from the RF bucket regime through transition and into the alpha-bucket regime is given in Fig. 3.2. For simplicity, α_2 has been assumed to be constant as α_1 is decreased and $\Delta\ell/\ell$ has been set to zero. The contribution from radiation losses has been neglected ($\varphi_s = 0$).

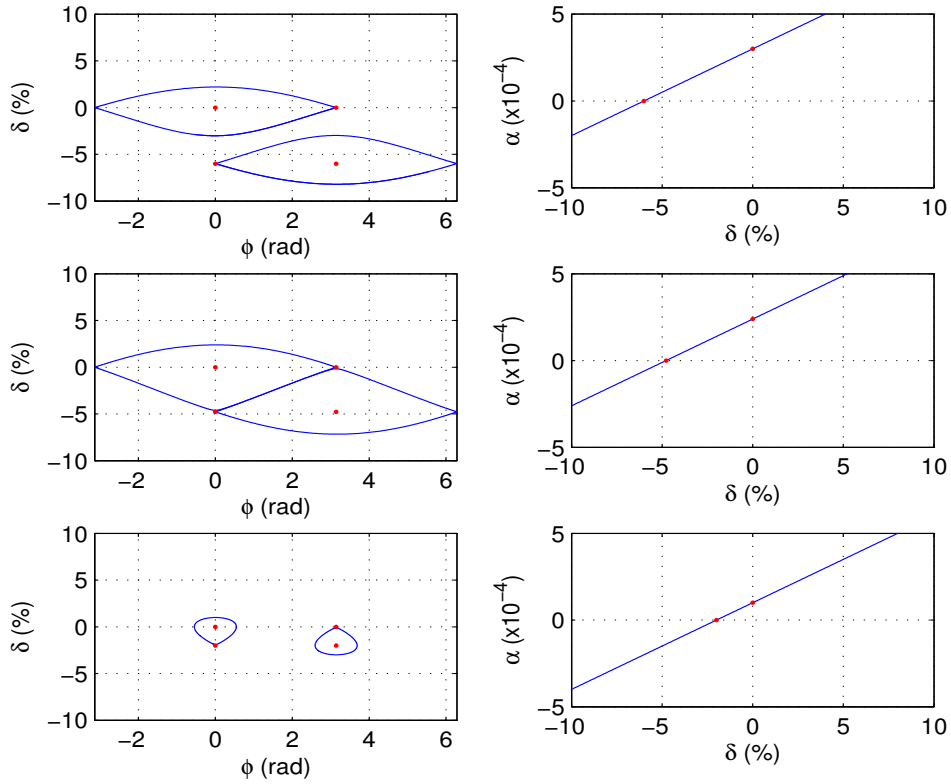

Figure 3.2: Figure showing how the seperatrices between stable and unstable motion vary as α_1 is reduced for a fixed value of $\alpha_2 = 5\times10^{-3}$ (left), with the corresponding values for $\alpha(\delta)$ (right). The 3 regimes illustrated are the RF bucket regime (top), transition (middle) and alpha-bucket regime (bottom). The red dots show the positions of the stable and unstable fixed points of motion.

3.1.3.3 Third Order Approximation

In order to gain an improved understanding of how α_3 influences the longitudinal motion, both α_2 and $\Delta\ell/\ell$ can be neglected. This simplification is justified, as for all practical lattices, α_2 is corrected to zero in order to maximise the momentum aperture. Similarly, the momentum-independent path lengthening term $\Delta\ell/\ell$ can be considered zero at low chromaticity [100], since the contribution from closed orbit distortions can always be compensated by adjusting the central RF frequency. In the following analysis, radiation losses are neglected ($\varphi_s = 0$) and to begin with only the case where $\alpha_3 < 0$ is considered.

For a comparatively large initial value of α_1, the longitudinal motion operates in the standard RF-bucket regime. There are now three stable regions in the longitudinal phase space, the on-momentum bucket centred at $(0,0)$ plus two off-momentum buckets centred at $\left(\pi, \pm\sqrt{-\alpha_1/\alpha_3}\right)$. The separatrices for these buckets are shown in Fig. 3.3. As α_1 is reduced, the three stable regions approach each other and the shapes of the buckets are distorted until they eventually merge. This is the transition between the conventional RF bucket regime into the alpha-bucket regime. As α_1 is further reduced with respect to α_3, the three buckets split again, this time with the UFPs swapped such that the two buckets centred at $\left(\pi, \pm\sqrt{-\alpha_1/\alpha_3}\right)$ share the one at $(\pi, 0)$, and the bucket centred at $(0,0)$ now has the two UFPs at $\left(0, \pm\sqrt{-\alpha_1/\alpha_3}\right)$. A further reduction of α_1 from positive to negative values leads the off-momentum solutions to equation (3.12) to become imaginary and the bucket centred at $(0,0)$ disappears. At the same time the two buckets centred at $\left(\pi, \pm\sqrt{-\alpha_1/\alpha_3}\right)$ merge to form a single on-

momentum bucket centred at $(\pi, 0)$; the momentum compaction factor is now entirely negative and the stable RF phase has switched from $\varphi = 0$ to $\varphi = \pi$.

For the case of positive α_3, the situation described above is reversed, i.e. as α_1 is made to pass from positive to negative values it is the bucket centred at $(0,0)$ that splits into two, rather than the two off-momentum buckets that merge to form a single on-momentum bucket. This transition can occur smoothly without loss of beam [101].

Transition between the RF and alpha bucket regimes occurs when the Hamiltonians for the separatrices of the three buckets are equal, namely when

$$H(\pi, 0) = H\left(0, \pm\sqrt{-\alpha_{1,transition}/\alpha_3}\right) \tag{3.18}$$

which eventually reduces to

$$\alpha_{1,transition} = -2\alpha_3 {\varepsilon_{RF}}^2 \tag{3.19}$$

As for the case of dominant α_2 this transition point can be used as a criterion for good lifetime, i.e. to stay in the RF bucket regime $\alpha_1 \geq \alpha_{1,\,transition}$. Once in the alpha-bucket regime the maximum momentum deviation is fixed by the distance between SFP and UFP, i.e. by

$$|\delta_{SFP} - \delta_{UFP}| = \sqrt{-\frac{\alpha_1}{\alpha_3}} \tag{3.20}$$

Crucially however, if both α_1 and α_3 have the same sign then the off-momentum fixed points are imaginary and this condition no longer applies. In this case the α_3 term creates a perturbation on the maximum stable momentum deviation of the linear RF bucket. The momentum acceptance can be found by equating the value of the Hamiltonian at the unstable fixed point to the value at the phase $\varphi = \varphi_s$, i.e.

$$H(0,0) = H(\pi, \delta_{max}) \tag{3.21}$$

which leads to the result

$$\delta_{max}{}^2 + \frac{\alpha_3}{2\alpha_1}\delta_{max}{}^4 = \varepsilon_{RF}{}^2 \tag{3.22}$$

In this regime, the α_3 term serves to increase the momentum aperture above the one found from the classical first order solution, and particles exhibit regular motion out to large momentum and phase deviations.

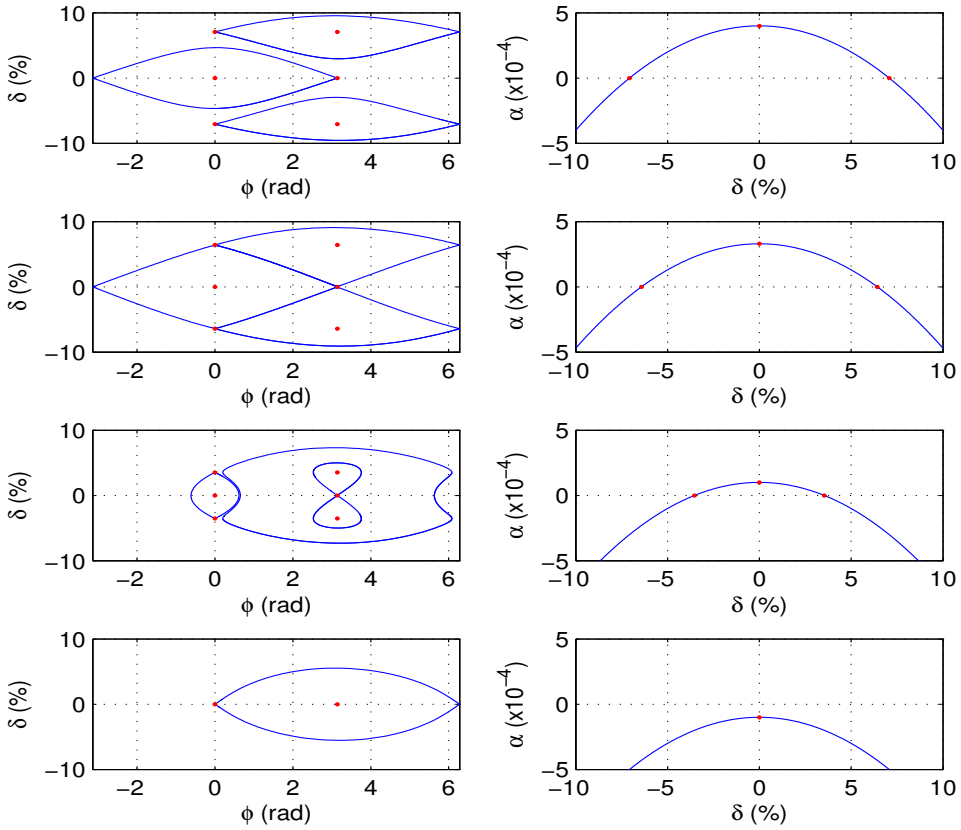

Figure 3.3: Figure showing the separatrices between stable and unstable motion and alpha as a function of $\ddot{o}$ as α_1 is reduced from positive to negative values for α_2 = 0 and α_3 = -0.08. The four stages illustrated are RF-bucket regime (top), transition (middle top), alpha-bucket regime (middle bottom) and negative alpha (bottom). The red dots show the positions of the stable and unstable fixed points of motion.

3.2 Low-Alpha Lattices for the Diamond Storage Ring

The vast majority of third generation synchrotron light sources are not optimised for the production of short electron bunches, but rather a low emittance is targeted to enable the generation of high brightness photon beams. However, as indicated by equations (3.5) to (3.7), it is possible to minimise alpha by an appropriate tuning of the lattice optical functions. This has been proposed or carried out at a number of light-sources worldwide [see, for example, 99, 101-112], for diverse reasons such as producing short x-ray pulses, generating coherent Far IR / THz radiation, operating a storage ring FEL, or for fundamental beam-dynamics investigations.

In this section the development of two low-alpha lattices for the Diamond storage ring is described. The first of these has a relatively high emittance in comparison to the standard user lattice, but is less demanding in terms of the sextupole requirements. The second lattice has a low emittance close to that of the standard user lattice, and its development was motivated by the desire to increase the x-ray source brightness above that of the first lattice [113, 114].

3.2.1 Practical Considerations for a Low-Alpha Lattice

An ideal low-alpha lattice should have small, controllable α_1, sufficient on-momentum dynamic aperture to be able to inject directly into the lattice without

shifting the working point or changing the optics, sufficient off-momentum dynamic aperture for good lifetime and injection, and small, controllable α_2 and transverse chromaticity. In addition it is desirable to have small vertical beta function in the ID straight sections and large horizontal beta function in the injection straight to ease the injection process.

In order to reduce α_1, equation (3.5) states that the integrated dispersion inside the bending magnets should be minimised. The way that this has been achieved in double-bend achromat (DBA) lattices elsewhere is to introduce negative dispersion in the straight sections [99, 101-102, 105-109], crossing from positive values between the bending magnets to negative values in the straight sections. The downside of this approach is that the horizontal emittance is significantly increased, as whilst the integrated dispersion inside the bending magnets is reduced, the chromatic invariant $H_x = \gamma_x\eta_x^2 + 2\alpha\eta_x\eta_x' + \beta\eta_x'^2$ is found to increase. The increase in horizontal emittance (ε_x) follows directly from this.

$$\varepsilon_x = \frac{55}{32\sqrt{3}}\frac{\hbar\gamma^2}{m_e c}\frac{I_5}{I_2 - I_4} \tag{3.23}$$

where

$$I_2 = \int \frac{1}{\rho(s)^2}\,ds\,; \qquad I_4 = \int \frac{\eta(s)}{\rho(s)^3}\,ds\,; \qquad I_5 = \int \frac{H_x(s)}{\rho(s)^3}\,ds$$

An alternative solution is to keep the dispersion positive everywhere except within the bending magnets [115, 116]. This allows both α_1 and ε_x to be minimised simultaneously. The variation of the dispersion through the bending magnets for these two options is illustrated in Fig. 3.4.

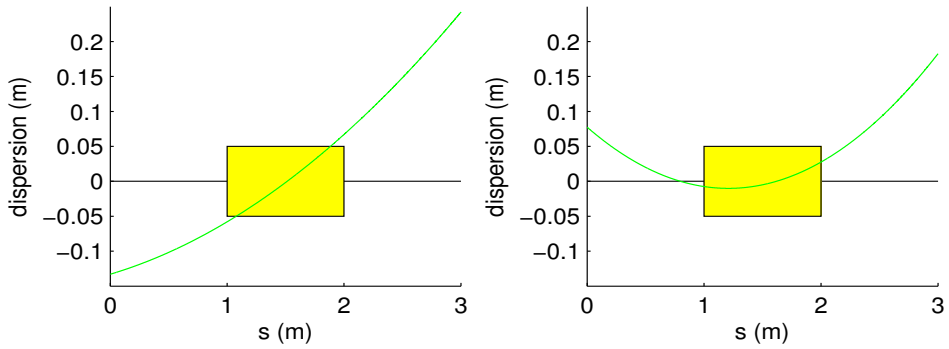

Figure 3.4: Variation of dispersion through a bending magnet for the case of $\alpha_1 = 0$. Left: High emittance solution. Right: Low emittance solution.

The goal of the nonlinear lattice optimisation is to correct the natural chromaticity and α_2 with minimal impact on the on and off momentum dynamic aperture. The success of this depends in part on the linear lattice [117, 118], and so the combined optimisation is by necessity an iterative process.

The interconnection between the linear and non-linear lattice optimisation can be clearly seen from the definition of the horizontal and vertical chromaticity (ξ_x and ξ_y):

$$\xi_x = \frac{dQ_x}{d\delta} = \frac{1}{4\pi}\int_0^{\ell_0} [2S(s)\eta(s) - K(s)]\,\beta_x(s)ds \tag{3.24}$$

$$\xi_y = \frac{dQ_y}{d\delta} = \frac{1}{4\pi}\int_0^{\ell_0} [-2S(s)\eta(s) + K(s)]\,\beta_y(s)ds \tag{3.25}$$

Here, K and S are the strengths of the quadrupole and sextupole magnets. Efficient correction of the two natural chromaticities requires sextupoles located in regions of high dispersion, and in order to minimise the cross-talk between the two variables the focussing sextupoles should be placed in regions of large β_x and small β_y and vice versa for the defocusing sextupoles. Efficient control of α_2 requires focussing sextupoles in regions of high horizontal dispersion, as shown by equation (3.8).

Optimisation of the linear lattice for Diamond was performed using Elegant [119] and various methods for the nonlinear lattice optimisation were tested using Matlab-based scripts linked to Elegant. For the nonlinear optimisation, rather than determining the on and off momentum dynamic apertures for each combination of sextupole strengths tested (a computationally expensive process), various proxies were calculated, such as the tune-shifts with amplitude, chromaticity, α_2, stability of a limited number of tracked particles etc. Using these parameters, a quantitive assessment could be made as to how well each solution met the requirements outlined above and could then used within the optimisation algorithms.

The first method tested involved calculating a response matrix to determine how small changes in sextupole strength affected tune-shifts with amplitude, linear and higher order chromaticities and α_2. This response matrix could then be inverted using singular value decomposition and used to iteratively act on the various parameters until an optimum final solution was found.

In the second method investigated an objective function was built based on the amplitude of the same parameters targeted in the first method, with different weighting factors applied according to the relative importance. Using this objective function, a simplex optimisation algorithm could be used to determine the optimum sextupole configuration.

A final method that targeted the horizontal dynamic aperture directly by maximising the survival rate for particles tracked at increasing amplitudes proved to be prohibitively slow for any meaningful number of particles and amplitude steps and was abandoned.

3.2.2 Low Alpha Lattice Solutions

The two solutions for low alpha lattices (namely the relaxed, high emittance lattice and the more demanding, low emittance lattice) have both been developed and implemented at Diamond. A summary of the main storage ring parameters in each case is given in Table 3.1, and the Twiss parameters for one super-period of the lattices are shown in Fig. 3.5. In each case, a comparison is also made to the standard (high-alpha) user lattice.

There are several key differences between the two solutions. Firstly, the horizontal integer tune point for the low emittance lattice is much larger than for the high emittance lattice at 29 compared to 21 (the standard user optics has an integer tune point of 27). This increase in horizontal focussing leads to an increase of the natural chromaticity, which combined with the reduction in dispersion at the sextupole locations results in a marked increase in the required sextupole strengths. This problem is exacerbated by the need to minimise α_2, (predominantly controlled by the focussing sextupoles in the centre of the arcs), as the peak dispersion is considerably reduced in the low emittance lattice. Peak sextupole strengths for the low emittance lattice are therefore unavoidably stronger than those required for the high emittance lattice ($31.3 m^{-3}$ compared to $23.3\ m^{-3}$, respectively), increasing the nonlinearity of longitudinal and transverse beam motion and thus shrinking the region of stable motion.

Parameter	Standard User Lattice	High Emittance Lattice	Low Emittance Lattice
Emittance	2.7nm.rad	35.2nm.rad	4.4nm.rad
α_1	1.7×10^{-4}	-3×10^{-6}	-1×10^{-5}
α_2 (with/without sextupoles)	1.7×10^{-3} / 5.1×10^{-3}	-6×10^{-5} / 0.012	-2×10^{-5} / 0.005
α_3 (with/without sextupoles)	-1.4×10^{-4} / 0.051	-0.043 / -0.193	0.004 / 0.008
Tune point (Q_x / Q_y)	27.205 / 12.360	21.150 / 12.397	29.390 / 8.284
Nat. chromaticity (ξ_{x0} / ξ_{y0})	-79 / -35	-37 / -26	-66 / -43
Max. beta ($\beta_{x,max}$ / $\beta_{y,max}$)	22.6m / 27.0m	20.2m / 22.7m	26.2m / 40.3m
Beta functions at IDs (β_x / β_y)	4.7m / 1.5m	8.2m / 2.4m	1.1m / 5.7m
Max. dispersion (η_x)	0.31m	0.45m	0.28m
Dispersion at IDs (η_x)	5.3cm	-9.7cm	5.6cm
Beam size at IDs (σ_x / σ_y) (0.2% coup.)	124μm / 2.9μm	545μm / 12.9μm	94μm / 7.0μm
Energy Spread	9.62×10^{-4}	9.62×10^{-4}	9.62×10^{-4}
Damping Times (Hor. / Long.)	11.2ms / 5.6ms	11.2ms / 5.6ms	11.2ms / 5.6ms
Natural bunch length (3MV)	10.0ps	1.3ps	2.4ps
Synchrotron frequency (3MV)	2608Hz	346Hz	629Hz
Synchronous phase (3MV)	0.34rad	2.80rad	2.80rad

Table 3.1: Main storage ring parameters for the standard and low-alpha lattices

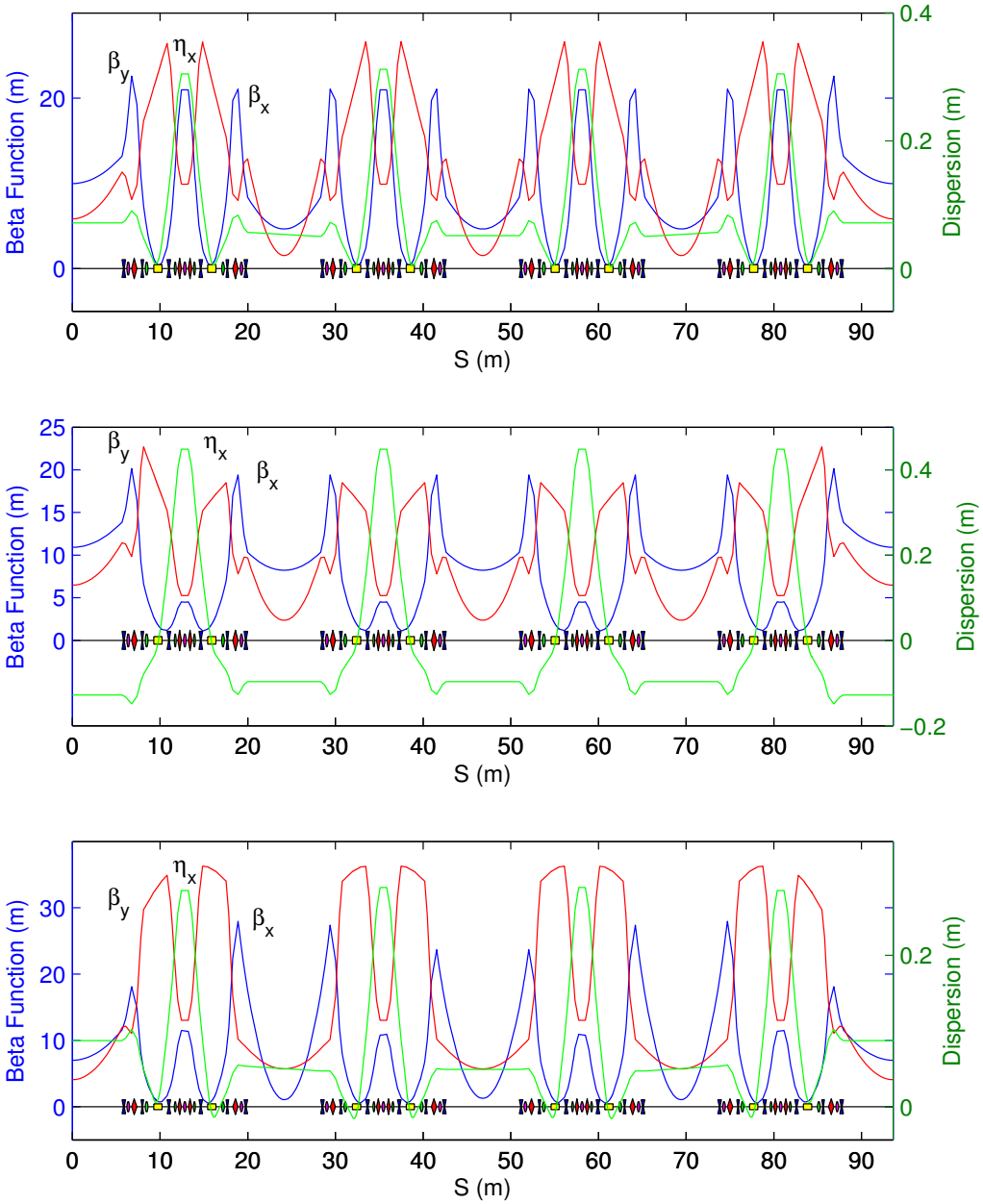

Figure 3.5: Optical functions for the standard user (top), high-emittance, low-alpha (middle) and low-emittance, low-alpha (bottom) lattices.

Based on experience gained during machine trials for the high emittance lattice, a larger absolute value for α_1 was targeted for the low emittance solution from the beginning. There are two main reasons for this decision. Firstly, whilst the larger α_1 gives a longer natural (zero-current) bunch length, the bunch length at moderate bunch currents rapidly becomes independent of α_1, i.e. there is no benefit in further reducing α_1 once a minimum bunch length has been achieved at any given current. Secondly, the horizontal closed orbit stability of the electron beam is found to be inversely proportional to α_1. This reduced closed orbit stability becomes important to users when the emittance of the beam is reduced. Selecting a slightly larger α_1 helps to reduce the impact of this increased sensitivity to transverse motion, without increasing the bunch length at the given operating current. Both these features are discussed in more detail in the following sections.

The final difference to note is that the sign of α_3 is positive for the low emittance and negative for the high emittance lattice. The results from Section 3.1.3.3 would suggest it is better to operate the low emittance lattice at positive α_1 in order to benefit from the removal of the off-momentum fixed points of motion and hence improved momentum aperture; however, when switching to positive α_1 the sign of α_3 is also found to reverse. As such, operation with negative α_1 is still preferred in order to benefit from the reduced bunch-lengthening with current compared to operating with positive α_1 (see Section 3.4.7.6).

3.3 Lattice Characterisation through Simulation

Before testing the low alpha lattices on Diamond, extensive simulations were carried out in order to determine their expected performance, particularly in terms of the on and off momentum dynamic aperture and hence injection efficiency and lifetime. These simulations provide a benchmark against which the measured machine performance can be assessed.

3.3.1 Longitudinal Motion

The momentum compaction factor for the two lattices was determined by tracking off-momentum particles through one turn of the storage ring model and calculating the distance travelled in one revolution. From this, a polynomial fit allows the individual terms in the expansion of alpha to be extracted. After assuming V_{RF} = 3MV, equations (3.9) and (3.10) were used to calculate the longitudinal phase space for the two lattices. These are shown in Fig. 3.6 along with the numerically determined values for alpha in each case.

Both high and low emittance lattices operate with negative alpha for small momentum deviations. Alpha is entirely negative for the high emittance lattice and is dominated by a strong α_3 component, and as such the only solution to equation (3.12) is $\delta = 0$. This lattice operates in the RF bucket regime with the stable phase shifted to $\varphi = \pi - \varphi_s$, and the longitudinal particle motion is well described by the analysis given in Section 3.1.3.3.

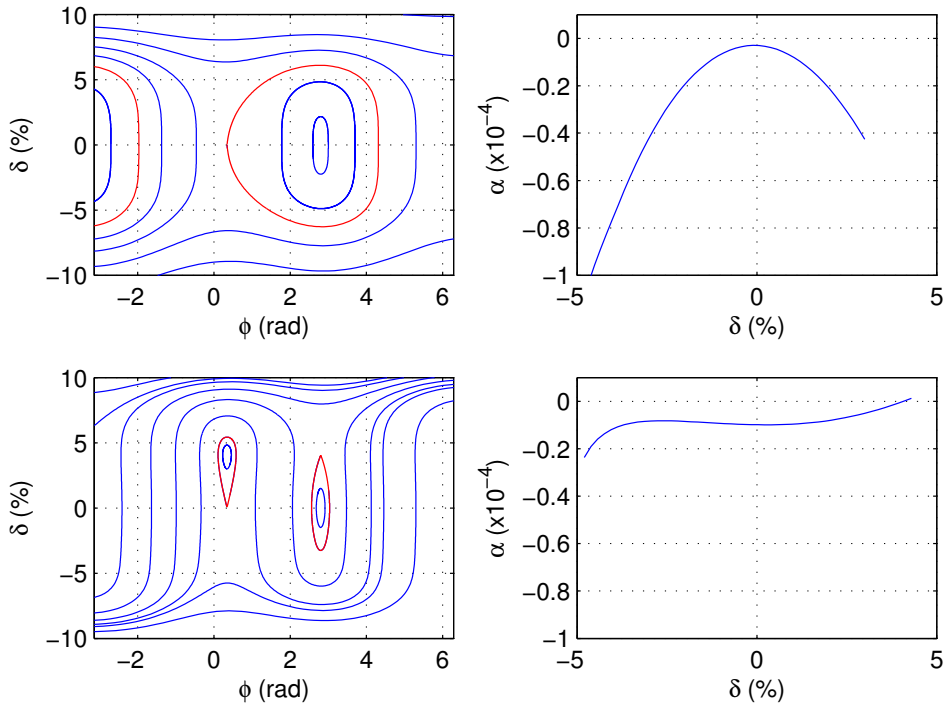

Figure 3.6: Longitudinal phase space plots (left) and corresponding alphas (right) for the high (top) and low (bottom) emittance low alpha lattices. Terms up to α_6 have been included in the fit, and the separatrices between stable and unstable motion have been highlighted in red. In the calculations, the main parameters were E_0 = 3GeV, f_{RF} = 499.654GHz, U_0 = 1.005MeV/turn and V_{RF} = 3MV.

For the low emittance lattice the longitudinal dynamics is much more complicated and many more terms in the expansion of alpha are required for an accurate description to be made. Alpha crosses from negative to positive values at δ = +4%, meaning that equation (3.12) now has two solutions and two stable regions appear (one on-momentum bucket centred at $\varphi = \pi - \varphi_s$ and one off-momentum centred at $\varphi = \varphi_s$). From the resulting phase-space plot, the low-emittance lattice can be seen to operate in the alpha-bucket regime.

3.3.2 Dynamic Aperture

In order to prevent particle loss when crossing resonances, part of the nonlinear lattice optimisation is to ensure that the tune-shifts with amplitude and momentum deviation are constrained to regions of tune-space that are relatively resonance-free. This process serves to increase the dynamic aperture (DA) for the ideal lattice, and also makes it more robust to the introduction of magnet field errors. The end goal in maximising the DA is to achieve good injection efficiency and long lifetime for the stored beam. Injection into the Diamond storage ring is carried out off-axis, with the injected bunches entering at a distance of -8.3mm from the stored beam [120], and so the DA must exceed this value.

Tune shifts with momentum deviation and amplitude have been determined for both lattices via particle tracking using the Accelerator Toolbox (AT) tracking code [121], with the tune values calculated using the NAFF algorithm [122]. The results of this are shown in Figs. 3.7 and 3.8 respectively. Following this, particle tracking was again carried out in order to determine the DA in each case, this time using the Tracy-II tracking code [123] with realistic magnet field and alignment errors and physical apertures added to the lattice [124]. The resulting on-momentum DAs are shown in Figs. 3.9 and 3.10. To assist in interpreting the results, the frequency maps for each case are also given [125].

The calculated DA for the high emittance lattice comfortably exceeds the -8.3mm requirement for on-axis injection, even when realistic magnetic field and alignment errors and physical apertures are included in the tracking. It is the $Q_x + 2Q_y$ sextupole resonance and $6Q_x$ resonance that appear most harmful to the on-momentum DA.

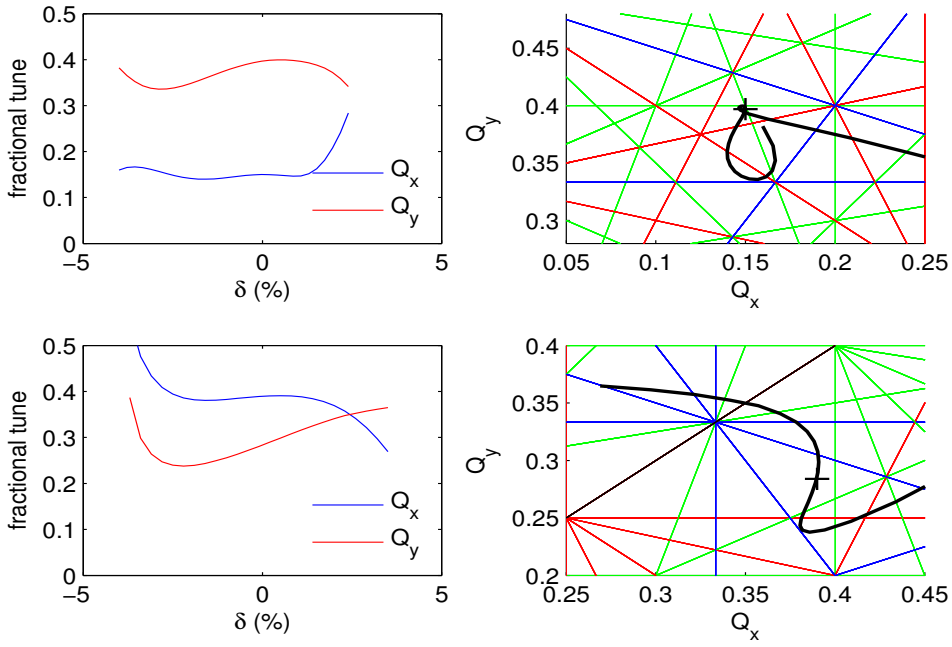

Figure 3.7: Variation of horizontal and vertical tune with momentum deviation for the high emittance (top) and low emittance (bottom) low alpha lattices. In each case, the left hand plot shows variation in tune with momentum deviation and the right hand plots show the same data in tune space. Resonance lines up to 5th order superimposed for reference.

Lowering the horizontal tune may help to reduce the sensitivity to these resonances; however, this may lead to problems during injection, as a significant phase advance is required for the injected beam to clear the septum plate whilst the injection bump is active [120]. As Fig. 3.7 shows, lowering the vertical tune would bring the off-momentum tune close to the $3Q_y$ skew-sextupole resonance and reduce the off-momentum DA (limiting the lifetime).

As expected, the increase in sextupole strengths for the low emittance lattice has led to a decrease in the size of the on-momentum DA; however, the -8.3mm aperture requirement has again been met. As with the high emittance lattice, it is the $Q_x + 2Q_y$

sextupole resonance that appears most harmful to the on-momentum DA, particularly when physical apertures are included in the tracking. Although lowering the vertical tune away from this resonance may benefit the on-momentum DA, Fig. 3.7 shows that this would lead to the off-momentum tune crossing the $4Q_y$ octupole resonance earlier, known to be excited by insertion devices [126].

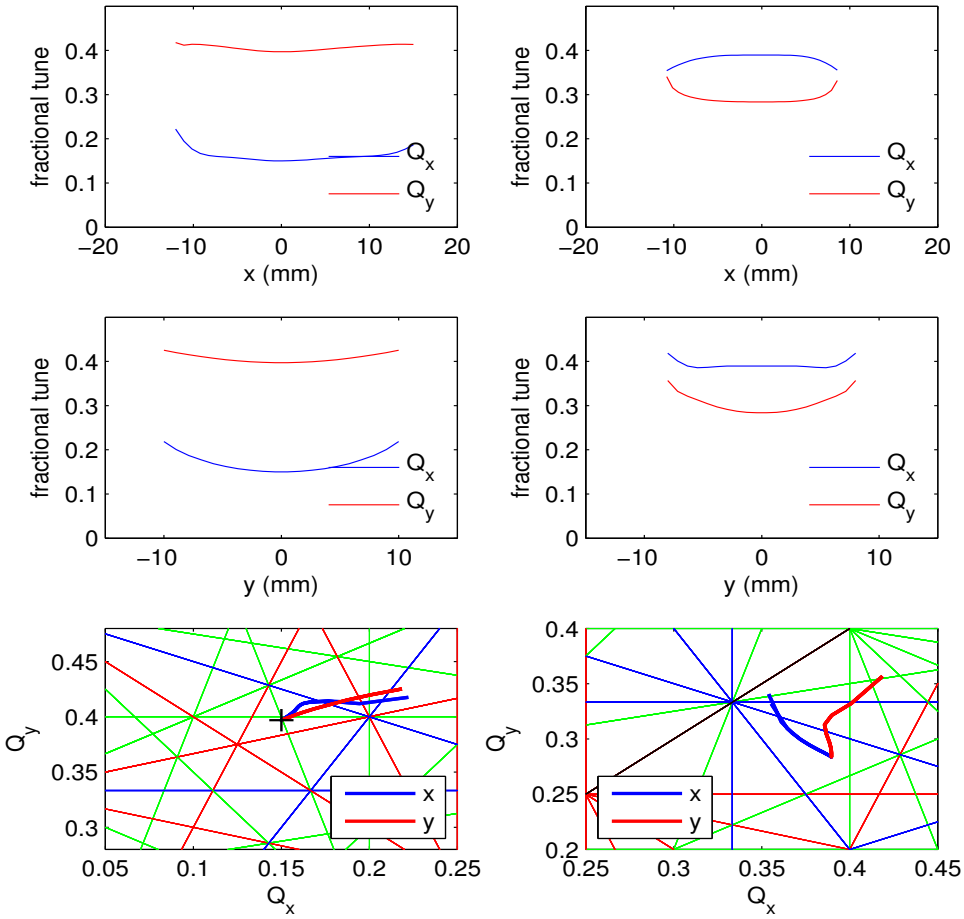

Figure 3.8: Variation of horizontal and vertical tune with transverse amplitude for the high emittance (left) and low emittance (right) low alpha lattices. In each case, the top plot shows variation in tune with horizontal position and the middle plot shows variation with vertical amplitude. The bottom plots show the same data in tune space, with resonance lines up to 5th order superimposed for reference.

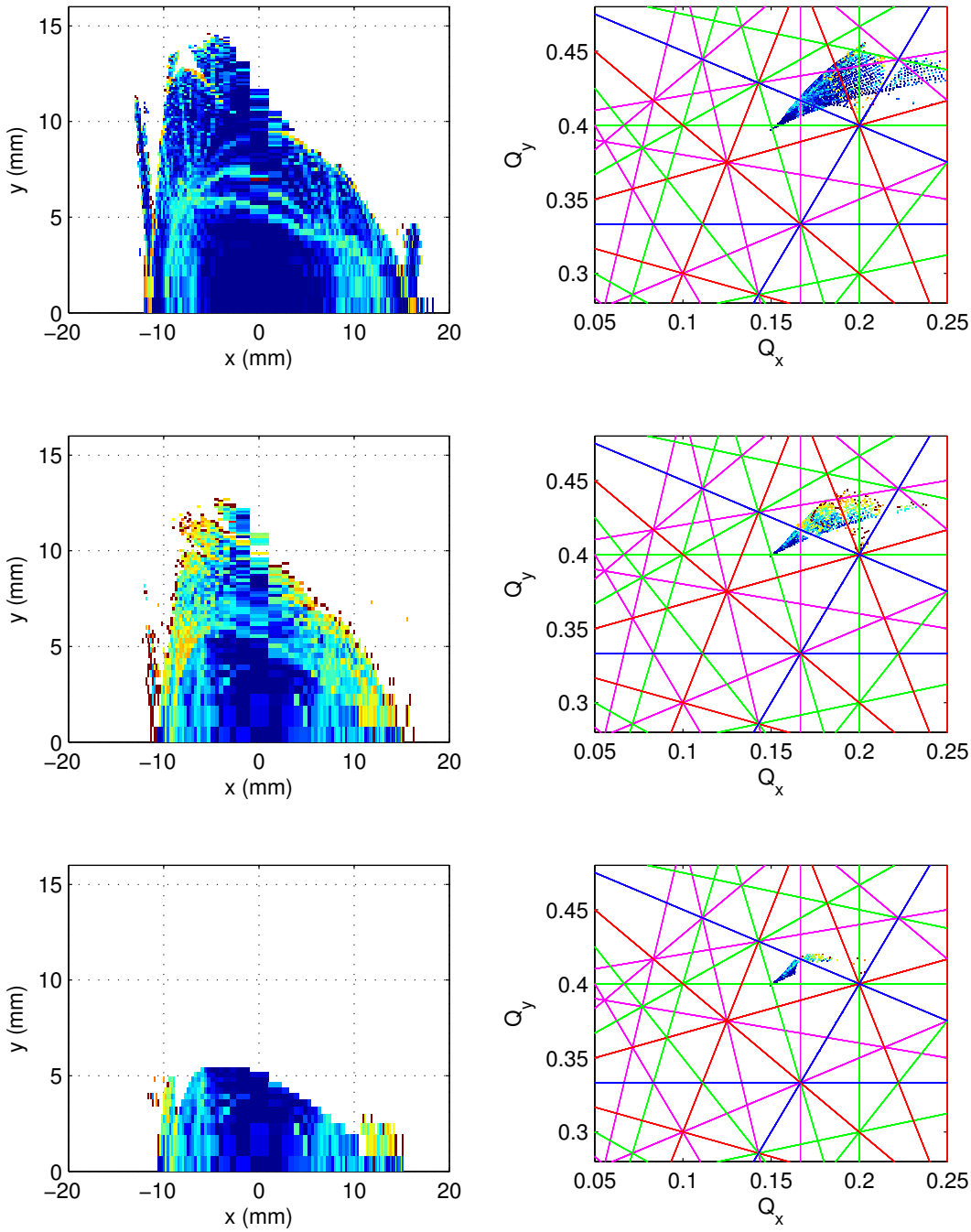

Figure 3.9: This figure shows the on-momentum dynamic apertures (left) for the high emittance low alpha lattice and corresponding frequency maps (right). The top plot shows the results for the ideal lattice, the middle plots were produced including magnet field and alignment errors and the lower plots also included physical apertures in the tracking. Particles were tracked for 1024 turns, with longitudinal motion neglected.

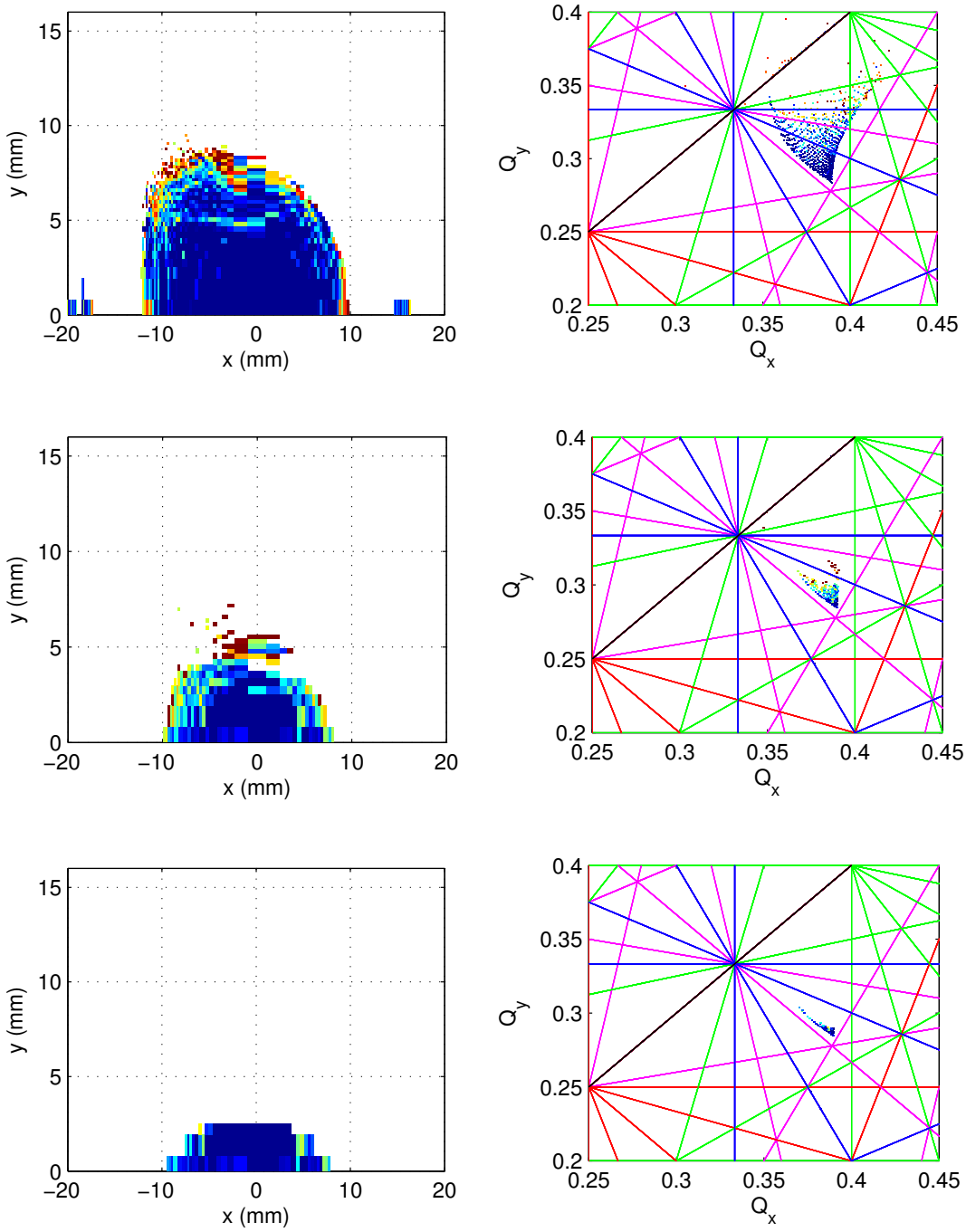

Figure 3.10: This figure shows the on-momentum dynamic apertures (left) for the low emittance low alpha lattice and corresponding frequency maps (right). The top plot shows the results for the ideal lattice, the middle plots were produced including magnet field and alignment errors and the lower plots also included physical apertures in the tracking. Particles were tracked for 1024 turns, with longitudinal motion neglected.

3.3.3 Momentum Acceptance

Accurate determination of the momentum acceptance is a key step to calculating the expected beam lifetime in the storage ring. For modern light sources, the dominant component to the overall lifetime [127] is the Touschek lifetime, an effect first observed in the AdA storage ring by B. Touschek [128]. In this effect, two electrons in the circulating bunch scatter from each other, transferring their transverse momenta into large longitudinal momentum deviations and ending up outside the momentum acceptance of the ring. An expected value for the Touschek lifetime can be calculated from the momentum acceptance using the Brück formula [129].

The analysis given in Section 3.3.1 showed the 1D longitudinal momentum acceptance provided by the RF bucket exceeds ±3.5% for both lattices. However, the final momentum acceptance for the lattice is a combination of both the momentum acceptance of the RF bucket and the off-momentum DA provided by the sextupoles. This is a property that can only be found through full 6D particle tracking [130], is asymmetric in energy and varies around the ring. The reason for this can be understood as follows. Before a scattering event, both particles are assumed to lie on the on-momentum closed orbit. The sudden change in particle momentum means that after the scattering event the electrons will perform betatron oscillations around the on-momentum closed orbit of amplitude $a_x(s,\delta)$ determined by the nonlinear dispersion $\eta(s,\delta)$ and chromatic invariant $H_x(s_0,\delta)$ at the point of scatter [131].

$$a_x(s,\delta) = \sqrt{\eta(s,\delta)^2 + \beta(s,\delta)H_x(s_0,\delta)}\delta \tag{3.26}$$

If $H_x(s_0,\delta)$ is small at the point of scatter, then for a given δ the amplitude of betatron oscillation will be small and the particle is more likely to survive and damp down to

the original conditions. Conversely, a large value of $H_x(s_0,\delta)$ results in large amplitude betatron oscillations, increasing the likelihood that the particle will be lost.

The procedure used for determining the momentum acceptance was to track a single particle for 512 turns in the storage ring at increasingly large momentum deviations, recording the value at which the particle is lost, and repeating this for different starting locations in the ring. For this task, the Tracy-II tracking code was used, with an assessment again made for the likely impact of magnetic field and alignment errors and the inclusion of physical apertures. The results for one super-period of the ring are shown in Fig. 3.11 for the high emittance lattices and Fig. 3.12 for the low emittance lattice.

The momentum acceptance for the high emittance lattices is strongly limited in the regions between the bending magnets in each arc where the dispersion is large, with minimum values of +0.6% recorded for the ideal lattice. The introduction of magnet field and alignment errors modifies the $H_x(s_0,\delta)$ function slightly, leading to a marginal improvement in the momentum acceptance between the bending magnets to ±1%. Elsewhere in the ring, the momentum acceptance varies between 2% to 4%.

Despite the fact that the on-momentum DA is smaller for the low emittance lattice, the momentum acceptance is generally larger due in part to the smaller dispersion and $H_x(s_0,\delta)$ function. The minimum value for the momentum acceptance in this case is -1.7%, with 2% to 4% more typical for the majority of the ring.

Touschek lifetime values for both high and low emittance lattices are summarised in Section 3.3.5. The calculated lifetime is always above 10h for both lattices, thanks in part to the assumed low bunch current of 50μA, and is sufficient to give adequate time between storage ring refills for user experiments to be carried out.

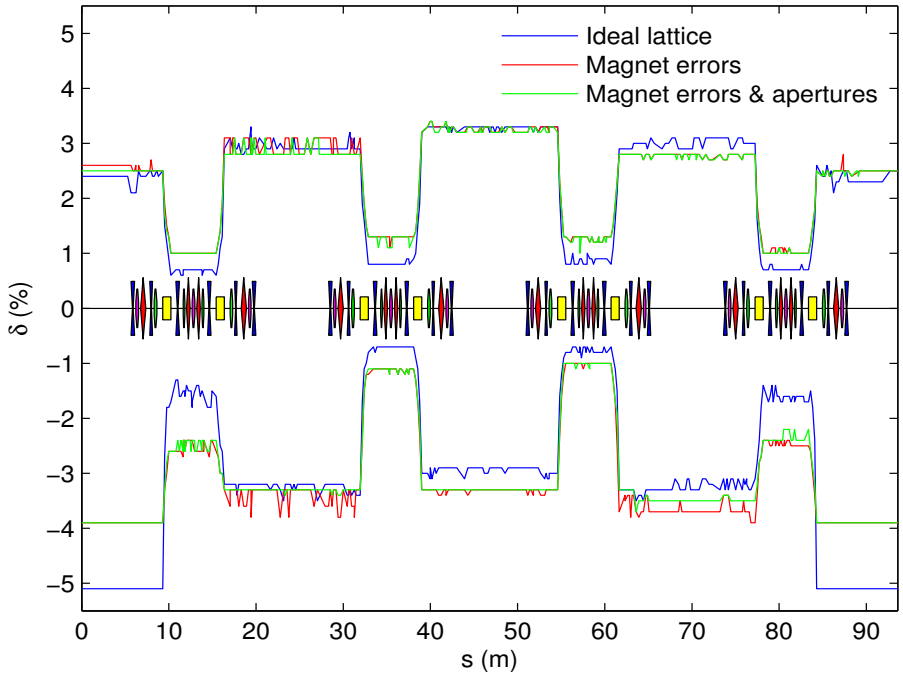

Figure 3.11: Calculated Momentum acceptance for the high emittance lattice. Particles were tracked for a maximum of 512 turns, and included longitudinal motion.

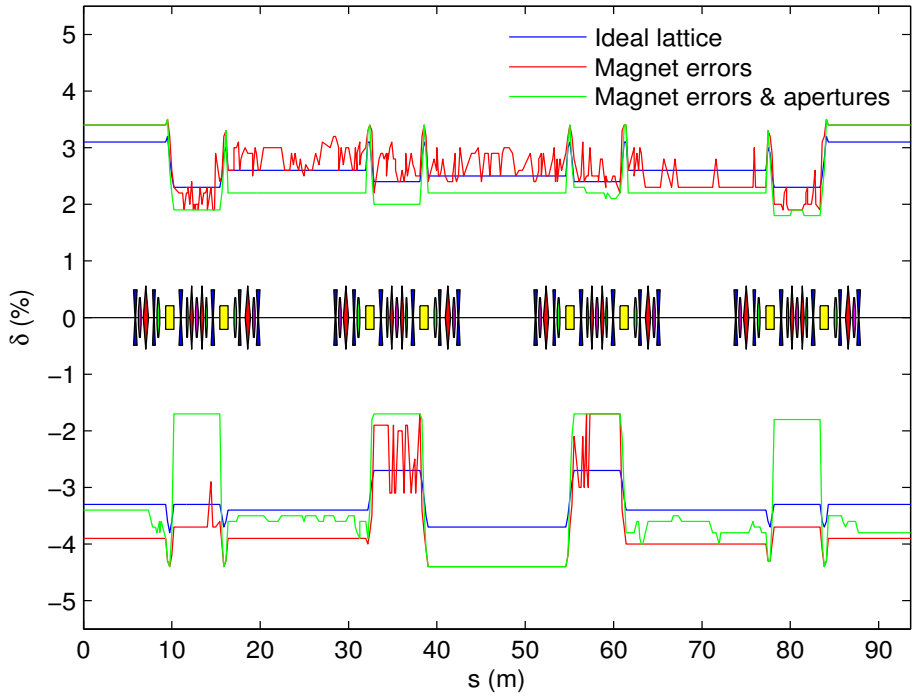

Figure 3.12: Calculated Momentum acceptance for the low emittance lattice. Particles were tracked for a maximum of 512 turns, and included longitudinal motion.

3.3.4 Injection Efficiency

The DAs and FMs calculated in Section 3.3.2 provide valuable information about the on-momentum transverse dynamics of the storage ring, but neglect the longitudinal motion. To understand the injection process properly, full 6D tracking simulations must be carried out using an electron bunch with the expected characteristics of the booster at extraction. This bunch can be up to 2 orders of magnitude longer than the natural bunch length in the storage ring when operated in low alpha conditions, and due to synchrotron motion, particles at the head and tail of the bunch can reach large values of δ before damping down to the equilibrium storage ring conditions.

Simulations of the injection process were carried out for both lattices using the Tracy II tracking code, with realistic magnetic field and alignment errors and physical apertures included in the simulations. The tracking was carried out for 12000 turns, corresponding to 4 longitudinal or 2 transverse damping times. The transverse and longitudinal phase space distributions of the bunch after various numbers of turns are shown in Figs. 3.13 and 3.14 for the high and low emittance lattices respectively, and the properties of the electron bunch at injection are listed in Table 3.2.

In both cases, after 1/4 of a synchrotron period particles at the head and tail of the electron bunch reach momentum deviations of up to ±4%. This is the stage at which the particle loss rate is highest. Those particles which survive beyond the first synchrotron period quickly damp down to the natural storage ring conditions and are more likely to survive the injection process. An examination of the final distributions shows that it is overwhelmingly particles at the head and tail of the bunch which are lost, with particles at the core of the bunch surviving to the end. Predicted injection efficiencies for each lattice are summarised in Section 3.3.5.

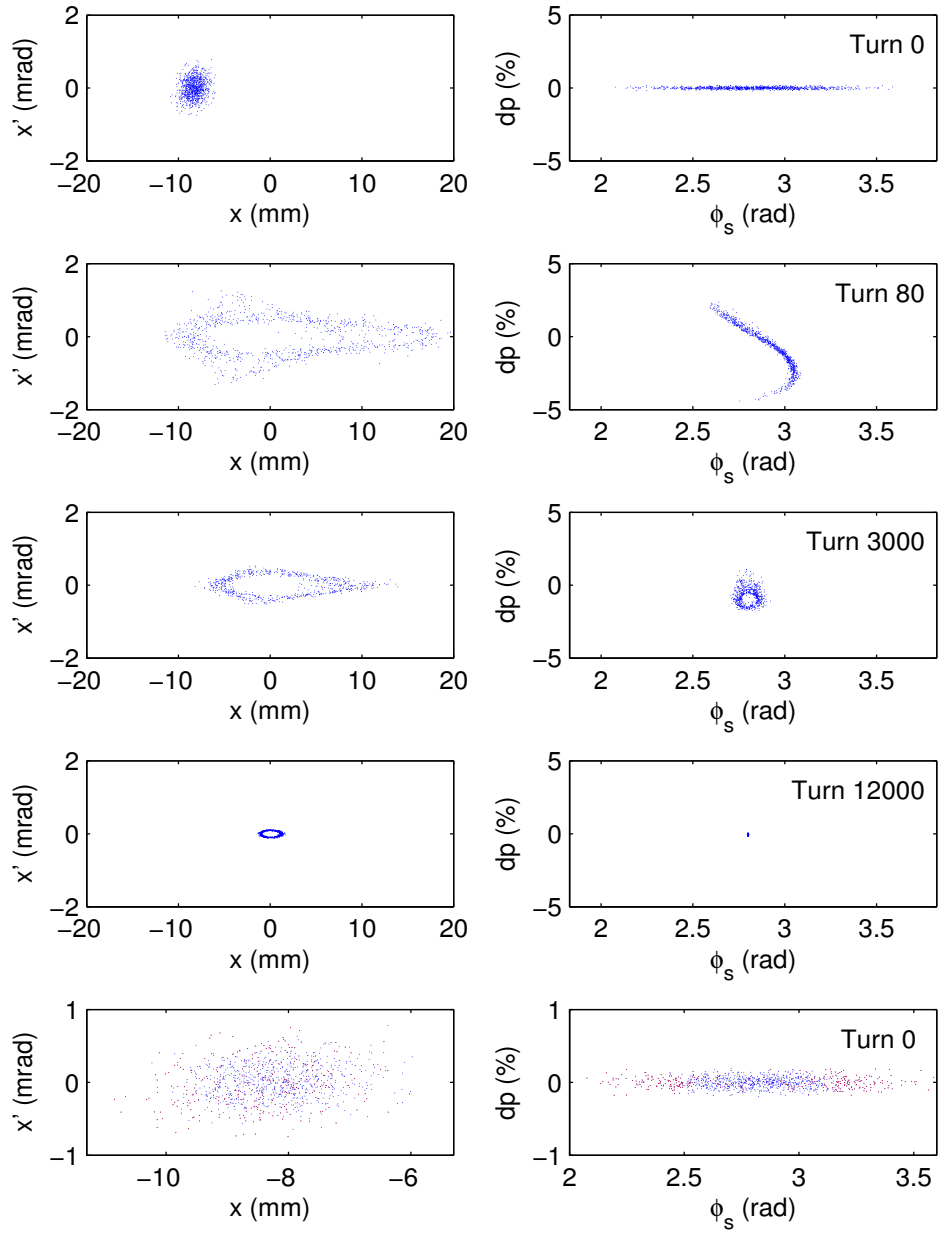

Figure 3.13: Simulation of injection into the high emittance low alpha lattice. The horizontal (left) and longitudinal (right) phase space distributions are shown at various stages, and show how the electron bunch distribution damps down to the natural storage ring conditions after a few damping times. The two plots in the bottom row show the initial phase space distributions, in which the particles which are eventually lost are highlighted in red.

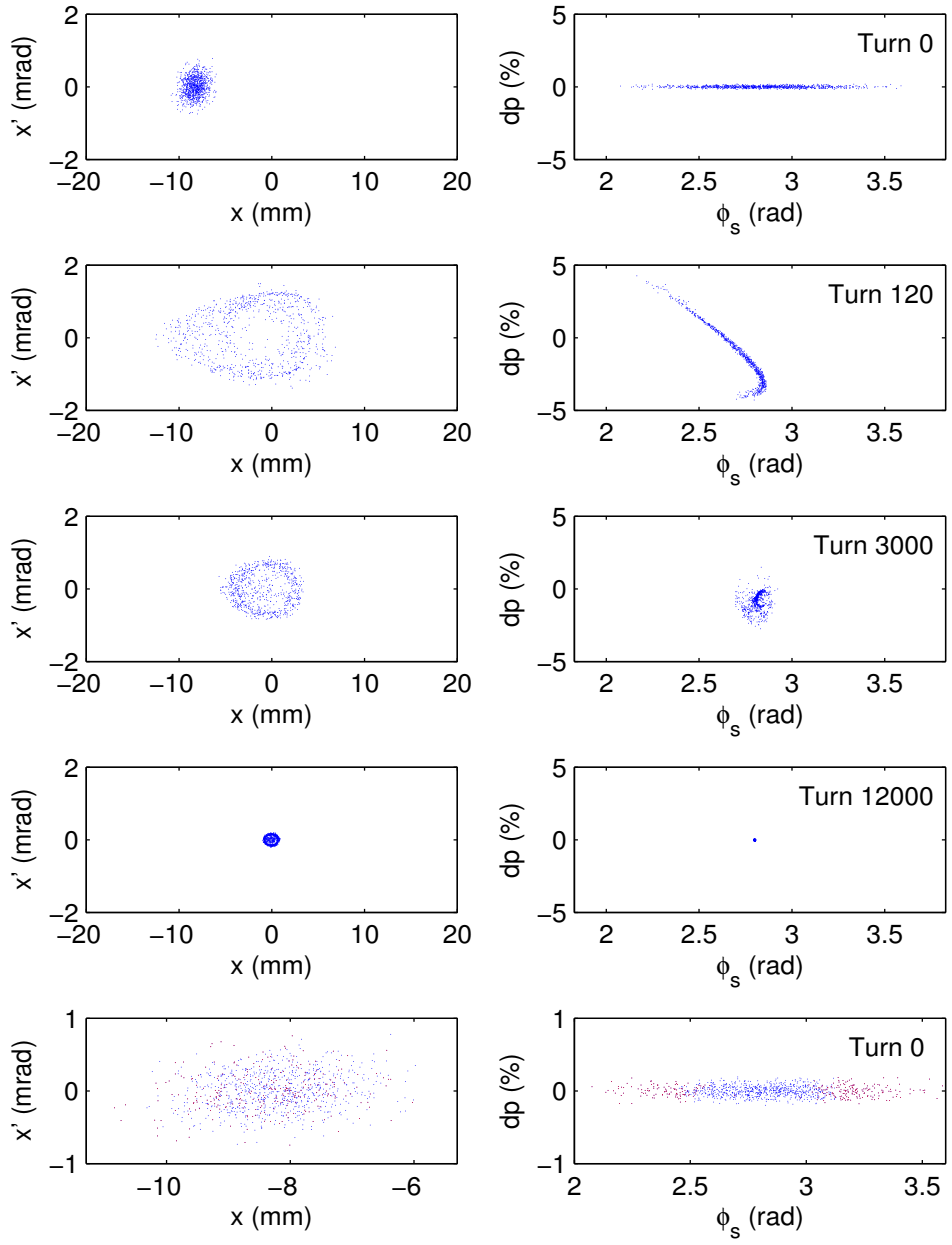

Figure 3.14: Simulation of injection into the low emittance low alpha lattice. The horizontal (left) and longitudinal (right) phase space distributions are shown at various stages, and show how the electron bunch distribution damps down to the natural storage ring conditions after a few damping times. The two plots in the bottom row show the initial phase space distributions, in which the particles which are eventually lost are highlighted in red.

Parameter	Value
Horizontal emittance	225nm.rad
Vertical emittance	15nm.rad
Energy spread	7.3×10^{-4}
Bunch length	26mm
β_x	3.18m
β_y	5.99m
α_x	-0.095
α_y	-0.162
η_x	0.072m
η_y	0m
Phase	2.800rad
Distance from stored beam	-8.3mm

Table 3.2: Properties of electron beam at injection into the Diamond storage ring

3.3.5 Summary of Simulations

A summary of the expected performance of each lattice is given in Table 3.3. For the Touschek lifetime calculation, the bunch current was assumed to be 50μA, the coupling was assumed to be 0.2% and no account was taken of the expected bunch lengthening with current. The cavity voltage has been assumed to be 3MV throughout.

		High emittance	Low emittance
On-momentum dynamic aperture	Bare lattice	-12.1mm / +16.8mm	-12.1mm / +9.8mm
	Field errors	-11.0mm / +15.3mm	-10.8mm / +8.8mm
	Errors / apertures	-10.7mm / +15.2mm	-10.8mm / +8.8mm
Momentum aperture (max / min / mean)	Bare lattice	5.1% / 0.6% / 2.4%	3.8% / 2.3% / 3.0%
	Field errors	3.9% / 1.0% / 2.6%	4.4% / 1.7% / 3.2%
	Errors / apertures	3.9% / 1.0% / 2.6%	4.4% / 1.7% / 2.8%
Touschek lifetime	Bare lattice	12.7h	23.0h
	Field errors	26.4h	25.8h
	Errors / apertures	24.7h	16.3h
Injection efficiency	Bare lattice	52.3%	55.5%
	Field errors	36.4%	44.9%
	Errors / apertures	31.4%	22.6%

Table 3.3: Summary of expected machine performance based on simulations of the high and low emittance low alpha lattices

3.4 Implementation of Low Alpha Lattices

Machine trials for the high emittance lattice began in September 2008, followed by a period of characterisation and optimisation. Once this stage was complete, the Diamond storage ring was run in low alpha mode for external users for four days in April 2009. As a result of this trial period, it was identified that the quality of experimental data taken in low alpha mode would be considerably enhanced if the emittance of the electron beam could be brought closer to the nominal beam

emittance of 2.7nm.rad. This prompted the development of the more demanding low emittance lattice. Once the numerical studies of this lattice were complete, the low emittance, low alpha lattice was implemented on the machine and optimised during February 2010, and was available for external users in April of the same year and again in February / March 2011.

In this section, the various measurements taken to characterise the high and low emittance lattices are presented. The section begins with emittance and beam dynamics measurements taken to confirm the model predictions and understand the practical limitations, before moving on to measurements of the bunch length taken under a variety of conditions. Preliminary measurements of coherent emission at mm-wavelengths are presented, as this provides confirmation of the short bunch lengths achieved. The section concludes with a summary of the lattice performances.

3.4.1 Emittance Measurement

The method used at Diamond to measure emittance (ε), coupling (χ) and energy spread (σ_E) involves fitting a Gaussian curve to the measured transverse beam profiles from two x-ray pinhole cameras [132], and using the known Twiss parameters at the image source point to extract the desired electron beam parameters using:

$$\begin{pmatrix} {\sigma_{x_1}}^2 \\ {\sigma_{y_1}}^2 \\ {\sigma_{x_2}}^2 \\ {\sigma_{y_2}}^2 \end{pmatrix} = \begin{pmatrix} \beta_{x_1} & 0 & {\eta_{x_1}}^2 \\ 0 & \beta_{y_1} & {\eta_{y_1}}^2 \\ \beta_{x_2} & 0 & {\eta_{x_2}}^2 \\ 0 & \beta_{y_2} & {\eta_{y_2}}^2 \end{pmatrix} \begin{pmatrix} \varepsilon_x \\ \varepsilon_z \\ {\sigma_E}^2 \end{pmatrix} \tag{3.27}$$

where the subscripts x and y refer to the horizontal and vertical planes, 1 and 2 refer to pinhole cameras 1 and 2 and σ_x and σ_y are the fitted x-ray beam sizes.

The horizontal and vertical emittances are defined as:

$$\varepsilon_x = \frac{\varepsilon}{1+\chi}; \qquad \varepsilon_y = \frac{\chi\varepsilon}{1+\chi} \tag{3.28}$$

The results of these measurements are summarised in Table 3.4. Note that because of the large contribution of the emittance to the beam size for the high emittance lattice, it was not possible to extract a reliable value of the energy spread for this lattice. Images of the electron beam taken from the first pinhole camera are shown in Fig. 3.15 for the high emittance lattice and in Fig. 3.16 for the low emittance lattice.

Parameter	High Emittance Lattice	Low Emittance Lattice
σ_{x1}	302.1 ± 1 μm	73.1 ± 1 μm
σ_{y1}	15.1 ± 1 μm	12.6 ± 1 μm
σ_{x2}	230.2 ± 1 μm	57.8 ± 1 μm
σ_{y2}	14.7 ± 1 μm	17.9 ± 1 μm
β_{x1}	2.4 ± 0.1 m	1.38 ± 0.1 m
η_{x1}	-0.036 ± 0.001 m	0.002 ± 0.001 m
β_{y1}	18.3 ± 0.1 m	37.3 ± 0.1 m
η_{y1}	0.001 ± 0.001 m	0.001 ± 0.001 m
β_{x2}	1.44 ± 0.1 m	0.67 ± 0.1 m
η_{x2}	0.031 ± 0.001 m	0.008 ± 0.001 m
β_{y2}	15.47 ± 0.1 m	38.5 ± 0.1 m
η_{y2}	-0.001 ± 0.001 m	0.001 ± 0.001 m
ε_x	37.2 ± 1.6 nm.rad	3.7 ± 0.3 nm.rad
σ_E	-	0.4 ± 0.3 %
Coupling	0.035 ± 0.01 %	0.15 ± 0.03 %

Table 3.4: Emittance, energy spread and coupling for the low alpha lattices

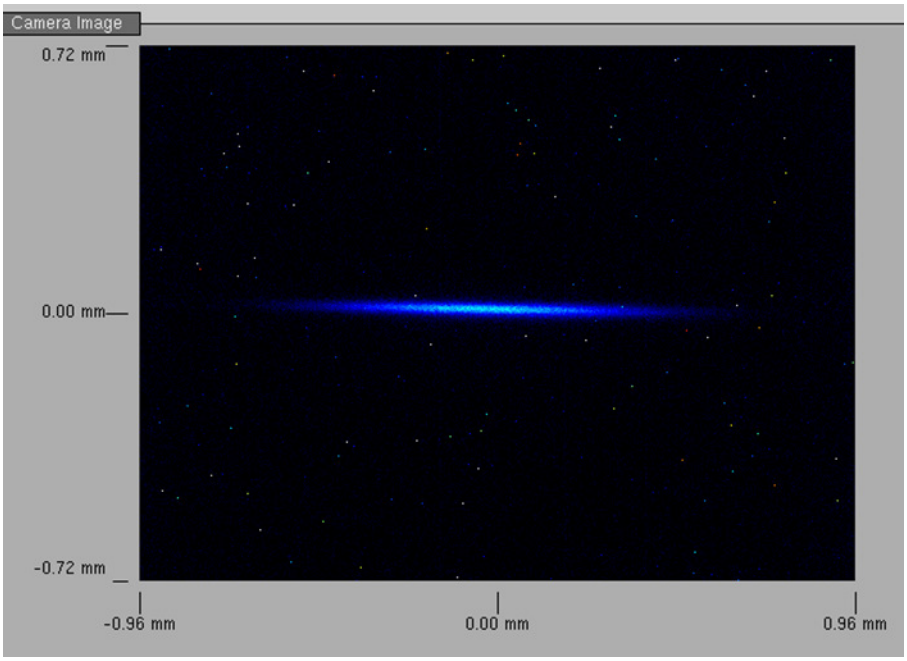

Figure 3.15: Image of the electron beam for the high emittance lattice. The beam is imaged using an x-ray pinhole camera system consisting of a 25×25μm pinhole aperture, a 5μm thick P43 scintillating screen and a CCD camera.

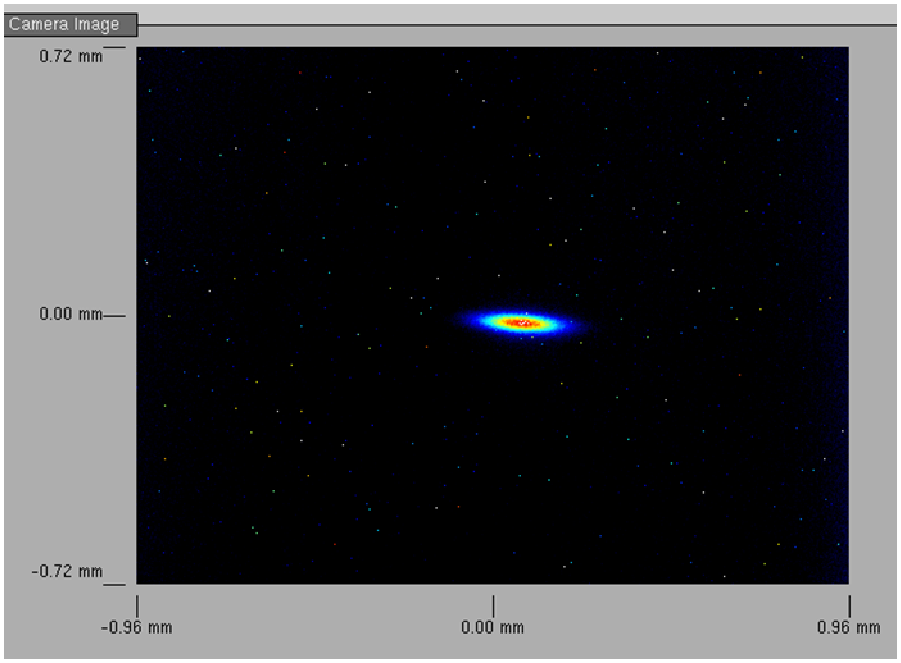

Figure 3.16: Image of the electron beam for the low emittance lattice. The beam is imaged using an x-ray pinhole camera system consisting of a 25×25μm pinhole aperture, a 5μm thick P43 scintillating screen and a CCD camera.

3.4.2 Momentum Compaction Factor Measurement

Alpha can be inferred from measurements of the synchrotron frequency, as given by equation (3.2). These measurements are subject to some uncertainty due to imprecise knowledge of the electron beam energy, energy loss per turn and RF cavity voltage. However, since α_1 is known to a high level of confidence for the standard user lattice, the value for any other lattice can be extracted by simply comparing the measured synchrotron frequencies in each case.

$$\alpha_{1,lat1} = \sqrt{\frac{f_{s,lat1}}{f_{s,lat2}}}\alpha_{1,lat2} \tag{3.29}$$

The synchrotron frequency is measured at Diamond by modulating the phase of the RF cavities, which in turn excites synchrotron oscillations in the beam. These oscillations can then be observed with a beam position monitor at a location of high transverse dispersion. Taking the Fourier transform of this data then allows the synchrotron frequency to be extracted with a high degree of precision. An example of such a measurement is given in Fig. 3.17.

The synchrotron frequency can also be used to extract information about the higher order terms in alpha by recording it as a function of RF frequency. Changing the RF frequency is equivalent to changing the momentum-independent path lengthening term $\Delta\ell/\ell$ in equation (3.11), and has the effect of shifting the stable fixed point of motion to higher or lower beam energies. Strictly speaking, this is not the same as exploring the off-momentum behaviour of the lattice since the whole RF bucket is shifted, changing the reference beam energy for the longitudinal beam motion. However, in the transverse planes the off-momentum dynamics are still explored, as magnet strengths remain valid for the original reference beam energy.

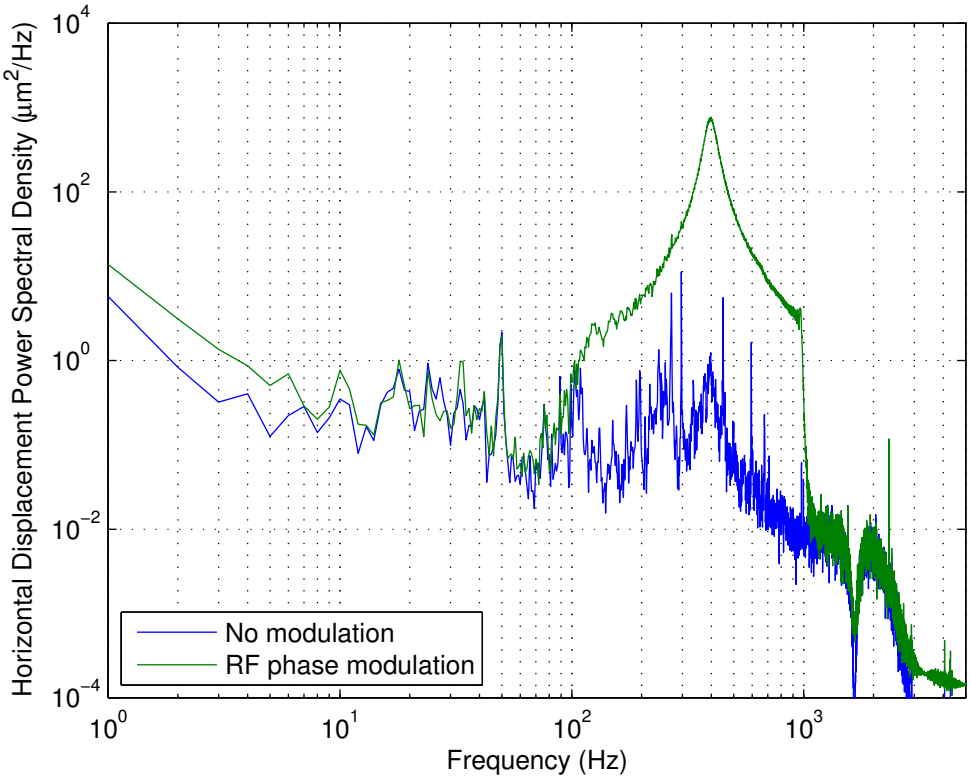

Figure 3.17: Comparison of synchrotron frequency measurements made with and without RF cavity phase modulation. Beam motion was recorded at a BPM with η_x = 0.28m. In this case, the RF cavity voltage was 1.5MV, giving a $|\alpha_1| = 1\times10^{-5}$.

The variation of synchrotron frequency with RF frequency for the low emittance lattice is shown in Fig. 3.18, where an equivalent simulation made using Elegant is overlaid for reference. In the simulation, a small adjustment of α_2 from 0 to 1.5×10^{-5} was made in order to produce the closest match to the machine data. During the measurement the RF cavity voltage was set to 1.8MV and $\alpha_1 = -1\times10^{-5}$. As can be seen, the agreement between the machine and model is very close, with the contribution of the higher order momentum compaction factor terms identified in Section 3.3.1 clearly evident.

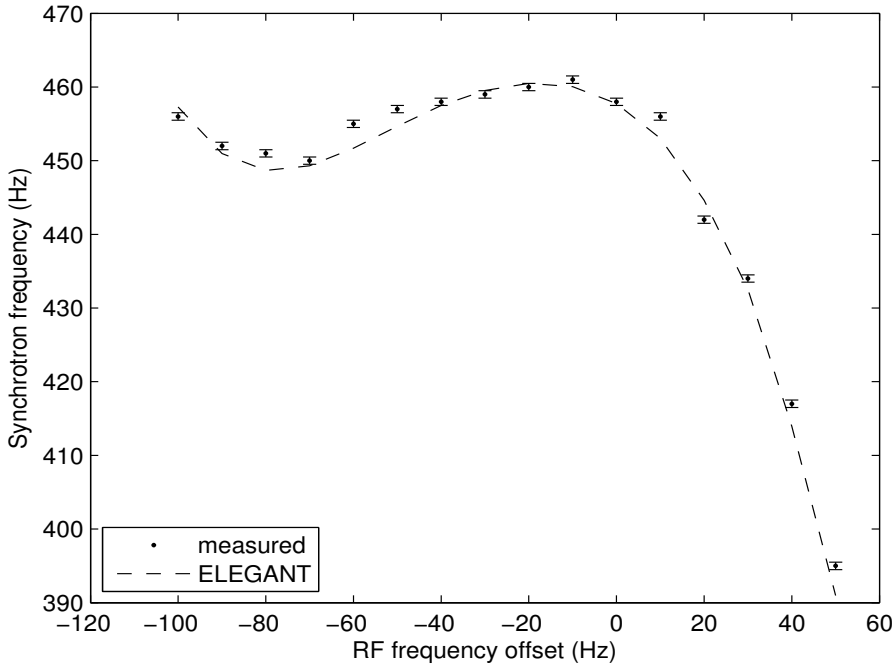

Figure 3.18: Machine to model comparison of synchrotron frequency vs. RF frequency measurements made for the low emittance lattice. The RF cavity voltage was set to 1.8MV, and α_1 was set to -1×10^{-5}.

3.4.3 Nonlinear Chromaticity Measurement

Measurements of the horizontal and vertical betatron tunes as a function of RF frequency were taken for the low emittance lattice at the same time as the synchrotron frequency measurements. These data sets give a measure of the nonlinear chromaticity in the machine, for which a comparison to the model can again be made. For this measurement, the linear horizontal and vertical chromaticities were set to +0.55 and -0.50 respectively. The results of the measurement are shown in Fig. 3.19. There is reasonable qualitative agreement between the model and machine in this case; however, both horizontal and vertical tunes begin to diverge from the model predictions at large momentum deviations, and particularly so in the vertical plane.

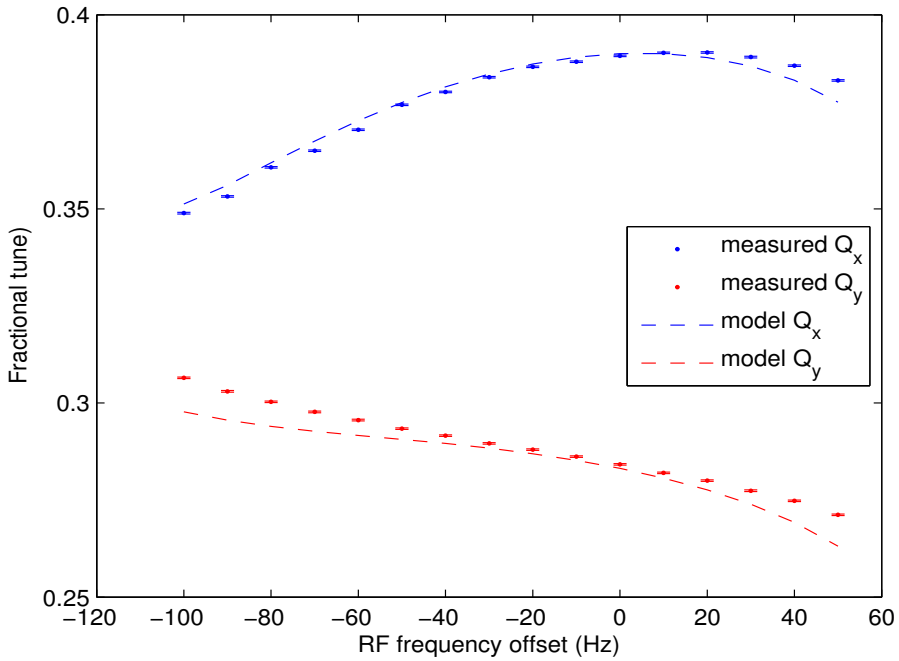

Figure 3.19: Comparison between machine measurements and model values for the betatron tunes vs. RF frequency (made for the low emittance lattice).

3.4.4 Dynamic Aperture and Frequency Map Measurement

The DA of the machine can be measured directly using two independent "pinger" magnets. These magnets can be used to excite large amplitude betatron oscillations in each plane, and the oscillation amplitude can be recorded at each turn using the electron beam position monitors (BPMs) installed in the storage ring. These data sets can then be processed to extract both the maximum oscillation amplitude (for the DA) and the betatron tunes as a function of the strength of the pinger magnets (for the frequency map (FM)).

The pinger magnets deliver a half-sine pulse with a total length of between 3.0μs (strong pulses) and 3.4μs (weak pulses), and are sufficiently strong to deflect the electron beam across the full range of available space inside the storage ring vacuum chamber. Since the revolution time for the storage ring is 1.87μs, only a small fraction of the storage ring can be filled with electron bunches if the pinger magnets are to provide a single impulse to the beam. This also helps to ensure that the strength of kick is as uniform as possible across the train of bunches. Ideally only a single electron bunch should be used for such experiments, but in this case the stored charge would be too low to be observable by the BPM system.

Once acquired from the BPM system, a number of corrections have to be applied to the turn-by-turn data in order to correctly reconstruct the betatron oscillation amplitudes [133]. These corrections include accounting for filtering within the BPM electronics (which results in a change in reported amplitude with oscillation frequency), correcting for geometrical non-linearities from the way the beam position is calculated from the BPM button response, and finally in compensating for linear gain and roll errors in the BPMs. Once this has been carried out, the turn-by-turn position signal can be used to extract both the amplitude and frequency of oscillations as a function of the pinger magnet strengths, which can then be used to reconstruct the DA and FM for the machine.

Using this procedure, the DA and FM was measured for the low emittance lattice. For this measurement, $\alpha_1 = -1\times10^{-5}$, $V_{RF} = 1.8$MV and the linear coupling of the machine was set to 0.2%. The resulting DA is shown in Fig. 3.20, and the corresponding FM is in Fig. 3.21. For convenience, the equivalent DA and FM from the model are also given.

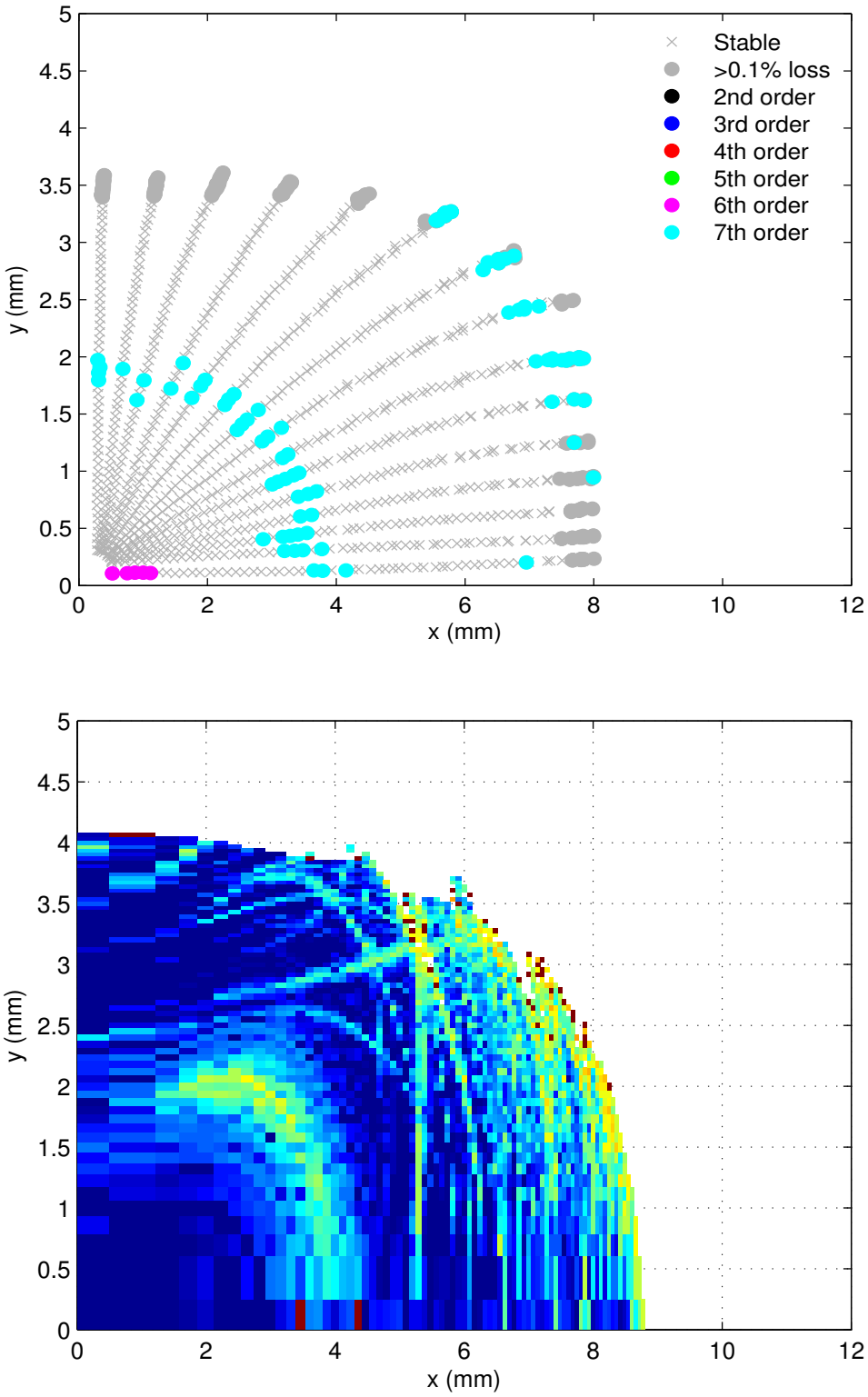

Figure 3.20: Measured (top) and simulated (bottom) dynamic apertures for the low emittance lattice. Realistic field errors and physical apertures were included in the simulation.

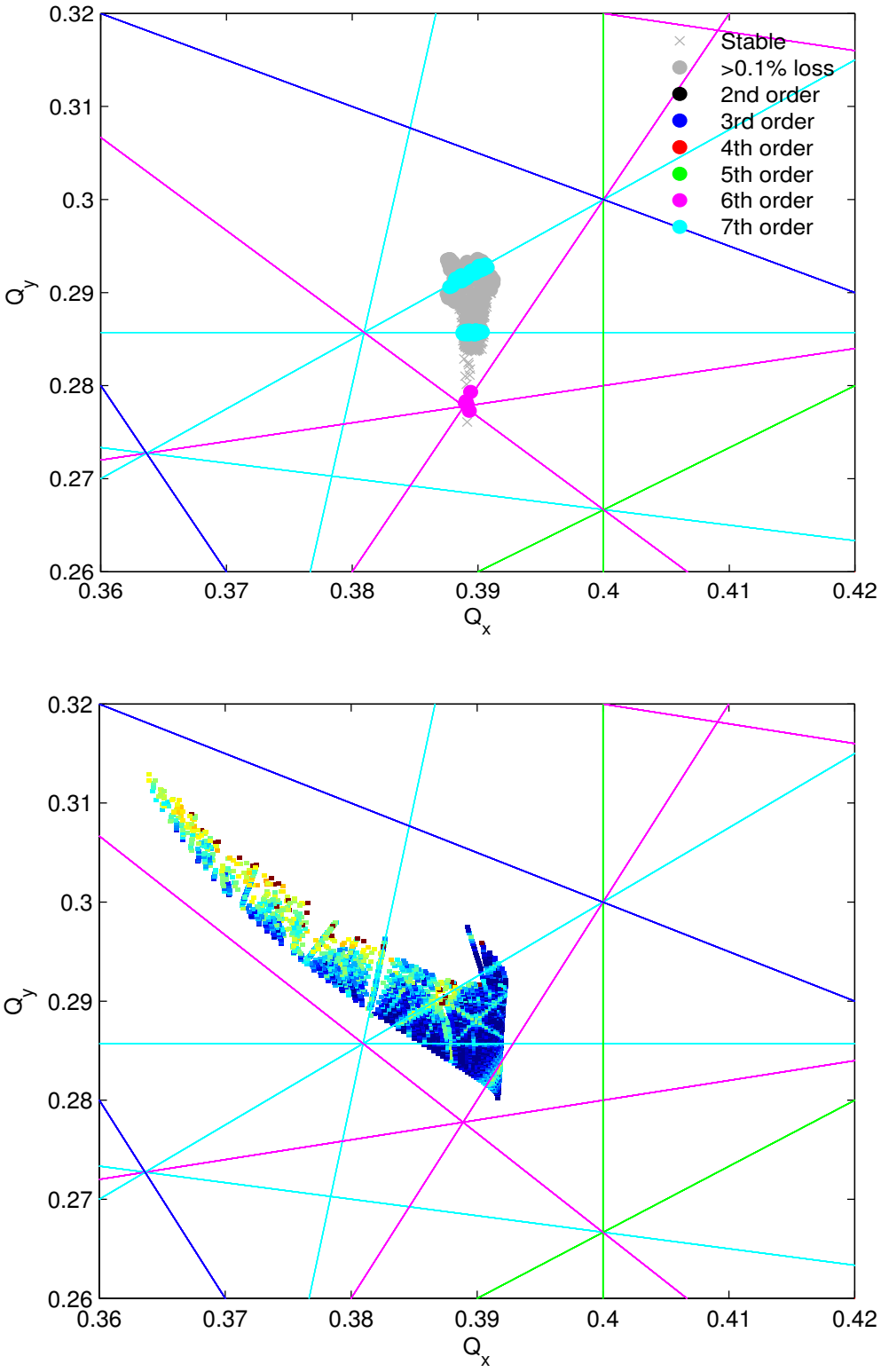

Figure 3.21: Measured (top) and simulated (bottom) frequency maps for the low emittance lattice. Realistic field errors and physical apertures were included in the simulation.

The measured DA shows good agreement with that predicted from the model, albeit marginally smaller in both planes. There are several possible reasons for this discrepancy. The first is that physical apertures in the machine may be slightly misaligned, leading to earlier particle loss than has been assumed in the model. The second is that the model does not correctly reproduce the real dynamics in the machine, either through incorrect magnet field strengths or an incomplete model. This possibility is supported by the different tune footprints shown in Fig. 3.21. The third possibility is that the BPM data sets were not correctly processed due to timing errors, gain errors etc. Lastly, the measured DA could be an underestimate of what exists in the machine, as due to the half-sine pulse, some parts of the bunch train will oscillate by a larger amount than others and be lost earlier, whilst the BPMs only report the centre of mass for the whole train. The measured FM is in qualitative agreement with the simulation, although the detuning with horizontal amplitude appears substantially reduced in the machine than predicted by the model. However, in both cases the region of tune space covered by the FMs is free from strong resonances, and the DA is sufficient to allow injection directly into the low-alpha lattice. As such, the discrepancies have had no apparent impact on the operational performance.

3.4.5 Orbit Stability Measurement

Increased transverse beam motion is a known problem for low-alpha lattices, particularly in the horizontal plane [107, 134]. Measurements taken with both low alpha lattices have shown this tendency, with the motion measured to be greater than that of the standard user lattice by up to two orders of magnitude. The beam motion is always dominated by a dispersive orbit pattern, implying the root cause of the

increase in horizontal motion is related to an increase in the amplitude of fluctuations in beam energy. The vertical motion also increases as α_I is reduced, but this is less apparent due to the smaller dispersion in the vertical plane.

Shown in Fig. 3.22 are measurements of the horizontal electron beam displacement power spectral density (PSD) for 4 different values of α_I for the high emittance lattice. The profile of the vibrations remains constant in each case, with only the amplitude of motion and the location of the synchrotron frequency peak changing as alpha is altered. The PSD profiles closely match the measured ground motion spectrum, suggesting it is primarily ground vibrations that are driving the horizontal electron beam motion.

Ground vibrations are the main cause of electron beam motion for the normal storage ring lattice [135], but the way they affect the electron beam in the low alpha optics is subtly different. In this case, rather than simply altering the closed orbit and causing the electron beam to move, quadrupole displacements cause the electron beam energy to change by creating small fluctuations in the electron path length for each revolution. Since the average circumference of the storage ring is fixed by the RF frequency, small changes to the electron path length will translate directly into changes in electron energy in inverse proportion to alpha, as can be seen from equation (3.3).

An estimate for the magnitude of path length fluctuations caused by ground motion can be made by considering quadrupole vibrations in regions of non-zero dispersion. In this case, the change in path length is given by

$$\Delta\ell = \sum_n K_n L_n \eta_n \langle \sigma_{quad} \rangle \tag{3.30}$$

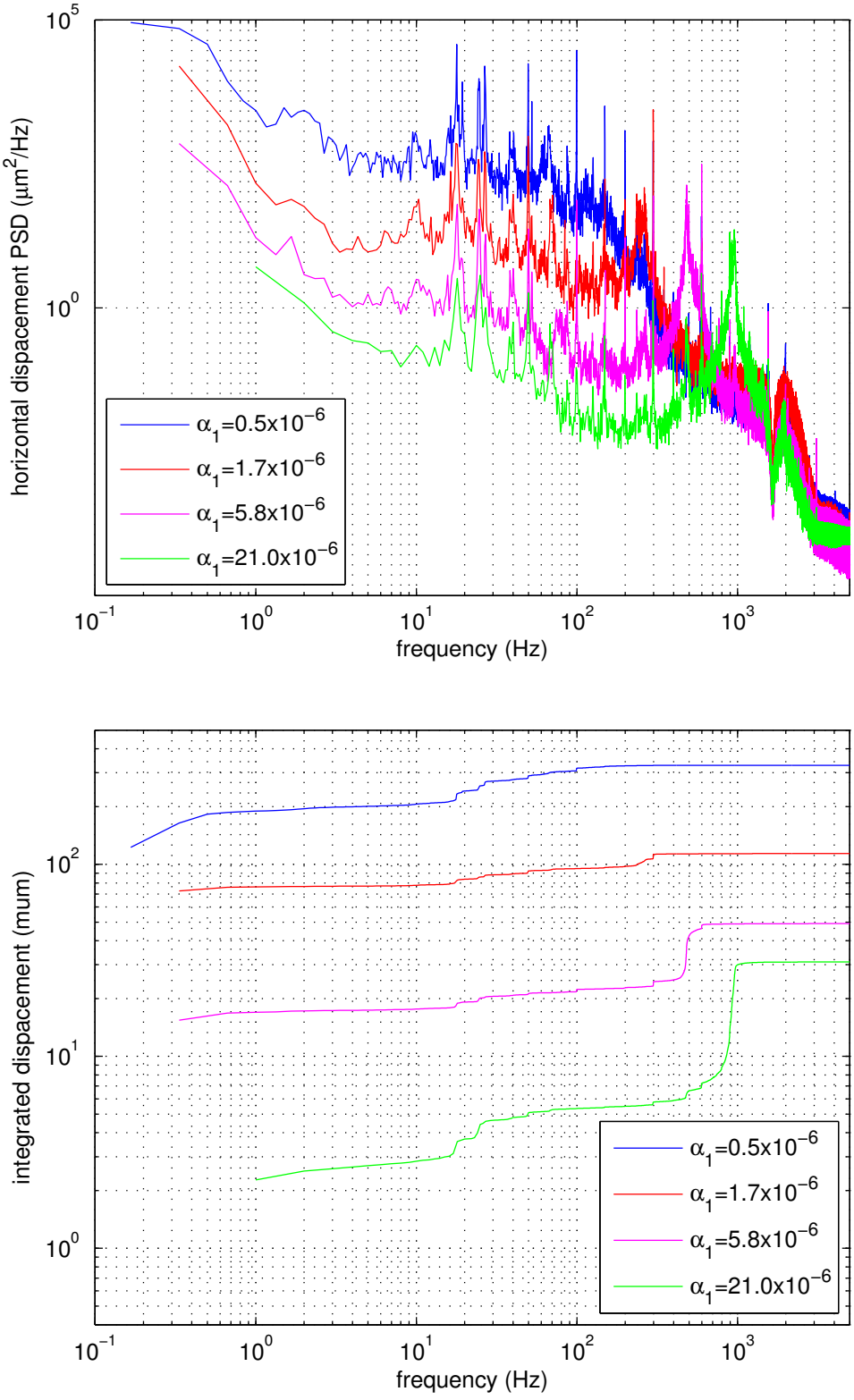

Figure 3.22: Measured horizontal displacement power spectral density as a function of alpha for the high emittance lattice (top). Integrated displacement as a function of frequency and alpha (bottom).

where K_n is the quadrupole strength, L_n is the magnet length, η_n is the dispersion at the magnet location and $<\sigma_{quad}>$ is the average transverse vibration amplitude for the magnets. For Diamond, the average amplitude of quadrupole vibrations is ~ 40nm, which in turn gives path length fluctuations of ~ 0.24μm. For the case of $\alpha_1 = -5\times10^{-7}$, the resulting energy fluctuations are δ ~ 0.085%, and for η_{BPM} = 0.45m this would result in ~380μm horizontal motion, consistent with the measured value.

3.4.6 Two Stored Beams

Along with the emittance and energy spread measurements, the x-ray pinhole cameras have also been used to confirm the existence of two stable regions in the longitudinal phase space for the low emittance lattice (see Section 3.3.1, Fig. 3.6). For this measurement, electrons were injected into the storage ring at $\varphi = \pi - \varphi_s$, before slowly shifting the RF cavity phase to $\varphi = \varphi_s$ and re-injecting without losing the original stored beam. In order to separate the two beams on the pinhole camera screens, the vertical dispersion was artificially enhanced by increasing the skew-quadrupole strengths. The pinhole camera image shown in Fig. 3.23 clearly shows the existence of two stored beams separated in space due to the different beam energies and finite vertical dispersion at the pinhole camera source points.

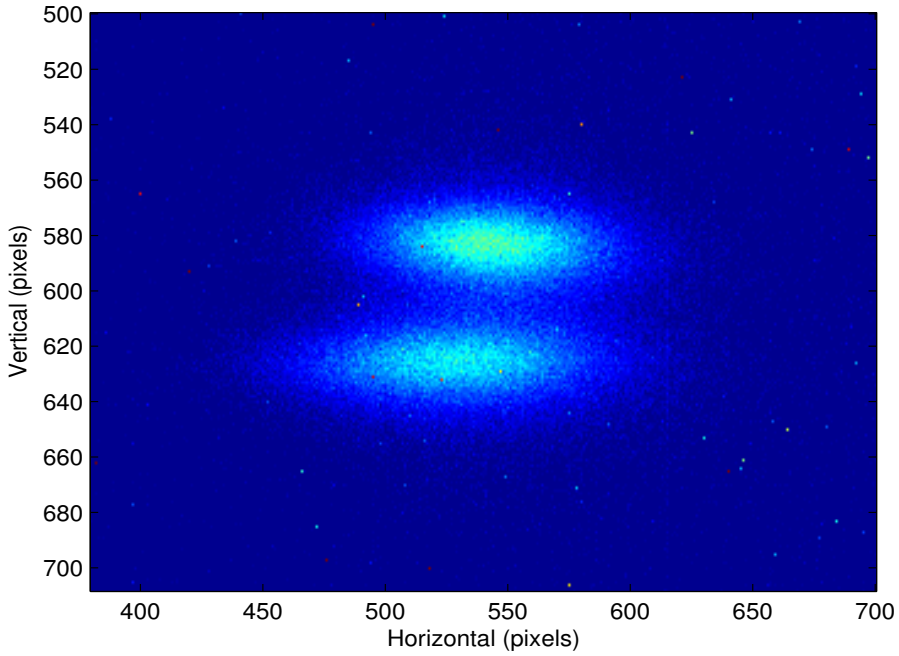

Figure 3.23: Image for the low emittance lattices showing two stored electron beams at phases $\varphi = \pi - \varphi_s$ and $\varphi = \varphi_s$. The vertical dispersion has been artificially enhanced to provide separation between the on- and off momentum beams.

3.4.7 Bunch Length Measurements

Equations (3.1) and (3.2) can be used to determine how the natural electron bunch length scales with different parameters such as alpha and RF cavity voltage. In addition, there are a number of current-related effects which alter the equilibrium electron bunch shape and therefore the length of the bunch.

For very low bunch currents (i.e. in the zero-current limit), the longitudinal bunch profile and energy distribution are Gaussian, resulting from the effects of radiation damping and excitation. As the current is increased, interaction of the electrons either with their surrounding environment (i.e. the vacuum chamber) or with the synchrotron radiation wakefield starts to become significant, leading to a potential

well distortion and a change in the equilibrium distribution and the electron bunch length [21, 59, 136-137]. At this stage, the energy spread remains unchanged. Above a threshold current longitudinal micro-bunching or microwave instabilities start to appear, increasing the energy spread and leading to a turbulent bunch lengthening above that of a pure potential well distortion [58, 60]. For low alpha operation, recent theoretical studies and experimental evidence indicate that both the potential well distortion and micro-bunching instabilities are driven primarily by interaction of the electron bunch with its own coherent synchrotron radiation (CSR) wakefield [58, 138-141].

In the next section, measurements of the electron bunch length are presented. The techniques used to measure the electron bunch length are described, follow by details of how the electron bunch length varies as a function of bunch current, synchrotron frequency, RF cavity voltage, emittance and sign of alpha.

3.4.7.1 Measurement Techniques

Electron bunch lengths have been measured using two complementary techniques. The first is a direct measurement using an Optronis dual-sweep streak camera [142]. The streak camera works by focussing the time-dependent photon distribution emitted by the electron bunch onto a photocathode, which in turn generates a secondary electron distribution which can be transversely deflected onto a phosphorous screen. The deflection takes place both horizontally and vertically; one axis is a fast sweep to image the individual bunch length, the second axis is a slow sweep to image successive bunches or successive turns in the storage ring. Although streak cameras with a resolution of 300fs are available, the resolution for this camera is estimated to

be in the range 1.5-3ps depending upon the details of the set-up. This makes bunch length measurements in low alpha mode extremely challenging at the shorter end of the scale, where the predicted bunch lengths are less than the camera resolution [143].

The second method is an indirect measurement in which the natural bunch length is inferred from the synchrotron frequency measurement.

$$\sigma_0 = \frac{cE_0\sigma_E}{h\cos\varphi_s eV_{RF}{f_{rev}}^2} f_s \tag{3.31}$$

As with the measurement of alpha, this method requires some assumptions to be made about the operating machine conditions, but for the shortest electron bunches and for low bunch currents this method is judged to be the most accurate form of bunch length measurement presently available. Measurements of this type provide a useful independent cross-check for measurements made with the streak camera.

3.4.7.2 Bunch Length vs. Current

The variation in bunch length with current is shown in Fig. 3.24 for a broad range of cavity voltages and alphas. In general, the electron bunch length is observed to grow as the bunch current increases. The exception to this is for lower cavity voltages and negative α_I, in which an initial bunch shorting is evident before the onset of bunch lengthening (discussed further in Section 3.4.7.6). At very low currents, the main trends evident in Fig. 3.24 are, as expected from equations (3.1) and (3.2), an increase in bunch length with increasing α_I and an increase in bunch length with decreasing cavity voltage. As the current increases the dependence of the bunch length on alpha quickly breaks down, and above ~20-30μA the bunch length becomes independent of α_I and converges to a common value for each cavity voltage.

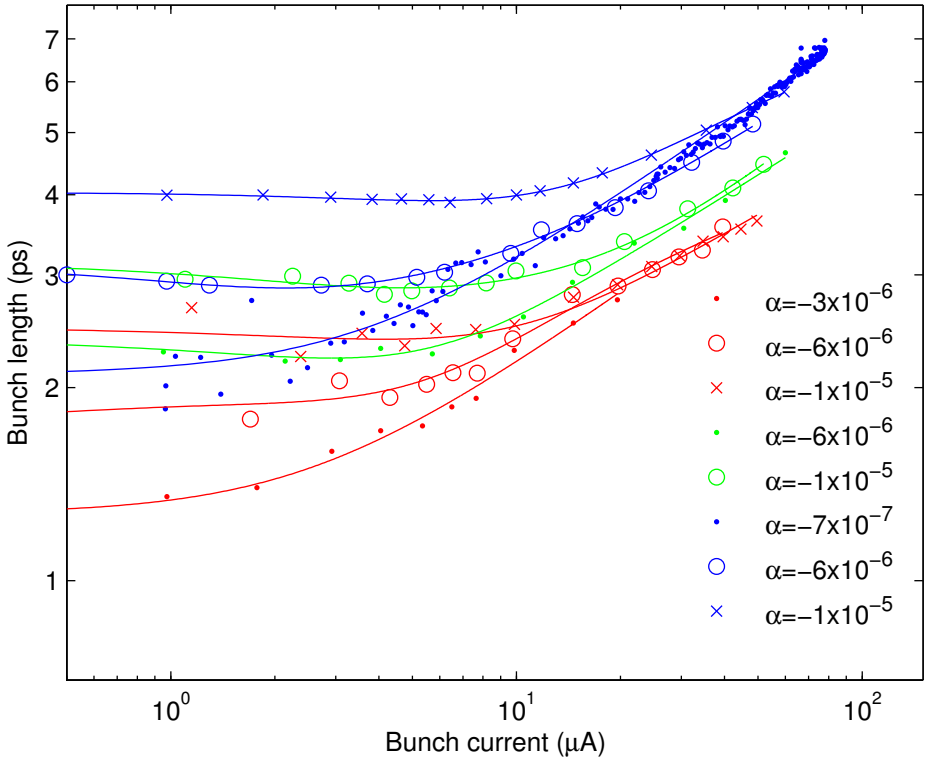

Figure 3.24: Bunch length as a function of current under a variety of conditions. Data was measured at 3.4MV (red), 2.2MV (green) and 1.5MV (blue), all using the low emittance lattice. The continuous lines are intended to guide the eye for each data set, and were calculated using a least-squares fit of the function $(\sigma_l/\sigma_{l0})^4 = (f_s/f_{s0})^4 + (I_b/I_{b0})^n + exp(-I_b/I_{b0}) - 1$, where $\sigma_{l0}, f_{s0}, I_{b0}$ and n are all fit parameters.

3.4.7.3 Bunch Length vs. Synchrotron Frequency

The natural electron bunch length is expected to vary linearly with the synchrotron frequency. This was tested by comparing the measurements taken using the streak camera to that inferred from the synchrotron frequency. For this measurement, the machine was operated in the high emittance lattice, the bunch current was held fixed at 4.2μA per bunch and the cavity voltage was set to 3MV. The results are shown in Fig. 3.25. Whilst the general trend of a shorter bunch length at lower synchrotron

frequency is evident, there is a clear discrepancy between the bunch lengths measured using the two different methods. The origin of this discrepancy is likely to be due to the non-zero bunch current used to acquire the data. The data shown in Fig. 3.24 shows that at 4.2μA and 3.4MV the bunch length is already above the zero-current value, and that at the given current the bunch-lengthening is more significant for smaller alpha. One further possibility is the resolution of the camera is larger than had been assumed, thus leading to an increasingly large over-estimate of the measured bunch length as alpha is reduced.

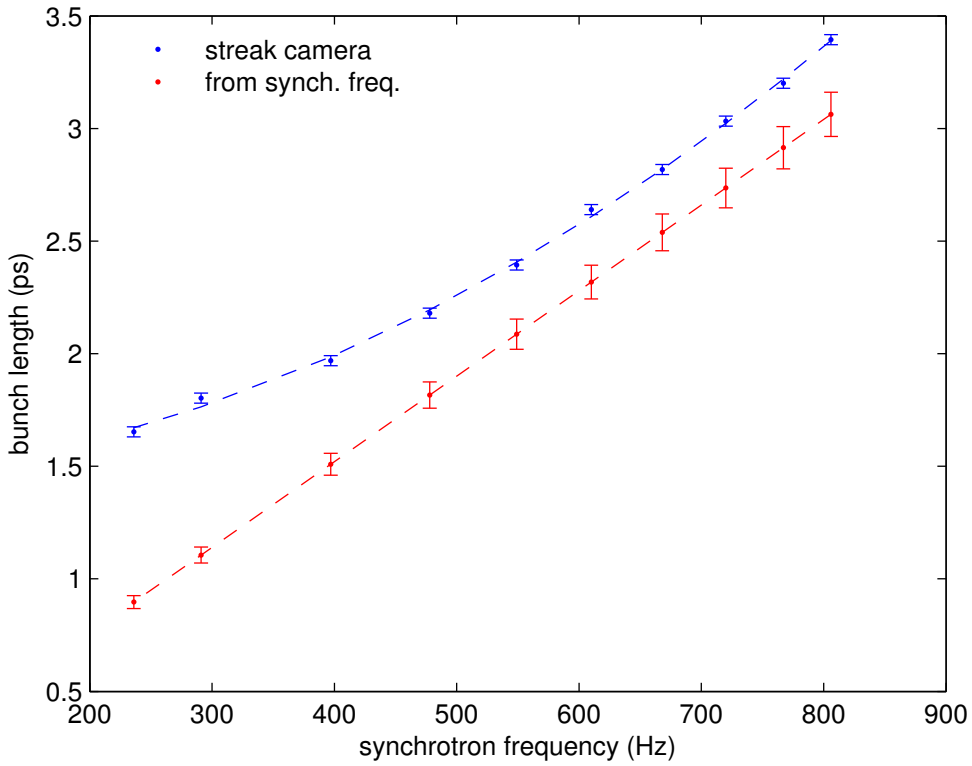

Figure 3.25: Comparison of bunch length measurements taken using the streak camera to those calculated from measurements of the synchrotron frequency. Error bars for the streak camera data indicate the standard deviation in measured bunch length divided by the square root of the number of samples. Error bars for the f_s data indicate the error on the calculated value assuming estimated errors for the f_s measurements and for the systematic errors introduced by equation (3.31).

3.4.7.4 Bunch Length vs. Cavity Voltage

According to equations (3.1) and (3.2), the natural bunch length is expected to vary with $1/\sqrt{\cos(\varphi_s)V_{RF}}$. This was investigated for the high emittance lattice for a fixed value of α_1 = -2.8×10^{-6}, holding the bunch current fixed at 4.2μA and varying the cavity voltage from 1.4MV to 3.0MV. The results are shown in Fig. 3.26.

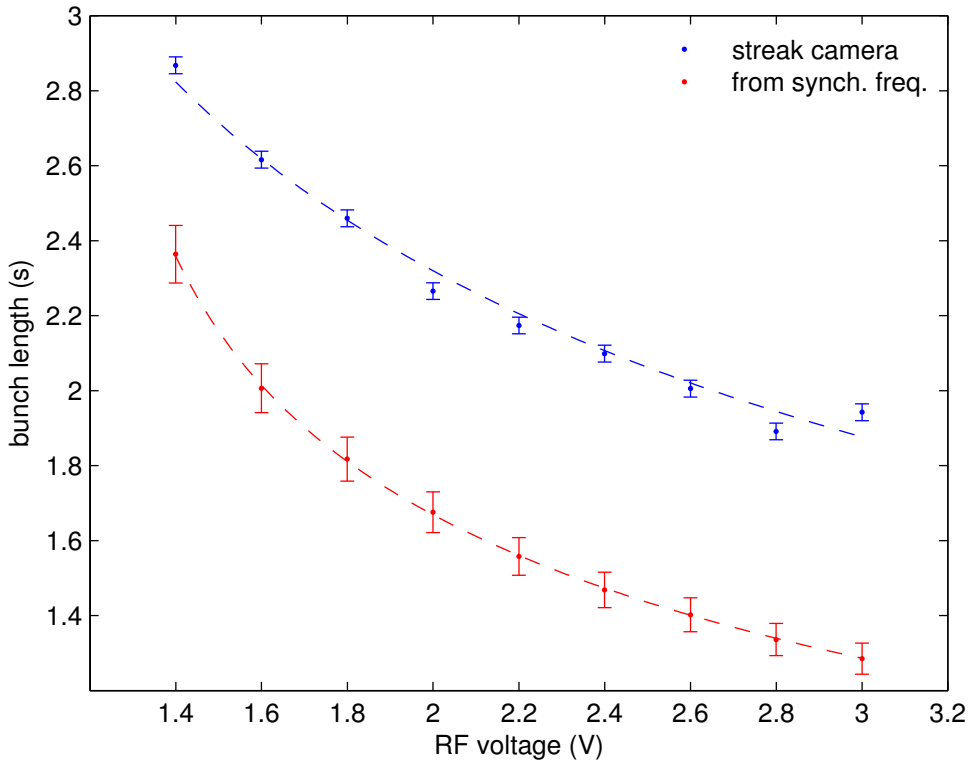

Figure 3.26: Comparison of bunch length vs. RF voltage measurements taken using the streak camera to those calculated from synchrotron tune measurements. Error bars for the streak camera data indicate the standard deviation in measured bunch length divided by the square root of the number of samples. Error bars for the synchrotron frequency data indicate the error on the calculated value assuming estimated errors for the synchrotron frequency measurements and for the systematic errors introduced by equation (3.31).

Similar to the results of Section 3.4.7.3, there is a clear discrepancy between the bunch lengths found using the two methods. This again likely to be due to the finite bunch currents used to take the measurements, or possibly an underestimate of the resolution of the streak camera. However, the expected scaling of the bunch length with cavity voltage is clearly evident.

3.4.7.5 Bunch Length vs. Emittance

The possibility to operate the Diamond storage ring in high and low emittance low alpha modes allows the bunch lengthening with current to be directly compared for the two cases. For this measurement, α_1 was held fixed at -6×10^{-6} and the cavity voltage was varied between 1.5MV and 2.2MV. The results are shown in Fig. 3.27. There is good agreement between the data-sets up to a bunch current of 42μA; however for the data taken at 62μA the measured bunch length for the low emittance was longer and was observed to emit "bursting" radiation due to micro-bunching [58]. This earlier onset of bursting radiation for the low emittance lattice can be explained as a direct consequence of the increase in electron density.

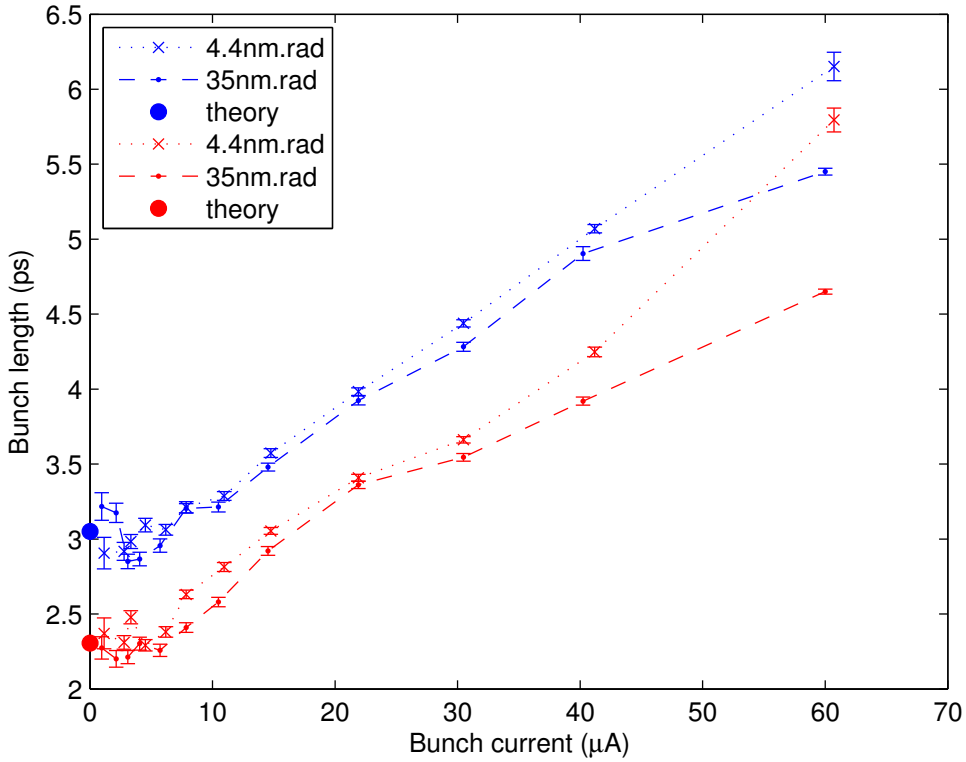

Figure 3.27: Comparison between bunch length measurements made for the high and low emittance lattices at $\alpha_I = -6\times10^{-6}$. The cavity voltage was varied between 1.5MV (blue) and 2.2MV (red). The natural bunch lengths given by equation (3.31) are marked as large dots at zero current. Error bars indicate the standard deviation in measured bunch length divided by the square root of the number of samples.

3.4.7.6 Bunch Length for Positive/Negative Alpha

For both lattices, α_I can be varied within certain bounds without significantly impacting upon the machine performance. This allows comparisons to be made for the bunch lengthening variation with current depending upon the sign of alpha. Measurements of this type are shown in Fig. 3.28. The measurements were carried

out for the low emittance lattice, in which the magnitude of alpha was held fixed at $|\alpha_1| = 1\times10^{-5}$ and the cavity voltage was set to 1.5MV. An initial reduction in bunch length with increasing current due to potential well distortion was observed for $\alpha_1 = -1\times10^{-5}$ before starting to grow again. In contrast to this, for $\alpha_1 = +1\times10^{-5}$ the bunch length grows immediately from the same initial zero-current bunch length.

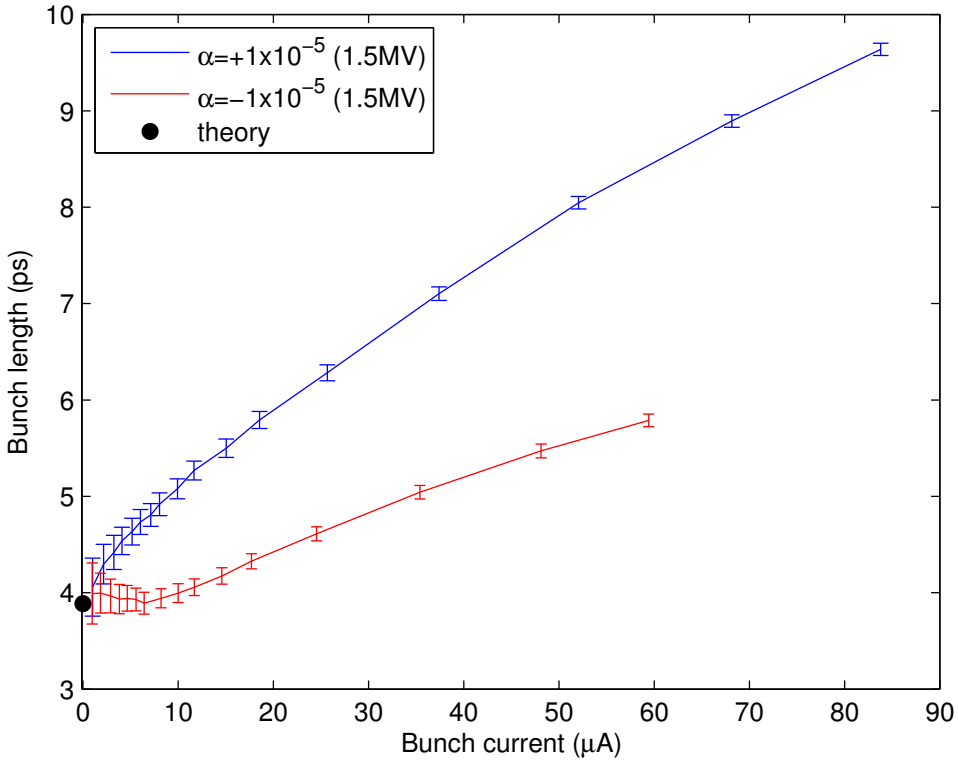

Figure 3.28: Comparison between bunch length measurements made for the low emittance lattice at $|\alpha_1| = 1\times10^{-5}$ and $V_{RF} = 1.5$MV. The bunch length given by eq. (3.31) is also given. Error bars indicate the standard deviation in measured bunch length divided by the square root of the number of samples.

3.4.8 CSR Measurements

A further confirmation of the short bunch lengths achieved with the low alpha lattices can be found by observing the emission at wavelengths comparable to or longer than the bunch length, at which point the bunch is expected to emit coherently. The total power radiated by the electron bunch at a given wavelength can be derived from the power emitted by a single electron ($P_e(\lambda)$), the number of electrons in the bunch (n_e) and a form factor (f_λ) [144].

$$P(\lambda) = P_e(\lambda)[n_e + n_e(n_e - 1)f_\lambda] \tag{3.32}$$

The form factor f_λ as defined in equation (1.19) is given by the square of the Fourier transform of the charge distribution and varies between 0 for an infinitely long bunch (incoherent emission) and 1 for a point-source (coherent emission). For large n_e (as is the case in electron storage rings), a clear indication that the emitted radiation is coherent is given if $P(\lambda)$ is proportional to n_e^2.

To detect coherent emission the Diamond storage ring is equipped with a Schottky Barrier Diode sensitive to the 60-90GHz bandwidth [145]. This detector has a response time of 250ps allowing the structure and evolution of the coherent emission to be studied on a turn-by-turn basis, albeit restricted to measuring mm-wave radiation longer than the expected bunch length.

The emitted radiation in this bandwidth is shown in Fig. 3.29 for a variety of machine conditions for the low emittance lattice. The radiation was emitted in a steady-state, i.e. the bunch current was kept below the bursting instability threshold (found to be in the range 50-55μA for these measurements). The data show that the power emitted in this bandwidth at a given RF voltage is initially higher for a reduced value of α_1

(when the bunch length is shorter), but as the current is increased and the bunch length becomes independent of α_1 the emitted power also becomes independent of α_1. As the RF voltage is increased, the bunch length is shortened and again the emitted power increases.

Further analysis of these data sets show that the differences in emitted power can be explained purely by the form factor f_λ for each data point. The form factors are extracted from streak camera images recorded at the same time as the mm-wave data, and show both a bunch lengthening and bunch distortion as the bunch current is increased. If the measured power is normalised to the numerically calculated form factor for λ = 5mm, then the power emitted becomes independent of machine parameters and proportional to I_b^2, as predicted by equation (3.32) for the case of $f_\lambda n_e >> 1$. The power normalised to $f_{\lambda=5mm}$ is shown in Fig. 3.30, and a selection of bunch profiles for increasing bunch current are shown in Fig. 3.31. Normalising the mm-wave data to a form factor calculated using a Gaussian bunch of equal FWHM significantly underestimates the power emitted at higher bunch currents; it is necessary to consider both a bunch lengthening and a bunch shape distortion to explain the measured data.

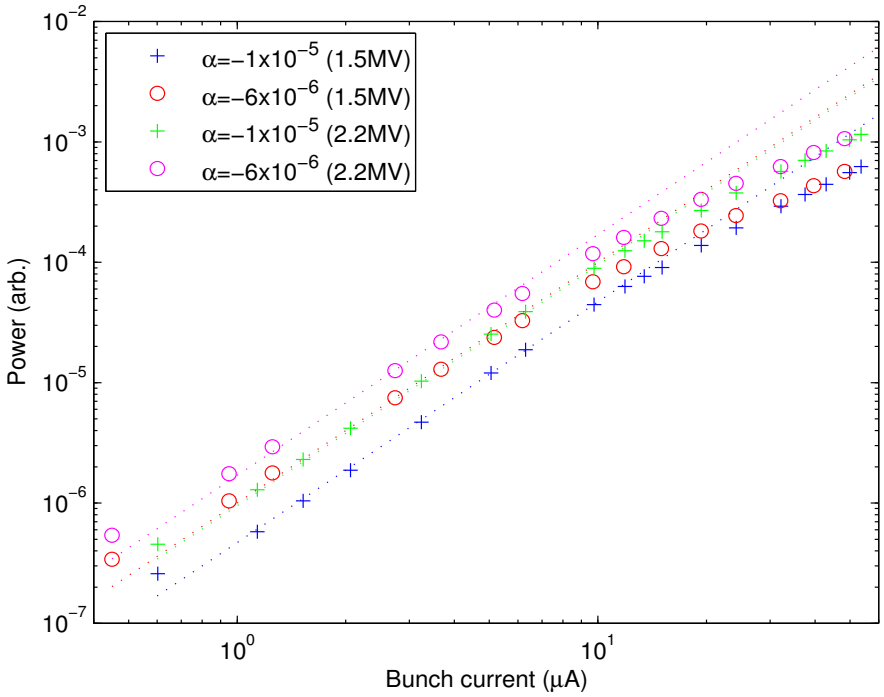

Figure 3.29: Power emitted in the 60-90GHz bandwidth as a function of current for two values of α_1. Data was measured at 1.5MV and 2.2MV.

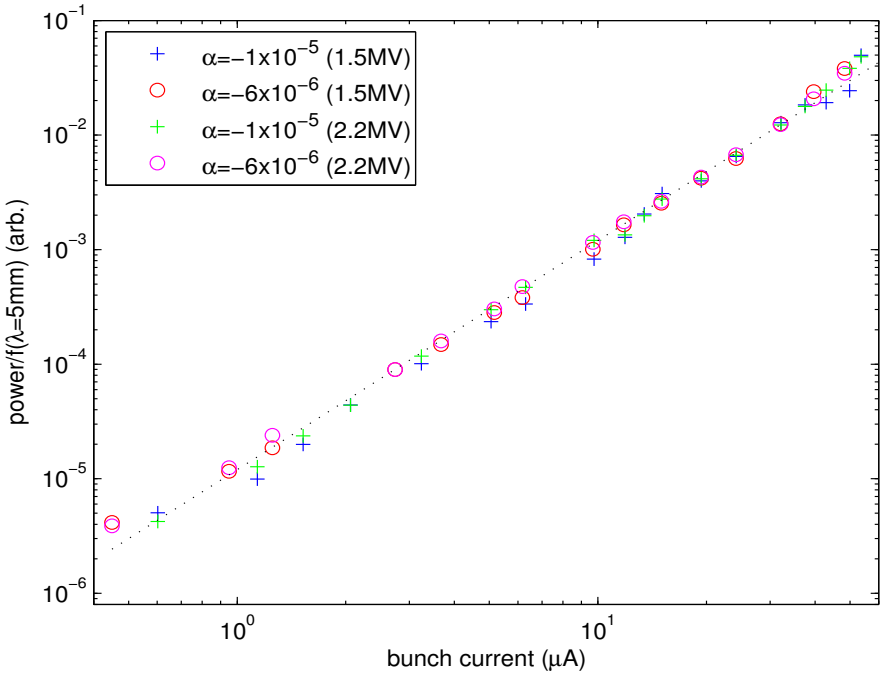

Figure 3.30: Power measured with the Schottky Barrier Diode normalised to the form factor calculated using the measured bunch profile.

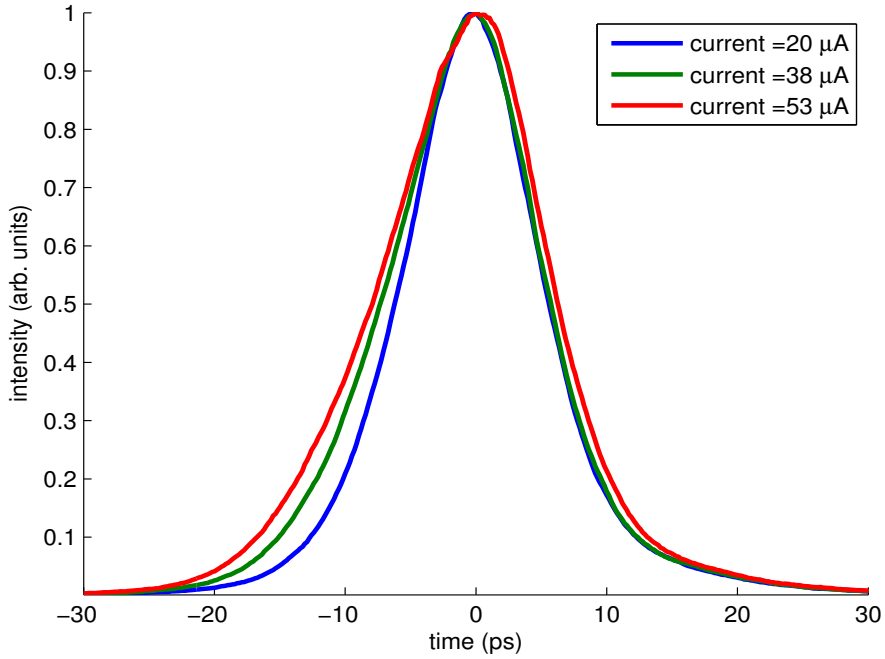

Figure 3.31: Bunch profiles recorded for $\alpha_1 = -1\times10^{-5}$ and $V_{RF} = 1.5$MV.

3.4.9 Summary of Lattice Performance

A comparison between the predicted and measured performance for the two low alpha lattices is given in Table 3.5. The quoted lifetime values for the model and machine are not strictly speaking comparable, as the values for the model only include the Touschek component and neglect all other contributions. There is reasonable agreement for the majority of other parameters, with the injection efficiency for the high emittance lattice a notable exception. The injection efficiency for this lattice has always been very poor, and substantially below what had been expected from the model. The injection efficiencies for both lattices are somewhat variable, and strongly depend upon how well the machine has been set up.

Overall, both high and low emittance lattices have performed close to their expected values, with both capable of delivering variable short-pulses in the 1-5ps range.

	High Emittance Lattice		Low Emittance Lattice	
	Model	Machine	Model	Machine
Emittance (nm.rad)	35.2	37.2 ± 1.6	4.4	3.7 ± 0.3
Dynamic Aperture (mm)	-10.7 / +15.2	-	-10.8 / +8.8	+8.1
Lifetime (h)	12.3 (3.0MV/100μA)	9.0 (3.0MV/100μA)	18.2 (2.2MV/38μA)	13.0 (2.2MV/38μA)
Injection Efficiency (%)	31.4	1-10	22.6	20-40

Table 3.5: Comparison between model and machine performance for some key parameters

Chapter 4

Short Pulse Generation from a Linac-Based Light Source

Section 2 described the different schemes that have been proposed to generate ultra-short radiation pulses using high-gain, single pass free-electron lasers (FELs). From an experimental perspective, an ideal radiation source would produce an isolated radiation pulse of femto-second duration and high peak power, synchronised to an external trigger, with high repetition rate and equi-spaced pulses also desirable. None of the schemes are able to meet this objective in entirety; however, the two which appear best suited are single spike (Section 2.2.1.2) and the tapered undulator scheme (Section 2.2.2.4). Single spike operation has the potential to produce isolated radiation pulses but lacks a tight synchronisation trigger. Conversely, the tapered undulator scheme is triggered by (and hence synchronised with) a modulating laser beam, but the fs-pulse contains a background signal generated by the remainder of the bunch. This scheme does however offer an improved contrast ratio between the fs pulse and background radiation compared to other laser slicing schemes.

In this Chapter both schemes are examined from a theoretical perspective and with extensive numerical simulations. The Chapter begins in Section 4.1 with a discussion on the need for numerical simulations and an overview of the model used during these studies. Single spike operation is discussed in Sections 4.2 and 4.3, and the tapered undulator scheme is presented in Sections 4.4 and 4.5.

4.1 Numerical Simulation Details

4.1.1 Requirement for Numerical Simulations

The 1D theory of a SASE-FEL presented in Section 1.2.4 neglects a number of effects which can degrade the performance of an FEL, such as the emittance and energy spread of the electron beam, diffraction of the radiation field and variation of the electron bunch parameters along its length. In order to account for these effects correctly it is necessary to use 3D, time-dependent numerical simulation codes such as Ginger [146], Genesis [147] or to a less extent Perseo [148], Similarly, the simulated electron bunches used to drive the FEL should be as realistic as possible. This is particularly true when high peak currents and low emittance beams are concerned, as collective effects such as coherent synchrotron radiation (CSR) [149, 150], longitudinal and transverse space charge forces (LSC, TSC) [151, 152] and wakefields can have a strong influence on the electron beam properties. Realistic values of the peak current and electron bunch slice parameters can only be arrived at through particle tracking studies using codes which take into account all collective effects such as Elegant [119] or IMPACT-T [153]. These codes use a simplified 1D model for the CSR forces to improve the speed of calculation; for a more detailed study of CSR effects a 3D code such as CSRtrack [154] should be used. At low (non-relativistic) energies, space charge effects are dominant and codes such as ASTRA [155] or Parmela [156] are more appropriate, as these include a full 3D description of the space charge forces.

4.1.2 The New Light Source

In order to carry out detailed studies of single spike operation and the tapered undulator scheme, the New Light Source (NLS) facility has been taken as the practical example [7]. This conceptual design describes a facility with a suite of three seeded FELs driven by a 2.25GeV superconducting linac, and operates with photon energies from 50eV to 1keV in the fundamental.

The main components of the NLS are:

- Normal conducting L-Band photocathode RF gun [157]
- 18 superconducting 1.3GHz TESLA-type RF cavity modules [158]
- Laser heater [159]
- 3.9 GHz superconducting XFEL type 3rd harmonic cavity (3HC) [160]
- 1 C-type (low energy) and 2 S-type bunch compressors (medium and high energy)
- Collimation and beam spreader section
- Three FEL lines

An image showing the location of the main components is shown in Fig. 4.1.

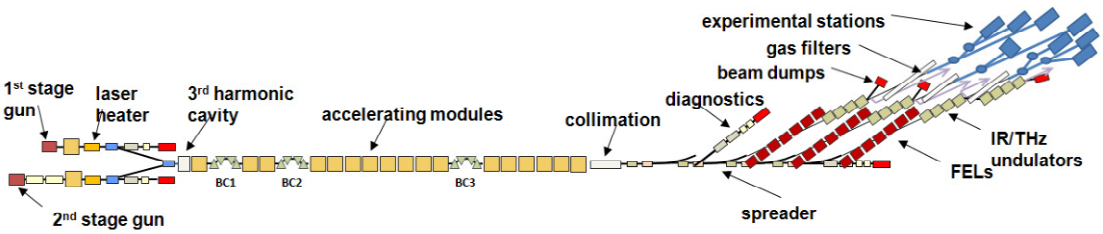

Figure 4.1: Schematic of the NLS facility layout.

The evolution of the electron bunch in the standard mode of operation along the length of the NLS facility is as follows. The electron bunch is first generated by the L-band electron gun and accelerated to ~120MeV by the first superconducting RF cavity module. This injector section was designed to provide electron bunches at 1kHz repetition rate with a charge in the range 1pC to 200pC and with low normalised emittance and low energy spread [161]. In the standard operating mode, the injector is tuned to operate with 200pC bunch charge.

Following the injector is a laser heater (laser beam and undulator section). Interaction with the laser heater increases the uncorrelated energy spread in the electron beam and has been included to suppress the gain of the micro-bunching instability [151, 152]. After the laser heater is a third harmonic cavity, whose purpose is to control the longitudinal phase space curvature of the bunch (see Section 2.2.1.1). The main linac takes the electron bunch from ~120MeV up to 2.25GeV by acceleration in the remaining RF cavities. During the acceleration, the electron bunch is gradually compressed from ~15ps FWHM to ~180fs FWHM in three magnetic chicanes. The bunch length compression factors for the three chicanes are ~2, ~4 and ~10.4 respectively. Following the main linac is a collimation section (designed to remove the beam halo and off-energy particles) and three spreader sections which distribute the beam to the FELs. The optical functions for the main linac are shown in Fig. 4.2, and the electron bunch properties at the exit of the spreader are shown in Fig. 4.3.

The FEL section consists of a series of undulator modules interleaved in a focussing-defocusing (FODO) structure quadrupole array. The standard operating mode of the NLS is to seed each of the FELs with a 20fs laser pulse at 50-100eV, with the desired FEL radiation wavelength reached by multiplying the seed laser frequency in a

cascaded harmonic generation scheme. To accommodate the expected arrival time jitter between the electrons and seed laser, the linac was optimised to provide electron bunches with roughly constant parameters in a 100fs long section. The undulator modules differ for each of the three FELs in that they are each optimised for different photon energy ranges. Studies of the single spike and tapered undulator schemes have all assumed the highest photon energy of 1keV (λ_r = 1.24nm), as this places the highest demands on the required electron bunch parameters.

From a modelling perspective, the facility can be conveniently broken down into three parts, namely the injector, main linac (from laser heater through to the end of the spreader) and the undulator section. The injector has been modelled using ASTRA, simulations of the main linac have been carried out using Elegant and the FEL section has been modelled with Genesis.

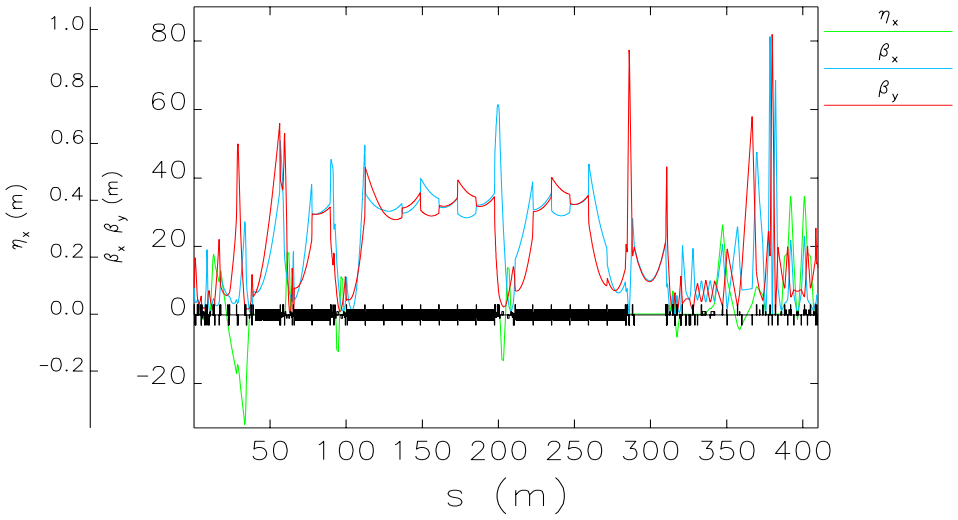

Figure 4.2: Twiss parameters for the NLS linac optimised for standard operation.

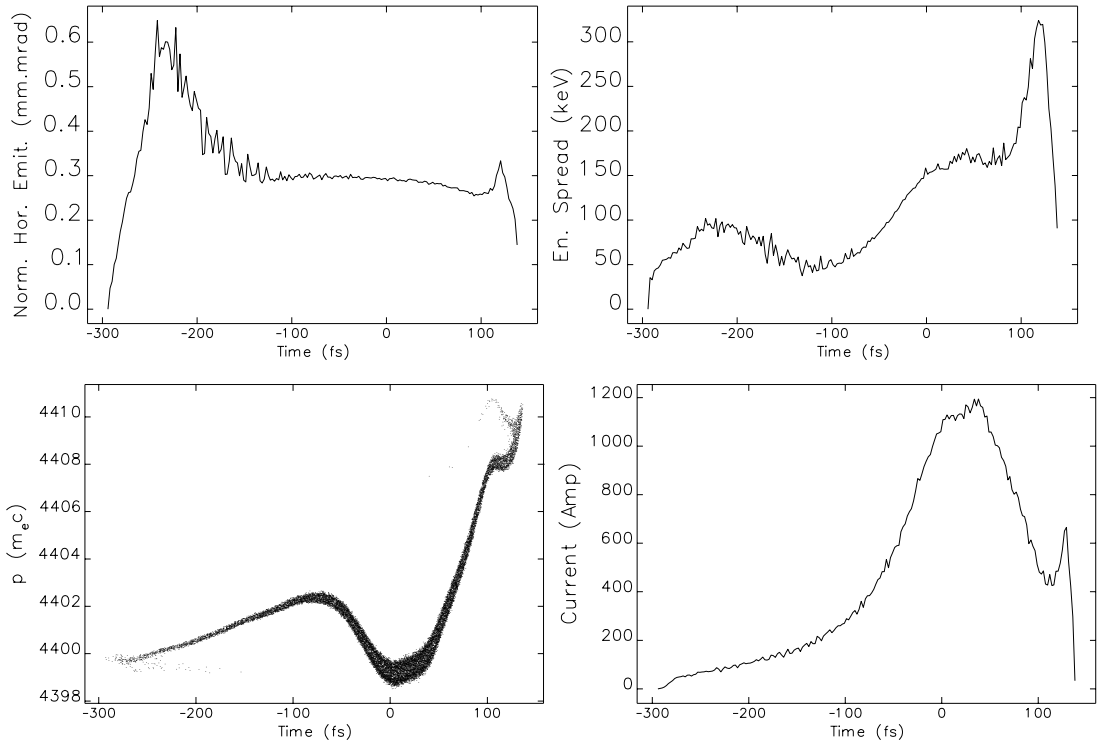

Figure 4.3: NLS 'standard bunch' at the exit of the spreader section. Normalised horizontal emittance (top left), energy spread (top right), longitudinal phase space (bottom left) and current profile (bottom right) are shown. Particle tracking was carried out in Elegant for 2M particles, and included CSR, LSC and wakefield effects.

4.2 Theory of Single-Spike Operation

The single-spike regime is a special case of a SASE-FEL. In this regime, the electron bunch length is tailored to match the cooperation length of the FEL such that it is possible for all electrons in the bunch to interact with each other through the radiation field. This leads to the development of a single, fully coherent SASE radiation spike [27, 68, 87].

For the FEL to be operating in the single spike regime the electron bunch length (L_e) must satisfy the condition

$$L_e \leq 2\pi L_C \leq \frac{\lambda_r}{2\sqrt{3}\rho_P} \tag{4.1}$$

Previous studies of this mode of operation for x-ray FELs have concentrated on using electron bunches with very low charges to drive the FEL (typically ~1-10pC) [87, 162-164]. There are several reasons for this choice. Firstly, at low charges the emittance from the electron gun is expected to be very low, since the contribution from space-charge effects will be small and the beam will be dominated by the thermal emittance [162]. Secondly, during the beam transport and acceleration from the electron gun to the undulator the collective effects are much reduced. This means that the electron bunch can be compressed to a much larger degree than is the case for 200pC operation, without the associated degradation in beam quality. The final electron beam brightness (defined as $I/\sigma_x\sigma_y$) in this case can be comparable to or even higher than that achieved for standard FEL operation, with the reduction in gain length that this implies.

An order of magnitude estimate can be made for the required electron bunch length based upon the 1D theory. Typical parameters for the electron bunch at the entrance to an undulator are a peak current of 1 to 2kA and a normalised slice emittance of 0.1 to 0.5mm.mrad. Assuming an electron energy of 2.25GeV and an undulator period of 0.032m, the Pierce parameter lies in the range 1×10^{-3} to 2×10^{-3} which gives a cooperation length of 0.1-0.2fs for a resonant wavelength of 1.24nm (1keV photon energy). According to equation (4.1), the required electron bunch length should therefore be approximately 0.6 to 1.2fs long.

Whilst it is necessary to carry out full start-to-end tracking simulations to accurately study the single spike mode of operation, it is worthwhile to consider if the

limitations of the 1D theory can be improved upon. The simplest way to do this is to make use of the Xie-scaling described in Section 1.2.4.2. By doing so the gain degradation effects can be partially accounted for by the Λ parameter, which from equations (1.25) and (1.27) will lead to an increase in the expected cooperation length, relaxing the constraint on the required bunch length for single spike operation given by equation (4.1).

Further insight into the workings of the scheme can also be gained by deriving an effective value for the Pierce parameter retrospectively from the results of the start-to-end simulations, as this implicitly includes all 3D degrading effects and the fast variation in properties along the bunch length. This effective value can be found by combining equations (1.21) and (1.24) to give

$$\rho_{eff} = \frac{\lambda_u}{4\pi\sqrt{3}} \frac{1}{P(z)} \frac{dP}{dz} \tag{4.2}$$

where both *P(z)* and *dP/dz* are extracted from the simulation results. This approach was suggested in [87] using steady-state Genesis calculations; however, this can easily be extended for full time-dependant calculations.

4.3 Numerical Study of Single-Spike Operation

4.3.1 Linac Optimisation

In order to generate a compressed electron bunch suitable for single spike operation, the charge from the electron gun was reduced to 2pC and the linac working point was re-optimised using the maximum peak current and electron bunch length as target

parameters. During the optimisation, limits were placed on the maximum chicane magnet bend angles in order to keep timing jitter as low as possible, and on the phases of the accelerating modules in order to minimise the final energy chirp on the electron bunch. The main parameters for the linac following this optimisation are given in Table 4.1.

Parameter	Value
RF Phase (modules 2-3)	17° off crest
RF Phase (modules 5-12)	5° off crest
RF Phase (modules 13-18)	0°
Bunch Compressor 1 R_{56}	-62.4 mm (10.9˚ bend angle)
Bunch Compressor 2 R_{56}	-97.9 mm (9.6˚ bend angle)
Bunch Compressor 3 R_{56}	-52.9 mm (5.65˚ bend angle)
RF Phase (third harmonic cavity)	174° off crest
RF Voltage (third harmonic cavity)	10.1 MV/m

Table 4.1: Linac parameters for maximum bunch compression (2pC bunch charge)

The current profiles and longitudinal phase space distributions for the electron bunch at various stages along the linac are shown in Figs. 4.4a and 4.4b below. The compression in the main linac takes the electron bunch from a peak current of 0.55A and 3.8ps FWHM at the exit of the injector to a peak current of 1.9kA and 0.7fs FWHM at the undulator entrance. The compression after the third bunch compressor (BC) is strong enough to re-introduce significant space charge effects, as can been seen by comparing the third and fourth phase space plots in Fig. 4.4b. Also, the final phase space plot in Fig. 4.4b shows that CSR in the spreader section leads to significant energy loss for the electrons in the core of the bunch.

The slice emittance and energy spread of the electron bunch at the entrance to the undulator are shown in Figs. 4.5 and 4.6, along with the current profile in the central region for reference. The normalised emittance in the centre of the bunch is 0.065mm.mrad, highlighting the excellent beam brightness that is possible when the gun charge is reduced. Whilst it remains challenging to produce such a beam, the value used here is consistent with values found in other studies and with operational experience at LCLS during low charge operation [86, 87]. The energy spread in the centre of the bunch is relatively high at 470keV, primarily due to the chirp given to the electron bunch during acceleration and compression.

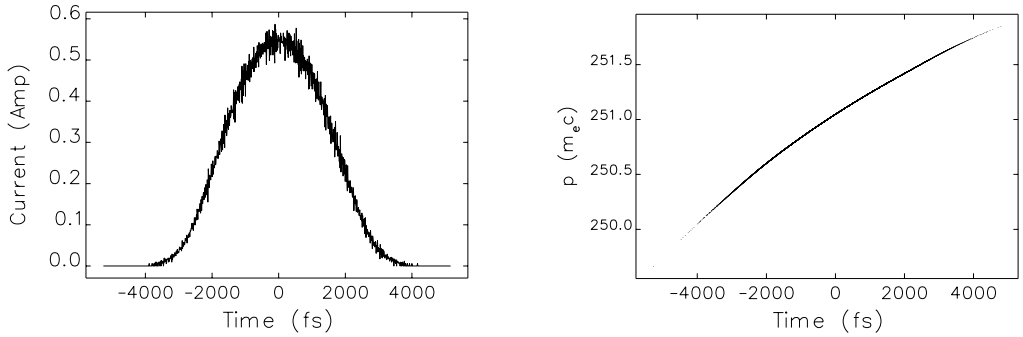

Figure 4.4a: Current profile and longitudinal phase space at exit of the injector.

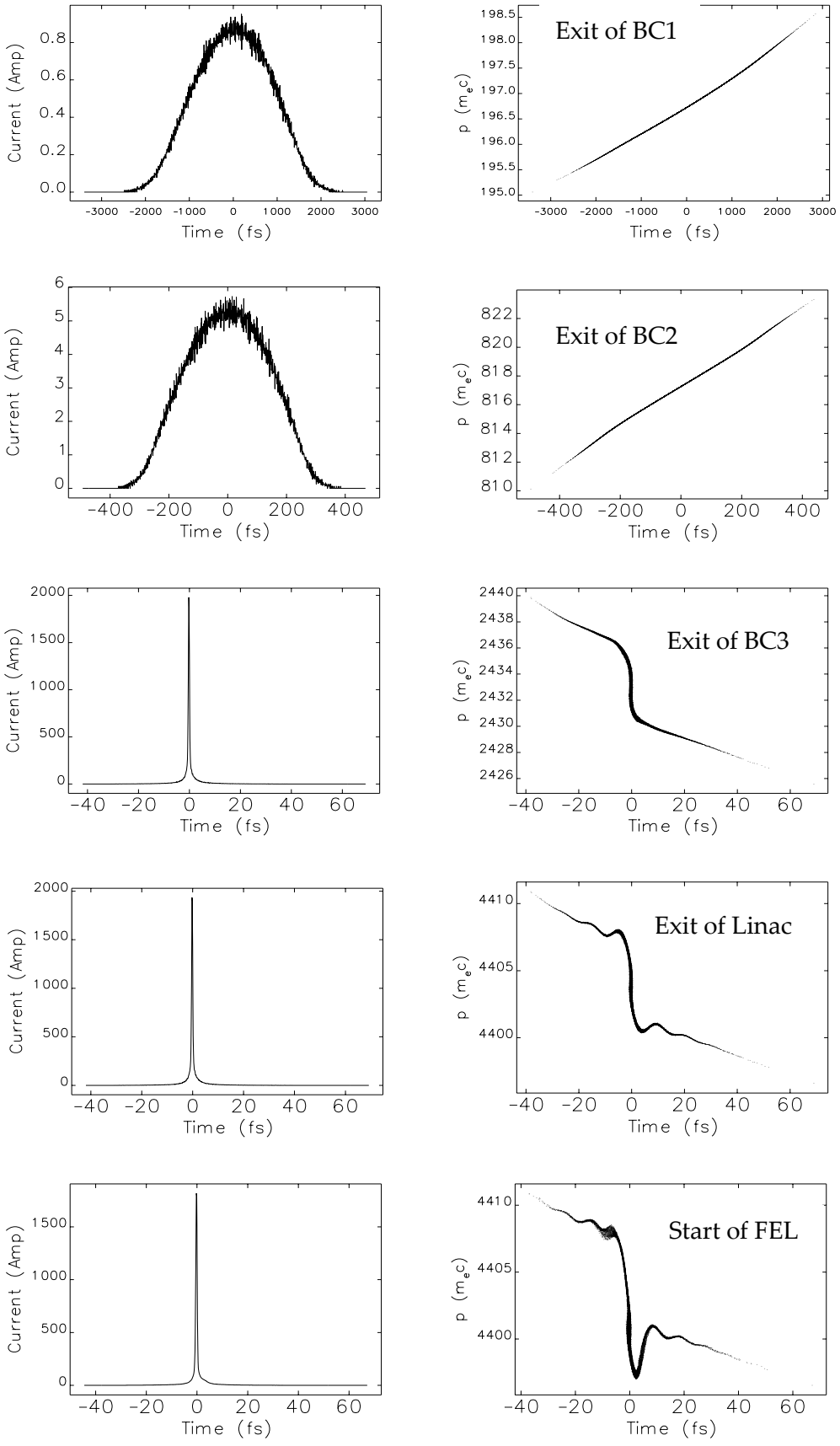

Figure 4.4b: Current profile and long. phase space at various locations along the linac.

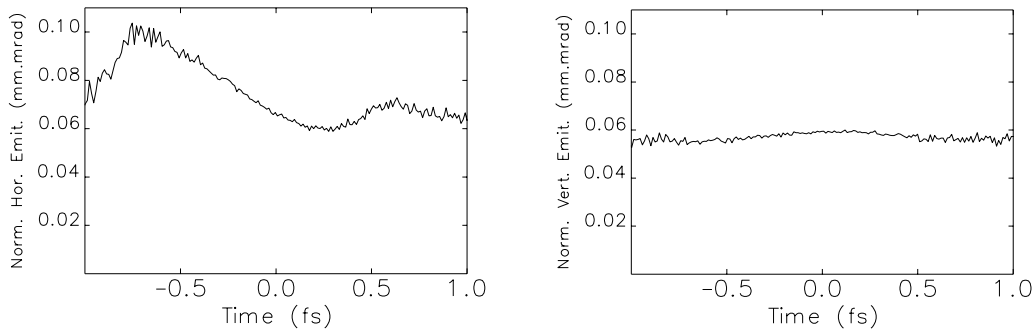

Figure 4.5: Hor. (left) and vert. (right) slice emittance at the undulator entrance.

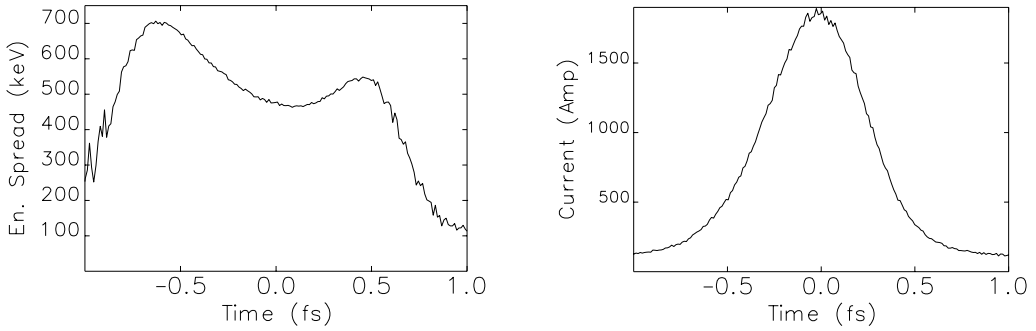

Figure 4.6: Energy spread (left) and current profile (right) at the undulator entrance.

4.3.2 Identification of Optimum Compression

Whilst the initial optimisation of the linac for operation in the single spike regime gives a high peak current and short bunch length, the relatively high energy spread caused by the energy chirp could prove to be detrimental for the FEL process. In order to determine whether operating slightly above or below maximum compression is more beneficial, a scan was carried out varying the electron bunch length from an under-compressed 4fs FWHM, through maximum compression (0.7fs FWHM) to an over-compressed 4fs FWHM. Reducing the energy spread in this way comes at the expense of lengthening the electron bunch and lowering the peak current; however,

the cooperation length is also increased, relaxing the bunch length constraint given by equation (4.1). This process also allows a numerical test of equation (4.1), explicitly identifying which bunch lengths will allow the FEL to operate in the single spike regime.

During the bunch length scan, all linac parameters were kept constant except for the strength of the chicane magnets in the third bunch compressor. A selection of the resulting current profiles and longitudinal phase space plots are shown in Fig. 4.7, and show a double-peak current profile for the under-compressed bunches and a single peak current profile for the bunch at maximum and over-compression. Note that the current profiles for the electron bunches are in general non-Gaussian.

Figure 4.8 shows how both the electron bunch length FWHM and standard deviation vary as a function of the strength of the third bunch compressor, and the values for the calculated cooperation length using the 1D theory, Xie-scaling and extracted from the numerical simulations are overlaid for reference. Assuming the electron bunch length standard deviation and numerically-extracted cooperation lengths are the key parameters, theory predicts electron bunch lengths between 4fs FWHM under-compressed to 1fs FWHM over-compressed will produce single-spike emission.

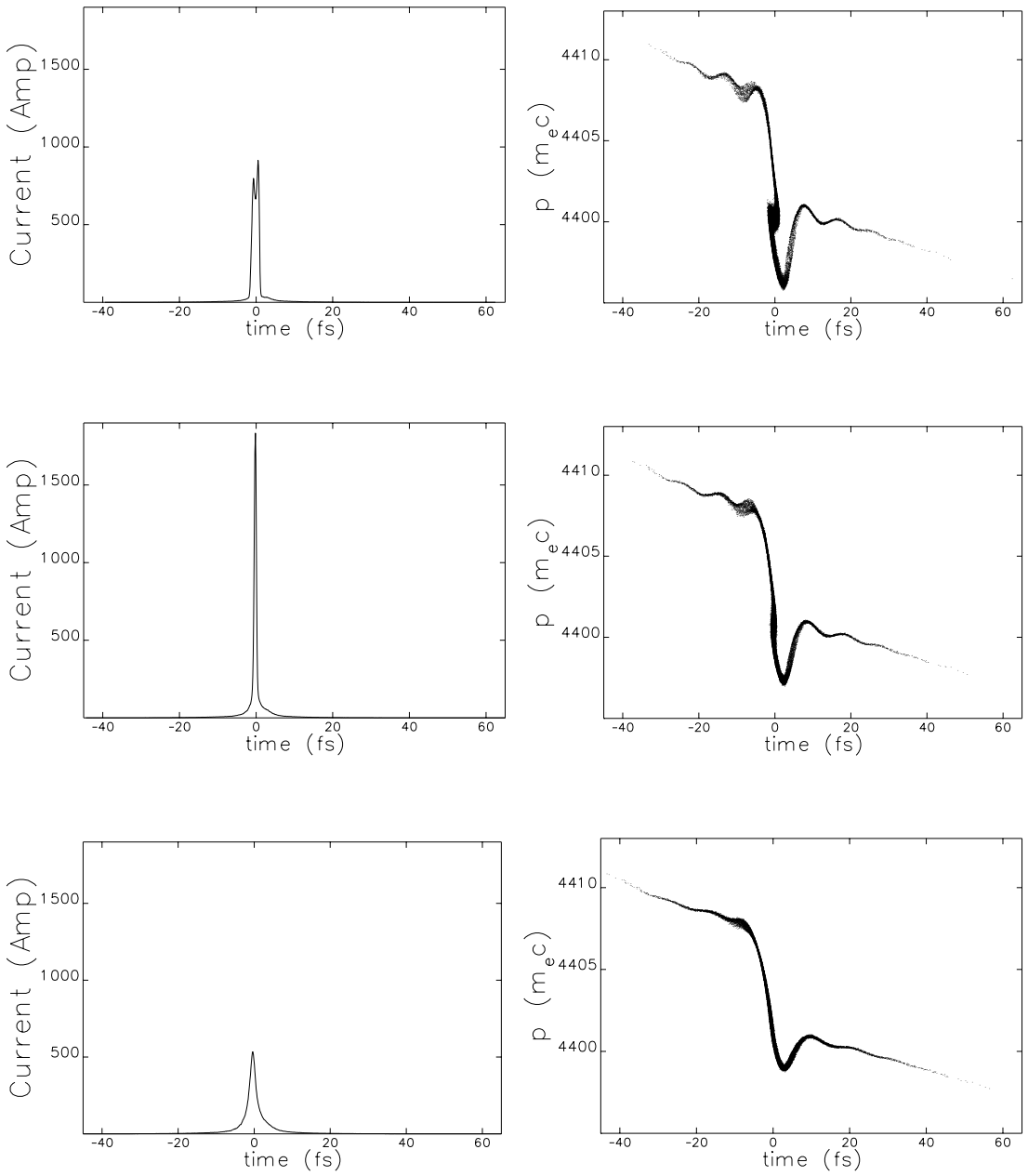

Figure 4.7: Current profiles (left) and longitudinal phase space (right) plots for the electron bunch during the bunch length scan. The images show an under-compressed 2fs FWHM bunch (top), maximum compression bunch (middle) and over compressed 2fs FWHM bunch (bottom).

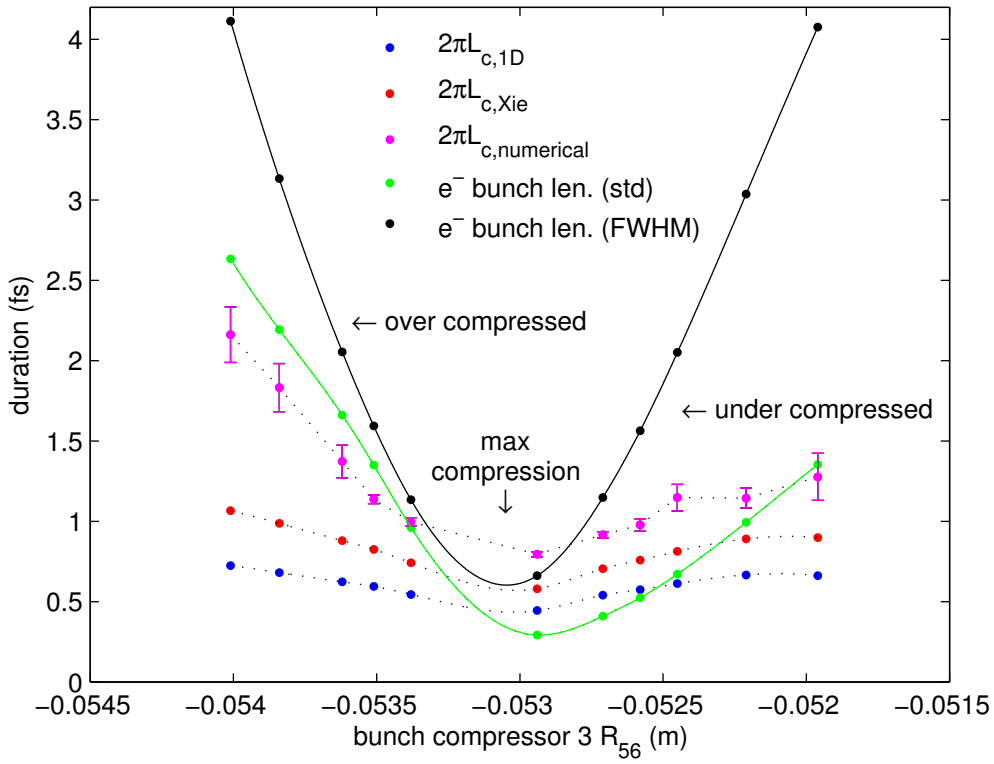

Figure 4.8: Electron bunch length FWHM and standard deviation as a function of third bunch compressor strength. The respective cooperation lengths calculated using the 1D theory, Xie-scaling and extracted from the numerical simulations are overlaid for reference.

For each electron bunch, 40 separate simulations were carried out using Genesis in time-dependant mode, each time using a different random seed for the starting shot-noise in the electron distribution (this initial shot-noise seed was varied to account for statistical fluctuations in the SASE process). For each case, the FEL saturation length, peak power and spectrum at saturation, pulse duration and line-width were calculated. The power growth along the undulator axis as a function of electron bunch length averaged over the 40 shot-noise seeds is shown in Fig. 4.9.

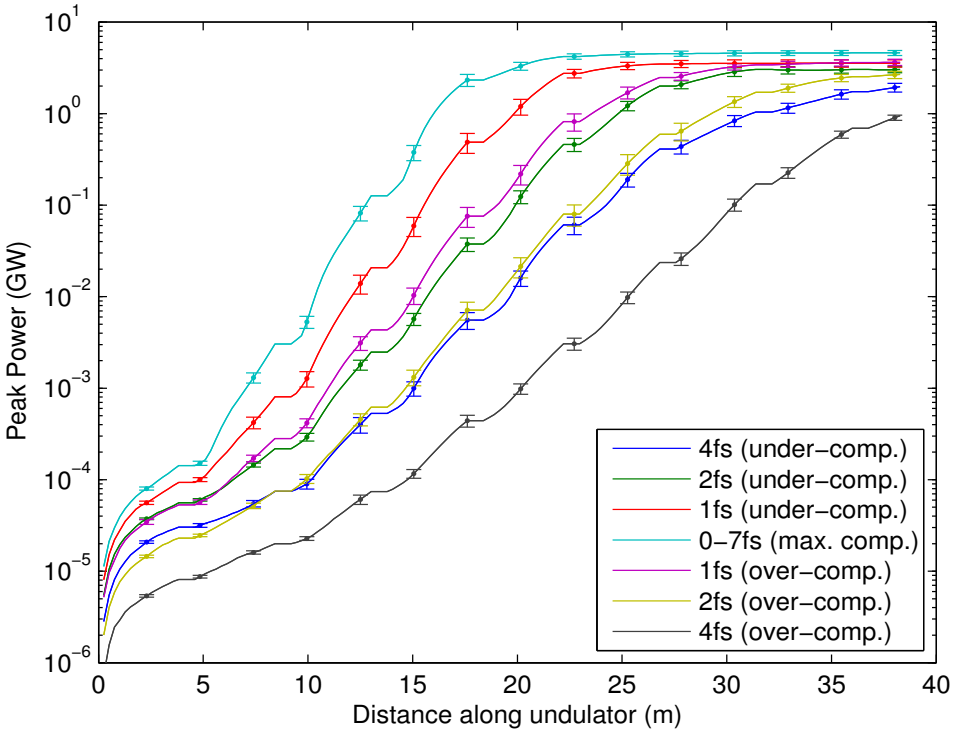

Figure 4.9: Mean power growth along the undulator axis as a function of electron bunch length (FWHM) over 40 samples. The error bars are calculated as the standard deviation divided by the square root of the number of samples. Shortest gain length and highest saturation power occurs for maximum bunch compression.

An examination of the resulting radiation pulses showed that only the bunch lengths between 1fs under-compressed and 3fs over-compressed showed single spike behaviour in the output, although there is no clear boundary separating the single spike regime. As the length of the electron bunch increased, the number of seeds giving rise to more than one radiation spike was also found to increase. The reason under-compressed electron bunches were less likely to produce single spike radiation than theory predicts was primarily due to their longitudinal profiles containing two current peaks, with each peak likely to generate its own FEL pulse. Clearly, the simple relation given by equation (4.1) is only sufficient to provide an initial estimate, and full numerical simulations are required to predict the FEL output accurately.

The average FEL peak power, total pulse energy, pulse duration and spectral line-width at saturation are shown in Fig. 4.10 as a function of the third bunch compressor strength. In this figure, data for bunches which produce single spike radiation for the majority of seeds have been highlighted in green, with data for maximum compression shown in red.

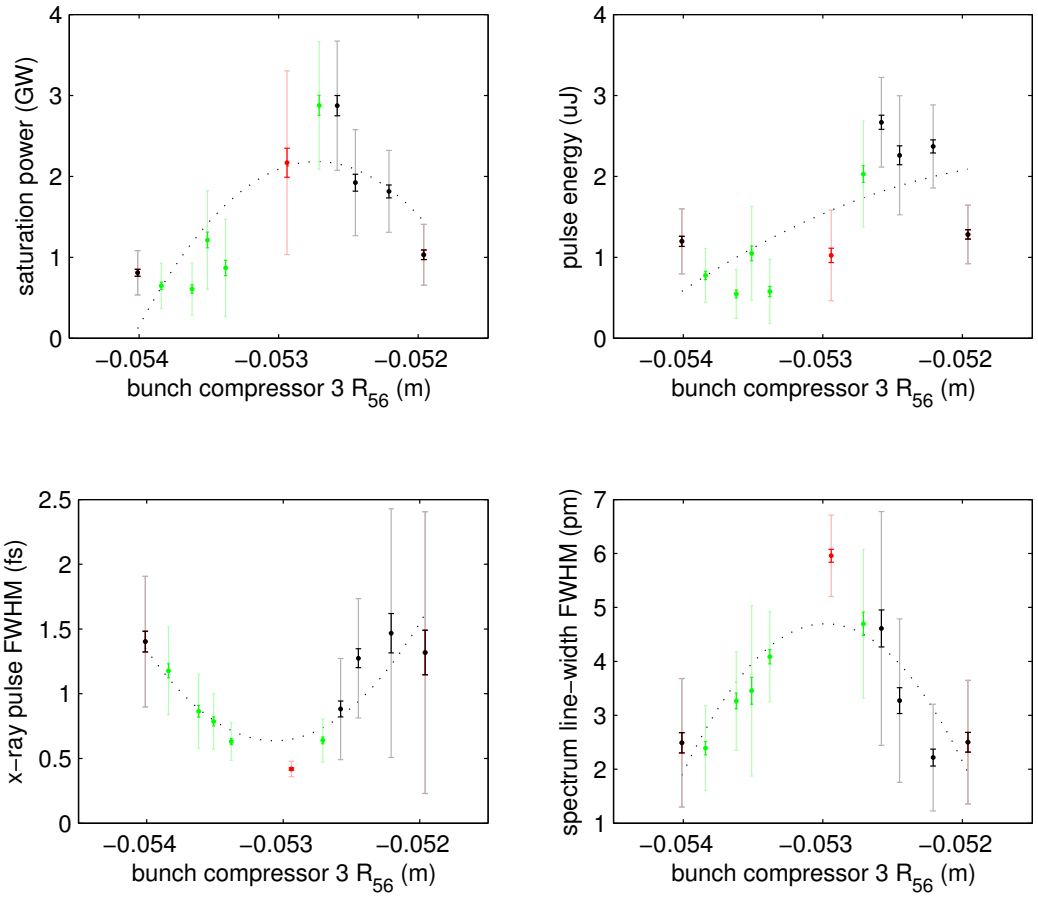

Figure 4.10: FEL pulse properties as a function of bunch compressor strength taken as averages over 40 shot-noise seeds. Shown are plots of peak power at saturation (top left), total pulse energy (top right), x-ray pulse duration (bottom left) and spectral line-width (bottom right). The results at maximum compression are plotted in red, and those which give single spike output for the majority of seeds have been highlighted in green. Bold error bars show the error on the mean value, and faint error bars show the standard deviation over 40 seeds.

From the bunch length scan it is apparent that operating just under maximum compression offers the best results in terms of peak power at saturation and total pulse energy. However, operating at over compression has a larger tolerance in terms of which bunch length will still produce single spike radiation. As expected, the shortest X-ray pulse occurs when the electron bunch is at maximum compression, at which point the line-width of the pulse is at a maximum. The time-bandwidth product remained approximately constant for all FEL pulses shown in Fig. 4.10, within the error bars of the simulations.

4.3.3 FEL Output at Maximum Bunch Compression

Under the assumption that the primary goal of the scheme is to optimise for minimum pulse duration rather than maximum pulse energy, the bunch length scans confirm that maximum compression of the electron bunch provides optimal performance of the scheme. Typical FEL pulse temporal profiles and spectra generated using this bunch are given in Fig. 4.11.

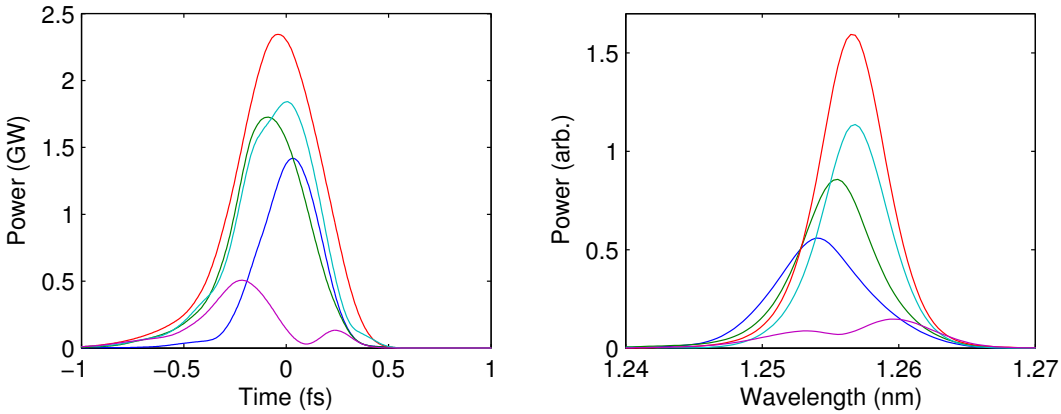

Figure 4.11: Selection of FEL temporal (left) and spectral (right) profiles at 17.7m along the undulator axis calculated using different shot-noise seeds.

The vast majority of radiation pulses show a clear single spike in both the temporal and spectral domains; however, occasional seeds produce a somewhat lower power with two spikes appearing. Further simulations were carried out using this electron bunch for 100 different shot-noise seeds. The mean power growth along the undulator is shown in Fig. 4.12, along with the variation in radiation beam size. If saturation is taken to occur at 22.2m, the x-ray temporal profiles are frequently found to be distorted or to have more than one radiation spike in the output. However, taking the radiation output one undulator module earlier at 17.7m, the pulse profiles are found to be much cleaner, consisting of a single radiation spike and to have a smaller pulse length (albeit with lower peak power). Note that 17.7m corresponds to 15.3m of active undulator length. Mean and standard deviation values of the x-ray pulse temporal and spectral profiles at 17.7m are shown in Fig. 4.13. The pulse properties averaged over the 100 shot-noise seeds are summarised later in Table 4.3.

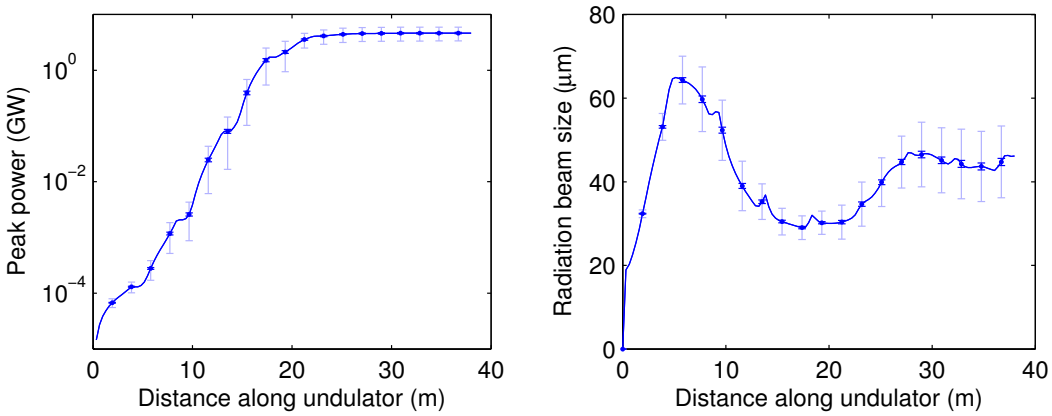

Figure 4.12: Mean power growth (top left) and radiation beam size (top right) along the undulator axis. Bold error bars show the error on the mean value, and faint error bars show the standard deviation over 100 seeds.

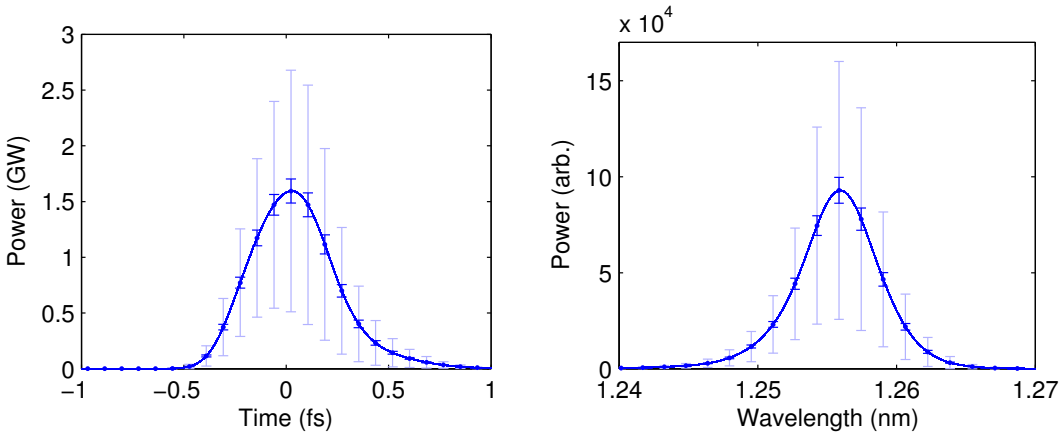

Figure 4.13: Mean FEL temporal (left) and spectral (right) power at 17.7m along the undulator axis. Bold error bars show the error on the mean value, and faint error bars show the standard deviation over 100 seeds.

The variation in gain length along the bunch length calculated from the electron bunch properties using the 1D analytic theory and adjusted using the Xie-scaling for the case of maximum bunch compression are shown in Fig. 4.14, along with the numerically calculated values extracted from the Genesis simulations. The numerically determined gain length is found to be ~1m at the peak of the current distributions and is lower for the head of the bunch than the tail. This is due to fact the radiation field slips forward over the bunch, meaning the front and centre experience exponential gain, whilst the tail remains in the lethargy region.

Fig. 4.15 shows the corresponding FEL cooperation lengths found by scaling each of the gain lengths using the relation $L_c = (\lambda_r / \lambda_u) L_G$. At the peak of the current distribution the 1D, Xie-scaled and numerically calculated values are 0.07fs, 0.09fs and 0.13fs respectively. The discrepancy between these three values again demonstrates that full, numerical simulations are required to account to predict the FEL output accurately.

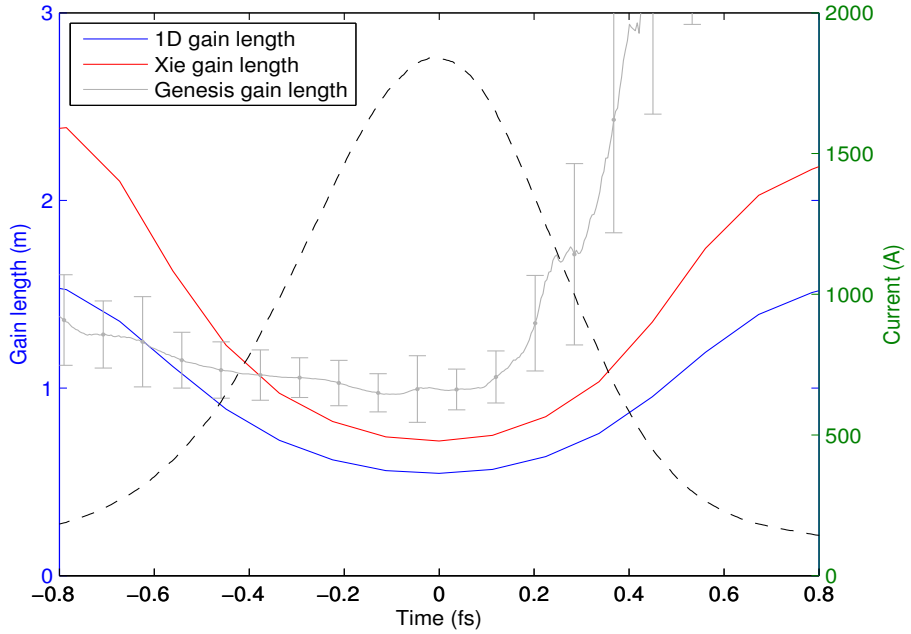

Figure 4.14: Comparison of gain lengths using the 1D theory, Xie parameterisation and the extracted numerical values. The current distribution is overlaid for reference. Error bars give the standard deviation divided by square root of number of samples.

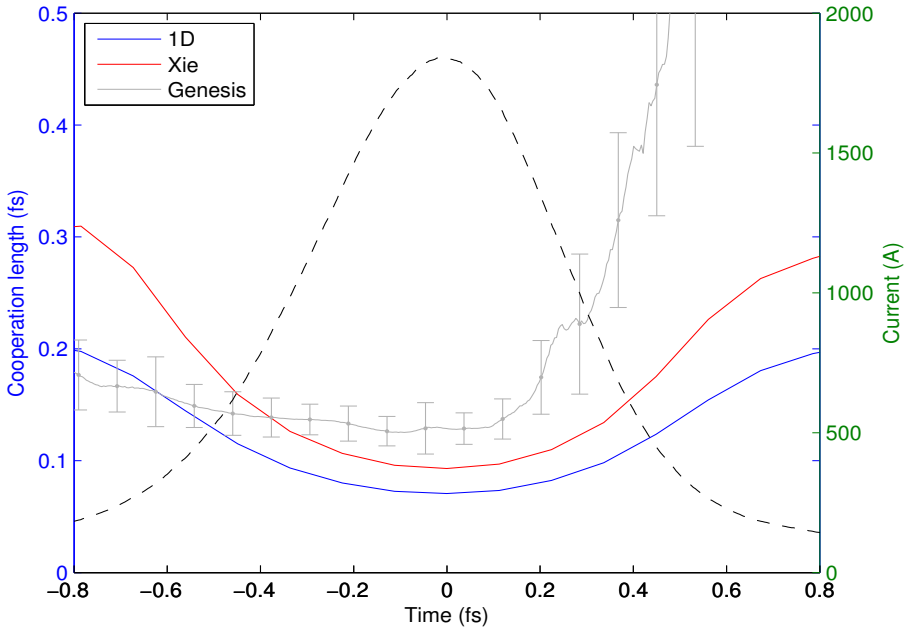

Figure 4.15: Comparison of cooperation lengths using the 1D theory, Xie parameterisation and the extracted numerical values. Error bars give the standard deviation divided by square root of number of samples.

4.3.4 Tolerance Studies

In the previous sections, the electron bunch distribution used was the result of a single, error-free start-to-end tracking simulation. A real accelerator suffers from shot-to-shot fluctuations, and any practical short pulse generation scheme must be able to cope with these changes. To investigate the sensitivity of single spike operation to these jitter sources, 100 start-to-end simulations using a combination of ASTRA, Elegant and Genesis were carried out after applying the jitter values detailed in Table 4.2. These jitter values were applied in Gaussian distributions truncated at 3 sigma, and were arrived at considering operational experience at FLASH (or modest improvement on these values) [165, 166]. When adding jitter values, the bunch compressors were assumed to be powered in series and each RF cavity in the cryomodules was modelled as being fed independently.

Source	Value
Solenoid field	0.01%
Gun RF phase	0.1°
Gun voltage	0.1%
Charge	1%
Gun laser spot offset	0.025mm
Linac cavity RF phase	0.01°
Linac cavity relative voltage	10^{-4}
3rd harmonic cavity RF phase	0.03°
3rd harmonic cavity relative voltage	3×10^{-4}
Bunch compressor power supply	10^{-5}

Table 4.2: Jitter sources included in the start-to-end simulations (r.m.s. values)

The mean power growth along the undulator and x-ray pulse profiles as a function of time are shown in Fig. 4.16, with a summary of pulse parameters given in Table 4.3. Somewhat surprisingly the majority of FEL pulse parameters are largely unaffected by the introduction of gun and linac jitter, with the most significant contribution to the shot-to-shot fluctuations still coming from the intrinsic SASE variability.

The one parameter which is affected is the r.m.s. arrival time of the x-ray pulse, which increases from 0.1fs to 12.7fs. This increase in arrival time jitter is overwhelmingly due to the arrival time jitter of the electron bunch. The root cause of this lies with small fluctuations in the mean energy of the electrons caused by linac RF fluctuations. When the off-energy electron bunches pass through a bunch compressor, the same effect that allows the tail of the electron bunch to catch up with the head also causes the whole bunch to arrive earlier or later than it would otherwise.

	Ideal 2pC Bunch	2pC with Jitter Sources
Mean peak power (GW)	1.71 ± 0.11	2.16 ± 0.16
Mean pulse length, FWHM (fs)	0.44 ± 0.01	0.46 ± 0.02
Mean line-width (pm)	6.3 ± 0.14	5.8 ± 0.1
Mean time-bandwidth product	0.53 ± 0.02	0.50 ± 0.01
Mean radiation beam size (μm)	29 ± 0.3	29 ± 0.3
Arrival time jitter (fs)	0.09	12.68

Table 4.3: Table of FEL pulse properties taken as averages over 100 shot-noise seeds

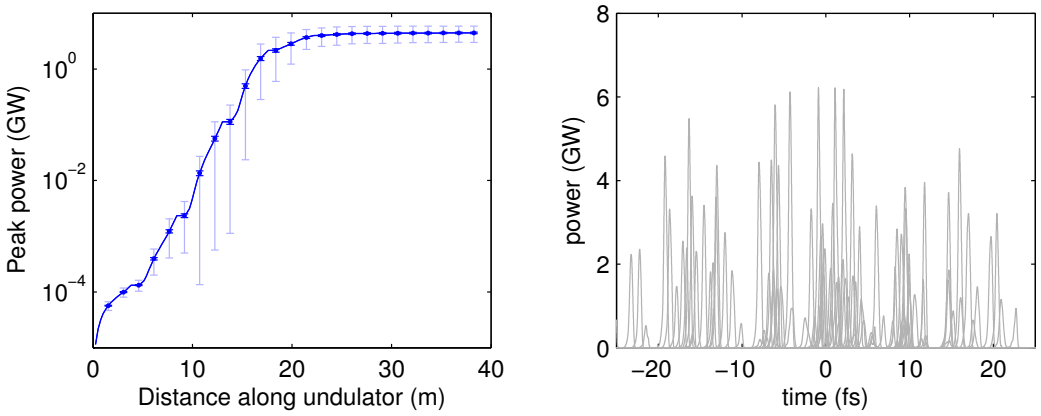

Figure 4.16: Mean power growth along the undulator (left) and power at saturation for 100 different random seeds. Bold error bars show the error on the mean value, and faint error bars show the standard deviation over 100 seeds. Calculations are performed including realistic gun and linac errors.

4.4 Theory of the Tapered Undulator Scheme

The tapered undulator scheme proposed by Saldin et al. makes use of a few-cycle laser pulse to produce an energy modulation in a short section of an electron bunch, and compensates for the resulting time-dependent energy chirp by tapering the gap of the main radiator undulator [75]. This restricts the exponential growth of the SASE process to the part of the bunch with the correct value of energy chirp to be matched to the taper. The rest of the bunch suffers from strong gain degradation, leading to an excellent contrast ratio between the short pulse radiation and the background from the remainder of the bunch.

The underlying physics of the scheme can be understood by considering an electron bunch with a constant gradient energy chirp. The radiation emitted by an electron

towards the back of the bunch will have a wavelength set by the undulator resonance condition for the given energy. As the bunch moves along the undulator, this radiation will gradually slip forwards to particles with a different energy. In order for the resonant wavelength to remain unchanged for the new energy of electrons, the a_u parameter for the undulator must be adjusted accordingly. By keeping the electrons in resonance with the radiation field, efficient bunching can be maintained and exponential growth will occur.

Aside from restricting the exponential growth to a small section of the bunch, tapering the undulator has two additional effects on the emitted radiation. Firstly, since the radiating part of the bunch has an energy gradient, the emitted radiation also has a frequency gradient which is maintained along the undulator. Secondly, in order for the resonant wavelength of each part of the radiation field to remain unchanged as it slips through the bunch, the overall FEL pulse must gradually shift towards red or blue as the bunch moves through the different gaps of undulators, with the direction of the shift depending upon the sign of the energy gradient and undulator taper.

4.4.1 Detailed Description

The main components of the scheme are shown in Fig. 4.17 below. These are a source of high-brightness, high energy electron bunches, a few-cycle carrier-envelope phase (CEP) stabilised laser, a short undulator to act as energy modulator and a long radiator undulator, in which the short FEL pulse develops due to the SASE process.

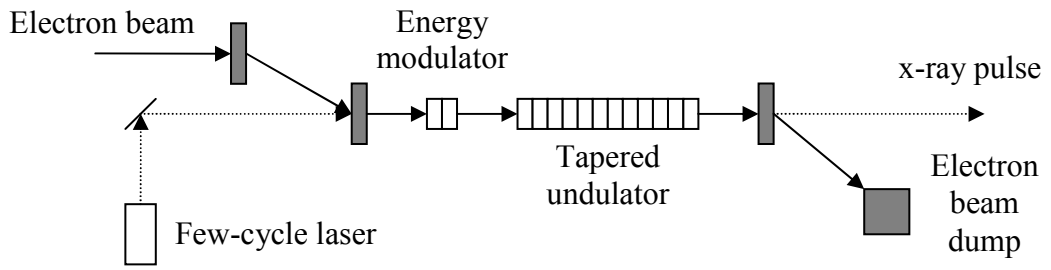

Figure 4.17: Main components of the tapered undulator scheme proposed by Saldin et al.

The slicing laser is focussed in the centre of the short (two period) modulator resonant at the external laser wavelength. The arrival of the laser pulse is timed to coincide with the peak of the electron bunch current distribution, the result of which is to modulate the energy of the electrons in the centre of the bunch. The (approximately linear) energy chirp at the centre of this modulation will be at a maximum when the phase of the laser is set to $\pi/2$ (sine mode), and depending upon the wavelength of the laser, can be of the order 1fs in duration. Additional linear energy chirps of diminishing gradient also appear at points separated by the laser period. An example of an energy-modulated electron bunch is shown in Fig. 4.18.

Once the energy of the electrons has been modulated by the external laser-undulator interaction, the electron beam is focussed along the main radiator undulator. A SASE FEL pulse will develop in the portion of the bunch with the correct gradient of energy chirp matched to the undulator taper. Where the energy gradient is wrong, the radiation field will quickly move out of resonance with the electrons and the gain is suppressed.

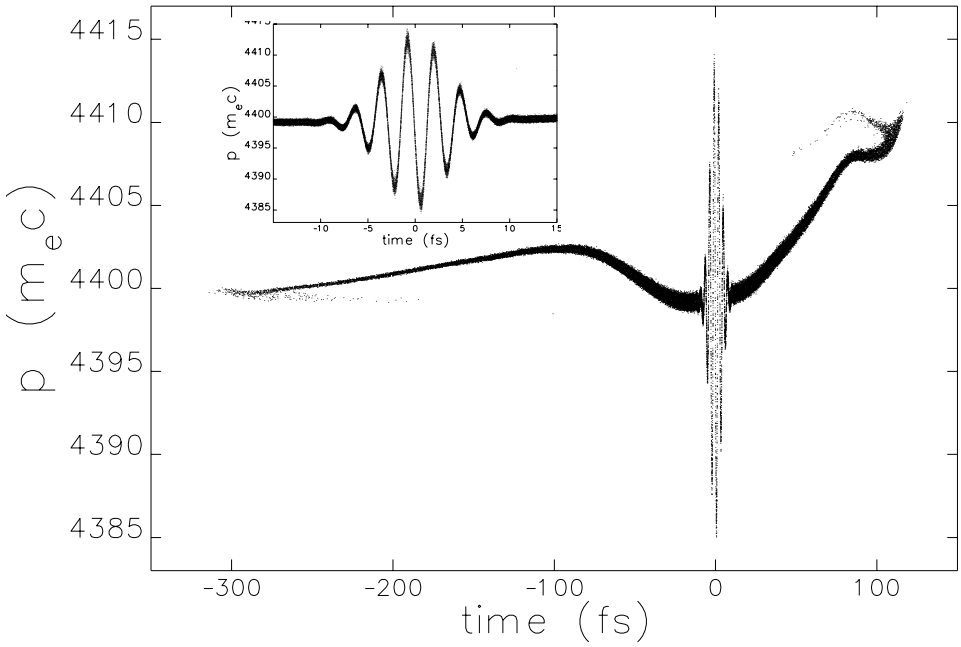

Figure 4.18: Energy modulation acquired by the NLS 'standard bunch' for a 0.4mJ, 5fs FWHM, 800nm laser pulse (see Section 4.1.2).

According to the work detailed in [75], the required undulator taper to compensate any given energy chirp can be calculated from the formula

$$\frac{1}{a_u}\frac{da_u}{dz} = -\frac{\lambda_r}{\lambda_u}\frac{(1+{a_u}^2)}{{a_u}^2}\frac{1}{c\gamma_0}\frac{d\gamma}{dt} \tag{4.3}$$

where z is the distance through the undulator, a_u is the r.m.s. strength parameter of the undulator, λ_r and λ_u are the resonant and undulator wavelengths and γ_0 is the relativistic parameter for the reference particle. Whilst this equation gives an 'exact' value for the undulator taper, it was noted in [75] that a mild, net positive energy chirp is actually beneficial to the SASE process, and that the performance of the scheme can be improved by introducing a slight mismatch between the energy chirp applied by the modulating laser and the taper in the undulator.

In analogy to single spike operation, for the FEL pulse to consist of a single SASE radiation spike and to reach saturation, the portion of the bunch with linear energy chirp must have a length matched to the cooperation length of the FEL. i.e.

$$L_{linear\ chirp} \cong 2\pi L_C \tag{4.4}$$

For the electron bunch parameters given in Section 4.2, $\rho_P = 1\times10^{-3}$ to 2×10^{-3}, and so the optimal linear energy chirp duration is again estimated to be ~0.6fs to ~1.2fs.

4.4.2 Energy Modulation by External Laser

The energy modulation given to the electrons by the external laser when passing through the short undulator can be calculated analytically using [20, 76, 167]

$$\frac{d\gamma}{d\hat{z}} = \frac{a_u}{\gamma_0}\sqrt{\frac{P_L}{P_0}}kqw_0[JJ]f(\hat{z},s) \tag{4.5}$$

where

$$f(\hat{z},s) = \frac{1}{1+(q\hat{z})^2}\cos(2\pi v\hat{z} + ks - \tan^{-1}(q\hat{z}))\exp\left(-\left(\frac{\hat{z}}{2\hat{\sigma_\tau}} - \frac{s}{2c\sigma_\tau}\right)^2\right) \tag{4.6}$$

In equation (4.5), P_L is the laser peak power, $P_0 = I_A mc^2/e$, I_A is the Alfvèn current, k is the laser wavenumber, $q = L_u/z_R$, z_R is the laser Rayleigh length, L_u is the length of the undulator, w_0 is the laser waist size (assumed to be at the centre of the undulator), the scaled position in the undulator is $\hat{z} = ct/L_u$, s is the electron position within the bunch, σ_τ is the r.m.s. duration of the laser intensity and $\hat{\sigma_\tau} = kc\sigma_\tau/(2\pi N)$ with N the number of undulator periods. The total energy modulation acquired by the electrons at position s within the bunch is therefore

$$\Delta\gamma(s) = \int_{-0.5}^{0.5} \frac{d\gamma}{d\hat{z}} d\hat{z} = \frac{a_u}{\gamma_0} \sqrt{\frac{P_L}{P_0}} kqw_0[JJ] \int_{-0.5}^{0.5} f(\hat{z}, s) d\hat{z} \tag{4.7}$$

As an alternative to an analytical calculation, the energy modulation can also be calculated numerically by directly integrating the Lorentz equation after substituting the required electric field from the laser and the local magnetic field from the undulator. This has been implemented in Elegant, with the two methods providing a valuable cross-check.

4.5 Numerical Study of the Tapered Undulator Scheme

As with the studies of the single spike scheme, a proper assessment of the tapered undulator scheme can only be made through numerical start-to-end simulations. However, for this scheme it was not necessary to re-optimise the injector and linac working point, as the required electron bunch parameters for the tapered undulator scheme are the same as for standard, seeded operation of the NLS; a key advantage of this technique. The NLS 'standard bunch' described in Section 4.1.2 has a peak current of 1120A (0.2nC total charge), 2.25GeV energy, 0.29nm slice emittance and 160keV energy spread. There is a ~50fs long region in the bunch with constant slice parameters, large enough to accommodate the expected jitter between slicing laser and electron bunch arrival times. Plots of the main bunch parameters at the entrance to the modulator were given in Fig. 4.3.

The energy modulator used in this study consists of a two-period planar undulator of λ_u = 140mm set to be resonant at the slicing laser wavelength. The main radiator

consists of APPLE-II helical undulator modules with λ_u = 32.2mm interleaved in a FODO focussing lattice, set to be resonant at 1.24nm in the first module. The start-to-end simulations were carried out using the codes ASTRA, Elegant and Genesis, with the effect of the energy modulator calculated using Elegant and the FEL interaction simulated with Genesis.

4.5.1 Performance Studies

Initial studies of the tapered undulator scheme concentrated on determining how each of the laser parameters affects the final properties of the FEL pulse. The parameters which were varied are the laser wavelength, laser pulse energy, pulse duration and undulator taper. The results of the parameter investigation are summarised in Figs. 20-23.

The general form of the FEL pulse produced by the scheme was found to be independent of the laser parameters. The pulse consists of a dominant, central radiation peak, with two or more satellite peaks separated from the central peak by the laser period. The satellite peaks are progressively reduced in amplitude due to the smaller gradient energy chirp and hence poorer match to the undulator taper. This general structure can be altered only within certain bounds by varying the modulating laser and undulator taper parameters. An example of a typical FEL pulse generated with this scheme is shown in Fig. 4.19, and was created using a 1600nm, 10fs FWHM, 0.4mJ laser pulse.

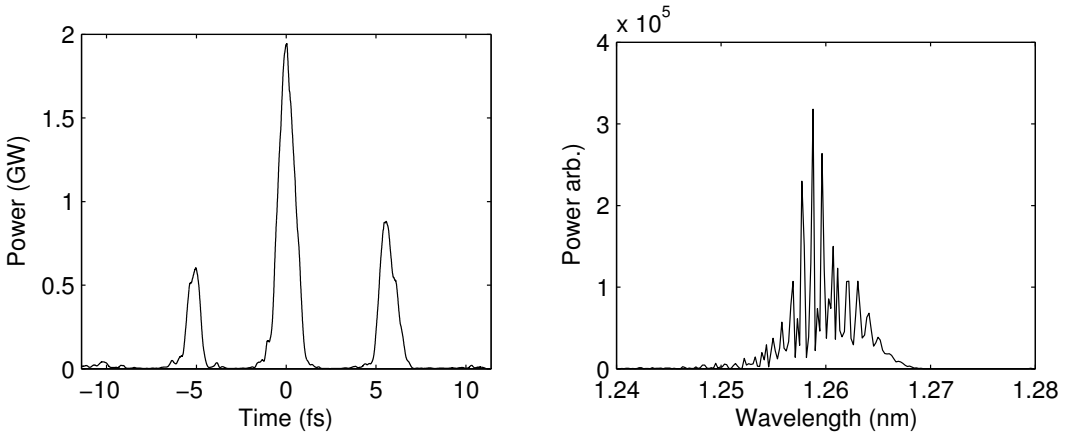

Figure 4.19: Typical temporal (left) and spectral (right) profiles for an FEL pulse generated with a tapered undulator and a 1600nm, 10fs FWHM, 0.4mJ laser pulse.

The effect of varying the laser wavelength from 800nm to 1600nm is shown in Fig. 4.20, and it was found to have a strong influence on the FEL output. Increasing the wavelength of the modulating laser leads to a higher power at saturation for the FEL pulse, a longer pulse duration, a narrower spectral line-width and a poorer contrast ratio between the main and the satellite radiation peaks. From equation (4.4) it was expected that, for the scheme to work efficiently, the length of the linear energy chirp should be well matched to the cooperation length of the FEL (i.e. ~1fs for the electron bunch investigated here). If it is too long then the FEL pulse will also be long, defeating the main goal of the scheme and potentially allowing more than one SASE radiation spike to develop. If it is too short then the FEL pulse saturates at a lower value than would otherwise be the case, and the pulse does not develop into a clean single spike. Of the laser wavelengths investigated here, only the 1600nm laser was able to provide a long enough linear energy chirp in the electron bunch, and it is this that resulted in the increasing peak power at saturation with laser wavelength.

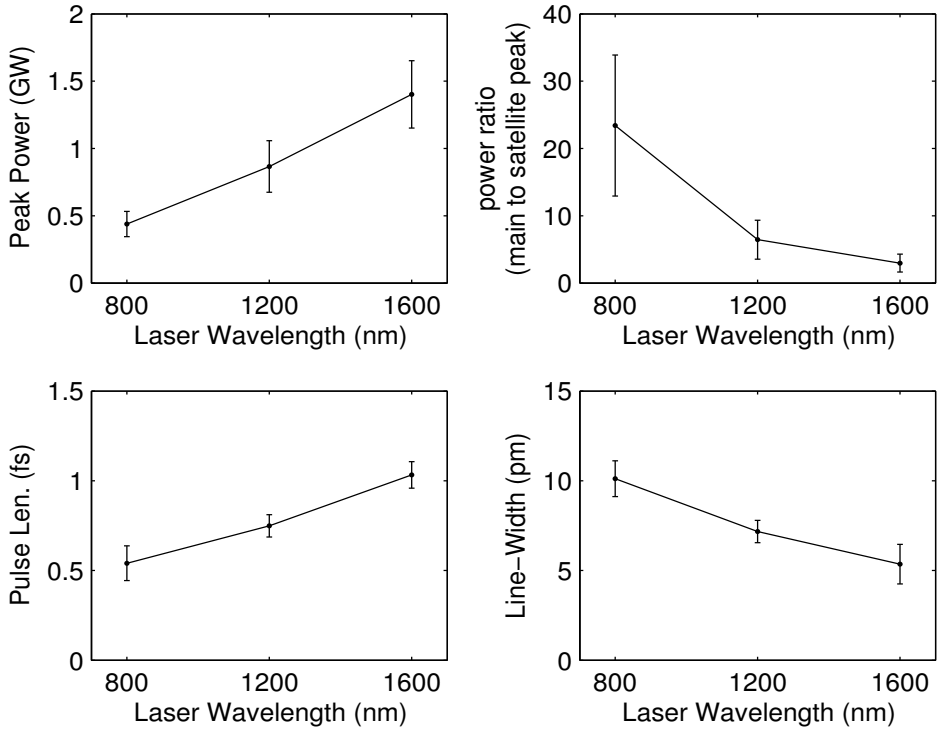

Figure 4.20: FEL pulse properties as a function of modulating laser wavelength. Error bars give the standard deviation divided by square root of number of samples.

The effect of varying the modulating laser pulse energy from 0.1mJ to 0.8mJ whist keeping the number of laser cycles fixed at 1.9 is shown in Fig. 4.21. Increasing the energy of the laser leads to a larger energy chirp developing in the bunch which in turn requires a stronger undulator taper to compensate. This has the effect of improving the contrast ratio between the main peak, satellite peaks and background radiation. The FEL pulse width is also marginally shortened and the line-width broadened. However, this comes at the expense of a decrease in saturation power. The best compromise between the different effects was judged to occur for a laser pulse energy of 0.4mJ.

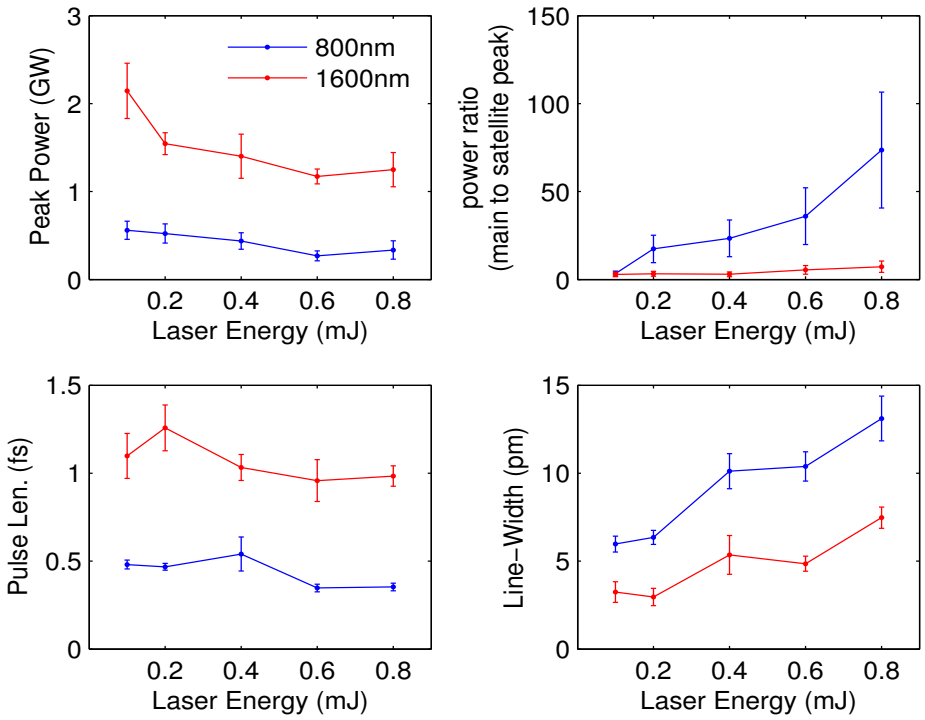

Figure 4.21: FEL pulse properties as a function of modulating laser pulse energy. Error bars give the standard deviation divided by square root of number of samples.

The effect of varying the number of optical cycles in the modulating laser pulse is shown in Fig. 4.22. The numbers of cycles investigated correspond to 5fs to 9fs long pulses for the 800nm laser and 10fs to 15fs long pulses for the 1600nm laser. The pulse energy was kept constant at 0.4mJ. The main result was found to be in changing the relative amplitude of the satellite peaks in the FEL pulse to the central one; the greater the number of cycles in the laser, the greater the number of sections in the electron bunch with energy chirp matched to the undulator taper. In the limit of a continuous modulating laser, a train of equi-spaced radiation pulses would be produced. The FEL pulse duration, line-width and peak power at saturation are only weakly affected by the number of laser cycles, with the variation mainly due to the stronger taper required for shorter laser pulses at fixed pulse energy.

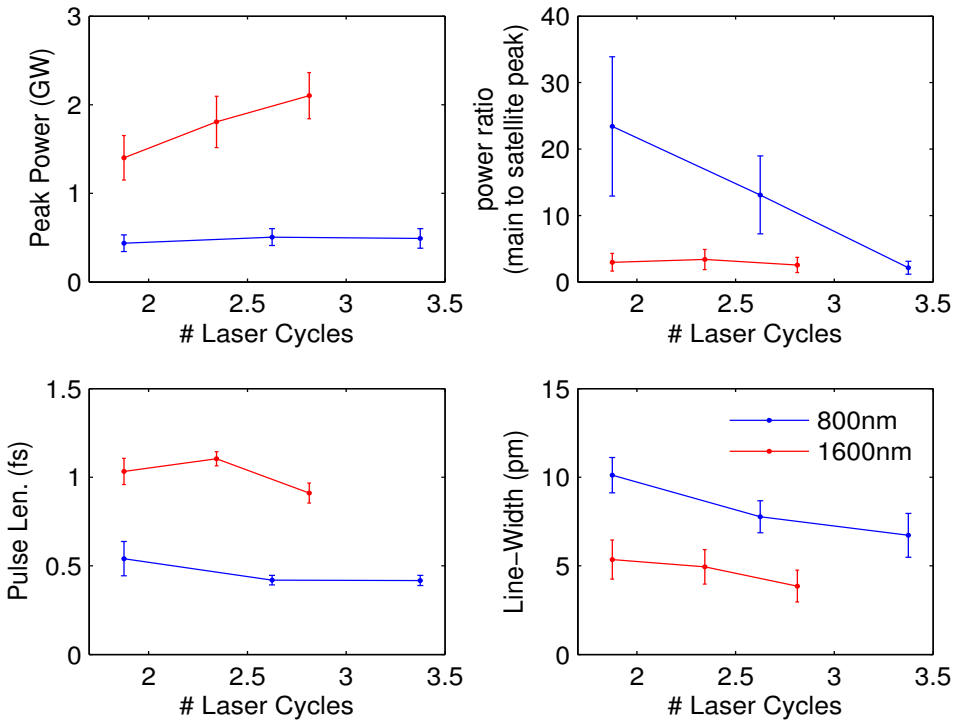

Figure 4.22: FEL pulse properties as a function of number of laser cycles. Error bars give the standard deviation divided by square root of number of samples.

The final parameter in the scheme that was investigated is the undulator taper, the results of which are shown in Fig. 4.23. In these plots, a taper depth of 100% refers to the value of undulator taper given by equation (4.3). For this part of the investigation, the laser pulse was set to contain 1.9 cycles and the energy was kept fixed at 0.4mJ per pulse. As expected, reducing the undulator taper was found to result in higher power at saturation. However, by having a smaller undulator taper, the gain for the rest of the bunch increases and so the contrast ratio is decreased. As with the number of laser cycles, the FEL pulse length and line-width are only weakly affected by the undulator taper mismatch. From these results, a taper of 90% of the value given by equation (4.3) appears to be optimal.

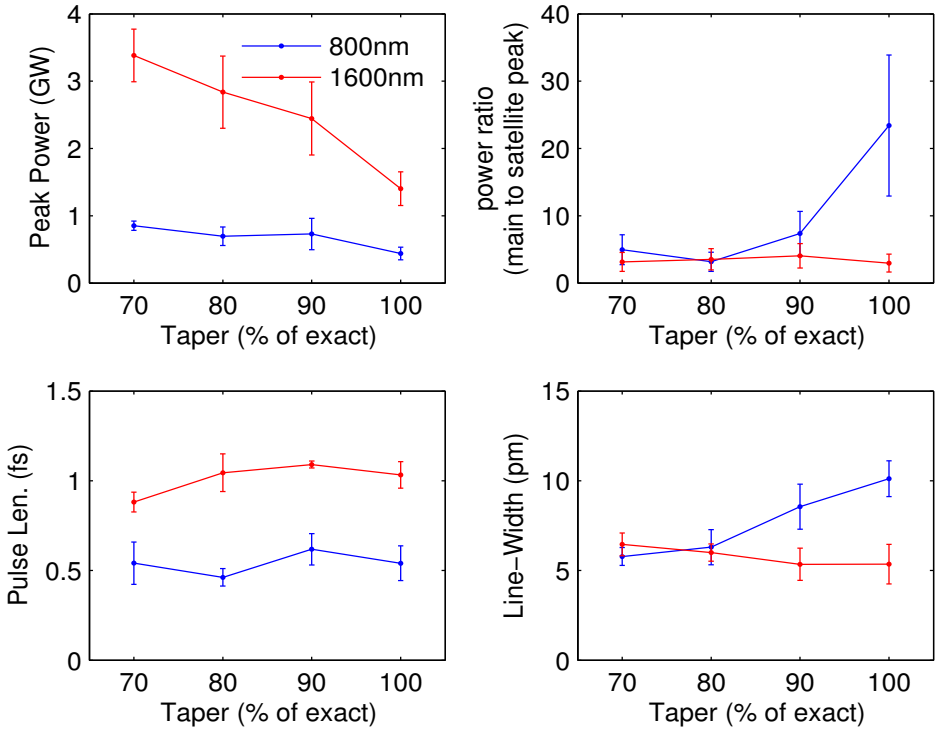

Figure 4.23: FEL pulse properties as a function of undulator taper. Error bars give the standard deviation divided by square root of number of samples.

4.5.2 Performance of Optimised Set-up

The results of the parameter study identified two possible operating scenarios. The first solution is based around using a 1600nm, 10fs long laser pulse with 0.4mJ pulse energy. The second one uses an 800nm, 5fs laser pulse, again with a pulse energy of 0.4mJ. This second solution has the advantage that the laser is technically feasible with current technology [168-170], and produces shorter FEL pulses on average. The 10fs duration for the 1600nm laser option was selected in order to keep the relative bandwidth between the two lasers constant, and is assumed to be the minimum value that is practically achievable. In both cases, the optimum taper was judged to be 90% of the value found using equation (4.3).

Shown in Fig. 4.24 is a comparison between the FEL outputs for the two options. Calculations were carried out based on a single electron bunch tracked from the gun to the main undulator and averaging the FEL output over 100 different shot-noise seeds. Pulse properties are summarised in Table 4.4. On average, saturation is found to occur after 34.4m which corresponds to 25.1m of active undulator length.

From the values given in Table 4.4, the benefits of using a longer modulating laser wavelength are clear; there is a four-fold increase in saturation power, which comes at the expense of an increase in FEL pulse duration. This increase in power is due to the 1600nm laser having a better match to the FEL cooperation length than the 800nm laser. The temporal profile and spectrum at saturation for a single shot-noise seed using the 800nm option is shown in Fig. 4.25. The temporal profile shows that in this case, rather than consisting of a single spike, the central radiation peak is in fact a series of sub-spikes. Each of these sub-spikes is predominantly the emission from the chirped region of the electron pulse within a single undulator module and is separated in time from the previous one by the slippage that occurs between each module. This behaviour is again a direct result of having too short a region of linear energy chirp compared to the cooperation length of the FEL, and is not observed when using a 1600nm modulating laser (where a better match is achieved, see Fig. 4.19). The radiation spectrum for both the 1600nm and 800nm cases show some fringing due to interference between the radiation emitted by the main peak and by the satellite peaks, with the separation of the fringes given by

$$\Delta\lambda = \frac{\lambda_r}{\Delta t}\frac{1}{c} \tag{4.8}$$

where Δt is the time separation between central and satellite radiation peaks. To remove these fringes from the spectrum, the modulating laser would need to consist of a true single cycle, or the amplitude of the satellite FEL radiation peaks would need to be negligibly small.

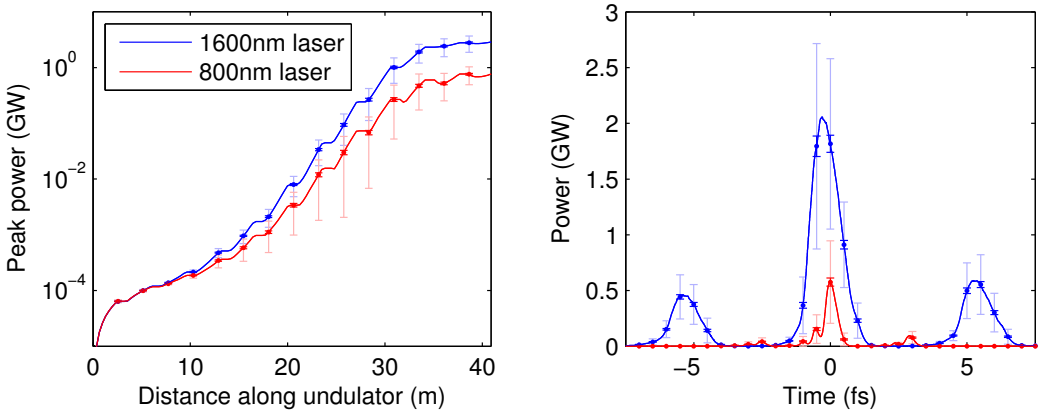

Figure 4.24: Peak power growth along the undulator (left) and power at saturation (right) for the 1600nm and 800nm modulating laser wavelength options. Bold error bars show the error on the mean value, and faint error bars show the standard deviation over 100 seeds.

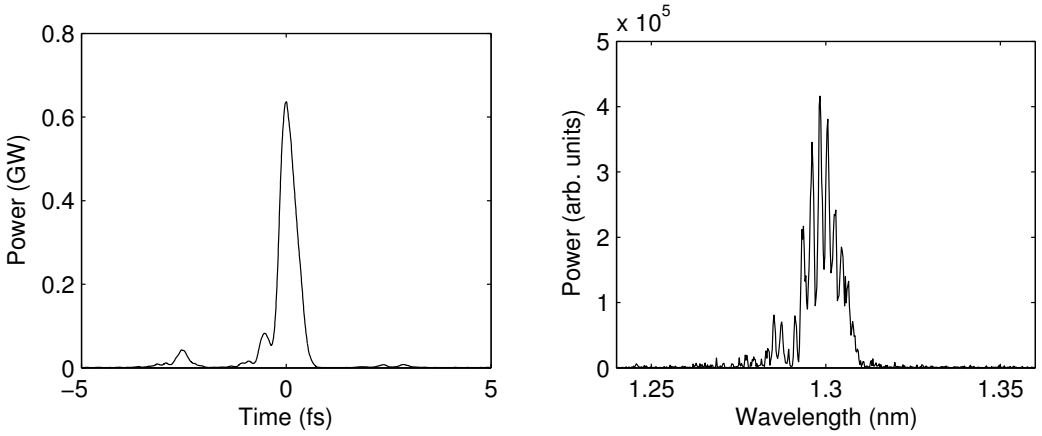

Figure 4.25: Typical temporal (left) and spectral (right) profiles for an FEL pulse generated with an 800nm, 5fs FWHM, 0.4mJ laser pulse.

4.5.3 Tolerance Studies

As with the single spike mode of operation, the final radiation pulse properties are expected to suffer from shot-to-shot fluctuations in electron gun, linac and modulating laser parameters. This has been studied using 100 different start-to-end simulations for the 800nm modulating laser option, in each case applying Gaussian-distributed realistic jitter values to each component. The jitter distributions used are the same as those listed in Table 4.2 with the addition of 0.2rad phase jitter for the modulating laser, and the resulting FEL pulse properties are summarised in Table 4.4.

The results of the jitter studies show that, whilst there is a small degradation in the majority of FEL pulse parameters, the power at saturation is largely unaffected by the introduction of realistic jitter sources and it is the intrinsic variability of the SASE process due to shot-noise in the electron distribution that still dominates.

4.5.4 Manipulation of the FEL Pulse

The properties of the FEL pulse produced by the scheme can be examined in more depth by taking a Wigner transform of the radiation field [92]. A Wigner transform of a signal gives a projection of the signal's energy distribution on the time-frequency plane, and is defined as

$$W(\omega,t)=\int_{-\infty}^{\infty}E\left(t-\frac{\tau}{2}\right)E^{*}\left(t+\frac{\tau}{2}\right)e^{i\omega\tau}d\tau \qquad (4.9)$$

The Wigner transform can be considered as the Fourier transform of the auto-correlation function of the input signal. The temporal and spectral profiles for the

example radiation pulse used for this part of the investigation is shown in Fig. 4.25, and were calculated by integrating the radiation field across a 1.4mm×1.4mm aperture at the observation point (34.4m along the undulator axis). This pulse was generated using an 800nm laser, for which the central, dominant radiation peak shows the sub-peaks from emission in each undulator module.

The Wigner transform of the FEL pulse is shown in Fig. 4.26. The first point to note is that, as mentioned in Section 4.4, the central wavelength has shifted from 1.24nm after the first undulator module to 1.30nm at saturation due to the taper in undulator gap. This shift in central wavelength after each undulator module suggests that the unwanted radiation emitted upstream of the final undulator can be filtered out with a relatively wide acceptance monochromator, restoring the central radiation peak to a clean single spike rather than a series of sub-spikes.

In addition to the shift in central wavelength there is a frequency chirp of ~0.01nm/fs across the radiation pulse. As noted in [92], this can be used to compress further the radiation pulse using a grating compressor [69]. The Wigner transform for the radiation pulse after filtering, compression and a combination of both processes is shown in Fig. 4.26 along with the unmodified pulse. The filter used for this was set to a pass bandwidth of 1×10^{-2}.

The filtering and compression of the radiation pulse can be carried out after the nominal saturation point thanks to the wavelength shift after each undulator, allowing a greater fraction of pulses to reach saturation. This is demonstrated in Fig. 4.27, in which the average over 100 unmodified radiation pulse at 37.7m is compared to that of 100 pulses which have been filtered and compressed. As a final point to note, although the cooperation length places a lower limit on the FEL pulse duration under

normal circumstances, filtering and compressing the radiation has effectively side-stepped this constraint and led to a reduction in pulse length to 0.42fs compared to the ~1fs predicted from the cooperation length; a significant improvement in the potential performance of the scheme. The main properties of the 100 filtered and compressed pulses are summarised in Table 4.4.

	1600nm Laser	800nm Laser	800nm Laser Filtering and Compression	800nm Laser Jitter Sources
Distance in undulator (m)	34.4	34.4	37.7	34.4
Peak Power (GW)	2.31 ± 0.08	0.59 ± 0.04	0.76 ± 0.05	0.66 ± 0.04
Energy in main peak (μJ)	2.36 ± 0.10	0.35 ± 0.03	0.37 ± 0.02	0.42 ± 0.03
Pulse length, FWHM (fs)	1.07 ± 0.02	0.45 ± 0.01	0.49 ± 0.01	0.52 ± 0.02
Line-width (pm)	4.65 ± 0.17	8.8 ± 0.2	9.0 ± 0.2	8.9 ± 0.3
Time-bandwidth product	0.96 ± 0.04	0.78 ± 0.03	0.85 ± 0.03	0.91 ± 0.05
Radiation beam size (μm)	38 ± 0.3	38 ± 0.5	35 ± 0.3	44 ± 1.7
Arrival time jitter (fs)	0.23	0.06	0.13	0.11
Av. Background power (MW)	7.5 ± 0.3	0.7 ± 0.01	0.1 ± 0.07	1.9 ± 0.07

Table 4.4: Summary of FEL pulse properties taken as averages over 100 seeds

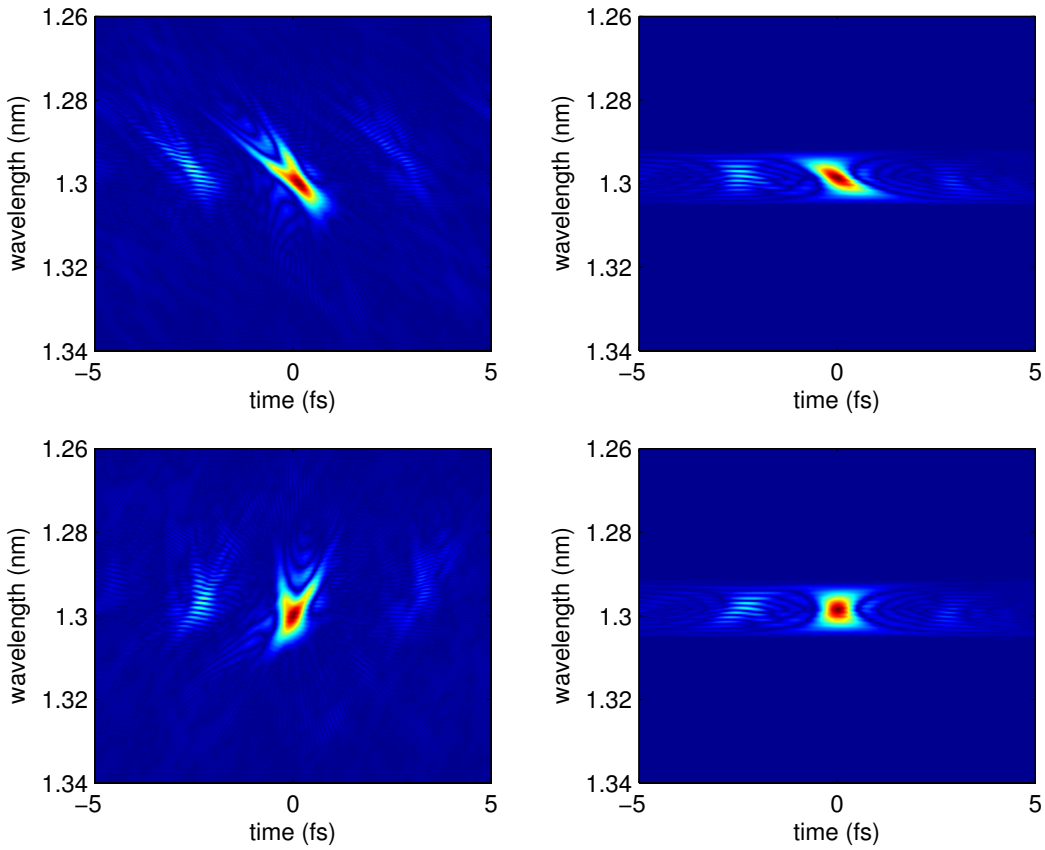

Figure 4.26: Wigner transform of the radiation field at 34.4m. The images show the unmodified (top left), filtered (top right), compressed (bottom left) and filtered and compressed pulses (bottom right).

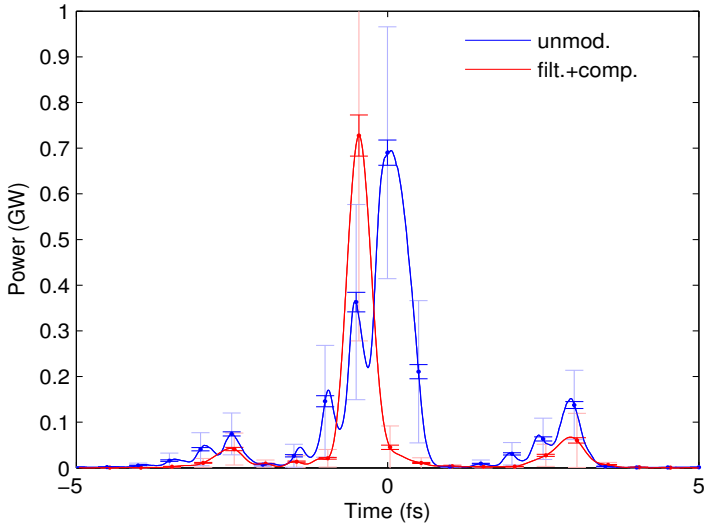

Figure 4.27: Comparison of unmodified to filtered and compressed radiation pulses at 37.7m along the undulator axis. Bold error bars show the error on the mean value, and faint error bars show the standard deviation over 100 seeds.

Chapter 5

Conclusions

New and brighter sources of short x-ray pulses will be required to facilitate areas of science that require imaging of dynamical processes (such as energy transfer in crystalline solids, chemical bond making and breaking, electron-electron scattering in solids, etc.). In order to meet the needs of these scientific communities, large scale short-pulse user facilities must be provided. The source of radiation must be reliable, practical to operate and generate light with properties that are required for current research. In recent years many schemes have been proposed for generating such pulses from existing or future synchrotron radiation sources. Pulse durations below 150fs FWHM have already been demonstrated in storage ring based light sources using femto-slicing, and more recently ~10fs FWHM on a linac-based light source using a low-charge electron bunch.

The work contained in this thesis aimed to investigate different methods of generating short pulses from synchrotron radiation sources, and identify which schemes are most suitable for use in a large-scale user facility. A review was made of the different schemes that have been proposed for both third and fourth generation synchrotron light sources, and the strengths and weaknesses of each scheme have been discussed. For third generation light sources, the scheme selected for in-depth investigation was

low-alpha operation, as this scheme provides moderately short pulses of radiation with a higher brightness, higher repetition rate and improved transverse stability than can be produced using some of the other schemes. In addition, low alpha operation does not require any additional hardware to be implemented and in principle can be applied to any existing light source. For fourth generation light sources, two schemes were chosen for further study, namely single spike operation and the tapered undulator scheme. Single spike operation has the potential to generate background-free, ultra short pulses of extremely high peak brightness thanks to the excellent electron beam properties that are possible with low-charge operation. The tapered undulator scheme can provide similarly short pulses with an improved contrast ratio over the background signal compared to other slicing schemes, and has the advantage that the pulses are synchronised to an external trigger.

5.1 Low Alpha Operation of the Diamond Light Source

Investigations into low alpha operation of the Diamond Light Source have highlighted the importance of higher order terms in alpha in the longitudinal beam dynamics. It is well known that as α_1 is reduced, α_2 must also be minimised in order to ensure that adequate momentum aperture is maintained. Studies at Diamond [39] and MLS [101] have shown that once α_2 has been minimised, α_3 quickly becomes dominant and must be taken into consideration. Depending upon the sign of α_1, α_3 can have either a beneficial or detrimental effect on the phase and momentum acceptance of the storage ring, and expressions for the momentum acceptance in each case have been presented.

From a practical point of view, α_1 is adjusted by varying the dispersion in the bending magnets. If α_1 is to be minimised, then the integrated dispersion in the bending magnets should be close to zero. The way in which this is achieved can have a big influence on the storage ring emittance (and hence photon beam brightness), and two different solutions were developed for the Diamond storage ring (one high emittance and one low emittance). Adjustment of the dispersion also has a big influence on the sextupole optimisation. For example, in the low emittance solution the dispersion at the central focussing sextupoles is much reduced, meaning the sextupole strengths must be greatly increased in order to correct both the horizontal chromaticity and α_2. This increases the nonlinearity of particle motion and reduces the size of the dynamic aperture. Similarly, dispersion in the insertion device straight sections is negative for the high emittance lattice, meaning the polarity of the sextupoles must be reversed in order for them to remain effective.

Extensive simulations were carried out on both lattices in order to determine the expected machine performance. During this it was identified that, for both lattices, the injection efficiency is likely to be limited by synchrotron motion of the electron bunch at injection. This process converts the long electron bunch length from the booster into a large energy spread, taking the injected electrons at the head and the tail of the bunch outside the momentum acceptance of the storage ring. The main limitation to the lifetime is expected to be from the off-momentum dynamic aperture provided by the sextupoles rather than the size of the RF bucket momentum acceptance (which is controlled by alpha).

Once the numerical simulations were complete, both lattices were tested on the Diamond storage ring with numerous measurements taken in order to characterise

their performance. Good agreement was found between the expected and measured emittance, and for the low emittance lattice the measured variation of betatron and synchrotron tunes with RF frequency is close to that predicted by simulation. Whilst the measured dynamic aperture for the low emittance lattice is in remarkable agreement with the one calculated from the model, frequency map analysis has highlighted that significant differences exist between the predicted and measured tune-shifts with amplitude.

In the limit of zero current, good agreement is found between the bunch length measured by the streak camera and that derived from the synchrotron frequency. As expected, a reduction in bunch length is observed with decreasing α_1 and with increasing RF cavity voltage. However, due to collective effects, the measured bunch length quickly deviates from its initial value as the current is increased. If α_1 is positive, the bunch length increases rapidly with current until the bunch becomes unstable. If α_1 is negative, an initial reduction in bunch length is observed before the bunch length begins to grow again (albeit at a lower rate than for positive α_1) before again becoming unstable. Observations of CSR at mm wavelengths have confirmed the short bunch lengths achieved in low alpha operation, and it was possible to understand the variation in power emitted as a function of current, voltage and α_1 purely in terms of the longitudinal form factor of the electron bunch.

Aside from the bunch current, the main limitation to the minimisation of the pulse duration is the increase in transverse beam motion as α_1 is reduced. Careful measurements of the horizontal displacement power spectral density have demonstrated that the increase in transverse motion is related to fluctuations in the electron path length altering the mean energy of the electron beam. These changes are

driven by vibrations of the quadrupole magnets and are inversely proportional to α_1. The optimal value for α_1 is therefore a compromise between minimising the bunch length and limiting the transverse beam motion. Similarly, the optimal bunch charge is the one that maximises the photon beam brightness for minimal pulse duration. Overall, for stable machine conditions, the photon pulse duration is found to lie in the range 1-5ps and the bunch current lies between 10-50μA. These values represent a factor 10 reduction in pulse duration and a factor of 100 reduction in current compared to standard machine operation.

There are many areas in which this work could be developed. In terms of a further reduction in pulse duration, the possibility of combining low alpha operation with one of the other schemes could be investigated. For example, if a higher harmonic cavity could be installed, this could give a substantial reduction in pulse length at a fixed bunch current. Alternatively, a fixed bunch length could be maintained with increased bunch charge and therefore increased photon beam brightness. Similarly, combining low alpha operation with RF cavity modulation could give a transient reduction in pulse length, although careful synchronisation between RF cavity modulation and experiment would be required. The possibility of tailoring the beta functions in a single straight could be investigated in order to reduce the sensitivity of a given beamline to transverse beam motion. Further work can be carried out in modelling and understanding the influence of collective effects in low alpha. For example, it would be of great benefit if the observed bunch lengthening with current could be reproduced for different values of α_1 and RF cavity voltage. This could potentially also lead to an improved understanding of the onset of instabilities in low alpha and how they relate to CSR emission in stable and bursting modes.

5.2 Single Spike Operation of the New Light Source

Studies of the single spike mode of operation began by considering what range of electron bunch lengths would be required in order to operate in this regime based upon the 1D analytic theory. This simple estimate predicted a bunch length in the range of 0.6fs to 1.2fs would be needed. In order to achieve this level of bunch compression, the model was adjusted to operate with very low bunch charge in order to avoid the severe degradation in beam quality from collective effects that would otherwise occur. Simulations of FEL pulse properties as a function of bunch length demonstrated that electron bunches between 1fs FWHM under-compressed to 3fs FWHM over-compressed showed single-spike behaviour in the output, in contrast to the 4fs FWHM under-compressed to 1fs over-compressed that had been predicted by theory using the cooperation lengths extracted from the numerical simulations. The reason for this discrepancy was the double-peak current profile of under-compressed electron bunches which led to two separate FEL pulses developing. The shorter FEL pulse was generated by the shorter electron bunches, although operating at slight under-compression was found to lead to higher peak-power and pulse energy at saturation.

Following this initial optimisation phase, extensive start-to-end simulations were carried out to assess the predicted FEL pulse properties both with and without sources of jitter in the electron gun and linac hardware. It was found that the performance of the scheme is largely insensitive to the introduction of jitter sources in terms of peak power and pulse duration, with the intrinsic variability of the SASE process found to dominate. The major difference between the two cases was the increase in arrival time jitter for the FEL pulse from 0.1fs to 12.7fs, primarily due to fluctuations in the

electron bunch arrival time caused by energy fluctuations combined with magnetic chicanes.

Overall, single spike operation of the New Light Source is expected to deliver pulses of ~2GW peak power with 0.5fs FWHM pulse duration and with negligible background signal. The work contained in this thesis has illustrated that the scheme is sufficiently robust to be able to cope with realistic machine jitter levels, and has confirmed that an accurate prediction of the final FEL pulse properties can only be achieved through extensive and detailed start-to-end simulations.

Future work on this topic should investigate whether it is possible to increase the operating bunch charge to aid the operation of machine diagnostics. The 2pC used in these studies was selected in order to avoid degradation in electron beam properties from collective effects. Even at this level of bunch charge, simulations demonstrated significant space-charge and CSR effects exist for present design. One way of achieving an increase in bunch charge would be to add an additional bunch compressor in the design immediately after the spreader section and before the main undulators in order to avoid having to transport an electron bunch with high peak current for long distances.

The main drawback for this scheme is the large arrival time jitter in the FEL pulse and lack of tight synchronisation control for the experiments. Future work should consider whether this jitter can be reduced either through improvements to the machine hardware or through re-optimising the operating conditions for the linac and bunch compressors. It is important to understand exactly how the FEL pulse is to be used in an experiment. For example, if it is to be used in pump-probe experiments it may be possible to use the electron bunch to produce both pump and probe signals, or

to use the radiation emitted by the electron bunch in a bending magnet to give a time-stamp for the FEL pulse.

A final topic to investigate is whether using shorter undulator modules would allow a greater degree of flexibility in selecting when to extract the FEL pulse from the undulator channel, potentially allowing a higher peak power and / or shorter pulse to develop before the pulse begins to become distorted.

5.3 Tapered Undulator Scheme for the New Light Source

The first part of the investigation into the tapered undulator short pulse scheme focussed on determining the optimal modulating laser pulse parameters. During this investigation it was identified that the modulating laser pulse should induce an approximately linear energy chirp in the electron bunch distribution that was well matched to the cooperation length of the FEL, or ~1fs in duration for the NLS electron bunch parameters. If the linear energy chirp is shorter than this, then the FEL pulse will saturate with a lower peak power and the main radiation peak will consist of a series of sub-peaks rather than a clean single spike. Two possible solutions were identified; one based around an 800nm laser pulse and one using a 1600nm pulse. The 800nm laser solution produces FEL pulses of a shorter duration and can be built using current technology; the 1600nm solution is well matched to the cooperation length of the FEL and provides a higher peak power, but has the drawback that these laser parameters are yet to be demonstrated experimentally.

Once the optimal laser and undulator taper parameters had been identified, extensive start-to-end simulations were carried out using both sets of modulating laser parameters to determine the predicted FEL pulse properties in each case. For the 800nm laser option, further studies were also carried out in which sources of error were applied to the machine model. This work demonstrated that the scheme was sufficiently robust to be able to cope in a realistic user facility environment, and as with the single spike scheme the dominant contribution to the shot-to-shot variability comes from the SASE process.

As a follow-up to this study, the possibility of improving the FEL pulse characteristics through filtering and pulse compression has also been investigated. The work contained in this thesis demonstrated that the shift in central wavelength of the FEL pulse after each undulator module allows the unwanted radiation emitted upstream of the final undulator to be removed with a relatively wide acceptance monochromator, improving the contrast ratio between the central radiation peak and the background signal from the main bunch. For the case of an 800nm laser, this filter also removes the sub-peaks from the temporal distribution, restoring the pulse to a clean single spike. The frequency chirp across the FEL pulse allows further pulse compression using a double-grating compressor, with the final pulse duration below that predicted by the cooperation length. Filtering and compressing the pulse can also be carried out after the nominal saturation point, allowing a greater fraction of FEL pulses to reach saturation.

Overall, this work has demonstrated the scheme is well-suited to application in a user-facility environment, is robust to realistic sources of jitter and can be implemented with minimal additional infrastructure. For the case of a 1600nm modulating laser,

the scheme is expected to deliver pulses of ~2GW peak power and ~1fs FWHM duration. For an 800nm laser the FEL pulse peak power is expected to be ~0.6GW with ~0.5fs pulse duration, improving to ~0.7GW with filtering and pulse compression.

Future studies of this scheme should concentrate on developing a practical layout that fits with the baseline NLS facility design. For example, space needs to be reserved before the main undulators for the energy modulator, and a path for the few-cycle laser beam needs to be incorporated. Matching quadrupoles need to be included to ensure the electron beam is focussed to a waist in the centre of the modulator. A decision also needs to be made as to which set of laser parameters should be pursued, and whether those parameters can be reliably achieved in practice.

5.4 Conclusions

The topic of short pulse generation in synchrotron radiation sources is a rapidly developing field, and particularly so for fourth generation light sources. Indications are that to go much below 1 ps is very challenging for third generation facilities, without suffering from a large reduction in photon flux. Fourth generation facilities are more naturally suited to the production of short pulses, but of the proposed schemes only single spike operation and the slotted foil method have been tested experimentally. All schemes that have been proposed for these facilities will benefit greatly from further experimental studies.

When considered purely in terms of the radiation pulse properties, the schemes that have been proposed for fourth generation light sources vastly out-perform storage

ring based methods. This gain in performance stems from the coherence properties of FEL radiation, in which the peak power can potentially scale with the square of the number of electrons involved in the interaction, compared to the linear dependence of spontaneous radiation sources used in third generation facilities. For the two fourth-generation light source schemes discussed in this thesis it was demonstrated that GW-level pulses lasting below 1fs can be generated with close to full temporal and transverse coherence. The repetition rate at which these pulses can be delivered to an experiment is dependent upon the repetition rate of the electron gun and main linac, and for the tapered undulator scheme on the repetition rate of the modulating few-cycle laser pulse. For the New Light Source baseline proposal, the FEL pulse repetition rate is therefore limited to a maximum of 1kHz.

Whilst third generation light sources cannot compete in terms of peak power, pulse duration or coherence, the areas in which they gain are in their excellent transverse stability, high repetition rate and hence high average brightness. A diverse range of schemes have been proposed for these facilities, with each scheme delivering radiation pulses of differing strengths and weaknesses. Pulse durations ranging from several tens of picoseconds down to hundreds of femtoseconds or below have been demonstrated with repetition rates of up to several hundred MHz. For Diamond, the work presented in this thesis has demonstrated that a storage ring lattice can provide low emittance and low alpha simultaneously. This combination has already proven to be a powerful tool for scientific research, enabling world-class science to be performed [171].

Related Publications

I. Martin, G. Rehm, C. Thomas, R. Bartolini, "*Experience with Low-Alpha Lattices at the Diamond Light Source*", PRST-AB **14**, 040705, (2011)

I. Martin, R. Bartolini, "*Comparison of Short Pulse Generation Schemes for a Soft X-Ray Free Electron Laser*", PRST-AB **14**, 030702, (2011)

I. Martin, R. Bartolini, "*Short Pulse Radiation from an Energy-Chirped Electron Bunch in a Soft X-Ray FEL*", Proc. FEL 2010, p. 358, (2010)

I. P. S. Martin, R. Bartolini, G. Rehm, J. H. Rowland, C. Thomas "*Low alpha Operation of the Diamond Storage Ring*", Proc. IPAC 2010, (2010)

C. Thomas, G. Rehm, I. Martin, "*Performance of a Stream Camera Using Reflective Input Optics*", Proc. IPAC 2010, p. 1170, (2010)

I. Martin, R. Bartolini, D. Dunning, N. Thompson, "*Short Pulse Options for the UK's New Light Source Project*", Proc. IPAC 2010, p. 2266, (2010)

R. Bartolini, I. Martin, J.-H. Han, J. Rowland, "*Single Spike Operation for the Generation of sub-fs Pulses in the New Light Source*", Proc. FEL 2009, p. 647, (2009)

G. Rehm, A. Morgun, R. Bartolini, I. Martin, P. Karataev, "*Ultra-Fast mm-Wave Detectors for Observation of Microbunching Instabilities in the Diamond Storage Ring*", Proc. DIPAC 2009, p. 369, (2009)

C. Thomas, I. Martin, G. Rehm, "*Investigation of Extremely Short Beam Longitudinal Measurement with a Streak Camera*", Proc. DIPAC 2009, p. 260, (2009)

I. P. S. Martin, R. Bartolini, J. Rowland, B. Singh, C. Thomas, "*A Low Momentum Compaction Lattice for the Diamond Storage Ring*", Proc. PAC 2009, (2009)

R. Bartolini, C. Christou, J.-H. Han, I. Martin, J. Rowland, D. Angal-Kalinin, F. Jackson, B. Muratori, P. Williams, "*A 1keV FEL Driven by a Superconducting Linac as a Candidate for the UK New Light Source*", Proc. PAC 2009, p. 1226, (2009)

Appendix A

Derivation of Leading Order Terms in the Expansion of Alpha

In this section, analytic expressions for the leading order terms in the expansion of the momentum compaction factor with momentum deviation are derived.

The change in path length for an electron in a single revolution of the storage ring with respect to the central orbit can be calculated using the formula [21, 99]

$$\frac{\Delta l}{l_0} = \frac{1}{l_0}\int_s^{s+\ell_0}\left[\sqrt{\left(1+\frac{x(s)}{\rho}\right)^2 + x'(s)^2 + y'(s)^2} - 1\right] ds \qquad \text{(A1)}$$

where l_0 is the circumference of the storage ring, ρ is the bending radius of the dipoles and x and y are the transverse particle coordinates with respect to the central orbit. Expanding this equation and keeping terms to third order, the change in path length becomes

$$\frac{\Delta l}{l_0} = \frac{1}{l_0}\int_s^{s+\ell_0} \frac{x(s)}{\rho} + \frac{x'(s)^2}{2} + \frac{y'(s)^2}{2} - \frac{x(s)x'(s)^2}{2\rho} - \frac{x(s)y'(s)^2}{2\rho} ds \qquad \text{(A2)}$$

Neglecting vertical dispersion contributions, the particle displacement coordinates can be expanded and expressed in terms of the betatron oscillation, closed orbit and momentum deviation amplitudes [98].

$$\begin{aligned} x &= x_\beta + x_{co} + \eta_1\delta + \eta_2\delta^2 + \eta_3\delta^3 \\ y &= y_\beta + y_{co} \\ x' &= x_\beta{}' + x_{co}{}' + \eta_1{}'\delta + \eta_2{}'\delta^2 + \eta_3{}'\delta^3 \\ y' &= y_\beta{}' + y_{co}{}' \end{aligned} \tag{A3}$$

where η is the dispersion function, η' is its spatial derivative and the subscripts 1, 2 and 3 refer to the order in the expansion with momentum deviation. Note the *s* argument has been dropped for conciseness. After noting that terms linear in the betatron amplitudes are oscillatory in nature, are independent of close orbit distortion and will average to zero, and that the closed orbit distortions are statistical quantities for which the linear terms will again average to zero, substituting A3 into A2 leads to the equation

$$\begin{aligned} \frac{\Delta l}{l_0} = \frac{\Delta \ell}{\ell} &+ \left[\frac{1}{l_0}\int_s^{s+\ell_0} \frac{\eta_1}{\rho}\,ds\right]\delta + \left[\frac{1}{l_0}\int_s^{s+\ell_0} \frac{\eta_1{}'^2}{2} + \frac{\eta_2}{\rho}\,ds\right]\delta^2 \\ &+ \left[\frac{1}{l_0}\int_s^{s+\ell_0} \eta_1{}'\eta_2{}' - \frac{\eta_1\eta_1{}'^2}{2\rho} + \frac{\eta_3}{\rho}\,ds\right]\delta^3 \end{aligned} \tag{A4}$$

The first term in A4 represents all momentum independent path lengthening, including those due to betatron oscillations, closed orbit distortions and changes to the central RF frequency. The integrals enclosed in square brackets can easily be identified as α_1, α_2 and α_3.

Bibliography

[1] H.N. Chapman, A. Barty, M.J. Bogan, S. Boutet, M. Frank, S.P. Hau-Riege, S. Marchesini, B.W. Woods, S. Bajt, W. Henry Benner, R.A. London, E. Plönjes, M. Kuhlmann, R. Treusch, S. Düsterer, T. Tschentscher, J.R. Schneider, E. Spiller, T. Möller, C. Bostedt, M. Hoener, D.A. Shapiro, K.O. Hodgson, D. van der Spoel, F. Burmeister, M. Bergh, C. Caleman, G. Huldt, M. Marvin Seibert, F.R.N.C. Maia, R.W. Lee, A. Szöke, N. Timneanu, J. Hajdu, "*Femtosecond Diffractive Imaging with a Soft X-Ray Free-Electron Laser*", Nat. Phys., **2**, 12, p. 839, (2006)

[2] A. Barty, "*Time-Resolved Imaging Using Free Electron Lasers*", J. Phys. B, **43**, (2010)

[3] P. B. Corkum, F. Krausz, "*Attosecond Science*", Nat. Phys. **3**, p. 381, (2007)

[4] S. Khan, "*Femtoslicing in Storage Rings*", Proc. PAC 2005, p. 590, (2005)

[5] M. Neeb, P. Wernet, H. Dürr, M. Sauerborn, W. Eberhardt, "*Workshop on Ultrafast Time-resolved Soft X-Ray Science*", Sync. Rad. News **18**, p.2, (2005)

[6] J. Corlett, W. Fawley, S. Lidia, H. Padmore, G. Penn, I. Pogorelov, J. Qiang, F. Sannibale, J. Staples, C. Steier, M. Venturini, W. Wan, R. Wilcox, A. Zholents, "*FEL Design Studies at LBNL: Activities and Plans*", ICFA Beam Dynamics Newsletter, No. 42, (2007)

[7] J. Marangos, R.P. Walker, G. Diakun (eds.), "*NLS Project: Conceptual Design Report*", available at www.newlightsource.org, (2010)

[8] F. R. Elder, A. M. Gurewitsch, R. V. Langmuir, H. C. Pollock, "*Radiation From Electrons in a Synchrotron",* Phys. Rev. **71**, Issue 11, p. 829, (1947)

[9] A. Liénard, "*Champ Électrique et Magnétique Produit Par une Charge Électrique Concentrée en un Point et Animée d'un Mouvement Quelconque*", L'Éclairage Électrique, Vol. 16, p. 5, 53, 106 (1898)

[10] T. Panesor, "*Synchrotron Light*", Institute of Physics Case Study, (2010), (available at http://www.iop.org/publications/iop/2011/file_47457.pdf)

[11] E. Wiechert, "*Elektrodynamische Elementargesetze*", Archives Néerlandaises de Sciences **5**, p. 549, (1900)

[12] G.A. Schott, "*Electromagnetic Radiation*", Cambridge Univ. Press, (1912)

[13] D. Ivanenko, I. Pomeranchuk, Phys. Rev. **65**, p. 343, (1944)

[14] J.P. Blewett, "*Radiation Losses in the Induction Electron Accelerator*", Phys. Rev. **69**, Issue 3, p. 87, (1946)

[15] F. Elder, R. Langmuir, H. Pollock, "*Radiation Emitted by Electrons Accelerated in a Synchrotron*", Phys. Rev. **74**, p. 52, (1948)

[16] D. Tomboulian and P. Hartman, "*Spectral and Angular Distribution of Ultraviolet Radiation from the 300-MeV Cornell Synchrotron*", Phys. Rev. **102**, p. 1423, (1956)

[17] I. Ado, P. Cherenkov, Soviet Physics Doklady 1, 517, (1956)

[18] J. Schwinger, "*On the Classical Radiation of Accelerated Electrons*", Phys. Rev. **75**, p. 1912, (1949)

[19] J.D. Jackson, "*Classical Electrodynamics*", 3rd Ed., J. Wiley and Sons, (1999)

[20] R.P. Walker, "*Insertion Devices: Undulators and Wigglers*", CERN Accelerator School, France, CERN 98-04, (1996)

[21] H. Weidemann, "*Particle Accelerator Physics I & II*", 2nd Ed., Springer, Berlin, (2003)

[22] L. Schiff, "*Production of Particle Energies Beyond 200MeV*", Rev. Sci. Inst. **17**, 1, (1946)

[23] Z. Huang, K. -J. Kim, "*Review of Free-Electron Laser Theory*", PRST-AB **10**, 034801, (2007)

[24] R. Bonifacio, C. Pellegrini, L.M. Narducci, "*Collective Instabilities and High-Gain Regime in a Free Electron Laser*", Opt. Comm. **50**, (1984)

[25] E. Saldin, E. Schneidmiller, M. Yurkov, "*The Physics of Free-Electron Lasers*", Springer-Verlag, Berlin, (2000)

[26] W.B. Colson, C. Pellegrini, A. Renieri, (eds.), "*Laser Handbook Vol. 6, Free Electron Lasers*", North-Holland, Amsterdam, (1990)

[27] R. Bonifacio, L. De Salvo, P. Pierini, N. Piovella, C. Pellegrini, "*Spectrum, Temporal Structure, and Fluctuations in a High Gain Free-Electron Laser Starting from Noise*", PRL **73**, p. 70, (1994)

[28] M. Xie, "*Design optimization for an X-Ray Free-Electron Laser driven by the SLAC LINAC*", Proc. PAC 1995, p. 183, (1995)

[29] http://www.lightsources.org/

[30] E. Seres, J. Seres, F. Krausz, C. Spielmann, "*Generation of Coherent Soft X-Ray Radiation Extending Far Beyond the Titanium L Edge*", PRL **92**, 163002, (2004)

[31] K.-J. Kim, S. Chattopadhyay, C. Shank, "*Generation of Femtosecond X-Rays by 90˚ Thompson Scattering*", NIM-A **341**, p351, (1994)

[32] R. Bartolini, C. Christou, R. Fielder, M. Jensen, A. Morgan, S. Pande, G. Rehm, C. Thomas, "*Analysis of Collective Effects at the Diamond Storage Ring*", Proc. EPAC 2008, p. 1574, (2008)

[33] J. Feikes, K. Holldack, P. Kuske, G. Wüstefeld, "*Sub-Picosecond Electron Bunches in the BESSY Storage Ring*", Proc. EPAC 2004, p. 1954, (2004)

[34] R.W. Schoenlein, S. Chattopadhyay, H.W. Chong, T.E. Glover, P.A. Heimann, C.V. Shank, A.A. Zholents, M.S. Zolotorev, "*Generation of Femtosecond Pulses of Synchrotron Radiation*", Science **287**, p. 2237, (2000)

[35] W. Guo, B. Yang, C.-X. Wang, K. Harkay, M. Borland, "*Generating Picosecond X-Ray Pulses in Synchrotron Light Sources Using Dipole Kickers*", PRST-AB **10**, 020701, (2007)

[36] G. Decker, M. Borland, D. Horan, A. Lumpkin, N. Sereno, B. Yang, S. Krinsky, "*Transient Bunch Compression Using Pulsed Phase Modulation in High Energy Electron Storage Rings*", PRST-AB **9**, 120702, (2006)

[37] S. Schreiber, B. Faatz, J. Feldhaus, K. Honkavaara, R. Treusch, "*FLASH Operation as an FEL User Facility*", Proc. PAC 2009, p. 3130, (2009)

[38] J. Frisch, R. Akre, J. Arthur, R. Bionta, C. Bostedt, J. Bozek, A. Brachmann, P. Bucksbaum, R. Coffee, F.-J. Decker, Y. Ding, D. Dowell, S. Edstrom, P. Emma, A. Fisher, S. Gilevich, J. Hastings, G. Hays, P. Hering, Z. Huang, R. Iverson, H. Loos, M. Messerschmidt, A. Miahnahri, S. Moeller, H.-D. Nuhn, G. Pile, D. Ratner, J. Rzepiela, D. Schultz, T. Smith, H. Tompkins, J. Turner, J. Welch, W. White, J. Wu, G. Yocky, J. Galayda, "*Operation and Upgrades of the LCLS*", SLAC-PUB-14251, (2010)

[39] I. Martin, G. Rehm, C. Thomas, R. Bartolini, "*Experience with Low-Alpha Lattices at the Diamond Light Source*", PRST-AB **14**, 040705, (2011)

[40] I. Martin, R. Bartolini, "*Comparison of Short Pulse Generation Schemes for a Soft X-Ray Free Electron Laser*", PRST-AB **14**, 030702, (2011)

[41] A. Zholents, M. Zolotorev, "*Femtosecond X-Ray Pulses of Synchrotron Radiation*", PRL **76**, (1996)

[42] P. Beaud, S.L. Johnson, A. Streun, R. Abela, D. Abramsohn, D. Grolimund, F. Krasniqi, T. Schmidt, V. Schlott, and G. Ingold, "*Spatiotemporal Stability of a Femtosecond Hard X-Ray Undulator Source Studied by Control of Coherent Optical Phonons*", PRL **99**, 174801, (2007)

[43] S. Khan, K. Holldack, T. Kachel, R. Mitzner, T. Quast, "*Femtosecond Undulator Radiation from Sliced Electron Bunches*", PRL **97**, 074801, (2006)

[44] R.W. Schoenlein, W. P. Leemans, A.H. Chin, P. Volfbeyn, T.E. Glover, P. Balling, M. Zolotorev, K.-J. Kim, S. Chattopadhyay, C.V. Shank, "*Femtosecond X-Ray Pulses at 0.4Å Generated by 90˚ Thomson Scattering: A Tool for Probing the Structural Dynamics of Materials*", Science **274**, p. 236, (1996)

[45] A. Zholents, P. Heimann, M. Zolotorev, J. Byrd, "*Generation of Sub-Picosec. X-Ray Pulses Using RF Orbit Deflection*", NIM-A **425**, p. 385, (1999)

[46] M. Borland, "*Simulation and Analysis of Using Deflecting Cavities to Produce Short X-Ray Pulses with the APS*", PRST-AB **8**, 074001, (2005)

[47] Y. H. Chin, "*Double RF System for Bunch Shortening*", Int. Workshop on Acc. For Assymetric B-Factories, Tsukuba, LBL-29622, (1990)

[48] D. Robin, E. Forest, C. Pellegrini, A. Amiry, "*Quasi-Isochronous Storage Rings*", Phys. Rev. E **48**, p. 2149, (1993)

[49] C. Steier, P. Heimann, S. Marks, D. Robin, R. Schoenlein, W. Wan, W. Wittmer, "*Successful Completion of the Femtosecond Slicing Upgrade at the ALS*", Proc. PAC 2007, p. 1194, (2007)

[50] A. Nadji, F. Briquez, M.-E. Couprie, J.-C. Denard, J.-M. Filhol, P. Hollander, C. Herbeaux, M. Labat, J.-F. Lamarre, C. Laulhé, V. Leroux, J. Luning, O. Marcouillé, J.-L. Marlats, M. Meyer, T. Moreno, P. Morin, P. Prigent, S. Ravy, F. Sirotti, "*Status of the SOLEIL Femtosecond X-Ray Source*", Proc. IPAC 2010, p. 2499, (2011)

[51] K. Harkay, M. Borland, Y.-C. Chae, G. Decker, R. Dejus, L. Emery, W. Guo, D. Horan, K.-J. Kim,R. Kustom, D. Mills, S. Milton, A. Nassiri, G. Pile, V. Sajaev, S. Shastri, G. Waldschmidt, M. White,B. Yang, A. Zholents, "*Generation of Short X-Ray Pulses Using Crab Cavities at the Advanced Photon Source*", Proc. PAC 2005, p. 668, (2005)

[52] M. Borland, J. Carwardine, Y. Chae, L. Emery, P. Den Hartog, K. Harkay, A. Lumpkin, A. Nassiri, V. Sajaev, N. Sereno, G. Waldschmidt, B. Yang, V. Dolgashev, "*Planned Use of Pulsed Crab Cavities for Short X-Ray Pulsed Generation at the APS*", Proc. PAC 2007, p. 1127, (2007)

[53] T. Fujita, H. Hanaki, T. Nakazato, K. Hosoyama, K. Akai, K. Ebihara, T. Furuya, K. Hara, T. Honma, A. Kabe, Y. Kojima, S. Mitsunobu, Y. Morita, H. Nakai, K. Nakanishi, M. Ono and Y. Yamamoto, M. Matsuoka, M.

Monde, K. Sennyu, T. Yanagisawa, "*Overview of Short Pulse X-Ray Generation Using Crab Cavities at SPRing8*", Proc. IPAC 2010, p. 39, (2010)

[54] R. Bartolini, M. Borland, K. Harkay, "*Plans for the Generation of Short Radiation Pulses at the Diamond Storage Ring*", Proc. EPAC 2006, p. 160, (2006)

[55] W. Guo, M. Borland, K. Harkay, C.-X. Wang, B. Yang, "*A kHz Picosecond X-Ray Pulse Generation Scheme*", Proc. PAC 2007, P. 1133, (2009)

[56] C. Mitsuda, K. Fukami, M. Masaki, A. Mochihashi, M. Oishi, J. Schimizu, Y. Shimosaki, M. Shoji, K. Soutome, K. Tamura, H. Yonehara, K. Kobayashi, T. Nakanishi, T. Ohshima, "*Development of Kicker Magnet for Generation of Short Pulse Synchrotron Radiation*", Proc. PAC 2009, p. 1171, (2009)

[57] C.T. Hlaing, D. Robin, F. Sannibale, W. Wan, W. Guo, "*Using Synchrobetatron Resonances to Generate a Crabbed Beam at the ALS*", Proc. PAC 2009, p. 1180, (2009)

[58] G. Stupakov, S. Heifets, "*Beam Instability and Microbunching due to Coherent Synchrotron Radiation*", PRST-AB **5**, 054402, (2002)

[59] K. Bane, S. Krinsky, J. Murphy, "*Longitudinal Potential Well Distortion Due to the Synchrotron Radiation Wakefield*", Proc. Micro Bunches Workshop, Upton NY, (1995)

[60] A. Chao, M. Tigner, "*Handbook of Accelerator Physics and Engineering*", World Scientific, (1998)

[61] A. Hoffmann, S. Myers, "*Beam Dynamics in a Double RF System*", 11th Conf. on High En. Accel., p. 610, (1980)

[62] S. Kramer, "*Higher Harmonic RF System for APS*", LS-96, (1988)

[63] R. Biscari, S.L. Kramer, G. Ramirez, "*Bunch Length Control in the NSLS VUV Ring*", NIM-A **336**, p. 26, (1995)

[64] M. Billardon, M.-E. Couprie, D. Nutarelli, G. Flynn, P. Marin, R. Roux, M. Sommer, "*Beam Dynamics in Super-ACO with a New 500 MHz Fifth Harmonic RF System*", Proc. EPAC 1998, p. 954, (1998)

[65] J. Feikes, P. Kuske, G. Wüstefeld, "*Towards Sub-Picosecond Electron Bunches: Upgrading Ideas for BESSY II*", Proc. EPAC 2006, p. 157, (2006)

[66] M. Dohlus, T. Limberg, P. Emma, "*Bunch Compression for Linac-Based FELs*", ICFA Beam Dynamics Newsletter #38, (2005)

[67] A. Loulergue, A. Mosnier, "*A Simple S-Chicane for the Final Bunch Compressor of TTF-FEL*", Proc. EPAC 2000, p. 752, (2000)

[68] R. Bonifacio, B. McNeil, A. Paes, L. de Salvo, R. Galvão, "*A Far Infrared Super Radiant FEL*", Int. J. Infrared Mm Waves **28**, p. 699, (2007)

[69] C. Pellegrini, "*High Power Femtosecond Pulses from an X-Ray SASE-FEL*", NIM-A **445**, p. 124, (2000)

[70] P. Emma, K. Bane, M. Cornacchia, Z. Huang, H. Schlarb, G. Stupakov, D. Walz, "*Femtosecond and Subfemtosecond X-Ray Pulses from a Self-Amplified Spontaneous-Emission-Based Free-Electron Laser*", PRL **92**, 074801, (2004)

[71] A. Zholents, W. Fawley, "*Proposal for Intense Attosecond Radiation from an X-Ray Free-Electron Laser*", PRL **92**, 224801, (2004)

[72] E. Saldin, E. Schneidmiller, M. Yurkov, "*Terawatt-Scale Sub-10-fs Laser Technology – Key to Generation of GW-Level Attosecond Pulses in X-Ray Free-Electron Laser*", Opt. Comm. 237, p. 153, (2004)

[73] E. Saldin, E. Schneidmiller, M. Yurkov, "*A New Technique to Generate 100 GW-Level Attosecond X-Ray Pulses from the X-Ray SASE FELs*", Opt. Comm. 239, p. 161, (2004)

[74] A. Zholents, G. Penn, "*Obtaining Attosecond X-Ray Pulses using a Self-Amplified Spontaneous Emission FEL*", PRST-AB **8**, 050704, (2005)

[75] E. Saldin, E. Schneidmiller, M. Yurkov, "*Self-Amplified Spontaneous Emission FEL with Energy-Chirped Electron Beam and its Application for Generation of Attosecond X-Ray Pulses*", PRST-AB **9**, 050702, (2006)

[76] A. Zholents, M. Zolotorev, "*Attosecond X-Ray Pulses Produced by Ultra Short Transverse Slicing Via Laser Electron Beam Interaction*", New J. Phys. **10**, 025005, (2008)

[77] D. Xiang, Z. Huang, G. Stupakov, "*Generation of Intense Attosecond X-Ray Pulses using Ultraviolet Laser Induced Microbunching in Electron Beams*", PRST-AB **12**, 060701, (2009)

[78] D. Vaughan (ed.), "*An Infrared Free-Electron Laser for the Chemical Dynamics Research Laboratory*", LBL-PUB-5335, (1992)

[79] "*Linac Coherent Light Source*", Concept. Design Rep., SLAC-R-593, (2002)

[80] "*The European X-Ray Free-Electron Laser*", Tech. Design Rep., DESY-2006-097, (2007)

[81] P. Piot, "*State-of-the-Art Electron Bunch Compression*", Proc. LINAC 2004, p. 528, (2004)

[82] Z. Huang, M. Borland, P. Emma, K-J Kim, "*Theory and Simulation of CSR Microbunching in Bunch Compressors*", NIM-A **507**, p. 318, (2003)

[83] M. Dohlus, A. Kabel, T. Limberg, "*Optimal Beam Optics in the TTF-FEL Bunch Compression Sections: Minimising the Emittance Growth*", Proc. PAC 1999, p. 1650, (1999)

[84] M. Cornacchia, J. Arthur, L. Bentson, R. Carr, P. Emma, J. Galayda, P. Krejcik, I. Lindau, J. Safranek, J. Schmerge, J. Stohr, R. Tatchyn, A. Wootton, "*A Sub-Picosecond Photon Pulse Facility for SLAC*", SLAC-PUB-8950, (2001)

[85] S. Schreiber, B. Faatz, J. Feldhaus, K. Honkavaara, R. Treusch, M. Vogt, J. Rossbach, "*FLASH Upgrade and First Results*", Proc. FEL 2010, p. 198, (2010)

[86] Y. Ding, A. Brachmann, F.-J. Decker, D. Dowell, P. Emma, J. Frisch, S. Gilevich, G. Hays, P. Hering, Z. Huang, R. Iverson, H. Loos, A. Miahnahri, H.-D. Nuhn, D. Ratner, J. Turner, J. Welch, W. White, J. Wu, "*Measurements and Simulations of Ultralow Emittance and Ultrashort Electron Beams in the Linac Coherent Light Source*", PRL **102**, 254801, (2009)

[87] S. Reiche, P. Musumeci, C. Pellegrini, J. Rosenzwieg, "*Development of Ultra-Short Pulse, Single Coherent Spike for SASE X-Ray FELs*", NIM-A **593**, p. 45, (2008)

[88] M. Boscolo, M. Ferrario, I. Boscolo, F. Castelli, S. Cialdi, V. Petrillo, R. Bonifacio, L. Palumbo, L. Serafini, "*Single Spike Operation in SPARC SASE-FEL*", NIM-A **593**, (2008)

[89] P. Emma, Z. Huang, M. Borland, "*Attosecond X-Ray Pulses in the LCLS Using the Slotted Foil Method*", Proc. FEL 2004, p. 333, (2004)

[90] L.-H. Yu, M. Babzien, I. Ben-Zvi, L.F. DiMauro, A. Doyuran, W. Graves, E. Johnson, S. Krinsky, R. Malone, I. Pogorelsky, J. Skaritka, G. Rakowsky, L. Solomon, X.J. Wang, M. Woodle, V. Yakimenko, S.G. Biedron, J.N. Galayda, E. Gluskin, J. Jagger, V. Sajaev, I. Vasserman, "*High-Gain Harmonic Generation Free-Electron Laser*", Science **289**, p. 932, (2000)

[91] Y. Ding, Z. Huang, D. Ratner, P. Bucksbaum, H. Merdji, "*Generation of Attosecond X-Ray Pulses with a Multicycle Two-Colour Enhanced Self-Amplification Spontaneous Emission Scheme*", PRST-AB **12**, 060703, (2009)

[92] W. Fawley, "*Production of Ultrashort FEL XUV pulses via a Reverse Undulator Taper*", NIM-A **593**, p. 111-115, (2008)

[93] G. Stupakov, "*Using the Beam-Echo Effect for Generation of Short-Wavelength Radiation*", PRL **102**, 074801, (2009)

[94] A. Zholents, G. Penn, "*Obtaining two Attosecond Pulses for X-Ray Raman Spectroscopy*", NIM-A **612**, p. 254-259, (2010)

[95] J. Yan, H.–X. Deng, D. Wang, Z.–M. Dai, "*EEHG-Assisted Schemes for Attosecond X-Ray Pulses Generation*", NIM-A **621**, p. 97-104, (2010)

[96] E. Schneidmiller, M. Yurkov, "*Using the Longitudinal Space Charge Instability for Generation of Vacuum Ultraviolet and X-Ray Radiation*", PRST-AB **13**, 110701, (2010)

[97] E. Saldin, E. Schneidmiller, M. Yurkov, "*Longitudinal Space Charge-Driven Microbunching Instability in the TESLA Test Facility Linac*", NIM-A **528**, p. 355-359, (2004)

[98] G. Stupakov, "*Beam Echo Effect for Generation of Short-Wavelength Radiation*", Proc. FEL 2009, p. 15, (2009)

[99] A. Nadji, P. Brunelle, G. Flynn, M.P. Level, M. Sommer, H. Zyngier, "*Quasi-Isochronous Experiments with the Super-ACO Storage Ring*", NIM-A **378,** p. 376, (1996)

[100] Y. Shoji, "*Dependence of Average Path Length Betatron Motion in a Storage Ring*", PRST-AB **8**, 094001, (2005)

[101] J. Feikes, M. von Hartrott, M. Reis, P. Schmid, G. Wüstefeld, A. Hoehl, R. Klein, R. Müller, G. Ulm, "*Metrology Light Source: The First Electron Storage Ring Optimised for Generating Coherent THz Radiation*", PRST-AB **14**, 030705, (2011)

[102] H. Hama, S. Takano, G. Isoyama, "*Control of the Bunch Length on an Electron Storage Ring*", NIM-A **329** 29-36, (1993)

[103] D. Robin, R. Alvis, A. Jackson, R Holtzapple, B. Podobedov, "*Low Alpha Experiments at the ALS*", SLAC-PUB-95-7015, (1995)

[104] D. Robin, H. Hama, A. Nadji, "*Experimental Results on Low Alpha Electron-Storage Rings*", Proc. Micro Bunches Workshop, Upton, NY, (1995)

[105] J. Feikes, K. Holdack, P. Kuske, G. Wüstefeld, "*Compressed Electron Bunches for THz Generation – Operating BESSY II in a Dedicated Low Alpha Mode*", Proc. EPAC 2004, p. 2290, (2004)

[106] A.-S. Muller, I. Birkel, B. Gasharova, E. Huttel, R. Kubat, Y.-L. Mathis, D.A. Moss, W. Mexner, R. Rossmanith, M. Wuensch, P. Wesolowski, F. Perez, M.

Pont, C.J. Hirschmugl, "*Far Infrared Coherent Synchrotron Edge Radiation at ANKA*", Proc. PAC 2005, p. 2518, (2005)

[107] X. Huang, J. Safranek, J. Corbett, Y. Nosochkov, J. Sebek, A. Terebilo, "*Low Alpha Mode for SPEAR3*", Proc. PAC 2007, p. 1308, (2007)

[108] Y.-R. E. Tan, R. Dowd, M. Boland, D. Appadoo, "*Low Alpha Configuration for Generating Short Bunches*", Proc. PAC 2009, p. 3711, (2009)

[109] L.O. Dallin, M.S. de Jong, "*Coherent Synchrotron Radiation Production at the Canadian Light Source*", Proc. PAC 2009, p. 1126, (2009)

[110] G. Brandt, J. Eden, R. Fliegauf, A. Gottwald, A. Hoehl, R. Klein, R. Muller, M. Richter, F. Scholze, R. Thornagel, G. Ulm, K. Burkmann, J. Rahn, G. Wustefeld, "*The Metrology Light Source – The New Dedicated Electron Storage Ring of PTB*", NIM-B **258** 445-452, (2007)

[111] N.P. Abreu, M. Böge, F. Müller, V. Schlott, H.C. Sigg, A. Streun, G. Amatuni, D. Gishyan, K. Manukyan, A. Sargsyan, "*Low-Alpha Operation of the SLS Storage Ring*", Proc. PAC 2009, p. 2285, (2009)

[112] D.A.G. Deacon, "*Theory of the isochronous storage ring laser*", Ph. D. Thesis, Stanford University, (1979)

[113] I.P.S Martin, R. Bartolini, J. Rowland, B. Singh, C. Thomas, "*A Low Momentum Compaction Lattice for the Diamond Storage Ring*", Proc. PAC 2009, p. 3769, (2009)

[114] I.P.S. Martin, R. Bartolini, G. Rehm, J.H. Rowland, C. Thomas "*Low alpha Operation of the Diamond Storage Ring*", Proc. IPAC 2010, p. 4599, (2010)

[115] R. Bartolini, "*Physics Studies for Generating Short Radiation Pulses at the Diamond Light Source*", Proc ICFA Mini-Workshop on Frontiers of Short Bunches in Storage Rings, Frascati, (2005)

[116] A. Nadji, "*Nonlinear Dynamics in the Low-Alpha Experiments at SOLEIL*", Proc. 2nd Workshop on Nonlinear Beam Dynamics in Storage Rings, Diamond Light Source, (2009)

[117] A. Streun, "*Practical Guidelines for Lattice Design*", SLS-TME-TA-1999-0014, (1999)

[118] J. Bengtsson, "*Non-Linear Transverse Dynamics for Storage Rings with Applications to the Low Energy Antiproton Ring (LEAR) at CERN*", CERN 88-05, (1988)

[119] M. Borland, "*ELEGANT: A Flexible SDDS-Compliant Code for Accelerator Simulation*", Advanced Photon Source LS-287, (2000)

[120] S. Smith, D. Holder, J. Jones, J. Varley, N. Wyles, R. Bartolini, I. Martin, B. Singh, "*Progress of the Diamond Storage Ring and Injector Design*", Proc. EPAC 2004, p. 2418, (2004)

[121] A. Terebilo, "*Accelerator Toolbox for MATLAB*", SLAC-PUB-8732, (2001)

[122] J. Laskar, C. Froeschlé, A. Celletti, "*The Measure of Chaos by the Numerical Analysis of the Fundamental Frequencies. Application to the Standard Mapping*", Physica D **56**, (1992)

[123] J. Bengtsson, "*Tracy-2 User's Manual*", unpublished

[124] I. Martin, "*Further Collimation Studies for Touschek Losses and Storage Ring Injection*", Diamond Internal Note, AP-SR-REP-0133, (2005)

[125] J. Laskar, "*Frequency Map Analysis and Particle Accelerators*", Proc. PAC 2003, p. 378, (2003)

[126] R.P. Walker, "*Wigglers*", CERN Accelerator School, Proc. 5th Advanced Accelerator Physics Course, Rhodes, CERN 95-06, (1995)

[127] A. Wrulich, "*Single Beam Lifetime*", CERN Accelerator School, Proc. 5th General Accelrator Physics Course, Finland, CERN 94-01, (1994)

[128] C. Bernardini, G.F. Corazza, G. Di Giugno, G. Ghigo, J. Haissinski, P. Marin, R. Querzoli, B. Touschek, "*Lifetime and Beam Size in a Storage Ring*", PRL **10**, p. 407, (1963)

[129] H. Brück, "*Accelerateurs Circulaires de Particules*", PUP, Paris, (1963)

[130] M. Belgroune, P. Brunelle, A. Nadji, L. Nadolski, "*Refined Tracking Procedure for the SOLEIL Energy Acceptance Calculation*", Proc. PAC 2003, p. 896, (2003)

[131] M. Zisman, S. Chattopadhyay, J. Bisognano, "*ZAP User's Manual*", LBL-21270, (1986)

[132] C. Thomas, R. Bartolini, I. Martin, G. Rehm, "*X-ray Pinhole Camera Resolution and Emittance Measurement*", PRST-AB **13**, 022805, (2010)

[133] R. Bartolini, I. Martin, G. Rehm, F. Schmidt, "*Calibration of the Nonlinear Ring Model at the Diamond Light Source*", PRST-AB **14**, 054003 (2011)

[134] J. Feikes, P. Kuske, R. Müller, G. Wüstefeld, "*Orbit Stability in the 'Low Alpha' Optics of the BESSY Light Source*", Proc. EPAC 2006, p. 3308, (2006)

[135] R. Bartolini, H. Huang, J. Kay, I. Martin, "*Analysis of Beam Orbit Stability and Ground Vibrations at the Diamond Storage Ring*", Proc. EPAC 2008, p. 1980, (2008)

[136] J. Haïssinski, "*Exact Longitudinal Equilibrium Distribution of Stored Electrons in the Presence of Self-Fields*", Il Nuo. Cimento B **18**, p. 72, (1973)

[137] S. Fang, K. Oide, K. Yokoya, B. Chen, J. Wang, "*Microwave Instabilities in Electron Rings with Negative Momentum Compaction Factor*", KEK Preprint 94-190, (1995)

[138] F. Sannibale, J.M. Byrd, A. Loftsdottir, M. Venturini, M. Abo-Bakr, J. Feikes, K. Holldack, P. Kuske, G. Wüstefeld, H.-W. Hübers, R. Warnock, "*A Model Describing Stable Coherent Synchrotron Radiation in Storage Rings*", PRL **93**, 094801, (2004)

[139] M. Venturini, R. Warnock, "*Bursts of Coherent Synchrotron Radiation in Electron Storage Rings: A Dynamical Model*", PRL **89**, 224802, (2002)

[140] J.M. Byrd, W.P. Leemans, A. Loftsdottir, B. Marcelis, M.C. Martin, W.R. McKinney, F. Sannibale, T. Scarvie, C. Steier, "*Observations of Broadband*

Self-Amplified Spontaneous Coherent Terahertz Synchrotron Radiation in a Storage Ring", PRL **89**, 224801, (2002)

[141] M. Abo-Bakr, J. Feikes, K. Holldack, G. Wüstefeld, H.-W. Hübers, "*Steady-State Far-Infrared Coherent Synchrotron Radiation Detected at BESSY II*", PRL **88**, 254801, (2002)

[142] C. Thomas, G. Rehm, "*Diamond Optical Diagnostics: First Streak Camera Measurements*", Proc. EPAC 2006, p. 1112, (2006)

[143] C. Thomas, G. Rehm, I. Martin, "*Performance of a Stream Camera Using Reflective Input Optics*", Proc. IPAC 2010, p. 1170, (2010)

[144] G. Wüstefeld, "*Short Bunches in Electron Storage Rings and Coherent Synchrotron Radiation*", Proc. EPAC 2008, p. 28, (2008)

[145] G. Rehm, A. Morgun, R. Bartolini, I. Martin, P. Karataev, "*Ultra-Fast mm-Wave Detectors for Observation of Microbunching Instabilities in the Diamond Storage Ring*", Proc. DIPAC 2009, p. 369, (2009)

[146] W.M. Fawley, "*A User Manual for GINGER and its Post-Processor XPLOTGIN*", LBNL Technical Report LBNL-49625-Rev.1, (2004)

[147] S. Reiche, "*GENESIS 1.3: A Fully 3D Time-Dependent FEL Simulation Code*", NIM-A **429**, p. 243, (1999)

[148] L. Giannessi, "Overview of PERSEO, A System for Simulating FEL Dynamics in MATHCAD", Proc. FEL 2006, p. 91, (2006)

[149] E. Saldin, E. Schneidmiller, M. Yurkov, "*On the Coherent Radiation of an Electron Bunch Moving in an Arc of a Circle*", NIM-A **398**, p. 373, (1997)

[150] M. Borland, "*Simple Method for Particle Tracking with Coherent Synchrotron Radiation*", PRST-AB **4**, 070701, (2001)

[151] E. Saldin, E. Schneidmiller, M. Yurkov, "*Longitudinal Space Charge Driven Microbunching Instability in TTF2 Linac*", DESY Report TESLA-FEL-2003-02, (2003)

[152] M. Borland, "*Modelling of the Microbunching Instability*", PRST-AB **11**, 030701, (2008)

[153] J. Qiang, S. Lidia, R. Ryne, C. Limborg-Deprey, "*Three-Dimensional Quasistatic Model for High Brightness Beam Dynamics Simulations*", PRST-AB **9**, 044204, (2006)

[154] M. Dohlus, T. Limberg, "*CSRtrack: Faster Calculation of 3-D CSR Effects*", Proc. FEL 2004, p. 18, (2004)

[155] K. Floettmann, ASTRA code, https://www.desy.de/~mpyflo

[156] L. Young, J. Billen, http://laacg.lanl.gov/laacg/services/parmela.html

[157] J. H. Han, H. Huang, S. Pande, "*Technical Design of the Baseline Gun for the NLS Project*", Proc. FEL 2009, p. 340, (2009)

[158] D. Proch, "*The TESLA Cavity: Design Considerations and RF Properties*", TESLA Note 1994-13, (1994)

[159] Z. Huang, M. Borland, P. Emma, J. Wu, C. Limborg, G. Stupakov, J. Welch, "*Suppression of Microbunching Instability in the Linac Coherent Light Source*", PRST-AB **7**, 074401, (2004)

[160] E. Vogel, M. Dohlus, H. Edwards, E. Harms, M. Huening, K. Jensch, T. Khabiboulline, A. Matheisen, W.-D. Moeller, A. Schmidt, M. Singer, "*Considerations on the third harmonic RF of the European XFEL*", Proc. SRF 2007, p. 481, (2007)

[161] J. H. Han, "*Design of a Normal Conducting L-Band Photoinjector*", Proc. PAC 2009, p. 497, (2009)

[162] J.B. Rosenzweig, D. Alesini, G. Andonian, M. Boscolo, M. Dunning, L. Faillace, M. Ferrario, A. Fukusawa, L. Giannessi, E. Hemsing, G. Marcus, A. Marinelli, P. Musumeci, B. O'Shea, L. Palumbo, C. Pellegrini, V. Petrillo, S. Reiche, C. Ronsivalle, B. Spataro, C. Vaccarezza, "*Generation of Ultra-Short, High Brightness Electron Beams for Single Spike SASE FEL Operation*", NIM-A **593**, p. 39, (2008)

[163] S. Reiche, H. Braun, Y. Kim, M. Pedrozzi, "*Low Charge Operation of SwissFEL*", Proc. FEL 2009, p. 59, (2009)

[164] J. Yan, M. Zhang, H.-X. Deng, "*Self-Consistent "Start-to-End" Simulation for Free Electron Laser*", NIM-A **615**, p. 249, (2010)

[165] S. Schreiber, B. Faatz, K. Honkavaara, "*Operation of FLASH at 6.5nm Wavelength*", Proc. EPAC 2008, p. 133, (2008)

[166] H. Schlarb, C. Gerth, W. Koprek, F. Loehl, E. Vogel, "*Beam Based Measurements of RF Phase and Amplitude Stability at FLASH*", Proc. DIPAC 2007, p. 307, (2007)

[167] A. Chao, "*Laser Acceleration – Focussed Laser*", SLAC-PUB-9574, http://www.slac.stanford.edu/~achao/LaserAccelerationFocussed.pdf, (Rev. 9 Jan 2009)

[168] A.L. Cavalieri, E. Goulielmakis, B. Horvath, W. Helml, M. Schultze, M. Fieß, V. Pervak, L. Veisz, V.S. Yakovlev, M. Uiberacker, A. Apolonski, F. Krausz, R. Kienberger, "*Intense 1.5-Cycle Near Infrared Laser Waveforms and Their Use for the Generation of Ultra-Broadband Soft X-Ray Harmonic Continua*", New J. Phys. 9, 242, (2007)

[169] J. Rauschenberger, T. Fuji, M. Hentschel, A.-J. Verhoef, T. Udem, C. Gohle, T.W. Hansch, F. Krausz, "*Carrier-Envelope Phase-Stabilized Amplifier System*", Las. Phys. Lett. **3**, p. 37, (2006)

[170] A.J. Verhoef, J. Seres, K. Schmid, Y. Nomura, G. Tempea, L. Veisz, F. Krausz, "*Compression of the Pulses of a Ti:Sapphire Laser System to 5 Femtoseconds at 0.2 Terawatt Level*", Appl. Phys. B **82**, (2006)

[171] H. Ehrke, R.I. Tobey, S. Wall, S.A. Cavill, M. Forst, V. Khanna, T. Garl, N. Stojanovic, D. Prabhakaran, A.T. Boothroyd, M. Gensch, A. Mirone, P. Reutler, A. Revcolevschi, S.S. Dhesi, A. Cavalleri, "*Photoinduced Melting of Antiferromagnetic Order in* $La_{0.5}Sr_{1.5}MnO_4$ *Measured Using Ultrafast Resonant Soft X-Ray Diffraction*", PRL **106**, 217401, (2011)